SISSA
Scuola
Internazionale
Superiore di
Studi Avanzati

Physics Area – PhD course in
Theory and Numerical Simulation of Condensed Matter

Static and dynamical properties of frustrated spin models

Candidate:
Francesco Ferrari

Advisor:
Dr. Federico Becca

Academic Year 2018-2019

Through the darkness of future's past,
the magician longs to see.
One chants out between two worlds...
"Fire... walk with me."

Twin Peaks - Epsisode 2

Table of Contents

Summary

This thesis is devoted to the numerical investigation of quantum spin models which describe the low-energy physics of frustrated magnets. At extremely low temperatures, these systems can host the so-called *spin liquid* phase, an unconventional state of matter characterized by a high degree of quantum entanglement and the absence of magnetic order. The experimental identification of the spin liquid phase in actual materials relies on the detection of its distinctive excitations (named *spinons*), which possess *fractional* quantum numbers and can be probed by inelastic neutron scattering experiments.

From the theoretical point of view, variational methods have been largely employed to tackle ground state properties of frustrated spin models. In particular, variational Monte Carlo techniques based on Gutzwiller-projected fermionic wave functions have been shown to provide accurate results for several frustrated systems. In this thesis, we pursue an extension of this variational scheme to target dynamical spectra, which are directly measured by inelastic neutron scattering experiments. Specifically, we compute the dynamical structure factor by constructing approximate excited states, which are obtained by applying two-spinon operators to the ground state wave function. Our results prove that this variational method can accurately describe the spectral features of different spin systems. Focusing on prototypical frustrated models on the square and triangular lattices, we observe how the dynamical structure factor reflects the phase transition between a magnetically ordered phase with spin wave excitations, to a spin liquid state with fractional degrees of freedom.

In addition to spectral properties, we also explore new directions to improve the accuracy of Gutzwiller-projected states by the application of a neural network correlator, in the form of a *restricted Boltzmann machine*. While this hybrid variational scheme provides a considerable improvement of the variational energy in the case of unfrustrated spin models, less satisfactory results are obtained for frustrated systems, which call for further refinements of the neural network variational *Ansätze*.

This thesis is organized as follows:

- ▷ in Chapter 1, we provide a short introduction to the exotic phases of matter which can be realized in frustrated magnets, and the way they can be characterized by inelastic neutron scattering experiments and numerical calculations;
- ▷ in Chapter 2, the *projective symmetry group* approach developed by Xiao-Gang Wen is discussed from a variational perspective; this chapter does not contain any new result in the field, and it is only meant to be a simplified review of the method;
- ▷ in Chapter 3, we outline the variational Monte Carlo techniques employed in this thesis, mainly focusing on the variational approach for the calculation of dynamical spectra;
- ▷ in Chapter 4, we present the numerical results for the dynamical structure factor of various frustrated spin models;
- ▷ in Chapter 5, we assess the accuracy of the variational wave functions based on the combination of Gutzwiller-projected *Ansätze* and restricted Boltzmann machines.

Finally, in Chapter 6, we summarize the results of the thesis, drawing our conclusions.

1

Introduction

CONTENTS

1.1 Topological order and fractionalization

Matter manifests itself in several different *phases*, which are the macroscopic outcomes of the microscopic arrangement of its fundamental constituents. For a long time before 1980s, physicists believed that all phases of matter could be distinguished on the basis of Landau's theory [1]: different phases of a physical system are identified by different kinds of *local order*, which are associated with preserved/broken *symmetries*. For example, water molecules form a "disordered" continuous medium in the liquid phase, while being "ordered" in a periodic arrangement within the solid phase. The phase transition between liquid water and ice, which can be driven by a change of temperature or pressure, is accompanied by the breaking of the continuous translational symmetry. In addition to classical phase transitions, Landau's paradigm was believed to capture also the underlying mechanism of quantum phase transitions, that occur at zero temperature ($T = 0$) and involve the change of the ground state of a quantum system as a consequence of the variation of some physical parameters of the Hamiltonian. The simplest example is the phase transition of the one-dimensional Ising model in transverse field from a ferromagnetic (ordered) to a paramagnetic (disordered) ground state [2].

All the known phases of matter seemed to fall within the bounds of Landau's theory until fractional quantum Hall effect was experimentally observed for the first time in 1982 [3]. Within this phenomenon, a two-dimensional electron gas subject to a strong magnetic field displays a set of quantized values of the Hall conductivity $\sigma_H = \frac{e^2}{h}\nu$, which depend upon specific rational values of the *filling factor* ν [4]. Surprisingly, the different phases of the fractional quantum Hall effect, which are labelled by different values of ν, possess exactly the same symmetries and cannot be discriminated by any conventional local order parameter, thus escaping Landau's paradigm. A key to access the fundamental properties of these phases was provided by the theoretical contribution of Laughlin, who devised a family of strikingly accurate variational *Ansätze* for the quantum states with filling fraction $\nu = 1/q$ ($q = 3, 5, ...$) [5].

The discovery of the fractional quantum Hall effect motivated the definition of a new kind of (global) order, named *topological order*, which goes beyond Landau's theory of phase transitions [6–8]. Topologically ordered phases are ground states of quantum many-body systems that exhibit long-range entanglement and a plethora of unconventional properties. One of the fingerprints of topological order is *fractionalization*, i.e. the emergence of quasiparticle excitations having quantum numbers that are non-integer multiples of those of the constituent particles. In fractional quantum Hall systems, this exotic phenomenon was first theoretically predicted by Laughlin [5] and then experimentally detected in the $\nu = 1/3$ phase, where the electrons decay into quasiparticles carrying one third of the electron charge [9].

Fractionalization is also observed in magnetic systems, where spin wave excitations can decay into more exotic quasiparticles. The simplest theoretical example in this sense is the antiferromagnetic $S = 1/2$ Heisenberg model on a one-dimensional chain, which is analytically solvable by Bethe Ansatz [10]. In this system, at $T = 0$, long-range magnetic order is hampered, in agreement with the generalized Mermin-Wagner theorem [11], and the elementary excitations of the model are $S = 1/2$ particles called *spinons* [12]. Since, for any chain with a fixed number of sites, the minimal change in the total spin is $\Delta S = \pm 1$, the existence of objects with $S = 1/2$ implies a fractionalization of the spin quantum number. However, this picture does not hold for the generalization of the model to two dimensions. Indeed, the $S = 1/2$ antiferromagnetic Heisenberg model on the square lattice is characterized by a magnetically ordered ground state, whose excitations are $S = 1$ spin waves (called *magnons*). In general, most magnetic systems in two and three dimensions are expected to develop long-range order when cooled down to zero temperature. The properties of these systems are qualitatively (and sometimes also quantitatively) captured by semi-classical approaches, such as spin-wave calculations, in which a classically ordered ground state is dressed by quantum fluctuations.

A notable exception to the above conventional picture in two and three dimensions is represented by *frustrated magnets*, which are physical systems in which the onset of long-range magnetic order at zero temperature is prevented by the presence of competing interactions between the spins that cannot be simultaneously satisfied [13]. Then, as a consequence of quantum fluctuations, which are particularly effective in magnetic systems with low spin values (e.g., $S = 1/2$) and low coordination numbers, exotic phases of matter can be stabilized, such as the *spin liquid* state. Spin liquids are not only characterized by the absence of any local order, but they also display some of the most peculiar features of topological order, such as long-range entanglement and the emergence of spinon excitations and gauge fields [14–17]. The existence of the spin liquid phase was first theorized by Anderson in 1973 as a variational guess for the ground state wave function of the $S = 1/2$ antiferromagnetic Heisenberg model on the triangular lattice [18, 19]. The idea of Anderson is built upon the concept of *resonating valence bond* (RVB) states, whose roots date back to the early works of the 1930s by Rumer [20] and Pauling [21] concerning the description of the chemical bonds in molecules, later generalized by Pauling to extended systems [22]. Within this framework, spin liquid wave functions are expressed as massive superpositions of all the possible states which are formed by pairing all the N spins of the lattice into $N/2$ singlets [23]. The result is a highly entangled quantum state[1] with no magnetization. Although the idea of Anderson for the ground state of the triangular lattice antiferromagnet turned out to be incorrect, because the system was proved to

[1] Following the argument of Ref. [15], we define an entangled wave function as a superposition state which cannot be transformed into a product state by a local change of basis. The RVB wave function of Anderson falls within the bounds of this definition (see also Section 1.2).

develop magnetic order at $T = 0$ [24–26], it gave origin to an intense research line aimed at finding an actual realization of the spin liquid phase in frustrated magnets.

The simplest source of frustration in magnetic systems comes from the geometric arrangement of the spins [14]. For this reason, the quest for an experimental realization of the spin liquid phase has first moved in the direction of exploring two- and three-dimensional materials whose magnetic constituents reside on the sites of geometrically frustrated lattices, as in the case of *Herbertsmithite*, which displays a kagomé lattice geometry [27]. The theoretical models which have been studied to account for the physics of these geometrically frustrated magnets are based on simple Heisenberg-like superexchange interactions between spins. Few modifications to this scenario have been considered, e.g. spin anisotropies, chiral couplings [28, 29], and ring-exchange interactions [30, 31], but, in general, the main origin of frustration has been encoded in the competition of different Heisenberg terms originating from the geometric structure of the lattice [13]. More recently, an alternative mechanism to induce frustration emerged: following the groundbreaking work by Kitaev, who introduced an exactly solvable model featuring a spin liquid ground state [32], Hamiltonians with bond-directional couplings have been intensively investigated [33–35]. This kind of spatially anisotropic interactions can arise in Mott insulators as a consequence of strong spin-orbit coupling effects [34–36].

Generally speaking, theoretical models for frustrated magnetism involve many-body Hamiltonians which are analytically intractable. Moreover, semi-classical approaches such as spin-wave analyses are doomed to fail when the magnetic order of the system is melted by quantum fluctuations, and in most situations quantum Monte Carlo calculations are prevented by the presence of "sign problem" due to frustration [37]. Therefore, apart from exact diagonalizations on small clusters, numerical treatments of frustrated models are commonly based on a variational framework, as in the case of variational Monte Carlo [38], density matrix renormalization group (DMRG) [39] and tensor networks techniques [40]. The investigation of frustrated magnetism is a hard task also from an experimental point of view since, due to the lack of any local order, the identification of a quantum spin liquid phase typically requires a combination of different experimental measurements [17]. Microscopic probes such as muon-spin relaxation and nuclear magnetic resonance can be exploited to rule out the presence of magnetic order at low temperatures ($T \ll J/K_B$, where J indicates the strength of the exchange coupling) [41]. This analysis is complicated by the fact that the absence of long-range order may be just a spurious effect caused by disorder in the experimental samples. Therefore, further evidence of the existence of a spin liquid phase is provided by experimental probes which are sensitive to fractional excitations, such as inelastic neutron scattering, resonant inelastic x-ray scattering, Raman spectroscopy, and thermal Hall conductivity measurements [41].

The central subject of this thesis is the numerical investigation of frustrated spin models by a variational Monte Carlo approach, with a specific focus on the calculation of excitation spectra which are directly measured by neutron scattering experiments. The remainder of this chapter is dedicated to the presentation of some fundamental aspects that will form the backbone of the topics studied in this thesis: in the next section, we take advantage of the RVB picture of Anderson to provide a brief (rather phenomenological) introduction to spin liquid states (and valence bond solids), and to their distinctive excitations; then, in Section 1.3, we discuss a key quantity for the characterization of spin liquid phases, namely the *dynamical structure factor*, and we supply a short summary of (some) past experimental and theoretical results regarding the excitation spectra of frustrated magnets; finally, in Sections 1.4 and 1.5, we introduce the *parton* construction on which the variational methods used in this thesis are based.

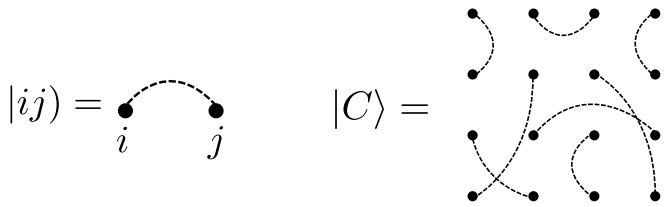

Figure 1.1: Sketch of a valence bond $|ij)$ (left figure) and a generic valence bond configuration $|C\rangle$ on the square lattice (right figure). Since $|ij)$ is an antisymmetric object under the exchange of sites $i \leftrightarrow j$, the definition of VB coverings depends upon a certain convention for the orientation of the singlets. However, for the sake of simplicity, we will ignore this rather technical aspect, since it is not relevant for the present discussion.

1.2 The RVB picture

Let us begin our discussion with a simple observation: the ground state wave function for a pair of $S = 1/2$ spins, $\mathbf{S}_i$ and $\mathbf{S}_j$, which interact through antiferromagnetic exchange, $\mathbf{S}_i \cdot \mathbf{S}_j$, is the singlet

$$|ij) = \frac{1}{\sqrt{2}}\Big(|\uparrow_i\downarrow_j\rangle - |\downarrow_i\uparrow_j\rangle\Big). \tag{1.1}$$

The state $|ij)$, called *valence bond* (VB), is a $S = 0$ object with no classical counterpart that constitutes a natural building block for the definition of nonmagnetic states. Indeed, for any given lattice model of N spins, we can introduce a set of *valence bond configurations*, named $\{|C\rangle\}$, which represents an overcomplete basis for the $S_{tot} = 0$ sector of the Hilbert space. The elements of this set are obtained by pairing all the spins of the lattice into $N/2$ (non overlapping) singlets (see Fig. 1.1)[42]. In other words, a generic VB configuration is a product state of singlets,

$$|C\rangle = |i_1 j_1) \otimes |i_2 j_2) \otimes \cdots \otimes |i_{N/2} j_{N/2}), \tag{1.2}$$

in which each site of the lattice appears only once. The basis set is formed by all the possible inequivalent ways of covering the lattice with $N/2$ singlets. We will consider two broad class of nonmagnetic states which can be expressed as linear combinations of VB configurations, namely *valence bond solids* and *spin liquids*.

1.2.1 Valence bond solids (VBS)

A valence bond solid (VBS) is a nonmagnetic state described by a superposition of VB configurations which displays some kind of long-range order in the arrangement of the singlets. In general, VBS states break some of the lattice symmetries of the spin model, thus representing (conventionally) ordered phases of matter, according to Landau's paradigm [23]. For the sake of clarity, let us introduce VBS states by resorting to simple examples on the square lattice.

In the top panels of Fig. 1.2, we depict the so-called horizontal and vertical *dimer* VBS states, which are described by single VB configurations in which the lattice is covered by a repeated pattern of horizontal and vertical singlets formed by neighboring spins. The periodic arrangement of the VB coverings clearly breaks both the translational and the rotational symmetries of the square lattice. This simple example shows the procedure through which a VBS state is constructed: at first, a certain number of spins is grouped

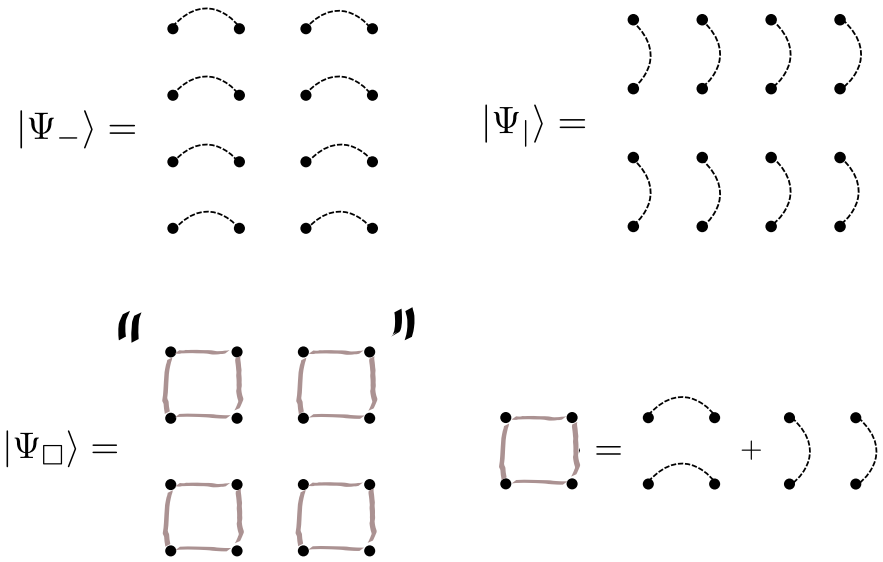

Figure 1.2: Schematic representation of the horizontal dimer (top left figure), vertical dimer (top right figure), and plaquette (bottom figure) VBS states on the square lattice.

to form a particular cluster (here, a first-neighbor VB); then, the lattice is covered by a periodic pattern of these clusters, and the VBS state is obtained by taking the tensor product of the wave functions of the various clusters. Another example on the square lattice is sketched in the bottom panel of Fig. 1.2, namely the *plaquette* VBS, which breaks the translational symmetry, but is rotationally invariant. The elementary cluster defining this state is a square plaquette of four spins which is formed by two pairs of resonating dimers (in a "Kekulé fashion"). The plaquette cluster is repeated all over the lattice in a periodic arrangement and the VBS wave function is obtained by taking the tensor product of all the plaquette states. The result is a linear superposition of 2^{N_p} VB coverings, with N_p being the number of plaquettes.

In the case of realistic spin Hamiltonians, VBS phases arise by a mechanism of order-by-disorder, in which certain periodic VB patterns become energetically favourable due to the effect of quantum fluctuations. As a consequence, the ground state wave function is in general a superposition of VB configurations which are connected to a certain ordered VB pattern (e.g. the dimer configuration of Fig. 1.2) by a number of local rearrangements of the singlets [23].

1.2.2 Spin liquids

Following the idea of Anderson, spin liquid states can be described by RVB wave functions, which are massive superpositions of VB coverings:

$$|\Psi_{RVB}\rangle = \sum_C \phi(C)|C\rangle. \tag{1.3}$$

In general, the above linear combination includes a number of VB configurations which grows exponentially with the system size. As a consequence of this macroscopic resonance, the resulting wave function is expected to possess a high degree of entanglement. Furthermore, at variance with the VBS case, in which the system is expected to display long-range order in some cluster-cluster correlation function, spin liquid states are completely disordered phases of matter. Indeed due to the absence of a preferred VB arrangement (see

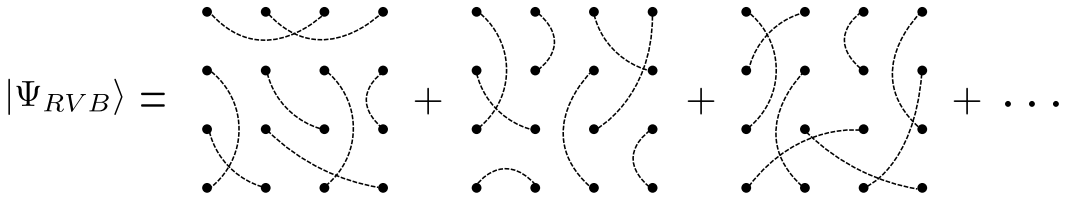

Figure 1.3: Schematic representations of RVB spin liquids. For the sake of simplicity, the expansion coefficients $\phi(C)$ of the linear combination (1.3) are not explicitly shown in the picture.

Fig. 1.3), the RVB wave function is completely symmetric and does not develop long-range order in any local order parameter [23].

A fundamental property that distinguishes VBS and spin liquid phases is the nature of their characteristic excitations. As pointed out previously, *fractionalization* is the hallmark of spin liquid states, whose elementary excitations are $S = 1/2$ spinons. Exploiting the VB construction for ground state wave functions, we are going to use a phenomenological argument to show why (isolated) spinons cannot be created in (2D) VBS states, and why this is instead possible in spin liquids.

1.2.3 Excitations in VBS and spin liquids

The simplest spin excitation which can be triggered by an external probe (e.g. a neutron scattering process) is a local spin flip, which is represented here by the raising operator $S_j^+ = S_j^x + iS_j^y$ transforming the singlet $|ij)$ into the $S^z = 1$ triplet $|\uparrow_i\uparrow_j\rangle$. For a pair of spins interacting through an exchange coupling of strength J, performing a spin flip starting from a VB configuration has a cost $\Delta E = J$. Once the spins of the VB have been "unpaired", we can ask ourselves what is the energy cost needed to bring them one far apart from each other, thus creating an actual pair of separate spinons.

As shown schematically in Fig. 1.4, in the prototypical example of the dimer VBS state, the separation of the two unpaired spins disrupts the original arrangement of the singlets and creates a string of misaligned dimers. The cost of the process of separation is approximately proportional to the length of this string, and this prevents the possibility of creating two independent $S = 1/2$ objects. In this scenario, the spinons are said to be *confined*. Therefore, in general, the elementary excitations of a VBS phase correspond to the creation of localized triplets (sometimes called *triplons*), carrying spin $S = 1$. From the point of view of inelastic neutron scattering experiments, triplons are expected to appear as sharp gapped modes [23].

Let us observe that the above argument does not hold in one dimension. As an example, we consider one of the two degenerate ground states of the Majumdar-Ghosh (MG) chain [43], which is a product state of nearest-neighbor singlets, as shown in the top panel of Fig. 1.5:

$$|\Psi_{MG}\rangle = \bigotimes_{i=1}^{N/2} |(2i-1)(2i)). \tag{1.4}$$

The other ground state of the model is obtained by simply shifting all the singlets of one lattice spacing[2]. Again, we imagine acting with an external probe which performs a spin flip and breaks a VB. As shown in Fig. 1.5, in this case the separation of the two unpaired

[2]Here we are assuming that the system is in the thermodynamic limit, or that it has an even number

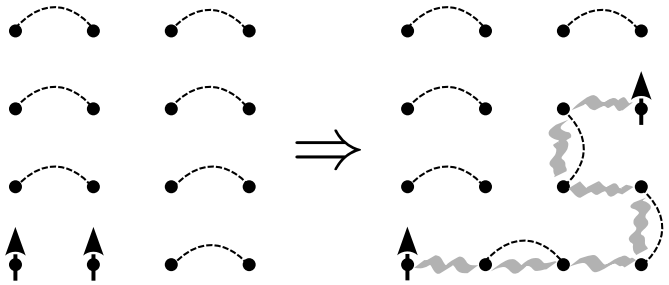

Figure 1.4: Schematic representation of a triplet excitation in the dimer VBS state on the square lattice. The attempt to separate the two unpaired spins is prevented by the energy cost associated with the disruption of the VB arrangement (grey string).

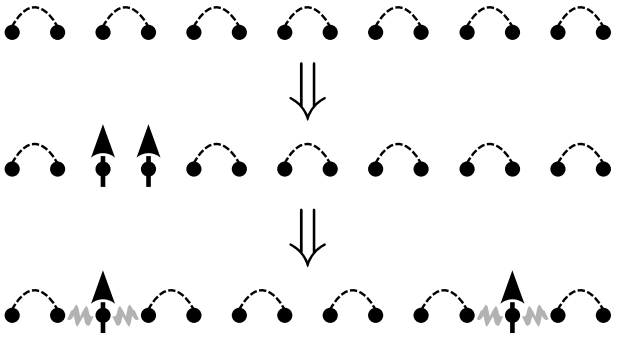

Figure 1.5: In the top panel we show a schematic representation of one of the two degenerate ground states of the Majumdar-Ghosh chain [$|\Psi_{MG}\rangle$, see Eq. (1.4)]. At variance with the VBS states in two dimensions, separating two unpaired spinons in the dimerized chain (central/bottom panel) doesn't require any additional cost because the singlets are rearranged in a regular pattern (corresponding to the one of the other ground state, $T|\Psi_{MG}\rangle$). Thus, the energy cost required for the excitation of two separate spinons is finite.

spins does not imply a disruption of the VB arrangement. Indeed, elementary excitations can be seen as defect boundaries between the two aforementioned ground states, which can freely propagate (the string of misaligned singlets, observed for the dimer VBS, is reduced here to pointlike domain walls) [44]. Thus, the cost required to create a pair of separate $S = 1/2$ objects is finite, and the system displays fractionalization of $S = 1$ excitations into spinons [45].

We conclude our analysis by considering the case of the RVB spin liquid state of Fig. 1.3. Here, the argument used to show the confinement of spinons in the VBS phase does not hold, since the wave function does not possess any particular order in the VB pattern. Therefore, the rearrangement of singlets associated to the spatial separation of two spinons simply corresponds to a reshuffling of the VB configurations entering the RVB superposition [23]. Quoting an expressive statement by Balents, in spin liquids "the

of sites and periodic boundary conditions. In both cases, $|\Psi_{MG}\rangle$ and $T|\Psi_{MG}\rangle$ (with T indicating the translation operator) are degenerate.

string (of misaligned dimers) is tensionless" [14]. In other words, spinons can be *deconfined* within the spin liquid phase.

From the experimental point of view, the signature of spinon deconfinement in neutron scattering spectra is the presence of a diffuse signal forming a broad continuum that extends both in energy and momentum [8, 23]. It is worth pointing out that, in general, spinon spectra can be gapped or gapless. The two possibilities can be explained with a handwaving argument in the RVB picture. Indeed, we can observe that breaking a long-range singlet requires less energy than breaking a short-range one when the Hamiltonian of the system only contains local couplings. Thus, RVB states containing only short-range VBs are usually expected to be gapped, while RVB states allowing for long-range singlets may display a gapless spectrum [14, 23].

Finally, let us mention that spin liquid states are known to support another class of excitations, known as *visons*, which carry $S = 0$ spin. In the framework of RVB wave functions for Z_2 spin liquids, visons can be constructed by changing the sign of the coefficients $\phi(C)$ of some selected VB configurations [23]. A more precise definition of the origin of these excitations is provided in the context of the *parton* construction introduced in Section 1.4, where visons are represented as fluctuations of emergent gauge fields [14, 45]. Most importantly, vison excitations are known to exist in the (exactly solvable) Kitaev model on the honeycomb lattice [32].

1.3 Spectral properties of magnets

Inelastic neutron scattering (INS) represents the experimental method of choice to probe the excitations of magnetic materials. As we have already pointed out, the nature of the excited states provides a clear indication of whether the system is in a magnetically ordered phase, or a more exotic VBS or spin liquid state. The INS process is a consequence of the interaction between the spins of the neutrons and the effective magnetic field generated by the magnetic moments of the material[3]. If we denote by q and ω the momentum and energy transferred by the neutron within the scattering process, we can write the following expression for the differential cross section,

$$\frac{d\sigma}{dEd\Omega} = F(q) \sum_{\alpha,\beta} \left(\delta_{\alpha,\beta} - \frac{q_\alpha q_\beta}{q^2} \right) S^{\alpha,\beta}(q,\omega), \tag{1.5}$$

which determines the intensity of the scattering signal [46]. The crucial quantity entering the above formula is the *dynamical structure factor*, which is the Fourier transform of the spin-spin correlation, and can be written in its spectral representation (at zero temperature) as follows[4]:

$$S^{\alpha,\beta}(q,\omega) = \sum_n \langle \Upsilon_0 | S^\alpha_{-q} | \Upsilon_n \rangle \langle \Upsilon_0 | S^\beta_q | \Upsilon_n \rangle \delta(\omega - E_n + E_0). \tag{1.6}$$

Here, S^α_q is the Fourier transform of the α-component of the spin ($\alpha = x, y, z$), $|\Upsilon_0\rangle$ and $\{|\Upsilon_n\rangle\}$ are the ground state and the set of all the excited states of the system, whose corresponding energy are denoted by E_0 and $\{E_n\}$, respectively. All the relevant

[3] We note that neutrons not only undergo magnetic scattering with spins, but they also scatter with atomic nuclei. Nevertheless, in INS experiments on single crystals, the contribution coming from magnetic scattering can be always separated from the one due to nuclear scattering [46].

[4] A precise derivation of this formula is given in Section 3.5.1.

information regarding the magnetic excitations of the system is encoded in the dynamical structure factor. This quantity can be directly obtained from the cross section of Eq. (1.5) since the factor $F(q)$ is a simple decreasing function of $|q|$, which can be ruled out by an appropriate correction of the spectral intensity [46]. We note that, due to the polarization factor $(\delta_{\alpha,\beta} - q_\alpha q_\beta/q^2)$ of Eq. (1.5), the only components of $S^{\alpha,\beta}(q,\omega)$ contributing to the signal are those which are perpendicular to the momentum q transferred by the neutron[5]. Nevertheless, all the desired terms of the dynamical structure factor can be reconstructed from INS experimental data by resorting to a polarization analysis [46, 47].

The remainder of this section is devoted to the discussion of some INS results from the literature, with the purpose of illustrating how the spectral features provide useful insights into the nature of the ground state of magnetic materials. In particular, we focus on antiferromagnetically ordered magnets and candidate spin liquid materials.

1.3.1 Magnetic order and spin waves

The INS spectra of magnetically ordered systems are dominated by the presence of intense Bragg peaks at $\omega = 0$ and $q = Q$, where Q is the ordering vector, namely the momentum of the Brillouin zone that determines the periodicity of the magnetic order [e.g., the antiferromagnetic Néel phase on the square lattice has ordering vector $Q = (\pi, \pi)$]. The elementary excitations of magnetically ordered systems are magnons, which are the Goldstone modes of the broken spin rotational symmetry. Within the linear spin wave approximation, magnons are coherent $S = 1$ excitations on top of the classically ordered ground state [48]. As such, they contribute to the dynamical structure factor with one delta peak for each momentum q. The result is a well-defined gapless branch displaying a strong intensity around the ordering vector Q. Going beyond the linear spin wave approximation, magnons become interacting objects and their effective Hamiltonian is usually treated by many-body perturbation theory methods. Typically, the energy and the intensity of the magnon branch get renormalized when interactions are taken into account. In case magnon decay is allowed, the spectrum acquires an incoherent part and the magnon peaks broaden due to the finite lifetime of the excitations [49]. Finally, we note that, in addition to the single-magnon branch, multi-magnon excitations are observed at higher energies in the dynamical structure factor.

Below we consider two examples of magnetically ordered systems, namely the square lattice and the triangular lattice Heisenberg antiferromagnets.

The square lattice antiferromagnet

An actual realization of the $S = 1/2$ antiferromagnetic Heisenberg model on the square lattice is represented by the metal-organic compound $Cu(DCOO)_2{\cdot}4D_2O$ (CFTD), which has been investigated by INS experiments [47, 50, 51]. In Fig. 1.6, we report some experimental and theoretical results taken from literature. For this material, the linear spin wave approach provides a good estimate of the magnon dispersion, especially at low-energies, namely around the gapless points $q = Q = (\pi, \pi)$ and $q = (0, 0)$. However, along the boundary of the magnetic Brillouin zone, where the spin wave theory predicts a flat dispersion, INS results show that the energy at $q = (\pi, 0)$ is smaller than the one at $q = (\frac{\pi}{2}, \frac{\pi}{2})$ by

[5] This fact can be explained with a simple argument [46]. If a neutron scatters with a spin oriented along z, it experiences an effective magnetic field pointing in the same direction, i.e. $B = (0, 0, B(r))$. According to Maxwell's equation we have that $\nabla \cdot B = \frac{\partial B(r)}{\partial z} = 0$, that translates into $q_z B(q) = 0$ in Fourier space. Since the momentum of the spin is equal to the one transferred by the neutron (q), we get a condition implying that q_z must be zero, i.e. the scattering vector must be perpendicular to the magnetic field. In other words, a neutron with a given momentum q can only probe spin components which are perpendicular to q.

7% (i.e., a roton mode appears). Furthermore, a largely suppressed spectral intensity is observed at $q = (\pi, 0)$, as shown in the lower right panel of Fig. 1.6 [47]. The physical origin of these two anomalous spectral features at the magnetic zone boundary is still under debate.

Numerical results, based on series expansions techniques [52, 54] and quantum Monte calculations [55, 56], have shown that the presence of the roton mode at $q = (\pi, 0)$ is a genuine feature of the square lattice Heisenberg model with nearest-neighbor interactions. Since this feature is not fully captured by spin wave expansions up to third order in $1/S$ [57], a non-perturbative many-body effect has been conjectured to be at the origin of the zone boundary anomaly. An intriguing interpretation of the spectral features at $q = (\pi, 0)$ involves the existence of nearly deconfined spinons [47, 58–61], while a more conventional picture resorts to strong attractive magnon-magnon interactions [62, 63].

Further aspects regarding the spectral properties of the square lattice antiferromagnet are discussed in Section 4.2, where the numerical results of this thesis are presented.

The triangular lattice antiferromagnet

A remarkably different scenario from the one outlined before is observed for the $S = 1/2$ antiferromagnetic Heisenberg model on the triangular lattice. As a consequence of the geometric arrangement of the spins, this model is characterized by strong quantum fluctuations which induce large deviations from the semiclassical limit. At variance with the square lattice antiferromagnet, the ground state of the system possesses a *noncollinear* magnetic order, with neighboring spins lying at 120° one with respect to each other [25, 26]. The noncollinearity of the magnetization implies that magnon excitations are subject to stronger interactions. In particular, perturbative studies based on the spin wave formalism [49, 64, 65] have shown that magnons are unstable in a large portion of the Brillouin zone due to the presence of three-magnon interactions (which are not allowed in the case of collinear magnetizations). Indeed, a kinematic analysis of linear spin wave energies is sufficient to conclude that magnons with certain momenta q can decay into pairs of magnons with momenta k and $q - k$, which have a lower energy. As a result of the decay processes, the linear spin wave dispersion is drastically renormalized (downward), and the magnon excitations acquire a finite lifetime, which is reflected by a broadening of the spectral branch (see Fig. 1.7) [49, 66].

Recently, experimental measurements on $Ba_3CoSb_2O_9$ have been reported, providing evidence that the low-energy physics of this material could be approximated by the $S = 1/2$ nearest-neighbor Heisenberg model on the triangular lattice [68]. In agreement with the aforementioned theoretical predictions, INS spectra of $Ba_3CoSb_2O_9$ show a strongly renormalized magnon dispersion with respect to linear spin wave results and a sizable line broadening, suggesting the possibility of magnon decay (see Fig. 1.8) [67]. On the other hand, the experimental data show the presence of an additional roton mode, which is not predicted by spin wave perturbative methods. This feature, which has been observed in recent DMRG calculations [69] and in the variational results discussed in this thesis (cf. Section 4.3) [70], could be related to a mechanism of avoided decay. Finally, the high-energy part of the INS spectra of $Ba_3CoSb_2O_9$ is dominated by a dispersive excitation continuum, whose origin is uncertain [67].

Further aspects regarding the spectral properties of the triangular lattice antiferromagnet are discussed in Section 4.3, where the numerical results of this thesis are presented.

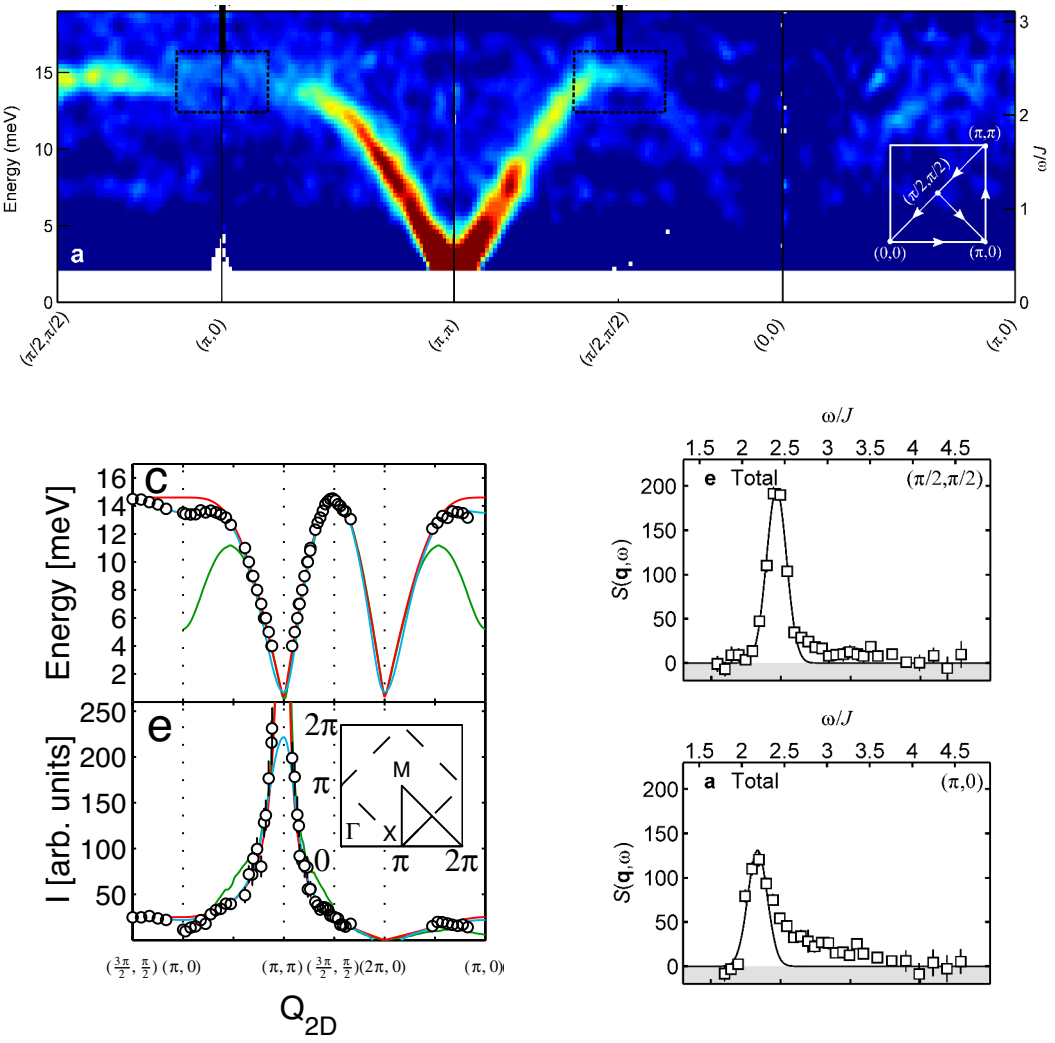

Figure 1.6: Top panel: INS spectrum of CFTD, as a function of energy and momentum, showing the presence of a well-defined magnon branch around $Q = (\pi, \pi)$. The figure has been taken from Ref. [47]. Lower left panel: magnon dispersion (above) and total spectral intensity (below) from INS data for CFTD (circles), compared with theoretical predictions by linear spin wave (red line), series expansion techniques (blue line) [52], and flux phase RVB (green line) [53]. We emphasize the difference between spin wave results and experimental data at the boundary of the magnetic Brillouin zone, namely between $q = (\frac{3\pi}{2}, \frac{\pi}{2})$ [equivalent to $q = (\frac{\pi}{2}, \frac{\pi}{2})$] and $q = (\pi, 0)$. The downward renormalization of the spectrum observed in INS experiments is recovered by series expansion results. The figure has been taken from Ref. [51]. Lower right panel: total dynamical structure factor $S(q, \omega)$ from INS data for CFTD. The value of $S(q, \omega)$ is plotted as a function of ω for scattering momenta $q = (\frac{\pi}{2}, \frac{\pi}{2})$ (top) and $q = (\pi, 0)$ (bottom). The experimental data (squares) have been fitted by Gaussian functions (solid lines). The figure, taken from Ref. [47], shows the smaller spectral intensity at $q = (\pi, 0)$ with respect to $q = (\frac{\pi}{2}, \frac{\pi}{2})$.

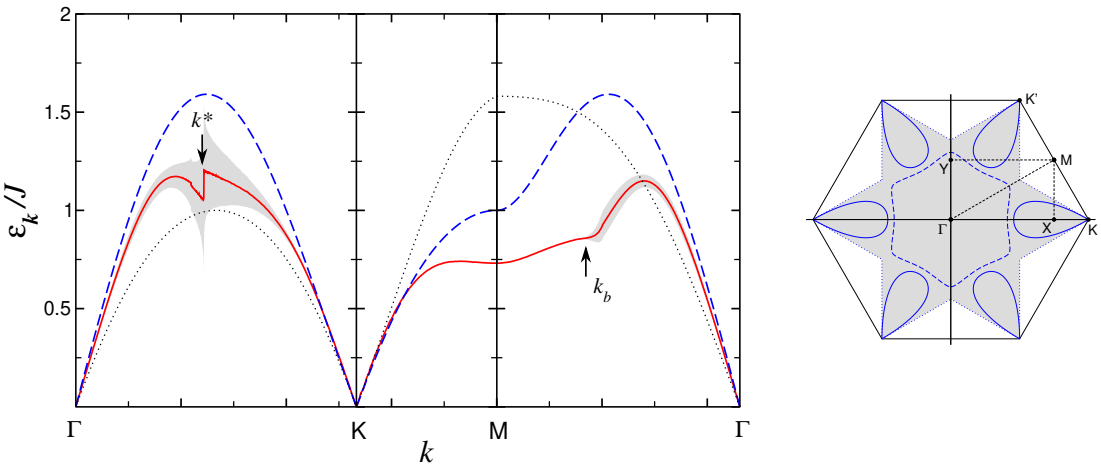

Figure 1.7: Left panel: magnon energies of the Heisenberg model on the triangular lattice within the linear spin wave approximation (blue dashed line) and with first-order $1/S$ corrections (red solid line). The downward renormalization of the spin wave branch is evident. We note that the shaded grey area represents the width of the magnon spectral peaks, which is related to the finite lifetime of the excitations due to magnon decay. Right panel: Brillouin zone of the triangular lattice. The grey shaded area corresponds to the region of the k-space in which magnon decay takes place. Both figures have been taken from Ref. [49].

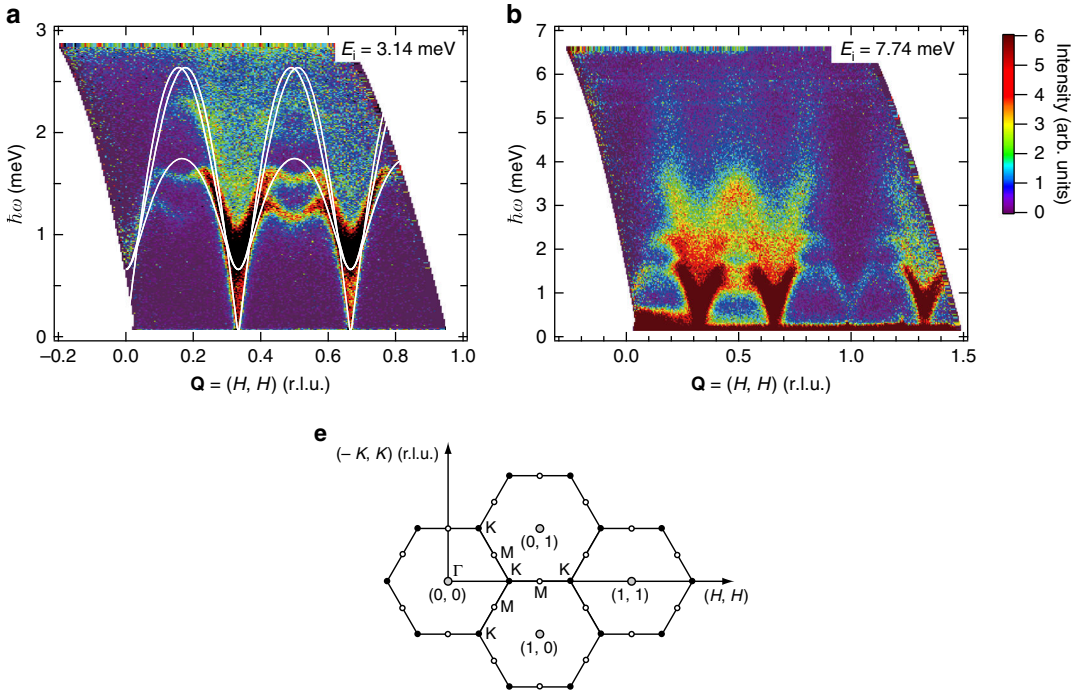

Figure 1.8: Top panels: INS spectra of $Ba_3CoSb_2O_9$ obtained by employing neutrons with incident energy of 3.14 meV (left) and 7.74 meV (right). The white solid lines correspond to the spin wave dispersion obtained by considering the small effects of easy-plane anisotropy and interlayer coupling (cf. Ref. [67] for details). Bottom panel: schematic representation of the high symmetry points of the Brillouin zone of the square lattice. The horizontal path, marked by (H, H), corresponds to the one of the plots of the top panels. Both figures have been taken from Ref. [67].

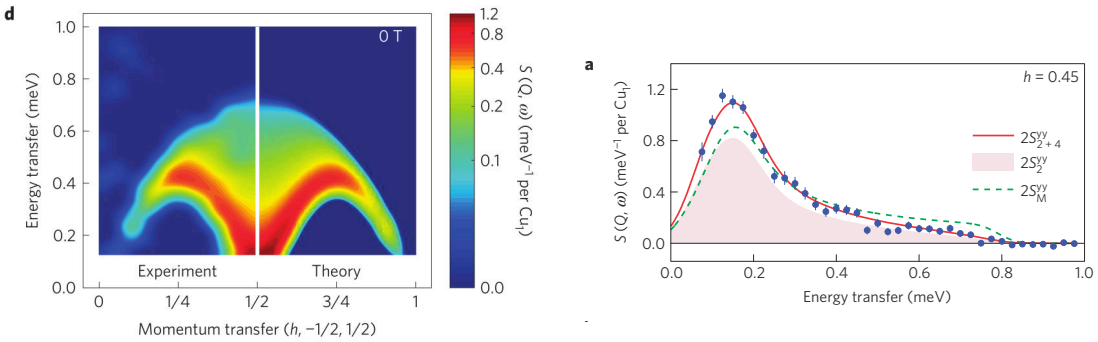

Figure 1.9: Left panel: INS spectrum of $CuSO_4{\cdot}5D_2O$ compared with theoretical predictions from the one-dimensional antiferromagnetic Heisenberg model. Right panel: dynamical structure factor at $q = 2\pi \times 0.45$ as a function of the energy transferred by the neutrons. Blue dots represent INS experimental results. We note that two-spinon excitations (pink shaded area) only account for part of the total spectral intensity. Including also four-spinon excitations (red line), a considerably better agreement with experimental results is achieved. Both figures have been taken from Ref. [71].

1.3.2 Fractionalized excitations

When fractionalization of $S = 1$ excitations into spinons takes place, INS spectra are expected to exhibit a broad continuum which extends in energy and momentum. Indeed, a neutron transferring a momentum q and an energy ω to the sample can excite any pair of $S = 1/2$ spinons with momenta k and $q - k$, whose energies, $\epsilon_s(k)$ and $\epsilon_s(q-k)$, need to satisfy the conservation law $\omega = \epsilon_s(k) + \epsilon_s(q-k)$. Therefore, for each value of q, a continuum of two-spinon excitations is observed for all the values of ω lying between the lower and upper boundaries of the convolution of spinon dispersions $\epsilon_s(k) + \epsilon_s(q-k)$.

As an example of the appearance of fractionalized excitations in INS spectra, we can mention the case of copper sulphate pentahydrate ($CuSO_4{\cdot}5D_2O$), which is well described by the antiferromagnetic Heisenberg model on a $S = 1/2$ spin chain [71]. As already pointed out, this model can be exactly solved by Bethe Ansatz [10] and its fractionalized spinon excitations are known to give rise to a gapless spectrum with a broad continuum of states (see left panel of Fig. 1.9) [72, 73]. As observed both theoretically [72, 74] and experimentally [71], two-spinon excitations only account for about 71% of the total spectral intensity, with the remaining contribution coming from higher-order spinon states (see right panel of Fig. 1.9).

For what concerns two-dimensional materials displaying fractionalization, we present the cases of Cs_2CuCl_4 and Herbertsmithite [$ZnCu_3(OH)_6Cl_2$].

Cs_2CuCl_4 and the anisotropic triangular lattice model

Cs_2CuCl_4 is a two-dimensional frustrated material which is described by a Heisenberg model on the triangular lattice with anisotropic couplings: as shown in the left panel of Fig. 1.10, the system can be regarded as a set of coupled spin chains, with the exchange interaction along the chains (J) being approximately three times larger than the interchain coupling (J'). Due to the presence of a tiny interlayer coupling ($\sim 0.05J$) in the direction orthogonal to the triangular lattice, the system develops an incommensurate magnetic order at low temperatures ($T < T_N = 0.62\ K$) [75, 76]. INS spectra for this material are dominated by a broad continuum of excitations which does not change significantly when the temperature crosses T_N. The main difference between the $T < T_N$ and $T > T_N$ regimes is the presence of a sharply defined low-energy mode in the former case [75, 76].

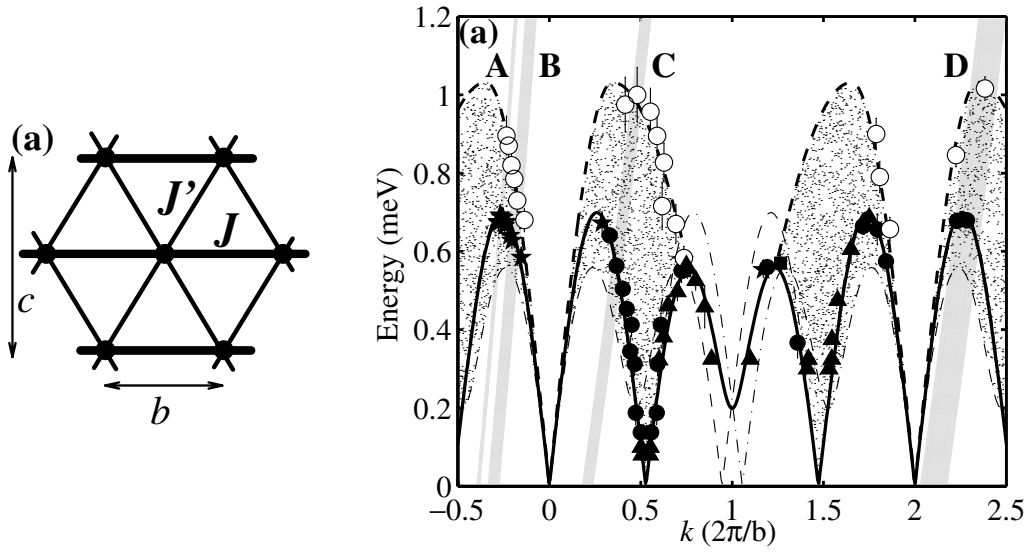

Figure 1.10: Left panel: schematic representation of the superexchange couplings of the effective Heisenberg model for Cs_2CuCl_4. One-dimensional chains of coupling constant J interact through the interchain superexchange J'. Right panel: INS spectrum of Cs_2CuCl_4 at $T = 0.1\ K < T_N$, which shows the presence of a broad (spinon) continuum above a sharp mode. Both figures have been taken from Ref. [75].

Due to its functional form, the continuum detected by INS (shown in Fig. 1.10) has been ascribed to the presence of spinons, rather than to a multi-magnon effect. Within the original picture of Refs. [75, 76], spinons were suggested to be deconfined above a certain energy threshold, while forming magnons through an attractive potential at low energies. For this reason, the existence of a genuine two-dimensional quantum spin liquid phase at temperatures slightly above T_N was theorized. However, more recently, a less unconventional explanation for the INS experimental findings has been proposed in Ref. [77], according to which the continuum observed in the spectrum is simply due to the "one-dimensional" spinons of the Heisenberg chains (which are coupled to form the triangular lattice). Due to the presence of the interchain coupling J', these spinons gain energy by forming triplon bound states which can propagate between the different chains. Within this scenario, the sharp peaks appearing in the low-energies part of INS spectra are interpreted as signatures of the triplon excitations[6] [77].

The kagomé lattice antiferromagnet

The clearest evidence of fractionalized excitations in a two-dimensional material is provided by the INS spectra of Herbertsmithite [$ZnCu_3(OH)_6Cl_2$], whose magnetic properties are ascribed to Cu^{2+} ions with effective $S = 1/2$ spins, which are arranged into kagomé lattice planes that are essentially decoupled one from each other. The simplest model that captures the low-energy physics of Herbertsmithite is the nearest-neighbor antiferromagnetic Heisenberg model on the kagomé lattice [27, 78]. The nature of the ground state of this model represents a long standing problem in the context of frustrated magnetism, with different approaches suggesting the existence of a spin liquid phase (with either gapless or gapped spinon excitations). This picture is supported by the INS spectrum of Herbert-

[6] We note that the picture of Ref. [77] holds only because interchain couplings are frustrated. Indeed, spin chains which are coupled to form a square lattice develop magnetic order as soon as J' becomes non zero (see Section 4.2 for a detailed discussion).

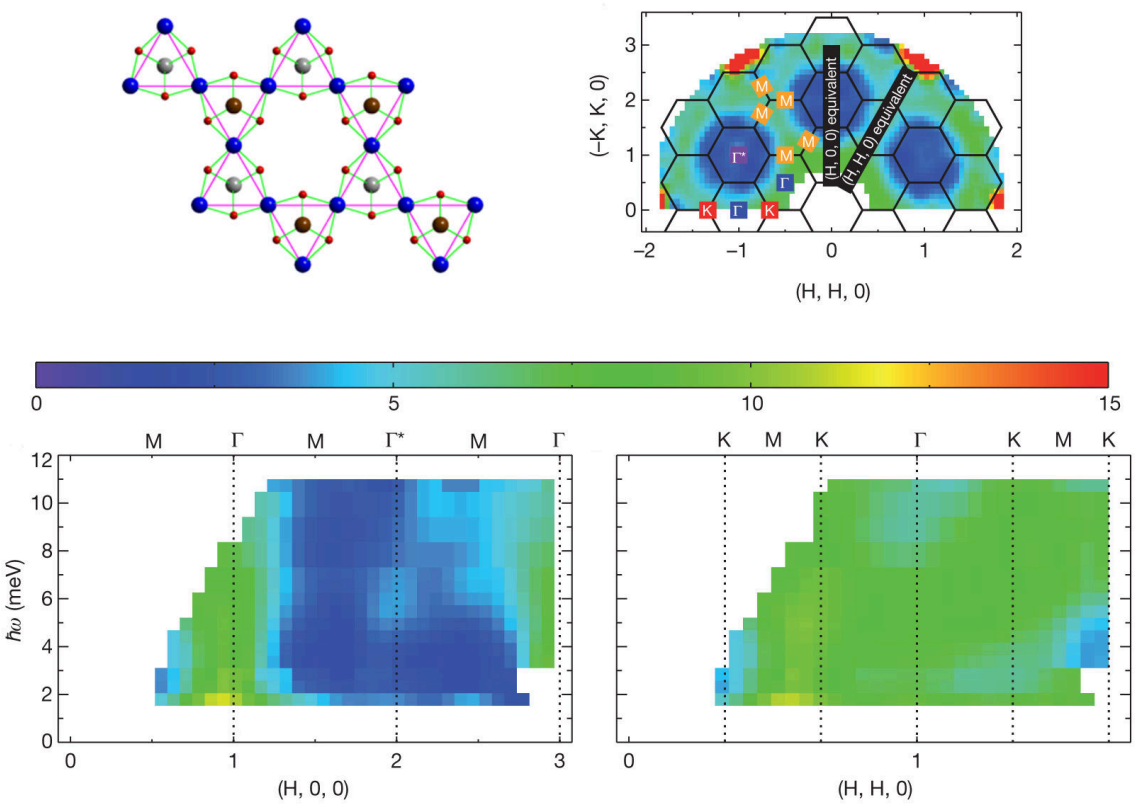

Figure 1.11: Upper left panel: schematic representation of the magnetic planes of Herbertsmithite, in which the Cu^{2+} ions (blue atoms) form a kagomé lattice structure (figure taken from Ref. [27]). Upper right panel: this figure, taken from Ref. [78], displays the integral in energy of the INS dynamical structure factor for different momenta in the extended Brillouin zone. The diffuse signal is interpreted as a signature of fractionalization. Lower panels: color maps of the INS spectral intensity as a function of momentum and energy. $(H, 0, 0)$ and $(H, H, 0)$ represent two high symmetry directions in reciprocal space, which are depicted in the figure in the upper right panel. In both spectra, which have been taken from Ref. [78], a broad continuum of excitations is observed.

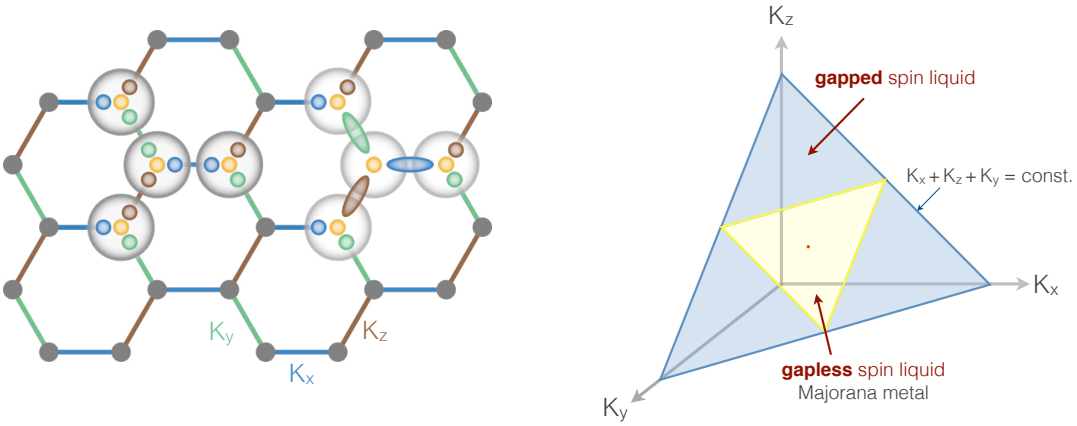

Figure 1.12: Left panel: schematic representation of the Kitaev model. The blue, green, and brown bonds correspond to the x, y, and z nearest-neighbor directions. Within the parton construction of Kitaev [32], the spin of each site is expressed in terms of four Majorana fermions: the blue, green, and brown circles respectively denote b^x, b^y, and b^z fermions, while the yellow circles denote the c fermions (see text). The b-fermions are recombined along each bond to form static bond variables (denoted by ovals). The remaining c-fermions are free to move in a background of static Z_2 gauge fluxes. Right panel: phase diagram of the Kitaev model. Both figures have been taken from Ref. [35].

smithite that is characterized by an almost dispersionless continuum of excitations (see Fig. 1.11), which is seemingly gapless over a wide range of momenta [78]. This feature has been interpreted as the fingerprint of the presence of spinon excitations. Furthermore, according to Ref. [79], the flat shape of the spectral continuum is due to the existence of $S = 0$ vison excitations, i.e. vortices of emergent gauge fields that interact with the spinons.

Visons are known to peculiarly contribute to the dynamical structure factor of the (exactly solvable) Kitaev model on the honeycomb lattice [32], which is briefly outlined in the following paragraph.

1.3.3 Vison excitations in the Kitaev model

The Kitaev model is a rare example of an exactly solvable (non-trivial) spin model which hosts a spin liquid ground state, with fractionalized excitations. Within this model, $S = 1/2$ spins sitting on the sites of a honeycomb lattice interact through bond-dependent Ising-like interactions:

$$\mathcal{H} = -K_x \sum_{\langle i,j\rangle \in x} \sigma_i^x \sigma_j^x - K_y \sum_{\langle i,j\rangle \in y} \sigma_i^y \sigma_j^y - K_z \sum_{\langle i,j\rangle \in z} \sigma_i^z \sigma_j^z. \tag{1.7}$$

Here, $\sigma_i^x, \sigma_i^y, \sigma_i^z$ are the three spin components of the spin at site i (a part for a factor 2, i.e. $\boldsymbol{\sigma}_i = 2\mathbf{S}_i$), and the notation $\langle\cdot\rangle \in \alpha$ indicates the three inequivalent nearest-neighbor directions depicted in Fig. 1.12 ($\alpha = x, y, z$). Depending on the relative strength of the coupling constants K_α, the spinon excitations of the spin liquid phase can be gapless or gapped (see the right panel of Fig. 1.12) [32].

The exact solution of the Kitaev model is based on a *parton* construction, in which the spin components are expressed in terms of four Majorana fermions (b^x, b^y, b^z, c), namely $\sigma_i^\alpha = i b_i^\alpha c$ $(\alpha = x, y, z)$[7]. In a nutshell, for each bond i, j of type α, the two neighboring b^α-

[7]The Majorana fermions representation of the spins artificially enlarges the Hilbert space, from 2^N

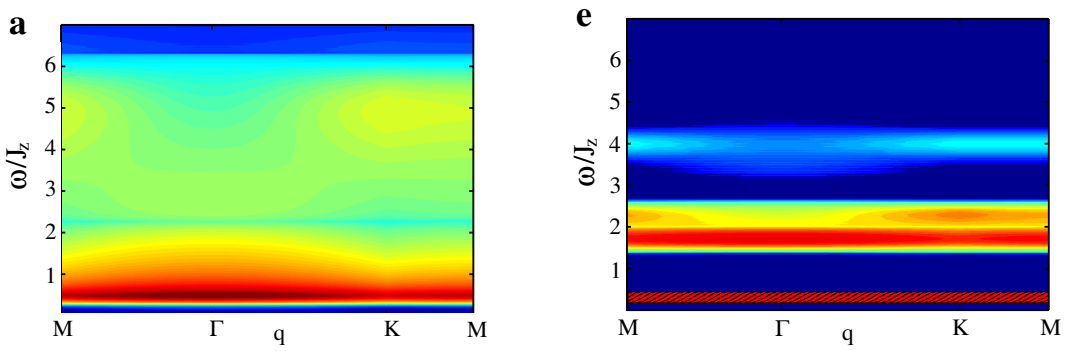

Figure 1.13: Spin dynamical structure factor of the Kitaev model in the cases $K_x = K_y = K_z$ (left panel) and $K_x = K_y = 0.15K_z$ (right panel), as a function of momentum and energy. Despite the fact that these two cases correspond, respectively, to a gapless and a gapped spectrum of the Majorana fermions, the dynamical response is gapped in both regimes due to the energy cost needed to excite a pair of visons. The spectrum on the left panel exhibits a broad continuum (as expected in presence of fractionalization), while the one on the right panel possesses a sharp mode at the vison gap. Both figures have been taken from Ref. [82].

Majorana fermions are recombined to form a bond operator $u_{i,j} = ib_i^\alpha b_j^\alpha$. The fundamental property which makes the Kitaev model exactly solvable lies in the fact that each bond operator $u_{i,j}$ commutes with the Hamiltonian. As a consequence, the operators $u_{i,j}$ are static variables which can take the values ± 1. The product of the $u_{i,j}$ surrounding a hexagonal plaquette p is a static Z_2 gauge flux denoted by W_p. Once the values of all the $u_{i,j}$ are fixed, we are left with a Hamiltonian of free c-Majorana fermions, whose coupling constants depend on the value of the gauge fluxes[8]. The ground state of the model is obtained by choosing a set $\{u_{i,j}\}$ which ensures that $W_p = 1$ for all plaquettes, e.g. $u_{i,j} = 1\ \forall i, j$ [32].

We note that the c-fermions of the Kitaev model correspond to the fractionalized spinon excitations of the spin liquid phase. Vison excitations instead are represented by vortices of the gauge flux, i.e. plaquettes with $W_p = -1$. Visons are always created in pairs by, for example, changing the sign of $u_{i,j}$ on a given bond. As shown by Baskaran and collaborators [80], a spin flip process, as the one triggered by INS, causes the creation of a pair of adjacent vison excitations, which is followed by a dynamical rearrangement of the c-fermions in response to the new configuration of gauge fluxes. Therefore, the dynamical structure factor of the Kitaev model, computed in Ref. [82], is strongly affected by the interplay of visons and Majorana fermions. Remarkably, the response of the model is gapped also in the region of the phase diagram in which c-fermions are gapless, and the gap corresponds to the energy required to excite a pair of visons starting from the ground state configuration of the fluxes. As shown in Fig. 1.13, two different regimes are identified: in one case the dynamical structure factor is dominated by a broad continuum, which is a signature of fractionalized excitations; in the other case, despite fractionalization, a sharp mode is observed right at the vison gap [82].

---

to 4^N states [80]. Therefore, the representation is valid only if it is restricted to the states $|\phi\rangle$ satisfying the constraints $c_i b_i^x b_i^y b_i^z |\phi\rangle = |\phi\rangle$, $\forall i$ [32]. The fictitious enlargement of the Hilbert space followed by a projection onto a physical subspace is a characteristic of parton constructions, e.g. the Abrikosov fermion approach defined in Section 1.4 and employed in this thesis.

[8]The role of the gauge fluxes is similar to the one of the magnetic fluxes in the Peierls' substitution approach for tight-binding models [81].

The Kitaev model represents a concrete example in which the elementary degrees of freedom of a spin model are exactly formulated in terms of fermionic particles and emergent gauge fields. In general, a convenient approach to tackle spin systems in which fractionalization is expected to occur is based on the introduction of partons. Within a parton construction, the spin operators are represented in terms of pairs of bosons or fermions, whose local Hilbert space is constrained to a subspace equivalent to the original Hilbert space of spins. This reformulation results in a rich theory of quasiparticles coupled to emergent gauge fields with the potential to shed light onto the underlying properties of the spin system. In the following sections, we introduce the fermionic representation of spins which is employed in this thesis to construct variational wave functions.

1.4 From spins to Abrikosov fermions

Let us consider, for the sake of generality, a $SU(2)$-invariant model for a frustrated magnet, which consists of a set of $S = 1/2$ spins sitting on the sites of a lattice and interacting through the Heisenberg exchange couplings $J_{i,j}$:

$$\mathcal{H} = \sum_{i<j} J_{i,j} \mathbf{S}_i \cdot \mathbf{S}_j. \tag{1.8}$$

The interplay of the different interactions forming the above Hamiltonian can lead to the stabilization of different phases of matter. In absence of frustration, i.e., when no competing couplings are present, the ground state may develop some kind of magnetic order, as in the case of the Heisenberg model on the square lattice. On the contrary, when different interactions compete with each other, magnetically disordered phases can arise, such as spin liquids and VBSs.

In the case of magnetically ordered systems a standard Curie-Weiss mean field decoupling of the interactions,

$$\mathcal{H}_{\mathrm{CW}} = \sum_{i<j} J_{i,j} \left[\langle \mathbf{S}_i \rangle \cdot \mathbf{S}_j + \mathbf{S}_i \cdot \langle \mathbf{S}_j \rangle - \langle \mathbf{S}_i \rangle \cdot \langle \mathbf{S}_j \rangle \right], \tag{1.9}$$

constitute the first approximate method to capture the physical properties of the model (e.g. the behaviour of the magnetization as a function of temperature) [83]. In the limit of zero temperature, quantum effects can be introduced by performing a linear spin wave approximation, in which small deviations around the classically ordered ground state are considered. However, both the aforementioned approaches fail when the ground state of the system is magnetically disordered. Within the linear spin wave approach, the effect of quantum fluctuations is strong enough to destroy the classical magnetic order, thus invalidating the basic assumptions of the method. Moreover, the absence of any magnetic order parameter ($\langle \mathbf{S}_i \rangle = 0$) prevents the possibility of performing even the simple Curie-Weiss mean field decoupling of Eq. (1.9) [84].

In order to define an appropriate mean field theory for magnetically disordered systems we can follow an alternative approach, based on a parton construction, in which the spin degrees of freedom $\mathbf{S}_i$ are decomposed into products of creation and annihilation operators of suitable slave particles. Concretely, we introduce auxiliary Abrikosov fermions, which form a projective representation of $S = 1/2$ spin operators:

$$\mathbf{S}_i = \frac{1}{2} \sum_{\alpha,\beta} c^{\dagger}_{i,\alpha} \boldsymbol{\sigma}_{\alpha,\beta} c_{i,\beta}. \tag{1.10}$$

Here $c_{i,\alpha}$ ($c^\dagger_{i,\alpha}$) destroys (creates) a fermion with spin $\alpha =\uparrow,\downarrow$ on site i, and the vector $\boldsymbol{\sigma} = (\sigma_x, \sigma_y, \sigma_z)$ is the set of Pauli matrices. The anticommutation relations among fermions ensure that the Abrikosov representation yields the correct commutation relations among different spin components. Still, in order to faithfully reproduce the Hilbert space of the original spin model, only configurations with one fermion per site must be considered, which implies that the Abrikosov fermions must satisfy the constraint:

$$n_i = c^\dagger_{i,\uparrow} c_{i,\uparrow} + c^\dagger_{i,\downarrow} c_{i,\downarrow} = 1, \tag{1.11}$$

where n_i is the *number operator* at site i, or equivalently:

$$c_{i,\downarrow} c_{i,\uparrow} = 0. \tag{1.12}$$

We note that the mapping (1.10) implies that

$$\mathbf{S}_i^2 = \frac{3}{4} n_i (2 - n_i). \tag{1.13}$$

Thus, the constraints (1.11-1.12) are necessary to correctly enforce $\mathbf{S}_i^2 = 3/4$, as required for $S = \frac{1}{2}$ spins.

Besides constant terms, the Hamiltonian of Eq. (1.8) can be rewritten in terms of Abrikosov fermions as follows [84]:

$$\mathcal{H} = -\frac{1}{2} \sum_{i<j} \sum_{\alpha,\beta} J_{i,j} \left(c^\dagger_{i,\alpha} c_{j,\alpha} c^\dagger_{j,\beta} c_{i,\beta} + \frac{1}{2} c^\dagger_{i,\alpha} c_{i,\alpha} c^\dagger_{j,\beta} c_{j,\beta} \right). \tag{1.14}$$

At this stage, the Hamiltonian (1.14) with the constraints of Eqs. (1.11) and (1.12) gives an *exact* representation of the original model. However, the parton construction allows us to perform a mean field decoupling to tackle the above interacting fermionic system [85]. Since we are interested in the case of magnetically disordered phases, we keep only the mean field terms that do not break the $SU(2)$ symmetry of the original spin model (1.9). The result is a quadratic Hamiltonian:

$$\begin{aligned} \mathcal{H}_0 &= \sum_{i,j} \sum_{\sigma} t_{i,j} c^\dagger_{i,\sigma} c_{j,\sigma} + \sum_{i,j} \Delta_{i,j} c_{i,\downarrow} c_{j,\uparrow} + h.c. \\ &+ \sum_i \mu_i (c^\dagger_{i,\uparrow} c_{i,\uparrow} + c^\dagger_{i,\downarrow} c_{i,\downarrow} - 1) + \sum_i \zeta_i c_{i,\downarrow} c_{i,\uparrow} + h.c., \end{aligned} \tag{1.15}$$

which contains a hopping term $t_{i,j}$ and a singlet pairing term $\Delta_{i,j}$, which are proportional to the expectation values $\langle c^\dagger_{j,\sigma} c_{i,\sigma} \rangle$ and $\langle c^\dagger_{i,\sigma} c^\dagger_{j,-\sigma} \rangle$, respectively. In addition, the one-fermion-per-site constraint of the parton construction is enforced in a *global* fashion by including a chemical potential μ_i and an onsite-pairing ζ_i as Lagrange multipliers in $\mathcal{H}_0$ [85]. Within the mere mean field approach, the parameters of $\mathcal{H}_0$ are computed self-consistently and define a low-energy effective theory for the spin model under investigation[9]. At the mean field level, the system is described by a model of free fermionic quasiparticles with spin $S = 1/2$, i.e. *spinons*, which do not possess any charge degrees of freedom. The fact that a system of spins has been rephrased in terms of free fermionic particles hints the possibility that something crucial has been swept under the carpet. Indeed, the missing ingredients in our mean field theory are the conditions of Eqs. (1.11)

[9] For the sake of clarity we omitted some constant terms in Eq. (1.15). However, one needs to take them correctly into account when computing the total mean field energy of $\mathcal{H}_0$. On the other hand, if $\mathcal{H}_0$ is used for a variational purpose (see Section 1.5), as done for the results of the present thesis, these constants do not play any relevant role.

and (1.12): the ground state of $\mathcal{H}_0$, named $|\Phi_0\rangle$, satisfies the one-fermion-per-site constraints only on average and, therefore, does not represent a legitimate wave function for spins. As a result, the mean field energy of $\mathcal{H}_0$ does not provide an accurate estimate of the ground state energy of $\mathcal{H}$[15]. Within the parton approach, a full treatment of the original spin model requires the inclusion of all the fluctuations of the parameters around the mean field solution [84], but this task is in general unfeasible, because it retains the same complexity of the initial many-body problem (1.9).

Nevertheless, following the argument of Wen [84], a first approximation to go beyond the simple mean field solution consists of discarding the amplitude fluctuations of the mean field parameters, which are expected to have a finite energy gap that makes them negligible at low energies, while including only the phase fluctuations. For example, if we consider a pure hopping Hamiltonian $\mathcal{H}_0$ for the sake of simplicity, we can insert the phase fluctuations by replacing $t_{i,j} \mapsto \bar{t}_{i,j} e^{-ia_{i,j}}$:

$$\mathcal{H}_0^{a_{i,j}} = \sum_{i,j} \sum_{\sigma} \bar{t}_{i,j} e^{-ia_{i,j}} c^{\dagger}_{i,\sigma} c_{j,\sigma} + \sum_i \mu_i (c^{\dagger}_{i,\uparrow} c_{i,\uparrow} + c^{\dagger}_{i,\downarrow} c_{i,\downarrow} - 1), \tag{1.16}$$

where $\bar{t}_{i,j}$ is the optimal mean field solution for the hoppings. Since the above Hamiltonian is invariant under the transformation

$$c_{i,\sigma} \mapsto e^{i\theta_i} c_{i,\sigma} \qquad\qquad a_{i,j} \mapsto a_{i,j} + \theta_i - \theta_j, \tag{1.17}$$

we can regard the degrees of freedom $a_{i,j}$ as $U(1)$ emergent *gauge fields* which reside on the bonds (i,j) of the lattice[10]. The resulting model is a theory of fermionic particles coupled by gauge fields[11]. In other words, going beyond mean field, we recover interaction between spinons. Quoting Wen [84], "we cut a spin into two halves" by introducing the parton mean field theory but we have to "glue them back together" to obtain physically meaningful results. We can observe that this theory can reproduce the original spin degrees of freedom if the gauge fields are in a confining phase, where pairs of spinons are strongly coupled by a potential which increases with their distance. On the other hand, in the deconfined phase (e.g. a spin liquid), spinons may become asymptotically free quasiparticles that constitute the low-energy excitations of the system [45].

The question to address at this point is whether this picture of fermionic spinons and gauge fields can be a valid description of the original spin model. Fortunately, we have already seen one example of a nontrivial spin model whose solution is exactly formulated in terms of (Majorana) fermions and emergent gauge fields, i.e. the Kitaev model [32]. In all the other cases, the parton machinery turns out to be (at least) a useful tool to devise variational wave functions for magnetically disordered phases of matter. The variational approach based on the parton construction constitutes the subject of the following section.

1.5 Gutzwiller-projected fermionic wave functions

Instead of trying to improve the parton mean field theory by including fluctuations of the parameters, an alternative route can be pursued, in which the Hamiltonian $\mathcal{H}_0$ is exploited

[10] We note that the structure of the gauge fields depends on the initial mean field theory [here a $U(1)$ theory], as pointed out in Chapter 2.

[11] This is similar to what we discussed for the Kitaev model, where, however, the gauge fluxes are perfectly static.

as a starting point for the definition of variational wave functions for the nonmagnetic phases of the original spin model (1.8)[15]. Within this approach, a Gutzwiller projector,

$$\mathcal{P}_G = \prod_i n_i(2 - n_i), \tag{1.18}$$

is applied to the ground state of $\mathcal{H}_0$ in order to exactly enforce the one-fermion-per-site constraint of Eqs. (1.11) and (1.12). The Gutzwiller projector has the effect of killing the fermionic configurations which contain empty or doubly occupied sites, such that the resulting wave function, $\mathcal{P}_G|\Phi_0\rangle$, is nonzero only in the subspace of spin configurations. We emphasize that, in general, the Gutzwiller projection cannot be treated analytically, due to its intrinsic many-body character, however, it can be enforced in a Monte Carlo sampling by excluding the fermionic configurations which do not satisfy the one-fermion-per-site constraint. At variance with the mean field treatment, in the variational approach the parameters of $\mathcal{H}_0$ are not computed self-consistently, but are optimized in order to minimize the energy of the Gutzwiller-projected *Ansatz* (see Chapter 3 for details).

The wave functions defined by Gutzwiller-projecting the ground state of $\mathcal{H}_0$ belong to the class of RVB states introduced by Anderson [18]. To understand this statement, let us consider, for the sake of simplicity, a lattice of N sites with $N/2$ fermions with spin up and $N/2$ fermions with spin down. In general, the ground state wave function of $\mathcal{H}_0$, which is a BCS Hamiltonian, has the following form (modulo a normalization factor) [38, 86]

$$|\Phi_0\rangle = \exp\left(\sum_{i,j} f_{i,j} c^\dagger_{i,\uparrow} c^\dagger_{j,\downarrow}\right)|0\rangle = \frac{1}{(N/2)!}\left(\sum_{i,j} f_{i,j} c^\dagger_{i,\uparrow} c^\dagger_{j,\downarrow}\right)^{\frac{N}{2}}|0\rangle, \tag{1.19}$$

where the second equality comes from the restriction to the chosen physical sector of N particles. Here $|0\rangle$ is the vacuum state and $f_{i,j} = f_{j,i}$ is the so-called pairing function, which can be obtained by the coefficients of the Bogoliubov transformation that diagonalizes $\mathcal{H}_0$. The above wave function is a superposition of all the physical states which can be constructed by arranging $N/2$ spin singlets between pairs of sites. At the fermionic level, this superposition contains states with doubly occupied and empty sites, or, in other words, states with overlapping singlets and unpaired sites. However, when the Gutzwiller projector is applied, these configurations are killed and the wave function reduces to a linear combination of VB coverings, as in the RVB picture of Anderson (see Fig. 1.14) [86].

In this framework, variational wave functions for both spin liquid and VBS states can be constructed. For what concern the former ones, a specific procedure, named projective symmetry group analysis [85], can be followed to classify all the possible quadratic Hamiltonians $\mathcal{H}_0$ whose Gutzwiller-projected ground states fulfill the symmetries of the lattice model. Within this technique, which is outlined in Chapter 2, the symmetries of the wave function are implemented projectively by taking advantage of a *gauge redundancy* which stems from the artificial enlargement of the Hilbert space introduced by the parton construction. On the other hand, VBS wave functions can be obtained by considering a Hamiltonian $\mathcal{H}_0$ which contains fermionic couplings that break some of the lattice symmetries of the model.

However, in general, the variational *Ansätze* defined by Gutzwiller-projecting the ground state of the fermionic Hamiltonian (1.15) do not display any magnetic order[12]. Then, for the purpose of constructing suitable wave functions for magnetically ordered phases, we can add an additional term to $\mathcal{H}_0$ which explicitly breaks the spin $SU(2)$

[12]In some special cases, a magnetic order may be present, see for example Ref. [87].

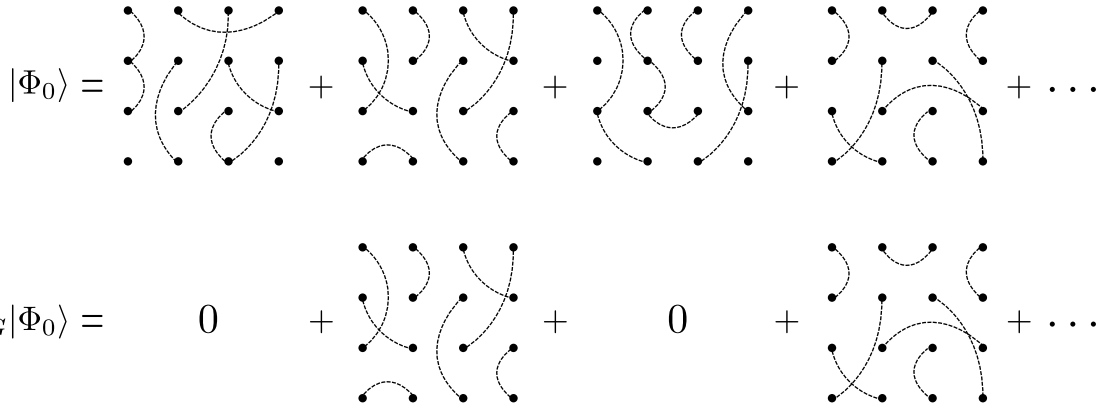

Figure 1.14: Schematic picture of the effect of the Gutzwiller projection on the ground state wave function of a BCS Hamiltonian [like the one of Eq. (1.15)]. All the states which contain overlapping singlets and unpaired sites are killed by $\mathcal{P}_G$, and the resulting wave function is a linear superposition VB configurations.

symmetry and induces magnetic order:

$$\mathcal{H}_0 \mapsto \mathcal{H}_0 + h \sum_i \left(e^{iQ\cdot R_i} c^\dagger_{i,\uparrow} c_{i,\downarrow} + e^{-iQ\cdot R_i} c^\dagger_{i,\downarrow} c_{i,\uparrow} \right). \tag{1.20}$$

Here, h is a *fictitious* magnetic field which lies in the xy-plane and displays a periodic pattern defined by the pitch vector Q. Since, in general, the ground-state wave function of the Hamiltonian (1.20) tends to overestimate the magnetic order of the model under investigation [38], further transverse quantum fluctuations are added through the application of a spin-spin Jastrow factor,

$$\mathcal{J}_s = \exp\left(\frac{1}{2} \sum_{i,j} v_{i,j} S^z_i S^z_j \right), \tag{1.21}$$

to the Gutzwiller-projected state. The *pseudopotential* $v_{i,j}$ is assumed to depend only on the distance $|R_i - R_j|$ and its values are fully optimized together with the fermionic parameters in the process of finding the best variational energy. Finally, the complete form of the variational wave functions employed for most of the results presented in this thesis is

$$|\Psi_0\rangle = \mathcal{P}_{S^z_{tot}} \mathcal{J}_s \mathcal{P}_G |\Phi_0\rangle, \tag{1.22}$$

where in addition to the Gutzwiller projection and the Jastrow factor, we apply a projector enforcing zero value for the z-component of the total spin ($\mathcal{P}_{S^z_{tot}}$). As for $\mathcal{P}_G$, also this second projector can be enforced exactly by Monte Carlo, sampling only the spin configurations which belong to the sector of the Hilbert space with $S^z_{tot} = \sum_i S^z_i = 0$.

2

Classification of spin liquids

CONTENTS

2.1 Introduction

In the last part of Chapter 1, we have seen how we can take advantage of a fermionic parton construction to define variational wave functions for spin systems (cf. Sections 1.4 and 1.5). Within this framework, spin operators are split into the product of two fermionic particles, which live in a larger Hilbert space. Then, a variational wave function for spins can be obtained by projecting a suitable fermionic state $|\Phi_0\rangle$ onto the physical Hilbert space of spins. Concretely, from the computational point of view, $|\Phi_0\rangle$ needs to be a sufficiently simple state to allow for efficient calculations, e.g. the ground state of a quadratic fermionic Hamiltonian [Eq. (1.15) or Eq. (1.20)]. The potential advantages of this approach come from two sides: on the one hand, splitting spin operators into partons may be a good strategy to describe fractionalization; on the other hand, the larger Hilbert space of fermions offers more "freedom" to define an accurate variational *Ansatz*, and even free-fermion states can give rise to nontrivial wave functions for spins after Gutzwiller projection.

Contrary to more unbiased variational wave functions, such as tensor networks [40] and neural network quantum states [88], Gutzwiller-projected fermionic wave functions contain a limited number of variational parameters which cannot be systematically increased. The parametrization of the wave function represents both a limitation and an advantage of

the present approach. Indeed, the variational parameters of fermionic states, contained in the auxiliary Hamiltonian $\mathcal{H}_0$, have a clear physical interpretation and can be chosen such that the resulting variational state possesses all the desired physical properties. In this respect, fermionic wave functions constitute a flexible tool to capture different phases of matter, from magnetically ordered phases to valence bond solids and spin liquids.

Variational states displaying magnetic order are constructed by introducing a fictitious magnetic field in $\mathcal{H}_0$, as done in Eq. (1.20). For VBS states, instead, one should take a $SU(2)$-invariant auxiliary Hamiltonian of the form (1.15) with some hoppings or pairings that break the translational symmetry of the model. For example, for the horizontal dimer phase on the square lattice depicted in Fig. 1.2, one may consider a stronger pairing on horizontal nearest-neighbor bonds, and a weaker pairing on vertical ones, plus other possible couplings at larger distances. For what concerns spin liquid states, however, the situation is more involved. In this case, one would like to define a variational wave function that retains all the symmetries of the lattice (and the spin $SU(2)$ symmetry of the model, if present). At first glance, the only possible solution to this task is taking an auxiliary Hamiltonian of the form (1.15) whose couplings are translationally invariant and satisfy the point group symmetries. However, quite surprisingly, this is not the only possible option, and a plethora of different spin liquid *Ansätze* can be defined within the fermionic framework, following a specific procedure that is outlined in this chapter.

This rich scenario stems from the artificial enlargement of the Hilbert space due to the parton construction. As a consequence of the redundancy of the Abrikosov fermion representation, different auxiliary Hamiltonians $\mathcal{H}_0$, which are connected by certain transformations, produce the same spin wave function after their ground states are Gutzwiller-projected. In other words, the parton construction brings along a *gauge freedom* in the definition of the variational states. Quoting Ref. [84], a "gauge theory is a theory where we use more than one label to label the same quantum state"; here, an infinite number of different auxiliary Hamiltonians $\mathcal{H}_0$ generate the same spin wave function $|\Psi_0\rangle$.

Following the intuition of Wen, it is possible to take advantage of this gauge redundancy to define different auxiliary Hamiltonians, which give rise to distinct spin liquid states $|\Psi_0\rangle$ after Gutzwiller-projection. Remarkably, even if some of these Hamiltonians do not fulfill all the symmetries of the lattice, the projected wave functions turn out to be fully symmetric. The procedure devised by Wen allows to classify all the distinct spin liquid states which can be constructed by Gutzwiller-projected *Ansätze*. Within Wen's theory, named *projective symmetry group* analysis, each symmetry of the lattice is complemented by a certain gauge transformation. The set of all inequivalent choices for these gauge transformations correspond to the list of all the possible spin liquid states [85].

In this chapter, we thoroughly discuss the projective symmetry group method. Even if this theory has important implications for the low-energy physics of spin liquids and the nature of emergent gauge fields, here we adopt a rather practical point of view which goes in the direction of providing a recipe to construct variational wave functions for spin liquid phases. For this purpose, we follow the original works by Wen [84, 85] and the theoretical framework of Ref. [89]. We mention that this chapter does not contain any new result in the field, and it is just meant to be a simple and detailed review of the projective symmetry group approach.

2.2 The SU(2) gauge structure

We begin by highlighting the aforementioned property of the fermionic parton construction, namely the presence of a *local gauge redundancy* which is a consequence of the artificial enlargement of the Hilbert space. For this purpose, we consider the unwrapped version of the Abrikosov mapping of Eq. (1.10):

$$\begin{aligned} S_i^x &= \frac{1}{2}\left(c_{i,\uparrow}^\dagger c_{i,\downarrow} + c_{i,\downarrow}^\dagger c_{i,\uparrow}\right) \\ S_i^y &= \frac{i}{2}\left(c_{i,\downarrow}^\dagger c_{i,\uparrow} - c_{i,\uparrow}^\dagger c_{i,\downarrow}\right) \\ S_i^z &= \frac{1}{2}\left(c_{i,\uparrow}^\dagger c_{i,\uparrow} - c_{i,\downarrow}^\dagger c_{i,\downarrow}\right), \end{aligned} \tag{2.1}$$

We note that the above equations are left invariant by any transformation which attaches a *local* (i.e. site-dependent) phase to the fermionic operators, i.e. $c_{i,\sigma} \mapsto e^{i\theta_i} c_{i,\sigma}$. This means that all the physical properties, which are written in terms of the true degrees of freedom of the system, i.e. the spins, do not depend on the local phase choice for the fermionic operators. In other words, the mapping of the spin degrees of freedom into fermionic annihilation/construction operators is a redundant representation. The arbitrary choice of the phase is not the only gauge freedom associated with the parton construction. For example, one can verify that also the particle-hole transformation $c_{i,\uparrow} \mapsto c_{i,\downarrow}^\dagger$, $c_{i,\downarrow} \mapsto -c_{i,\uparrow}^\dagger$ leaves the spin operators unchanged. In general, all the operations on the Abrikosov fermions which do not affect the physical degrees of freedom are called *gauge transformations* and they can be shown to form a $SU(2)$ gauge group. In order to prove this statement, let us introduce a compact formalism which will be used in the following.

The mapping of Eq. (1.10) can be rewritten as follows:

$$S_i^a = -\frac{1}{4}\,\mathrm{Tr}\left[\Psi_i \sigma_a^* \Psi_i^\dagger\right] \quad (a = x, y, z) \tag{2.2}$$

where

$$\sigma_x = \begin{pmatrix} 0 & 1 \\ 1 & 0 \end{pmatrix} = \sigma_1 \qquad \sigma_y = \begin{pmatrix} 0 & -i \\ i & 0 \end{pmatrix} = \sigma_2 \qquad \sigma_z = \begin{pmatrix} 1 & 0 \\ 0 & -1 \end{pmatrix} = \sigma_3 \tag{2.3}$$

are the three Pauli matrices[1] and

$$\Psi_i = \begin{pmatrix} c_{i,\uparrow} & c_{i,\downarrow} \\ c_{i,\downarrow}^\dagger & -c_{i,\uparrow}^\dagger \end{pmatrix}. \tag{2.4}$$

The asterisk of Eq. (2.2) indicates the complex conjugation of all the matrix entries and the trace is taken over the elements of the resulting 2×2 matrix. The above notation can be used also to express the constraints (1.11) and (1.12) in a more compact form:

$$\mathrm{Tr}\left[\Psi_i^\dagger \sigma_a \Psi_i\right] = 0 \quad (a = x, y, z). \tag{2.5}$$

Using the property of the trace, we can easily show that the spin operators are invariant

[1] Throughout this thesis we interchangeably label the Pauli matrices with letters, x, y, z, or numbers, $1, 2, 3$. This redundant (and apparently unwise) notation helps improving the clarity of some formulae.

under the left-multiplication of Ψ_i by a *local* $SU(2)$ matrix[2]

$$\Psi_i \mapsto G_i^\dagger \Psi_i \implies \mathbf{S}_i \mapsto \mathbf{S}_i \tag{2.6}$$

This proves the fact that the Abrikosov representation possesses a local $SU(2)$ gauge structure. All the physical operators, which are written in terms of spins, e.g. the Heisenberg-like Hamiltonian of Eq. (1.8), are unaffected by the above gauge transformations. On the other hand, the three equivalent constraints of Eq. (2.5) are simply mixed by a gauge change (2.6), thus retaining their validity.

On the other hand, a right-multiplication of Ψ_i by a $SU(2)$ matrix R_i corresponds to a rotation of the physical spin at site i. For example, $R_i = \exp[-i(\theta/2)\sigma_3]$ rotates the i-th spin of an angle θ around the S^z-axis. We emphasize that the Hamiltonian of Eq. (1.8) is invariant only under *global* spin rotations ($R_i = R\ \forall i$).

2.3 The fermionic mean field Hamiltonian

The matrices Ψ_i of Eq. (2.4) can be exploited to define a compact formulation of the Abrikosov fermion mean field approach outlined in Section 1.4. The most general mean field decomposition of the Hamiltonian of Eq. (1.14) can contain

$$\begin{aligned}
&\text{four hopping terms} \ \rightarrow \quad t_{i,j}^{\uparrow\uparrow} c_{i,\uparrow}^\dagger c_{j,\uparrow} \quad t_{i,j}^{\uparrow\downarrow} c_{i,\uparrow}^\dagger c_{j,\downarrow} \quad t_{i,j}^{\downarrow\uparrow} c_{i,\downarrow}^\dagger c_{j,\uparrow} \quad t_{i,j}^{\downarrow\downarrow} c_{i,\downarrow}^\dagger c_{j,\downarrow} \\
&\text{four pairing terms} \ \rightarrow \quad \Delta_{i,j}^{\uparrow\uparrow} c_{i,\uparrow} c_{j,\uparrow} \quad \Delta_{i,j}^{\uparrow\downarrow} c_{i,\uparrow} c_{j,\downarrow} \quad \Delta_{i,j}^{\downarrow\uparrow} c_{i,\downarrow} c_{j,\uparrow} \quad \Delta_{i,j}^{\downarrow\downarrow} c_{i,\downarrow} c_{j,\downarrow}
\end{aligned} \tag{2.7}$$

for each bond i, j. Thus, the fermionic couplings along i, j are specified by a total of 16 real parameter, namely four complex hoppings t and four complex pairings Δ. We can introduce a convenient formulation to wrap up all the above terms [90]:

$$H_{\mathrm{MF}} = H_0 + H_x + H_y + H_z, \tag{2.8}$$

where

$$H_0 = \frac{1}{2} \sum_{i,j} \mathrm{Tr} \left[\Psi_i^\dagger u_{i,j}^0 \Psi_j \right], \tag{2.9}$$

$$H_x = \frac{1}{2} \sum_{i,j} \mathrm{Tr} \left[\sigma_x \Psi_i^\dagger u_{i,j}^x \Psi_j \right], \tag{2.10}$$

$$H_y = \frac{1}{2} \sum_{i,j} \mathrm{Tr} \left[\sigma_y \Psi_i^\dagger u_{i,j}^y \Psi_j \right], \tag{2.11}$$

$$H_z = \frac{1}{2} \sum_{i,j} \mathrm{Tr} \left[\sigma_z \Psi_i^\dagger u_{i,j}^z \Psi_j \right]. \tag{2.12}$$

The summations of the above formula run over all sites, counting each bond twice (hence the factor $1/2$ in front of the trace), and $u_{i,j}^a$ are (complex-valued) 2×2 matrices, each of which is fully specified by four real parameters. The Hermiticity condition for the mean field Hamiltonian is ensured by assuming $u_{j,i}^a = [u_{i,j}^a]^\dagger$. For a detailed discussion of the

[2] The convention used for the definition of the gauge transformation looks somehow counterintuitive, since the gauge matrix is represented by the adjoint of G_i. However, the advantage of this choice comes from the fact that the projective symmetry group equations match the notation used in Ref. [85], which is the one commonly adopted in literature.

various terms appearing in the mean field Hamiltonian H_{MF}, we refer to Appendix A, where the precise form of the bond matrices $u^a_{j,i}$ is outlined.

The first part of the mean field Hamiltonian, namely H_0, is invariant under any global spin rotation R and is therefore called singlet term. On the other hand, the remaining contributions, H_x, H_y, H_z, are called triplet terms, because they get linearly combined between themselves under the effect of R:

$$\Psi_i \mapsto \Psi_i R,\ \forall i \ \Rightarrow\ \begin{cases} H_0 \mapsto \frac{1}{2}\sum_{i,j} \mathrm{Tr}\left[R^\dagger \Psi_i^\dagger u^0_{i,j} \Psi_j R\right] = H_0 \\ H_a \mapsto \frac{1}{2}\sum_{i,j} \mathrm{Tr}\left[(R\sigma_a R^\dagger)\Psi_i^\dagger u^a_{i,j}\Psi_j\right] \quad (a=x,y,z). \end{cases} \tag{2.13}$$

If one is interested in defining a mean field theory for a spin-rotationally invariant Hamiltonian, as the one of Eq. (1.8), it is sufficient to keep only the term H_0, which is the only one that does not break the spin $SU(2)$ symmetry. The same argument applies when the mean field Hamiltonian is exploited to construct variational wave functions which are required to fulfill all the symmetries of the spin Hamiltonian[3]. Since the main focus of this thesis is on spin Hamiltonians containing only Heisenberg couplings, we restrict ourselves to considering only the spin $SU(2)$ invariant mean field theory, i.e. $H_{\mathrm{MF}} = H_0$. As shown in Appendix A, the resulting mean field Hamiltonian contains *singlet* hoppings and *singlet* pairings, and coincides with the one of Eq. (1.15) once we take[4]

$$u^0_{i,j} = u_{i,j} \equiv \begin{pmatrix} t_{i,j} & \Delta^*_{i,j} \\ \Delta_{i,j} & -t^*_{i,j} \end{pmatrix}, \tag{2.14}$$

and we add an extra term to account for the constraints of Eq. (2.5) [or, equivalently, Eqs. (1.11) and (1.12)]:

$$\mathcal{H}_0 = \frac{1}{2}\sum_{i,j} \mathrm{Tr}\left[\Psi_i^\dagger u_{i,j}\Psi_j\right] + \sum_i \mathrm{Tr}\left[\Psi_i^\dagger \lambda_i \Psi_i\right]. \tag{2.15}$$

Due to Hermiticity we have that $u_{j,i} = u^\dagger_{i,j}$, which implies $t_{j,i} = t^*_{i,j}$ and $\Delta_{j,i} = \Delta_{i,j}$. Moreover, we have set

$$\lambda_i = \mathrm{Re}(\zeta_i)\sigma_1 + \mathrm{Im}(\zeta_i)\sigma_2 + \mu_i\sigma_3 = \begin{pmatrix} \mu_i & \zeta_i^* \\ \zeta_i & \mu_i \end{pmatrix}, \tag{2.16}$$

where, as discussed in Section 1.4, μ_i is a real chemical potential and ζ_i is a complex onsite pairing. We emphasize the fact that the extra term encoding the constraint of Eq. (2.5) is invariant under global spin rotations, and, therefore, does not break the spin $SU(2)$ symmetry of our mean field construction. From this point on, we focus only on the mean field Hamiltonian of Eq. (2.15) as the starting point for the definition of variational wave functions for $SU(2)$-invariant spin models. We want to describe the projective symmetry group method, which gives a set of rules to classify all the possible spin liquid wave functions which can be constructed by Gutzwiller-projecting the ground state of $\mathcal{H}_0$. Before doing so, we introduce the concept of gauge equivalent *Ansätze*.

[3] In the case of spin models with $U(1)$ symmetry, which are invariant only under global rotations around the z-axis, i.e. $R = \exp(i\theta\sigma_z)$, both the terms H_0 and H_3 are needed for a complete parametrization of the mean field Hamiltonian.

[4] The $u_{i,j}$ matrix of Eq. (2.14) becomes equivalent to the $u^0_{i,j}$ matrix of Eq. (A.6) if we set $t_{i,j} = \alpha^{0,3}_{i,j} + i\alpha^{0,0}_{i,j}$ and $\Delta_{i,j} = \alpha^{0,1}_{i,j} + i\alpha^{0,2}_{i,j}$.

2.4 Gauge equivalent Ansätze

As discussed also in Section 1.5, nonmagnetic variational wave functions for spin systems are obtained by Gutzwiller-projecting the ground state of $\mathcal{H}_0$ [Eq. (2.15)]. The parametrization of the variational state is encoded in the choice of the matrices defining $\mathcal{H}_0$, i.e. the bond matrix $u_{i,j}$ (2.14), and the onsite matrix λ_i (2.16). Throughout this chapter, the set $(u_{i,j}, \lambda_i)$ is dubbed *variational Ansatz*. Here we show that two variational *Ansätze* which are related by a (local) $SU(2)$ gauge transformation G_i, i.e.

$$(u_{i,j}, \lambda_i) \quad \text{and} \quad (\tilde{u}_{i,j}, \tilde{\lambda}_i) = (G_i u_{i,j} G_j^\dagger, G_i \lambda_i G_i^\dagger), \tag{2.17}$$

yield the same spin wave function after Gutzwiller projection. This property lies at the heart of the projective symmetry group method.

We focus on a spin model containing $N_\uparrow$ $\uparrow$-spins and $N_\downarrow$ $\downarrow$-spins, whose configurations can be written in terms of Abrikosov fermions as follows:

$$|\{i\}\rangle = \left(\prod_{j \in \{i\}} S_j^+ \right) | \downarrow\downarrow \cdots \downarrow\rangle = \left(\prod_{j \in \{i\}} c_{j,\uparrow}^\dagger c_{j,\downarrow} \right) | \downarrow\downarrow \cdots \downarrow\rangle. \tag{2.18}$$

Here S_j^+ is the raising operator, $| \downarrow\downarrow \cdots \downarrow\rangle$ is the configuration in which each site contains one fermion with $\downarrow$-spin, and $\{i\} = \{i_1, i_2, ..., i_{N_\uparrow}\}$ is a given set of $N_\uparrow$ lattice sites.

Let us consider two different fermionic Hamiltonians of the form (2.15) specified by the *Ansätze* $(u_{i,j}, \lambda_i)$,

$$\mathcal{H}_0^{(u_{i,j}, \lambda_i)} = \frac{1}{2} \sum_{i,j} \mathrm{Tr} \left[\Psi_i^\dagger u_{i,j} \Psi_j \right] + \sum_i \mathrm{Tr} \left[\Psi_i^\dagger \lambda_i \Psi_i \right], \tag{2.19}$$

and $(\tilde{u}_{i,j}, \tilde{\lambda}_i) = (G_i u_{i,j} G_j^\dagger, G_i \lambda_i G_i^\dagger)$,

$$\mathcal{H}_0^{(\tilde{u}_{i,j}, \tilde{\lambda}_i)} = \frac{1}{2} \sum_{i,j} \mathrm{Tr} \left[\Psi_i^\dagger (G_i u_{i,j} G_j^\dagger) \Psi_j \right] + \sum_i \mathrm{Tr} \left[\Psi_i^\dagger (G_i \lambda_i G_i^\dagger) \Psi_i \right]. \tag{2.20}$$

If we Gutzwiller-project the ground state of the first Hamiltonian (named $|\Phi_0^{(u_{i,j}, \lambda_i)}\rangle$), we obtain a wave function which can have nonzero elements only on the physical spin configurations $|\{i\}\rangle$ of Eq. (2.18):

$$|\Psi_0^{(u_{i,j}, \lambda_i)}\rangle = \mathcal{P}_G |\Phi_0^{(u_{i,j}, \lambda_i)}\rangle = \sum_{\{i\}} A_{\{i\}}^{(u_{i,j}, \lambda_i)} |\{i\}\rangle = \sum_{\{i\}} A_{\{i\}}^{(u_{i,j}, \lambda_i)} \left(\prod_{j \in \{i\}} c_{j,\uparrow}^\dagger c_{j,\downarrow} \right) | \downarrow\downarrow \cdots \downarrow\rangle. \tag{2.21}$$

Here $A_{\{i\}}^{(u_{i,j}, \lambda_i)}$ indicates the coefficient of the expansion of the projected wave function relative to the configuration $|\{i\}\rangle$. On the other hand, for the second Hamiltonian, we can imagine the $G_i^\dagger$ matrices as if they were acting on Ψ_i [as the gauge transformation of Eq. (2.6)], yielding a new set of fermionic operators. If we define $\tilde{\Psi}_i = G_i^\dagger \Psi_i$, we have

$$\mathcal{H}_0^{(\tilde{u}_{i,j}, \tilde{\lambda}_i)} = \frac{1}{2} \sum_{i,j} \mathrm{Tr} \left[\tilde{\Psi}_i^\dagger u_{i,j} \tilde{\Psi}_j \right] + \sum_i \mathrm{Tr} \left[\tilde{\Psi}_i^\dagger \lambda_i \tilde{\Psi}_i \right]. \tag{2.22}$$

We can now regard the second Hamiltonian as if it had the same couplings $(u_{i,j}, \lambda_i)$ as the first one, but gauge-transformed fermionic operators (denoted by $\tilde{c}$). For this reason,

the ground state wave function of the second Hamiltonian has the same expansion coefficients of the one of the first Hamiltonian, but the expansion is written in terms of the configurations of $\tilde{c}$-fermions:

$$|\Psi_0^{(\tilde{u}_{i,j},\tilde{\lambda}_i)}\rangle = \mathcal{P}_G|\Phi_0^{(\tilde{u}_{i,j},\tilde{\lambda}_i)}\rangle = e^{i\Phi}\sum_{\{i\}} A_{\{i\}}^{(u_{i,j},\lambda_i)} \left(\prod_{j\in\{i\}} \tilde{c}_{j,\uparrow}^\dagger \tilde{c}_{j,\downarrow}\right)|\downarrow\downarrow\cdots\downarrow\rangle. \tag{2.23}$$

Here, we have exploited the fact that any configuration with one fermion per site, such as $|\downarrow\downarrow\cdots\downarrow\rangle$, can at most acquire a global phase $e^{i\Phi}$ upon gauge transformations, as shown in Appendix B. Moreover, since the raising operators S_j^+ do not depend on the gauge choice, we note that

$$c_{j,\uparrow}^\dagger c_{j,\downarrow} = \tilde{c}_{j,\uparrow}^\dagger \tilde{c}_{j,\downarrow}. \tag{2.24}$$

Therefore, we conclude that the variational wave functions obtained by Gutzwiller-projecting the fermionic *Ansätze* $(u_{i,j},\lambda_i)$ and $(G_i u_{i,j} G_j^\dagger, G_i\lambda_i G_i^\dagger)$ are identical, modulo an irrelevant global phase. In this case, we say that the two *Ansätze* are *gauge equivalent*, because, after projection, they turn out to be just two different labels referring to the same physical state [85].

2.5 The projective symmetry group

The ability to construct quantum states which fulfill the symmetries of the model under investigation is a crucial task of variational approaches. This aspect turns out to be of fundamental importance in the case of spin liquid wave functions which, by definition, are required to satisfy all lattice symmetries. Here we address the issue of constructing fully symmetric Gutzwiller-projected wave functions, by introducing the projective symmetry group method developed by Wen [85].

Suppose we are interested in defining a variational state which fulfills a given lattice symmetry T that maps site $i \mapsto T(i)$. The naive solution to this problem is taking a symmetric *Ansatz*, which is invariant under the effect of T:

$$u_{T(i),T(j)} = u_{i,j} \quad \text{and} \quad \lambda_{T(i)} = \lambda_i. \tag{2.25}$$

However this is not the only way we have to reach our target. Indeed, we can take advantage of the gauge redundancy of the Abrikosov fermion representation to implement lattice symmetries in a projective fashion. Concretely, let us take a generic *Ansatz* $(u_{i,j},\lambda_i)$ which does not satisfy Eq. (2.25). Under the effect of T the fermionic operators transform as $\Psi_i \mapsto \Psi_{T(i)}$, and the auxiliary Hamiltonian becomes:

$$\mathcal{H}_0 = \frac{1}{2}\sum_{i,j} \mathrm{Tr}\left[\Psi_i^\dagger u_{T^{-1}(i,j)}\Psi_j\right] + \sum_i \mathrm{Tr}\left[\Psi_i^\dagger \lambda_{T^{-1}(i)}\Psi_i\right], \tag{2.26}$$

where we have redefined the indices of summation $[T(i),T(j)\mapsto i,j]$ and used the shorthand notation $T^{-1}(i,j) = T^{-1}(i),T^{-1}(j)$. If we are able to find a gauge transformation[5] $\Psi_i \mapsto G_T^\dagger(i)\Psi_i$ which makes the *Ansatz* $(u_{T^{-1}(i,j)},\lambda_{T^{-1}(i)})$ equivalent to the original one,

[5] We note that here we use a slightly different notation, in which the sites to which the gauge change is applied are reported in brackets.

i.e. $(u_{i,j}, \lambda_i)$, we can restore the initial form of $\mathcal{H}_0$. Such a gauge transformation must satisfy the following equations:

$$G_T(i) u_{T^{-1}(i,j)} G_T^\dagger(j) = u_{i,j} \quad \text{and} \quad G_T(i) \lambda_{T^{-1}(i)} G_T^\dagger(i) = \lambda_i. \tag{2.27}$$

If the above gauge transformation exists, the spin wave function obtained by Gutzwiller-projecting the ground state of $\mathcal{H}_0$ is invariant under the symmetry T. Essentially, thanks to the $SU(2)$ gauge redundancy, we have a way to construct symmetric variational wave functions for the spins, starting from non-symmetric fermionic Hamiltonians: the invariance is recovered by combining the symmetry operator with an appropriate gauge change.

Given a certain *Ansatz*, we can introduce its projective symmetry group (PSG), which is formed by all the pairs of symmetry operations (T)-gauge transformations (G_T) which leave the *Ansatz* unchanged. Following the notation of Ref. [89], we label the different elements of the PSG as $Q_T = (G_T, T)$ and we define their action on the matrices of the fermionic *Ansatz* $(u_{i,j}, \lambda_i)$ as follows:

$$Q_T(u_{i,j}) \equiv G_T(i) u_{T^{-1}(i,j)} G_T^\dagger(j), \tag{2.28}$$

$$Q_T(\lambda_i) \equiv G_T(i) \lambda_{T^{-1}(i)} G_T^\dagger(i). \tag{2.29}$$

Thus, the conditions defining the PSG of the *Ansatz* are

$$Q_T(u_{i,j}) = u_{i,j} \qquad Q_T(\lambda_i) = \lambda_i. \tag{2.30}$$

If the above equations are true for all the $u_{i,j}$ and λ_i matrices, the wave function obtained by Gutzwiller-projecting the *Ansatz* $(u_{i,j}, \lambda_i)$ is symmetric under the effect of T [cf. Eq (2.27)]. Here, we'd like to stress the fact that, in general, the gauge transformation G_T has a local structure, i.e. its form can vary from one lattice site to another.

As shown in Appendix C, we can derive a formula for the product between two elements of the PSG [89]:

$$Q_{T_1} Q_{T_2} = (G_{T_1}, T_1)(G_{T_2}, T_2) = (G_{T_1} T_1 G_{T_2} T_1^{-1}, T_1 T_2) \tag{2.31}$$

where $T_1 G_{T_2} T_1^{-1} = T_1 \left[\otimes_i G_{T_2}(i)\right] T_1^{-1} = \otimes_i G_{T_2}(T_1^{-1}(i))$. As a consequence, the inverse of Q_T is defined as follows:

$$Q_T^{-1} = (G_T, T)^{-1} = (T^{-1} G_T^\dagger T, T^{-1}) \tag{2.32}$$

Within the above formalism, a pure gauge transformation G is represented by the element $Q = (G, \mathcal{I})$, where $\mathcal{I}$ indicates the identity transformation $[\mathcal{I} : (u_{i,j}, \lambda_i) \mapsto (u_{i,j}, \lambda_i)]$. The PSG of a given *Ansatz* always contains a special subgroup named *invariant gauge group* (IGG), which is made of all the pure gauge transformations under which the *Ansatz* is invariant [84]:

$$Q_{\mathcal{I}} = (G_{\mathcal{I}}, \mathcal{I}) \in \text{IGG} \;\Rightarrow\; Q_{\mathcal{I}}(u_{i,j}) = G_{\mathcal{I}}(i) u_{i,j} G_{\mathcal{I}}^\dagger(j) = u_{i,j} \tag{2.33}$$

$$Q_{\mathcal{I}}(\lambda_i) = G_{\mathcal{I}}(i) \lambda_i G_{\mathcal{I}}^\dagger(i) = \lambda_i. \tag{2.34}$$

From the above definitions we can observe that if $Q_T = (G_T, T)$ belongs to the PSG of a certain *Ansatz*, also the element $Q_{\mathcal{I}} Q_T$ (with $Q_{\mathcal{I}} \in$ IGG) belongs to the same PSG. This means that the number of PSG elements Q_T associated to a given symmetry T coincides with the number of elements of the IGG. Mathematically speaking, Q is a mapping from the group of the symmetries of the model to the quotient group PSG/IGG. Therefore, the PSG is a projective representation of the group of symmetries [84].

Example. *To understand why any symmetry T has a number of equivalent PSG elements Q_T which coincides with the number of the elements of the IGG, let us resort to a simple example. Suppose that the PSG of a certain Ansatz contains an element Q_R associated to a rotation R, whose corresponding gauge transformation is global, e.g. $G_R(j) = G_R = i\sigma_3$. Let us also assume that the Ansatz has a Z_2 IGG, formed by two elements, $Q^+_{\mathcal{I}} = (\mathbb{1}, \mathcal{I})$ and $Q^-_{\mathcal{I}} = (-\mathbb{1}, \mathcal{I})$. Then both $Q^+_{\mathcal{I}} Q_R = (i\sigma_3, R)$ and $Q^-_{\mathcal{I}} Q_R = (-i\sigma_3, R)$ are valid elements of the PSG, and form the coset[6] of the IGG in the PSG with respect to the element Q_R. In other words, the set $\{Q^+_{\mathcal{I}} Q_R, Q^-_{\mathcal{I}} Q_R\}$ is the equivalence class containing all the equivalent PSG elements that can be associated to the symmetry R. For all practical purposes, one can choose any of the elements of the equivalence class to be the representative PSG element for R. This explains why the mapping Q goes from the group of symmetries to the quotient group PSG/IGG, whose elements are the various equivalence classes corresponding to each of the symmetries. The IGG itself is the equivalence class of the identity operator $\mathcal{I}$.*

We note that a PSG can be defined for every fermionic *Ansatz*[7]. We say that two PSGs are equivalent if they are PSGs of two gauge equivalent *Ansätze* (cf. Section 2.4):

$$\begin{array}{l} u^{(1)} = (u_{i,j}, \lambda_i) \\ u^{(2)} = (G_i u_{i,j} G_j^\dagger, G_i \lambda_i G_i^\dagger) \end{array} \implies \mathrm{PSG}^{(1)} \sim \mathrm{PSG}^{(2)} \tag{2.35}$$

The gauge transformation connecting $u^{(2)}$ to $u^{(1)}$ is compactly written as $u^{(2)} = Q(u^{(1)})$, with $Q = (G, \mathcal{I})$. Using this expression, we can quickly derive the equation connecting $Q_T^{(1)} = (G_T^{(1)}, T)$ and $Q_T^{(2)} = (G_T^{(2)}, T)$, namely the projective representations of the symmetry T in the two equivalent PSGs:

$$Q_T^{(1)}(u^{(1)}) = u^{(1)} \;\Rightarrow\; Q_T^{(1)}\left[Q^{-1}(u^{(2)})\right] = Q^{-1}(u^{(2)}) \;\Rightarrow\; Q Q_T^{(1)} Q^{-1}(u^{(2)}) = u^{(2)}. \tag{2.36}$$

This implies that

$$Q_T^{(2)} = Q Q_T^{(1)} Q^{-1} \implies G_T^{(2)}(i) = G(i) G_T^{(1)}(i) G^\dagger\left(T^{-1}(i)\right) \;\forall i. \tag{2.37}$$

For our purposes, the PSG constitutes a tool to characterize the different spin liquid wave functions which can be constructed by Gutzwiller-projecting a mean field fermionic state. In the following of this chapter we will show that, through the analysis of the PSG, which somehow represents an augmented version of the symmetry group, we will be able to distinguish different states of matter which possess the same physical symmetries. Thus, within our variational approach, the PSG represents the key to describe "quantum order", in the same way as classical order is characterized according to broken symmetries [45, 84]. Beside being useful to classify different quantum states, the PSG provides direct information on the nature of the emergent gauge fields which are associated to a certain fermionic *Ansatz*. Indeed, Wen argued that, within a mean field treatment, the relevant (i.e. low-energy) fluctuations of the parameters of $\mathcal{H}_0$ are determined by the IGG group [85]. To give a concrete example, if the IGG of a particular spin liquid *Ansatz* is formed by all the global $U(1)$ gauge transformations of the form $G = \exp(i\theta\sigma_3)$, as in the generic case of an *Ansatz* with just real hoppings and chemical potentials ($u_{i,j} = t_{i,j}\sigma_3, \lambda_i = \mu_i\sigma_3$), we say that the wave function resulting from Gutzwiller projection represents a $U(1)$ spin liquid phase. At low-energy, the emergent gauge degrees of freedom take the form of phase

[6] Since the left and right cosets of the IGG are equal, the IGG is a normal subgroup of the PSG.

[7] In the case of states which break all the symmetries of the model, the PSG trivially coincides with the IGG.

fluctuations of the hoppings, see Eq. (1.16). On the other hand, the short range RVB wave function on the square lattice [91], which corresponds to the fermionic *Ansatz*

$$\begin{cases} u_{i,i\pm x} = \Delta\sigma_1 \\ u_{i,i\pm y} = \Delta\sigma_2 \\ u_{i,i\pm 2x} = u_{i,i\pm 2y} = -\frac{\Delta}{4}\sigma_3 \end{cases} \quad \text{with } x = (1,0) \text{ and } y = (0,1), \tag{2.38}$$

is a Z_2 spin liquid state, and the low-energy fluctuations of its mean field parameters are Z_2 gauge fields sitting on the bonds of the lattice. In general, the "high-energy" $SU(2)$ gauge structure of the Abrikosov fermions representation, can be reduced to a $U(1)$ or Z_2 gauge structure (i.e. the structure of the IGG group) at low energies [85]. We note that the IGG of any fermionic *Ansatz* can be determined through an analysis of the mean field fluxes (see Ref. [89] for a detailed discussion).

2.6 PSG classification

Strictly speaking, in the previous section we discussed what is usually referred to as the *invariant* PSG, which is the set of symmetries+gauge transformations under which an *Ansatz* $(u_{i,j}, \lambda_i)$ is invariant. According to this definition, the invariant PSG is a property of a particular *Ansatz* [85, 89]. Here we aim at introducing the PSG classification of spin liquid phases for a specific spin model: following a well-defined procedure, we will be able to enumerate all the possible auxiliary Hamiltonians $\mathcal{H}_0$ whose ground states fulfill all the symmetries of the model after Gutzwiller projection. The PSG classification is based on the definition of the so-called *algebraic* PSG, which is an extension of the symmetry group of the spin model. In a nutshell, within the algebraic PSG, each symmetry is supplemented by a corresponding gauge transformation, such that the algebraic relations between symmetries are reproduced in a *projective* fashion. Concretely, below we outline the main steps leading to the classification of spin liquids.

Choosing the symmetries

First, we need to define the group of symmetries that we want to be projectively fulfilled by the spin liquid *Ansätze*. Typically, the algebraic PSG of a *fully symmetric* spin liquid includes all lattice symmetries, namely translations and point group symmetries (reflections, rotations, inversion, ...), plus time reversal. The latter symmetry represents a particular case which requires a special treatment, thoroughly discussed in Appendix D. Here, we only report the fact that, according to the definition of Eq. (D.8), time reversal has the effect of inverting the sign of the parameters of the fermionic *Ansätze*, i.e. $\Theta : (u_{i,j}, \lambda_i) \mapsto (-u_{i,j}, -\lambda_i)$. If one is interested in constructing *chiral* spin liquids, time reversal needs to be ignored or allowed to be broken within the classification [89].

We note that choosing an auxiliary Hamiltonian of the form (2.15) automatically implies that the resulting spin liquid *Ansätze* trivially (i.e. non-projectively) satisfy the spin $SU(2)$ symmetry. Including some additional mean field terms from the Hamiltonians H_x, H_y, H_z of Eqs. (2.10-2.12), one can classify spin liquid states with lower spin rotational symmetries, e.g. $U(1)$ rotational invariance or more involved cases. Recently, following the discovery of the so-called Kitaev materials [35], a lot of interest has been put on magnetic materials with strong spin-orbit coupling effects. These systems are typically described by spin Hamiltonians with bond-dependent couplings that break the $SU(2)$ spin symmetry. In these cases, the most general fermionic *Ansätze* for spin liquids include triplet hoppings

and pairings, and require a more involved PSG classification (see, for example, Refs. [90, 92–94]). Finally, we mention that, in principle, the $SU(2)$ symmetry can be implemented also projectively, as done in Ref. [95].

Algebraic relations between PSG elements

Once the symmetry group is defined, we introduce the corresponding PSG, in which a gauge transformation G_T is associated to each of the symmetries T. The freedom in the choice of the gauge transformations is constrained by the algebraic relations between symmetries, which need to be satisfied *projectively*. For example, if we consider two symmetries which commute, $T_1T_2 = T_2T_1$, then we have to require that their PSG elements satisfy the same equation, modulo a gauge transformation of the IGG (denoted by $Q_{\mathcal{I}}$). Translated in formulae, this becomes

$$Q_{T_1}Q_{T_2} = Q_{\mathcal{I}}Q_{T_2}Q_{T_1}, \tag{2.39}$$

or, equivalently,

$$Q_{T_1}Q_{T_2}Q_{T_1}^{-1}Q_{T_2}^{-1} \in \text{IGG}. \tag{2.40}$$

We note that here the situation is reversed with respect to what we have discussed in the previous section. Indeed, while in the context of the invariant PSG, we start from a given *Ansatz* and we can find its corresponding IGG, here, in order to construct the algebraic PSG, we need to choose a desired form for the IGG at the beginning. In general, we can choose any subgroup of the $SU(2)$ gauge group. If, for example, we fix the IGG to be the global Z_2 group, i.e. $\{\pm\mathbb{1}\}$, we obtain a classification for the Z_2 spin liquids [84, 89].

The classification of spin liquids consists of finding sets of gauge transformations which fulfill all the PSG algebraic relations. Concretely, the list of all these relations defines a set of equations that depend upon certain parameters $\{\varepsilon\}$, related to the choice of the IGG. For every possible set of values for $\{\varepsilon\}$, one can look for a set of PSG elements that solve the aforementioned equations. If a solution is found, the corresponding PSG defines a spin liquid *Ansatz*. Thus, different values of $\{\varepsilon\}$ (can) give rise to different spin liquid solutions. Enumerating all the possible solutions, we perform a full classification of all the spin liquid phases which can be defined within our framework.

Constructing the Ansätze

From the results of the classification, we want to explicitly construct the matrices $(u_{i,j}, \lambda_i)$ which define the variational *Ansätze*. These matrices need to be compatible with the corresponding PSG solutions, namely they have to satisfy $Q_T(u_{i,j}) = u_{i,j}$ and $Q_T(\lambda_i) = \lambda_i$ for all the implemented symmetries T. Let us assume the following generic expression for the definition of the *Ansatz* (cf. Appendix A):

$$u_{i,j} = it^I_{i,j}\mathbb{1} + \Delta^R_{i,j}\sigma_1 + \Delta^I_{i,j}\sigma_2 + t^R_{i,j}\sigma_3, \tag{2.41}$$

$$\lambda_i = \zeta^R_i\sigma_1 + \zeta^I_i\sigma_2 + \mu_i\sigma_3. \tag{2.42}$$

All the parameters entering the above equations are real. For the bond matrix $u_{i,j}$ we have split the hopping (pairing) term into its real part, $t^R_{i,j}$ ($\Delta^R_{i,j}$), and imaginary part, $t^I_{i,j}$ ($\Delta^I_{i,j}$). For the onsite matrix λ_i, μ_i is the chemical potential and ζ^R_i and ζ^I_i are the real and the imaginary part of the onsite pairing, respectively.

First, we need to require that the matrices $(u_{i,j}, \lambda_i)$ are invariant under the gauge transformations of the IGG. For example, in the case of the classification of $U(1)$ spin liquids, we can always assume that IGG $= \{Q_\theta\}_\theta$, where $Q_\theta = (\exp(i\theta\sigma_3), \mathcal{I})$ and $\theta \in [0, 2\pi)$ is a continuous parameter (this is often referred to as the *canonical gauge* [85]). This generates the constraints

$$Q_\theta(u_{i,j}) = e^{i\theta\sigma_3}u_{i,j}e^{-i\theta\sigma_3} = u_{i,j}\ (\forall\theta) \quad \Rightarrow\ \Delta^R_{i,j} = \Delta^I_{i,j} = 0, \tag{2.43}$$

$$Q_\theta(\lambda_i) = e^{i\theta\sigma_3}\lambda_i e^{-i\theta\sigma_3} = \lambda_i \ (\forall\theta) \quad \Rightarrow \ \zeta_i^R = \zeta_i^I = 0, \tag{2.44}$$

which imply that, within the chosen gauge, a $U(1)$ spin liquid *Ansatz* can only contain hopping terms and chemical potentials. On the other hand, the Z_2 IGG, which contains only $\pm\mathbb{1}$, does not impose any relevant constraint on the matrices of the *Ansätze*.

As a next step, the form of $(u_{i,j}, \lambda_i)$ is further constrained by the PSG elements of the symmetries of the model. The simplest case to consider is time reversal (Θ), which does not act on lattice sites and imposes the following conditions:

$$Q_\Theta(u_{i,j}) = -G_\Theta(i)u_{i,j}G_\Theta^\dagger(j) = u_{i,j}, \tag{2.45}$$

$$Q_\Theta(\lambda_i) = -G_\Theta(i)\lambda_i G_\Theta^\dagger(i) = \lambda_i. \tag{2.46}$$

In addition to Θ, for the onsite matrix λ_i, we need to consider the set of all symmetry transformations T_1 which leave the site i of the lattice invariant ($T_1(i) = i$). For each of these symmetries, we impose $Q_{T_1}(\lambda_i) = \lambda_i$. On the other hand, for the bond matrix $u_{i,j}$, we need to take into account both the symmetries T_2 which leave the pair of sites (i,j) invariant $[T_2(i,j) = (i,j)]$ and the symmetries $\overline{T}_2$ which exchange the two sites $[\overline{T}_2(i,j) = (j,i)]$. For the former transformations we require that $Q_{T_2}(u_{i,j}) = u_{i,j}$, while for the latter we impose $Q_{\overline{T}_2}(u_{i,j}) = u_{j,i} = u_{i,j}^\dagger$. Typically, these constraints have the effect of reducing the number of variational parameters of the *Ansatz*.

From the practical point of view, the construction of the *Ansatz* is organized in the following way. We start from onsite terms and we apply the above constraints to the matrices λ_i of the sites i which lie inside the unit cell. Then, all the other onsite matrices can be obtained by applying the translational symmetries of the lattice and the corresponding gauge transformations. For the bond matrices, we start with first-neighbor terms and we perform the same procedure, first applying the constraints to a given bond and then propagating the results to the remaining of the lattice using the PSG elements (both translations and point group symmetries are usually needed). After first-neighbor matrices are obtained, we can move to second neighbors and repeat the same steps. From the variational point of view, when studying a spin Hamiltonian whose couplings are limited to a certain range, we typically consider spin liquid *Ansätze* whose matrices $u_{i,j}$ are nonzero up to (at least) the same range.

In the following section, we provide a concrete example of a PSG classification, looking for Z_2 spin liquids on the square lattice, which have been listed by Wen in his seminal paper [85]. As a consequence of the gapped nature of the low-energy gauge fluctuations, Z_2 spin liquids are generally considered to be stable quantum phases [15, 92].

2.7 Z_2 spin liquids on the square lattice: PSG equations

Let us consider an infinite square lattice whose sites positions are labelled by integer coordinates (x, y). We denote by T_x and T_y the translations of the unit vectors $x = (1, 0)$ and $y = (0, 1)$, respectively:

$$T_x(x,y) = (x+1, y) \qquad T_y(x,y) = (x, y+1). \tag{2.47}$$

The point group symmetry of the lattice can be represented by three reflections

$$P_x(x,y) = (-x, y), \qquad P_y(x,y) = (x, -y), \qquad P_{xy}(x,y) = (y, x), \tag{2.48}$$

as done in Ref. [85]. An equivalent choice corresponds to taking P_{xy} and a C_4 rotation R, such that $R(x,y) = (-y,x)$.

In order to achieve a classification of Z_2 spin liquids, we fix the IGG to be the set of global Z_2 transformations, namely IGG $= \left\{Q_{\mathcal{I}}^+, Q_{\mathcal{I}}^-\right\}$, where $Q_{\mathcal{I}}^+ = (\mathbb{1}, \mathcal{I})$ and $Q_{\mathcal{I}}^- = (-\mathbb{1}, \mathcal{I})$.

2.7.1 Translation along x

As the first step of the PSG classification, we consider one of the two translational symmetries, T_x in this case, and we assume that its associated gauge transformation takes an initial form $G^0_{T_x}(x,y)$. At this stage, being T_x the only symmetry into play, $G^0_{T_x}(x,y)$ can be any generic $SU(2)$ matrix because there are no algebraic relations constraining its form. Wen showed that it is always possible to choose a particular gauge in which $Q_{T_x} = (\mathbb{1}, T_x)$ (globally!) [84]. We want to determine the gauge transformation $W(x,y)$ which can be applied to transform our initial guess for the PSG element of T_x, namely $Q^0_{T_x} = (G^0_{T_x}, T_x)$, into the "trivial" element $Q_{T_x} = (G_{T_x}, T_x) = (\mathbb{1}, T_x)$. If we denote by $Q_W = (W, \mathcal{I})$ the PSG element of the gauge transformation W, we can exploit the result of Eq. (2.37) to write:

$$Q_{T_x} = Q_W Q^0_{T_x} Q_W^{-1} \implies G_{T_x}(x,y) = W(x,y) G^0_{T_x}(x,y) W^\dagger(x-1,y). \tag{2.49}$$

Thus, if we want to end up in the gauge in which $G_{T_x}(x,y) = \mathbb{1}$, we need to choose $W(x,y)$ such that

$$W(x-1,y) = W(x,y) G^0_{T_x}(x,y). \tag{2.50}$$

The above iterative formula can be applied starting from $x \to \infty$ and going backward, to yield the desired result [89].

Once we have fixed $G_{T_x}(x,y) = \mathbb{1}$, we can ask ourselves what is the remaining *gauge freedom* we have, i.e. what is the most generic gauge transformation $W(x,y)$ which would not change the form of $G_{T_x}(x,y)$, modulo the multiplication by an element of the Z_2 IGG[8]. An answer is found by requiring that

$$W(x,y) G_{T_x}(x,y) W^\dagger(x-1,y) = \pm G_{T_x}(x,y) \;\Rightarrow\; W(x,y) W^\dagger(x-1,y) = \pm \mathbb{1}, \tag{2.51}$$

where the $\pm$ sign comes from the possible multiplication by an IGG element. The above equation implies that $W(x,y)$ can only take the form $W(x,y) = W(y)$ or $W(x,y) = (-)^x W(y)$.

2.7.2 Translation along y

When seeking the PSG element of the second translational symmetry, Q_{T_y}, we need to take into account the algebraic relation between translations, $T_x T_y = T_y T_x$, which implies that $Q_{T_x} Q_{T_y} = Q_{\mathcal{I}} Q_{T_y} Q_{T_x}$, with $Q_{\mathcal{I}}$ being an element of the IGG. Since the latter contains only the global gauge transformations $\pm\mathbb{1}$, using the product rule of Eq. (2.31), we can write

$$(G_{T_x} T_x G_{T_y} T_x^{-1}, T_x T_y) = (\varepsilon_T G_{T_y} T_y G_{T_x} T_y^{-1}, T_y T_x), \tag{2.52}$$

where ε_T is an integer parameter that can take only the values ± 1. Exploiting the fact that $G_{T_x}(x,y) = \mathbb{1}$, we get the following equation for the gauge transformations:

$$G_{T_y}(x-1,y) = \varepsilon_T G_{T_y}(x,y). \tag{2.53}$$

[8] We point out again that if Q_T is an element of the PSG associated to the symmetry T, also $Q_I Q_T$ ($Q_I \in$ IGG) is a valid element of the PSG. For the classification of Z_2 spin liquids, this means that we are always free to change the global sign of the gauge transformation G_T of any $Q_T = (G_T, T)$ belonging to the algebraic PSG. In this sense, the solutions $Q_{T_x} = (\mathbb{1}, T_x)$ and $Q_{T_x} = (-\mathbb{1}, T_x)$ are completely equivalent.

As a consequence, G_{T_y} takes the simple form $G_{T_y}(x,y) = (\varepsilon_T)^x \tilde{G}_{T_y}(y)$, in which the dependency on x is only in the factor $(\varepsilon_T)^x$.

So far, the precise form of $\tilde{G}_{T_y}(y)$ is not known, but we can try to perform a gauge transformation to fix $\tilde{G}_{T_y}(y) = \mathbb{1}$ (again globally!) [84]. As emphasized before, in order not to change $G_{T_x}(x,y) = \mathbb{1}$, we can perform a gauge transformation of the form $W(x,y) = W(y)$:

$$W(y)\tilde{G}_{T_y}(y)W^\dagger(y-1) = \mathbb{1}. \tag{2.54}$$

As in the previous case, the gauge change $W(y)$ is defined by an iterative formula, i.e. $W(y-1) = W(y)\tilde{G}_{T_y}(y)$, which can be solved starting from $y \to \infty$ and going backward [89]. Once this is done, we are left with the following PSG elements for translations:

$$\boxed{G_{T_x}(x,y) = \mathbb{1} \qquad G_{T_y}(x,y) = (\varepsilon_T)^x \mathbb{1}} \tag{2.55}$$

This means that, restricting the symmetry group to translations yields two classes of PSG solutions for Z_2 spin liquids. Before projection, the *Ansätze* of the class defined by $\varepsilon_T = 1$ are translationally invariant, while the ones of the class defined by $\varepsilon_T = -1$ require a doubled unit cell in the y-direction. However, both classes provide translational invariant wave functions after projection.

In conclusion of this paragraph, we want to find out what is the remaining gauge freedom. We already know that the gauge transformations that do not affect $G_{T_x}(x,y) = \mathbb{1}$ take the form I) $W(x,y) = W(y)$ or II) $W(x,y) = (-)^x W(y)$. Now we require also $G_{T_y}(x,y) = (\varepsilon_T)^x \mathbb{1}$ to be preserved, modulo an element of the IGG:

$$W(x,y)G_{T_y}(x,y)W^\dagger(x,y-1) = \pm G_{T_y}(x,y) \;\Rightarrow\; W(x,y)W^\dagger(x,y-1) = \pm\mathbb{1}. \tag{2.56}$$

For both the cases I) and II), the above equation implies that

$$W(y) = \pm W(y-1) \;\Rightarrow\; W(y) = (\pm)^y W \;\Rightarrow\; \begin{cases} \text{I) } W(x,y) = (\pm)^y W, \\ \text{II) } W(x,y) = (-)^x(\pm)^y W, \end{cases} \tag{2.57}$$

where W is a global $SU(2)$ transformation. Thus, wrapping everything up, we have the options $W(x,y) = (\pm)^x(\pm)^y W$ and $W(x,y) = (\pm)^x(\mp)^y W$.

2.7.3 Reflection with respect to the y=x axis

The next symmetry we consider is the reflection P_{xy}. Two algebraic conditions constrain the form of the gauge transformation associated to P_{xy}

$$P_{xy}^2 = \mathcal{I} \implies Q_{P_{xy}}Q_{P_{xy}} = (\varepsilon_{xy}\mathbb{1}, \mathcal{I}), \tag{2.58}$$

$$T_x P_{xy} = P_{xy} T_y \implies Q_{T_x}Q_{P_{xy}} = (\varepsilon_{TP}\mathbb{1}, \mathcal{I})Q_{P_{xy}}Q_{T_y}, \tag{2.59}$$

where both ε_{xy} and ε_{TP} account for a sign ± 1 (Z_2 IGG). Let us start from the second condition, which implies that

$$\begin{aligned} G_{T_x}(x,y)G_{P_{xy}}(x-1,y) &= \varepsilon_{TP}G_{P_{xy}}(x,y)G_{T_y}(y,x) \\ &\implies G_{P_{xy}}(x-1,y) = \varepsilon_{TP}(\varepsilon_T)^y G_{P_{xy}}(x,y). \end{aligned} \tag{2.60}$$

The solution to the above equation is given by $G_{P_{xy}}(x,y) = (\varepsilon_T)^{xy}(\varepsilon_{TP})^x \tilde{G}_{P_{xy}}(y)$, where $\tilde{G}_{P_{xy}}$ is a gauge transformation which depends only on the y-coordinate. If we then apply the constraint of Eq. (2.58), we get

$$\begin{aligned} G_{P_{xy}}(x,y)G_{P_{xy}}(y,x) &= \varepsilon_{xy}\mathbb{1} \\ &\implies \cancel{(\varepsilon_T)^{xy}}(\varepsilon_{TP})^x \tilde{G}_{P_{xy}}(y)\cancel{(\varepsilon_T)^{yx}}(\varepsilon_{TP})^y \tilde{G}_{P_{xy}}(x) = \varepsilon_{xy}\mathbb{1} \\ &\implies (\varepsilon_{TP})^x \tilde{G}_{P_{xy}}(x) = \varepsilon_{xy}(\varepsilon_{TP})^y \tilde{G}^\dagger_{P_{xy}}(y). \end{aligned} \tag{2.61}$$

In the last line of the above equation, the left-hand side of the equality only depends on x, while the right-hand side only depends on y. Therefore, the product $(\varepsilon_{TP})^y \tilde{G}_{P_{xy}}(y)$ cannot depend on the coordinate y and must be a global gauge transformation $g_{P_{xy}}$ that satisfies $g^2_{P_{xy}} = \varepsilon_{xy}\mathbb{1}$. Then, we can write that $\tilde{G}_{P_{xy}}(y) = (\varepsilon_{TP})^y g_{P_{xy}}$, which leads to

$$G_{P_{xy}}(x,y) = (\varepsilon_T)^{xy}(\varepsilon_{TP})^{x+y} g_{P_{xy}} \qquad [\text{with } g^2_{P_{xy}} = \varepsilon_{xy}\mathbb{1}]. \tag{2.62}$$

This solution can be further simplified because the sign $(-)^{x+y}$ which appears in the case $\varepsilon_{TP} = -1$ can always be canceled by the application of a gauge transformation of the form $W(x,y) = (-)^y\mathbb{1}$. As shown previously, under the effect of this gauge change, G_{T_x} remains invariant, and G_{T_y} acquires a global minus sign, which can be removed by the multiplication with $Q^-_{\mathcal{I}}$ (element of the IGG). Therefore, while the PSG solutions for translations remain the ones of Eq. (2.55), the final form of the PSG element of the P_{xy} reflection becomes:

$$\boxed{G_{P_{xy}}(x,y) = (\varepsilon_T)^{xy} g_{P_{xy}} \qquad [\text{with } g^2_{P_{xy}} = \varepsilon_{xy}\mathbb{1}]} \tag{2.63}$$

Once more, we determine the remaining gauge freedom, finding the gauge transformations $W(x,y)$ which preserve $G_{P_{xy}}(x,y)$, i.e.

$$W(x,y)G_{P_{xy}}(x,y)W^\dagger(y,x) = \pm G_{P_{xy}}(x,y) \;\Rightarrow\; W(x,y)g_{P_{xy}}W^\dagger(y,x) = \pm g_{P_{xy}}. \tag{2.64}$$

We substitute in the above equation the two possible gauge transformations which do not affect the form of $G_{T_x}(x,y)$ and $G_{T_y}(x,y)$, namely

$$W(x,y) = (\pm)^x(\pm)^y W \;\Rightarrow\; W g_{P_{xy}} W^\dagger = \pm g_{P_{xy}} \;\Rightarrow\; [W, g_{P_{xy}}]_\pm = 0, \tag{2.65}$$

$$W(x,y) = (\pm)^x(\mp)^y W \;\Rightarrow\; (-)^{x+y} W g_{P_{xy}} W^\dagger = \pm g_{P_{xy}} \;\Rightarrow\; \text{no solution}. \tag{2.66}$$

Here, we indicate by $[W, g_{P_{xy}}]_\pm = 0$ the fact that W commutes or anticommutes with $g_{P_{xy}}$, i.e. $[W, g_{P_{xy}}] = 0 \vee \{W, g_{P_{xy}}\} = 0$. Therefore, the remaining gauge freedom only consists of gauge transformations of the form $W(x,y) = (\pm)^{x+y}W$, where W is a $SU(2)$ matrix satisfying $[W, g_{P_{xy}}]_\pm = 0$.

We note that, up to this point, the PSG formulae we obtained are valid also for spin liquids on the triangular lattice, if we replace T_x and T_y by the translations along a_1 and a_2, x and y by the integer numbers specifying the lattice position with respect to a_1 and a_2, and P_{xy} by the reflection symmetry which exchanges a_1 and a_2. However, in the next two paragraphs we are going to consider the reflection transformations P_x and P_y, which are specific symmetries of the square lattice.

2.7.4 Reflection with respect to the y axis

The introduction of P_x within our classification brings along three constraints for the PSG elements, descending from the following algebraic relations [85]:

$$P_x^2 = \mathcal{I} \;\Rightarrow\; Q_{P_x}Q_{P_x} = (\varepsilon_{xx}\mathbb{1}, \mathcal{I}), \tag{2.67}$$

$$T_xP_xT_xP_x = \mathcal{I} \;\Rightarrow\; Q_{T_x}Q_{P_x}Q_{T_x}Q_{P_x} = (\varepsilon_A\mathbb{1}, \mathcal{I}), \tag{2.68}$$

$$T_yP_x = P_xT_y \;\Rightarrow\; Q_{T_y}Q_{P_x} = (\varepsilon_B\mathbb{1}, \mathcal{I})Q_{P_x}Q_{T_y}. \tag{2.69}$$

Once more, ε_{xx}, ε_A and ε_B are three parameters which can only have value ± 1. The last of the above equations implies that

$$\begin{aligned} G_{T_y}(x,y)G_{P_x}(x,y-1) &= \varepsilon_B G_{P_x}(x,y)G_{T_y}(-x,y) \\ \Longrightarrow\; G_{P_x}(x,y-1) &= \varepsilon_B G_{P_x}(x,y), \end{aligned} \tag{2.70}$$

where we have used the results of Eq. (2.55). Thus, G_{P_x} can only depend on y through a staggering factor $(\varepsilon_B)^y$, namely $G_{P_x}(x,y) = (\varepsilon_B)^y \tilde{G}_{P_x}(x)$. Now we can take the explicit formulae for gauge transformations deriving from Eq. (2.67),

$$G_{P_x}(x,y)G_{P_x}(-x,y) = \varepsilon_{xx}\mathbb{1}, \tag{2.71}$$

and Eq. (2.68),

$$G_{P_x}(x-1,y)G_{P_x}(-x,y) = \varepsilon_A\mathbb{1}, \tag{2.72}$$

and substitute our expression for $G_{P_x}(x,y)$. As a result, we obtain the following conditions:

$$\left.\begin{array}{l}\tilde{G}^\dagger_{P_x}(-x) = \varepsilon_{xx}\tilde{G}_{P_x}(x) \\ \tilde{G}^\dagger_{P_x}(-x) = \varepsilon_A\tilde{G}_{P_x}(x-1)\end{array}\right\} \Rightarrow\ \tilde{G}_{P_x}(x) = \varepsilon_A\varepsilon_{xx}\tilde{G}_{P_x}(x-1). \tag{2.73}$$

The solution to the above system of equations is $\tilde{G}_{P_x}(x) = (\varepsilon_A\varepsilon_{xx})^x g_{P_x}$, where g_{P_x} is a global gauge transformation satisfying $g^2_{P_x} = \varepsilon_{xx}\mathbb{1}$. Since both ε_{xx} and ε_A are free to take values ± 1, we can redefine $\varepsilon_A\varepsilon_{xx} \mapsto \varepsilon_A$ without any loss of generality. Then, we get to the final form of the PSG element for P_x:

$$\boxed{G_{P_x}(x,y) = (\varepsilon_A)^x(\varepsilon_B)^y g_{P_x} \qquad [\text{with } g^2_{P_x} = \varepsilon_{xx}\mathbb{1}]} \tag{2.74}$$

In order to determine the remaining gauge freedom, we can apply $W(x,y) = (\pm)^{x+y}W$ and require $G_{P_x}(x,y)$ to be invariant modulo a sign:

$$W(x,y)G_{P_x}(x,y)W^\dagger(-x,y) = \pm G_{P_x}(x,y)\ \Rightarrow\ W g_{P_x} W^\dagger = \pm g_{P_x}. \tag{2.75}$$

This implies that the global gauge transformation W must satisfy also $[W, g_{P_x}]_\pm = 0$.

2.7.5 Reflection with respect to the x axis

The addition of the reflection symmetry P_y to our classification introduces six new equations for the PSG elements. Let us first consider three of these equations, which actually mirror the PSG conditions introduced in the previous paragraph:

$$P_y^2 = \mathcal{I}\ \Rightarrow\ Q_{P_y}Q_{P_y} = (\varepsilon_{yy}\mathbb{1}, \mathcal{I}), \tag{2.76}$$

$$T_yP_yT_yP_y = \mathcal{I}\ \Rightarrow\ Q_{T_y}Q_{P_y}Q_{T_y}Q_{P_y} = (\varepsilon_C\mathbb{1}, \mathcal{I}), \tag{2.77}$$

$$T_xP_y = P_yT_x\ \Rightarrow\ Q_{T_x}Q_{P_y} = (\varepsilon_D\mathbb{1}, \mathcal{I})Q_{P_y}Q_{T_x}. \tag{2.78}$$

The above equations exactly correspond to Eqs. (2.67-2.69), once we change $x \leftrightarrow y$ and we replace $(\varepsilon_{xx}, \varepsilon_A, \varepsilon_B)$ with $(\varepsilon_{yy}, \varepsilon_C, \varepsilon_D)$. Therefore, following essentially the same steps discussed for the case of P_x, we can find the PSG element of P_y

$$G_{P_y}(x,y) = (\varepsilon_C)^y(\varepsilon_D)^x g_{P_y} \qquad [\text{with } g^2_{P_y} = \varepsilon_{yy}\mathbb{1}]. \tag{2.79}$$

However, this is not the end of the story since other three algebraic relations need to be taken into account. Let us start from the two relations which involve all the three reflection symmetries:

$$P_xP_{xy} = P_{xy}P_y\ \Rightarrow\ Q_{P_x}Q_{P_{xy}} = (\varepsilon_{P_1}, \mathcal{I})Q_{P_{xy}}Q_{P_y}, \tag{2.80}$$

$$P_yP_{xy} = P_{xy}P_x\ \Rightarrow\ Q_{P_y}Q_{P_{xy}} = (\varepsilon_{P_2}, \mathcal{I})Q_{P_{xy}}Q_{P_x}. \tag{2.81}$$

The above equations yield the following constraints for the gauge transformations:

$$G_{P_x}(x,y)G_{P_{xy}}(-x,y) = \varepsilon_{P_1}G_{P_{xy}}(x,y)G_{P_y}(y,x), \tag{2.82}$$

$$G_{P_y}(x,y)G_{P_{xy}}(x,-y) = \varepsilon_{P_2} G_{P_{xy}}(x,y)G_{P_x}(y,x). \tag{2.83}$$

Here we observe that, in each of the two equations above, G_{P_x} and G_{P_y} appear only *once*. Therefore, we can perform a trick to fix $\varepsilon_{P_1} = 1$ and $\varepsilon_{P_2} = 1$, exploiting the fact that any PSG element can be freely multiplied by an element of the IGG. Indeed, if we assume to incorporate an extra minus sign in the definition of, e.g., G_{P_x}, we can get rid of ε_{P_1} and ε_{P_2}. This is possible because these terms represent gauge dependent signs [96], as in the case of ε_{TP} (cf. Section 2.7.3). So, from now on we assume $\varepsilon_{P_1} = \varepsilon_{P_2} = 1$.

Let us consider first Eq. (2.82), in which we insert the explicit expression for the PSG gauge elements. After reshuffling the various factors, we obtain:

$$(\varepsilon_A)^x(\varepsilon_C)^x g_{P_x} g_{P_{xy}} = (\varepsilon_B)^y(\varepsilon_D)^y g_{P_{xy}} g_{P_y}. \tag{2.84}$$

Since the left-hand side of the equation depends only x, while the right-hand side depends only on y, we necessarily conclude that both $\varepsilon_A\varepsilon_C$ and $\varepsilon_D\varepsilon_B$ must be equal to 1. This means that we can fix $\varepsilon_C = \varepsilon_A$ and $\varepsilon_D = \varepsilon_B$, and arrive to the final expression for the PSG element of P_y:

$$\boxed{G_{P_y}(x,y) = (\varepsilon_A)^y(\varepsilon_B)^x g_{P_y} \qquad [\text{with } g_{P_y}^2 = \varepsilon_{yy}\mathbb{1}]} \tag{2.85}$$

Using the above expression into Eqs. (2.82) and (2.83), we get:

$$\boxed{g_{P_x} g_{P_{xy}} = g_{P_{xy}} g_{P_y}} \tag{2.86}$$

$$\boxed{g_{P_y} g_{P_{xy}} = g_{P_{xy}} g_{P_x}} \tag{2.87}$$

If we multiply the left-hand side of the former equation by the right-hand side of the latter, and viceversa (being careful to the order of the matrix product), we get:

$$g_{P_x} g_{P_{xy}}^2 g_{P_x} = g_{P_{xy}} g_{P_y}^2 g_{P_{xy}} \;\Rightarrow\; \varepsilon_{xy} g_{P_x}^2 = \varepsilon_{yy} g_{P_{xy}}^2, \tag{2.88}$$

which imposes the following constraint on the signs

$$\boxed{\varepsilon_{xx} = \varepsilon_{yy}} \tag{2.89}$$

Finally, we consider the commutation of P_x and P_y,

$$P_x P_y = P_y P_x \;\Rightarrow\; Q_{P_x} Q_{P_y} = (\varepsilon_P, \mathcal{I}) Q_{P_y} Q_{P_x}, \tag{2.90}$$

whose corresponding equation for the gauge transformations,

$$G_{P_x}(x,y)G_{P_y}(-x,y) = \varepsilon_P G_{P_y}(x,y)G_{P_x}(x,-y), \tag{2.91}$$

produces the following constraint:

$$\boxed{g_{P_x} g_{P_y} = \varepsilon_P g_{P_y} g_{P_x}} \tag{2.92}$$

Analogously to what we observed in the previous paragraph, preserving the present form of $G_{P_y}(x,y)$ adds a new condition for the remaining gauge freedom: the global transformation W entering the expression $W(x,y) = (\pm)^{x+y}W$ must satisfy also $[W, g_{P_y}]_\pm = 0$.

2.7.6 Time reversal

The last symmetry we need to include in our classification is time reversal. Due to its definition (D.8), we have that $\Theta^2 = 1$, which implies that $G^2_\Theta(x,y) = \varepsilon_\Theta \mathbb{1}$. Moreover, time reversal commutes with all lattice symmetries. Let us start by considering translations, for which we have

$$\begin{aligned} Q_\Theta Q_{T_x} &= (\varepsilon_1 \mathbb{1}, \mathcal{I}) Q_{T_x} Q_\Theta \;\Rightarrow G_\Theta(x,y) = \varepsilon_1 G_\Theta(x-1,y), \\ Q_\Theta Q_{T_y} &= (\varepsilon_2 \mathbb{1}, \mathcal{I}) Q_{T_y} Q_\Theta \;\Rightarrow G_\Theta(x,y) = \varepsilon_2 G_\Theta(x,y-1). \end{aligned} \tag{2.93}$$

The solution to the above equations is $G_\Theta(x,y) = (\varepsilon_1)^x (\varepsilon_2)^y g_\Theta$, where g_Θ is a global gauge transformation, such that $g^2_\Theta = \varepsilon_\Theta \mathbb{1}$. If we consider the commutation with P_{xy}, $Q_\Theta Q_{P_{xy}} = (\varepsilon_{\Theta xy}\mathbb{1}, \mathcal{I}) Q_{P_{xy}} Q_\Theta$, we get

$$\begin{aligned} &G_\Theta(x,y) G_{P_{xy}}(x,y) = \varepsilon_{\Theta xy} G_{P_{xy}}(x,y) G_\Theta(y,x) \\ &\qquad \Longrightarrow \; (\varepsilon_1\varepsilon_2)^{x+y} g_\Theta g_{P_{xy}} = \varepsilon_{\Theta xy} g_{P_{xy}} g_\Theta \end{aligned} \tag{2.94}$$

In the last expression, only the left-hand side depends on the lattice positions, implying that $\varepsilon_1\varepsilon_2 = 1$. If we define $\varepsilon_{\Theta T} = \varepsilon_1 = \varepsilon_2$, we can write

$$\boxed{G_\Theta(x,y) = (\varepsilon_{\Theta T})^{x+y} g_\Theta \qquad [\text{with } g^2_\Theta = \varepsilon_\Theta \mathbb{1}]} \tag{2.95}$$

$$\boxed{g_\Theta g_{P_{xy}} = \varepsilon_{\Theta xy} g_{P_{xy}} g_\Theta} \tag{2.96}$$

Finally, the commutation relations between time reversal and P_x, P_y yield

$$\begin{aligned} &Q_\Theta Q_{P_x} = (\varepsilon_{\Theta x}\mathbb{1}, \mathcal{I}) Q_{P_x} Q_\Theta \\ &\quad \Longrightarrow \; G_\Theta(x,y) G_{P_x}(x,y) = \varepsilon_{\Theta x} G_{P_x}(x,y) G_\Theta(-x,y), \end{aligned} \tag{2.97}$$

$$\begin{aligned} &Q_\Theta Q_{P_y} = (\varepsilon_{\Theta y}\mathbb{1}, \mathcal{I}) Q_{P_y} Q_\Theta \\ &\quad \Longrightarrow \; G_\Theta(x,y) G_{P_y}(x,y) = \varepsilon_{\Theta y} G_{P_y}(x,y) G_\Theta(x,-y). \end{aligned} \tag{2.98}$$

Inserting the expressions of Eq. (2.74), Eq. (2.85) and (2.95), we get the last two constraints of our classification:

$$\boxed{g_\Theta g_{P_x} = \varepsilon_{\Theta x} g_{P_x} g_\Theta} \tag{2.99}$$

$$\boxed{g_\Theta g_{P_y} = \varepsilon_{\Theta y} g_{P_y} g_\Theta} \tag{2.100}$$

In order to preserve the form of G_Θ, our gauge freedom is reduced by a further constraint, i.e. $[W, g_\Theta]_\pm = 0$. So, the final form of the transformation which leaves all the above PSG elements invariant (modulo the multiplication by an element of the IGG) is $W(x,y) = (\pm)^{x+y} W$, together with the conditions

$$[W, g_{P_{xy}}]_\pm = 0, \qquad [W, g_{P_x}]_\pm = 0, \qquad [W, g_{P_y}]_\pm = 0, \qquad [W, g_\Theta]_\pm = 0. \tag{2.101}$$

In Table 2.1 we summarize all the equations which define the possible Z_2 spin liquids on the square lattice. We note that we have used specific labels for these equations, i.e. (T1-T15), because they will be referenced many times in the following.

(T1)	$G_{T_x}(x,y) = \mathbb{1}$
(T2)	$G_{T_y}(x,y) = (\varepsilon_T)^x \mathbb{1}$
(T3)	$G_{P_{xy}}(x,y) = (\varepsilon_T)^{xy} g_{P_{xy}}$
(T4)	$G_{P_x}(x,y) = (\varepsilon_A)^x (\varepsilon_B)^y g_{P_x}$
(T5)	$G_{P_y}(x,y) = (\varepsilon_A)^y (\varepsilon_B)^x g_{P_y}$
(T6)	$G_\Theta(x,y) = (\varepsilon_{\Theta T})^{x+y} g_\Theta$
(T7)	$g_{P_{xy}}^2 = \varepsilon_{xy}\mathbb{1}$
(T8)	$g_{P_x}^2 = g_{P_y}^2 = \varepsilon_{xx}\mathbb{1} = \varepsilon_{yy}\mathbb{1}$
(T9)	$g_\Theta^2 = \varepsilon_\Theta \mathbb{1}$
(T10)	$g_{P_x} g_{P_{xy}} = g_{P_{xy}} g_{P_y}$
(T11)	$g_{P_y} g_{P_{xy}} = g_{P_{xy}} g_{P_x}$
(T12)	$g_{P_x} g_{P_y} = \varepsilon_P g_{P_y} g_{P_x}$
(T13)	$g_\Theta g_{P_{xy}} = \varepsilon_{\Theta xy} g_{P_{xy}} g_\Theta$
(T14)	$g_\Theta g_{P_x} = \varepsilon_{\Theta x} g_{P_x} g_\Theta$
(T15)	$g_\Theta g_{P_y} = \varepsilon_{\Theta y} g_{P_y} g_\Theta$

Table 2.1: List of all the equations governing the PSG classification of Z_2 spin liquids on the square lattice.

2.8 Z_2 spin liquids on the square lattice: PSG solutions

The next step of our classification consists in finding all the distinct solutions of the equations of Table 2.1. The result of this procedure is the algebraic PSG for Z_2 spin liquids on the square lattice. Before undertaking the actual solution of the aforementioned equations, we discuss the role of the PSG parameters and we give some preliminary remarks.

2.8.1 The PSG parameters

Finding the solutions of the PSG equations summarized in Table 2.1 means determining explicit expressions for the global $SU(2)$ transformations $g_{P_{xy}}$, g_{P_x}, g_{P_y}, and g_Θ. The form of these transformations is constrained by Eqs. (T7-T15). Different sets of values of the ε parameters give rise to different PSG solutions. As a first step, let us divide these parameters into three groups, according to their role in the PSG equations:

$$\begin{aligned} \mathcal{E}_s &= \{\varepsilon_T, \varepsilon_A, \varepsilon_B, \varepsilon_{\Theta T}\}, \\ \mathcal{E}_g &= \{\varepsilon_{xy}, \varepsilon_{xx} = \varepsilon_{yy}, \varepsilon_\Theta\}, \\ \mathcal{E}_{gg} &= \{\varepsilon_P, \varepsilon_{\Theta xy}, \varepsilon_{\Theta x}, \varepsilon_{\Theta y}\}. \end{aligned} \tag{2.102}$$

The parameters of $\mathcal{E}_s$ only dictate the spatial dependence of the gauge transformations, and do not need to be fixed in advance when seeking a solution of the PSG equations. Actually, when a solution for the global transformations $\{g_{P_{xy}}, g_{P_x}, g_{P_y}, g_\Theta\}$ is found, it automatically correspond to 16 distinct spin liquid *Ansätze*, due to the fact that each of the parameters of $\mathcal{E}_s$ can take values ± 1. On the contrary, the parameters contained in $\mathcal{E}_g$ play a major role in the definition of the actual form of the g-matrices, since they characterize expressions of the form $g^2 = \varepsilon\mathbb{1}$. We will scan over the possible values of these parameters

in order to find all possible solutions for the various g. Finally, the parameters of $\mathcal{E}_{gg}$ define the commutation/anticommutation relations between gauge transformations. As we will see, in some cases, once a given choice for $\mathcal{E}_g$ is formulated, some of the parameters of $\mathcal{E}_{gg}$ will be forced to assume certain values and won't constitute a further degree of freedom for the solutions.

2.8.2 Towards the solution: preliminary remarks

Here we would like to make a couple of preliminary remarks which will facilitate the solution of the equations of Table 2.1. For this purpose, let us consider an extremely simplified example, namely a minimal set of PSG equations:

$$g^2 = \varepsilon \mathbb{1} \tag{2.103}$$

$$\tilde{g}^2 = \tilde{\varepsilon} \mathbb{1} \tag{2.104}$$

Here, g and $\tilde{g}$ are global $SU(2)$ matrices, and $\varepsilon, \tilde{\varepsilon}$ can take values ± 1. Let us suppose we start the solution of the above equations by looking for an explicit form for g. If $\varepsilon = 1$, the only possible solution for Eq. (2.103) is $g = \mathbb{1}$. On the contrary, if $\varepsilon = -1$, a generic solution of Eq. (2.103) is given by the linear combination

$$g = i(a_1\sigma_1 + a_2\sigma_2 + a_3\sigma_3), \tag{2.105}$$

where a_i are real coefficients satisfying $a_1^2 + a_2^2 + a_3^2 = 1$. The above linear combination can be seen as a unit vector in the $(i\sigma_1, i\sigma_2, i\sigma_3)$ space. Within this picture, applying a global gauge transformation to g simply corresponds to rotating the representative vector around a certain axis. At this stage, since g is the first PSG element we consider in our solution process, we can always imagine to perform a global gauge transformation to rotate g in a desired direction. In other words, all the linear combinations of the form (2.105) correspond to gauge equivalent solutions of the first equation of our PSG set. In this case, we face a situation that will be referred to as Scenario 1:

Scenario 1. *If we are free to perform any global gauge transformation, we can always choose a gauge in which $g = i\sigma_a$ is the solution of the equation $g^2 = -\mathbb{1}$.*

By fixing a certain solution, e.g. $g = i\sigma_3$, we reduce the remaining *gauge freedom*. Indeed, the only global gauge transformations which do not affect the form of g, modulo a multiplication by an element of the IGG, i.e. a change of sign, are those which either commute or anticommute with g. The former ones, which leave g invariant, correspond to global rotations of an angle θ around the σ_3 axis, i.e.

$$W_3^\theta = \exp[i(\theta/2)\sigma_3]; \tag{2.106}$$

the latter ones, which map $g \mapsto -g$, are linear combinations of the form $i(a_1\sigma_1 + a_2\sigma_2)$, where $a_1^2 + a_2^2 = 1$. Without loss of generality, linear combinations of this kind can always be expressed as the product of a generic rotation around σ_3, i.e. W_3^θ, and a transformation $W_1^\pi = i\sigma_1$ (π-rotation around σ_1) or, equivalently, $W_2^\pi = i\sigma_2$ (π-rotation around σ_2). Therefore, in this situation, we say that our remaining gauge freedom consists of $[U(1) \times Z_2]_3$ global transformations, where the subscript indicates the axis of the $U(1)$ rotational symmetry (σ_3 in this example).

Let us now move to Eq. (2.104) to find a solution for $\tilde{g}$. If $\tilde{\varepsilon} = 1$, we necessarily conclude that $\tilde{g} = \mathbb{1}$, and we define the first two PSG solutions:

$$\varepsilon = 1,\ \tilde{\varepsilon} = 1 \implies g = \mathbb{1},\ \tilde{g} = \mathbb{1}; \tag{2.107}$$

$$\varepsilon = -1,\ \tilde{\varepsilon} = 1 \implies g = i\sigma_3,\ \tilde{g} = \mathbb{1}. \tag{2.108}$$

Instead, if $\tilde{\varepsilon} = -1$ the solution of the PSG equations depends on the value we obtained for g. If $g = \mathbb{1}$ (corresponding to $\varepsilon = 1$), our remaining gauge freedom consists of all global $SU(2)$ transformations, and we are back to the Scenario 1 for $\tilde{g}$. In this case, the PSG solution reads

$$\varepsilon = 1,\ \tilde{\varepsilon} = -1 \implies g = \mathbb{1},\ \tilde{g} = i\sigma_3. \tag{2.109}$$

On the other hand, if we obtained $g = i\sigma_3$, the situation gets more involved. Indeed, we are left only with the gauge freedom of rotating $\tilde{g}$ of any angle around the σ_3 axis, plus the freedom of rotating $\tilde{g}$ of π around the σ_1 or σ_2 axes. Given these constraints, we can find three inequivalent solutions for $\tilde{g}^2 = -\mathbb{1}$:

- $\tilde{g}_\parallel = i\sigma_3$ (i.e., $\tilde{g}$ is parallel to the σ_3 axis);
- $\tilde{g}_\perp = i(a_1\sigma_1 + a_2\sigma_2)$ (i.e., $\tilde{g}$ is perpendicular to the σ_3 axis);
- $\tilde{g}_\angle = i(a_1\sigma_1 + a_2\sigma_2 + a_3\sigma_3)$, with $(a_1 \neq 0 \vee a_2 \neq 0) \wedge a_3 \neq 0$ (i.e., $\tilde{g}$ has nonzero components both on the σ_3 axis and in the plane perpendicular to it).

Using geometric intuition, we can easily convince ourselves that the above three solutions cannot be transformed one into each other by means of generic rotations around σ_3, and/or π-rotations around σ_1 or σ_2. However, we can still exploit the global $[U(1) \times Z_2]_3$ gauge freedom to fix a desired orientation for $\tilde{g}_\perp$ and $\tilde{g}_\angle$. The result is summarized in the following Scenario:

Scenario 2. *Suppose that our global gauge freedom consists of generic rotations around the σ_a axis, and π-rotations around an axis perpendicular to σ_a, i.e. $[U(1) \times Z_2]_a$ gauge freedom. Then, the equation $\tilde{g}^2 = -\mathbb{1}$ has three inequivalent solutions, which can be written as $\tilde{g}_\parallel = i\sigma_a$, $\tilde{g}_\perp = i\sigma_b$ $(b \neq a)$, and $\tilde{g}_\angle = \frac{i}{\sqrt{2}}(\sigma_a + \sigma_c)$ $(c \neq a)$.*

Therefore, the last three solutions of our PSG equations can be chosen to be

$$\varepsilon = -1,\ \tilde{\varepsilon} = -1 \implies \begin{cases} g = i\sigma_3,\ \tilde{g} = i\sigma_3; \\ g = i\sigma_3,\ \tilde{g} = i\sigma_1; \\ g = i\sigma_3,\ \tilde{g} = \frac{i}{\sqrt{2}}(\sigma_1 + \sigma_3). \end{cases} \tag{2.110}$$

A schematic representation of the steps leading to all the PSG solutions is reported in Fig. 2.1

In general, the structure of the PSG equations is much more involved than the one presented in this section. In particular, one should at least expect an additional equation relating g and $\tilde{g}$, which imposes further constraints to the above solutions. Anyhow, the example discussed here will serve as a useful reference for the solution of the PSG equations of Table 2.1, since the Scenarios 1 and 2 will be encountered several times.

2.8.3 PSG solutions

We start by dividing the solutions of the PSG equations (T7-T15) in two broad classes, according to the form of the global gauge transformation associated with time reversal, g_Θ, which is determined by the value of ε_Θ [cf. Eq (T9)]. Indeed, if $\varepsilon_\Theta = 1$, then we have $g_\Theta^2 = \mathbb{1}$, whose only solution is $g_\Theta = \mathbb{1}$. We emphasize that this trivial solution leaves a considerable gauge freedom because g_Θ remains unchanged under any global $SU(2)$ transformation. On the other hand, if $\varepsilon_\Theta = -1$, then we have $g_\Theta^2 = -\mathbb{1}$ and, according

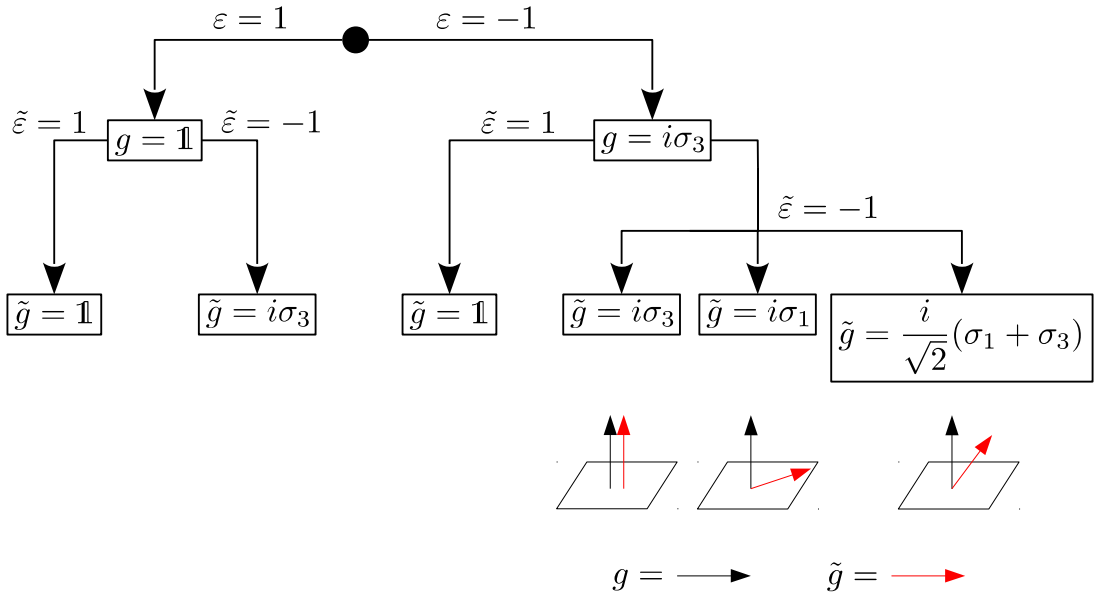

Figure 2.1: Schematic representations of the steps leading to the solutions of the PSG equations (2.103) and (2.104). For the last three solutions on the right, we depicted the PSG solutions for g and $\tilde{g}$ as vectors in the $(i\sigma_1, i\sigma_2, i\sigma_3)$ space.

to the Scenario 1 we are free to choose a gauge in which $g_\Theta = i\sigma_3$. With this choice, the remaining gauge freedom is reduced to $[U(1) \times Z_2]_3$ (see Section 2.8.2).

In the following paragraphs we separately discuss the PSG classes obtained by fixing $g_\Theta = \mathbb{1}$ and $g_\Theta = i\sigma_3$.

PSG solutions with $g_\Theta = \mathbb{1}$

Inserting $g_\Theta = \mathbb{1}$ in the last three equations of Table 2.1 automatically implies that $\varepsilon_{\Theta xy} = \varepsilon_{\Theta x} = \varepsilon_{\Theta y} = 1$. As previously mentioned, these parameters (and their corresponding equations) won't play any role in the definition of $g_{P_{xy}}$, g_{P_x}, and g_{P_y}. Let us consider the two possible values of ε_{xy} [cf. Eq. (T7)].

- If $\varepsilon_{xy} = 1$, then $g_{P_{xy}} = \mathbb{1}$. As a consequence, due to Eqs. (T10-T11), we have that $g_{P_x} = g_{P_y}$ [which implies $\varepsilon_P = 1$, cf. Eq. (T12)]. We emphasize that the trivial solution for $g_{P_{xy}}$ does not reduce the gauge freedom.

  ▷ If $\varepsilon_{xx} = \varepsilon_{yy} = 1$, then we conclude that $g_{P_x} = g_{P_y} = \mathbb{1}$, and we can write the first of our PSG solutions (which is the trivial one with all identities):

$$\boxed{g_\Theta = \mathbb{1} \quad g_{P_{xy}} = \mathbb{1} \quad g_{P_x} = \mathbb{1} \quad g_{P_y} = \mathbb{1}} \tag{PSG1}$$

  ▷ On the other hand, if $\varepsilon_{xx} = \varepsilon_{yy} = -1$, we find ourselves in the Scenario 1 for g_{P_x} $(= g_{P_y})$. Exploiting the gauge freedom, we can fix $g_{P_x} = g_{P_y} = i\sigma_3$ and obtain the following PSG solution:

$$\boxed{g_\Theta = \mathbb{1} \quad g_{P_{xy}} = \mathbb{1} \quad g_{P_x} = i\sigma_3 \quad g_{P_y} = i\sigma_3} \tag{PSG2}$$

- If $\varepsilon_{xy} = -1$, we can choose a gauge in which $g_{P_{xy}} = i\sigma_3$ (cf. Scenario 1). As a consequence, the remaining gauge freedom is reduced to $[U(1) \times Z_2]_3$. Inserting the above expression for $g_{P_{xy}}$ in Eqs. (T10-T11), we obtain the constraint $g_{P_y} = \sigma_3 g_{P_x} \sigma_3$.

▷ In the case $\varepsilon_{xx} = \varepsilon_{yy} = 1$, the only possible solution is $g_{P_x} = g_{P_y} = \mathbb{1}$ [which fixes $\varepsilon_P = 1$, cf. Eq. (T12)]:

$$\boxed{g_\Theta = \mathbb{1} \quad g_{P_{xy}} = i\sigma_3 \quad g_{P_x} = \mathbb{1} \quad g_{P_y} = \mathbb{1}} \tag{PSG3}$$

▷ The case $\varepsilon_{xx} = \varepsilon_{yy} = -1$ is more involved. For the sake of clarity, let us consider first the gauge transformation g_{P_x}, whose expression is determined by $g_{P_x}^2 = -\mathbb{1}$. Since our remaining gauge freedom is $[U(1) \times Z_2]_3$, we end up into Scenario 2. Therefore, three gauge inequivalent solutions for g_{P_x} exist, and for each of these solutions, the corresponding g_{P_y} is uniquely determined by $g_{P_y} = \sigma_3 g_{P_x} \sigma_3$:

$$g_{P_x} = i\sigma_3 \;\Rightarrow\; g_{P_y} = i\sigma_3; \tag{2.111}$$

$$g_{P_x} = i\sigma_1 \;\Rightarrow\; g_{P_y} = -i\sigma_1; \tag{2.112}$$

$$g_{P_x} = \frac{i}{\sqrt{2}}(\sigma_1 + \sigma_3) \;\Rightarrow\; g_{P_y} = \frac{i}{\sqrt{2}}(-\sigma_1 + \sigma_3). \tag{2.113}$$

This is not the end of the story, because we need to verify that the above pairs g_{P_x}, g_{P_y} satisfy Eq. (T12) for a given choice of ε_P. One can readily prove that this requirement is fulfilled by $\varepsilon_P = 1$ for the first two cases, and $\varepsilon_P = -1$ for the last one. In conclusion, we can write:

$$\boxed{g_\Theta = \mathbb{1} \quad g_{P_{xy}} = i\sigma_3 \quad g_{P_x} = i\sigma_3 \quad g_{P_y} = i\sigma_3} \tag{PSG4}$$

$$\boxed{g_\Theta = \mathbb{1} \quad g_{P_{xy}} = i\sigma_3 \quad g_{P_x} = i\sigma_1 \quad g_{P_y} = -i\sigma_1} \tag{PSG5}$$

$$\boxed{g_\Theta = \mathbb{1} \quad g_{P_{xy}} = i\sigma_3 \quad g_{P_x} = \frac{i}{\sqrt{2}}(\sigma_1 + \sigma_3) \quad g_{P_y} = \frac{i}{\sqrt{2}}(-\sigma_1 + \sigma_3)} \tag{PSG6}$$

We note that, in principle, we are allowed to get rid of the minus sign in the expression for g_{P_y} of Eq. (PSG5), because any PSG solution can be freely multiplied by an element of the IGG. However, for the sake of clarity, we prefer to keep these extra signs here and in the following.

A schematic representation of the procedure to get to the PSG solutions (PSG1-PSG6) is reported in Fig. 2.2.

PSG solutions with $g_\Theta = i\sigma_3$

We now turn to the PSG solutions with $g_\Theta = i\sigma_3$, for which we follow a procedure similar to the one outlined above. The main difference from the previous case is that here the initial gauge freedom is $[U(1) \times Z_2]_3$ (i.e. transformations which commute or anticommute with g_Θ, see Section 2.8.2). Another asymmetry with respect to the previous section is the fact that here the last three equations of Table 2.1 are not trivial:

$$g_{P_{xy}} = \varepsilon_{\Theta xy} \sigma_3 g_{P_{xy}} \sigma_3 \tag{2.114}$$

$$g_{P_x} = \varepsilon_{\Theta x} \sigma_3 g_{P_x} \sigma_3 \tag{2.115}$$

$$g_{P_y} = \varepsilon_{\Theta y} \sigma_3 g_{P_y} \sigma_3. \tag{2.116}$$

Let us start again by considering the possible expressions for $g_{P_{xy}}$ which solve Eq. (T7). When $\varepsilon_{xy} = 1$, the unique solution is $g_{P_{xy}} = \mathbb{1}$, as before. On the contrary, the choice $\varepsilon_{xy} = -1$ gives rise to more than one solution, at variance with the situation of the previous paragraph: solving the equation $g_{P_{xy}}^2 = -\mathbb{1}$ in presence of the $[U(1) \times Z_2]_3$ gauge

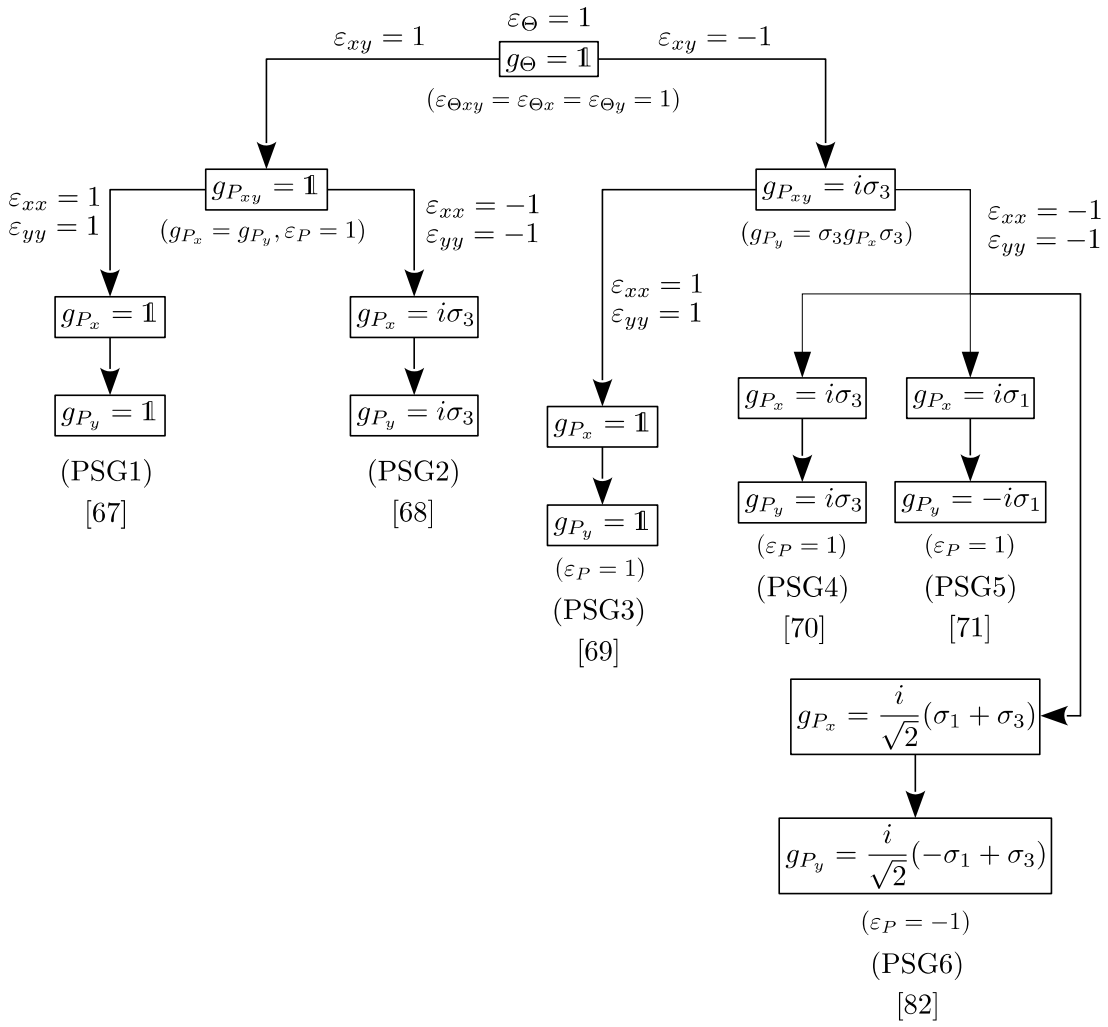

Figure 2.2: Schematic representation of the steps leading to the classification of Z_2 spin liquids on the square lattice. Only the PSG classes in which $g_\Theta = \mathbb{1}$ are included in this figure. Under each PSG solution we report, between square bracket, the label of the corresponding PSG class of Ref. [85].

freedom exactly corresponds to the example of Scenario 2, according to which $g_{P_{xy}}$ has three (potential) gauge inequivalent solutions. Two of them, $g_{P_{xy}} = i\sigma_3$ (parallel to σ_3 axis) and $g_{P_{xy}} = i\sigma_1$ (perpendicular to σ_3 axis), turn out to be valid solutions, while the third one, $g_{P_{xy}} = \frac{i}{\sqrt{2}}(\sigma_1 + \sigma_3)$, is incompatible with the constraint of Eq. (T13) and needs to be discarded. Indeed, if we insert the last formula for $g_{P_{xy}}$ into Eq. (2.114), we get

$$g_{P_{xy}} = \frac{i}{\sqrt{2}}(\sigma_1 + \sigma_3) = \varepsilon_{\Theta xy}\sigma_3 g_{P_{xy}}\sigma_3 = \varepsilon_{\Theta xy}\frac{i}{\sqrt{2}}(-\sigma_1 + \sigma_3), \tag{2.117}$$

which is impossible for any value of $\varepsilon_{\Theta xy}$. Conversely, the cases $g_{P_{xy}} = i\sigma_3$ and $g_{P_{xy}} = i\sigma_1$ are compatible with Eq. (T13) if $\varepsilon_{\Theta xy} = 1$ and $\varepsilon_{\Theta xy} = -1$, respectively.

Therefore, we have a total of three possible expressions for $g_{P_{xy}}$, i.e. $g_{P_{xy}} = \mathbb{1}$ (with $\varepsilon_{xy} = 1$), $g_{P_{xy}} = i\sigma_3$ and $g_{P_{xy}} = i\sigma_1$ (both with $\varepsilon_{xy} = -1$). Let us analyze these three cases one by one.

- The first case under investigation is $\varepsilon_{xy} = 1$, $g_{P_{xy}} = \mathbb{1}$, which implies $\varepsilon_{\Theta xy} = 1$. As a consequence, due to Eqs. (T10-T11), we have that $g_{P_x} = g_{P_y}$ [which causes $\varepsilon_P = 1$, cf. Eq. (T12)]. Then, combining Eq. (2.115) and Eq. (2.116), we can conclude that $\varepsilon_{\Theta x}\varepsilon_{\Theta y} = 1$. We remark that, at this stage, our remaining gauge freedom is still $[U(1) \times Z_2]_3$.

  ▷ In the case $\varepsilon_{xx} = \varepsilon_{yy} = 1$ the only possible solution is $g_{P_x} = g_{P_y} = \mathbb{1}$, and we have

  $$\boxed{g_\Theta = i\sigma_3 \quad g_{P_{xy}} = \mathbb{1} \quad g_{P_x} = \mathbb{1} \quad g_{P_y} = \mathbb{1}} \tag{PSG7}$$

  This solution necessarily requires that $\varepsilon_{\Theta x} = \varepsilon_{\Theta y} = 1$.

  ▷ If, on the other hand, $\varepsilon_{xx} = \varepsilon_{yy} = -1$, we end up into Scenario 2 for g_{P_x} ($= g_{P_y}$). Once more, only two of the potential solutions are valid, while the third one is forbidden. The allowed solutions are $g_{P_x} = g_{P_y} = i\sigma_3$ (corresponding to $\varepsilon_{\Theta x} = \varepsilon_{\Theta y} = 1$) and $g_{P_x} = g_{P_y} = i\sigma_1$ (corresponding to $\varepsilon_{\Theta x} = \varepsilon_{\Theta y} = -1$). These expressions give rise to the following PSG solutions:

  $$\boxed{g_\Theta = i\sigma_3 \quad g_{P_{xy}} = \mathbb{1} \quad g_{P_x} = i\sigma_3 \quad g_{P_y} = i\sigma_3} \tag{PSG8}$$

  $$\boxed{g_\Theta = i\sigma_3 \quad g_{P_{xy}} = \mathbb{1} \quad g_{P_x} = i\sigma_1 \quad g_{P_y} = i\sigma_1} \tag{PSG9}$$

  The last potential solution would be the one in which g_{P_x} has a nonzero component both along the σ_3 axis and perpendicular to it, e.g. $g_{P_x} = \frac{i}{\sqrt{2}}(\sigma_1 + \sigma_3)$. In analogy to what we observed for $g_{P_{xy}}$, this expression is incompatible with Eq. (2.115).

- The second case we consider is $\varepsilon_{xy} = -1$, $g_{P_{xy}} = i\sigma_3$, which implies $\varepsilon_{\Theta xy} = 1$. As a consequence of Eq. (T10), we observe that $g_{P_y} = \sigma_3 g_{P_x}\sigma_3$. Moreover, we note that since g_Θ and $g_{P_{xy}}$ are "parallel" in this case, the remaining gauge freedom is still $[U(1)\times Z_2]_3$.

  ▷ In the case $\varepsilon_{xx} = \varepsilon_{yy} = 1$ the only possible solution is $g_{P_x} = g_{P_y} = \mathbb{1}$, and we have

  $$\boxed{g_\Theta = i\sigma_3 \quad g_{P_{xy}} = i\sigma_3 \quad g_{P_x} = \mathbb{1} \quad g_{P_y} = \mathbb{1}} \tag{PSG10}$$

  This solution necessarily requires that $\varepsilon_{\Theta x} = \varepsilon_{\Theta y} = \varepsilon_P = 1$.

  ▷ If, on the other hand, $\varepsilon_{xx} = \varepsilon_{yy} = -1$, we end up into Scenario 2 for g_{P_x}. Repeating the same steps employed to determine (PSG8) and (PSG9), we find two valid

solutions for g_{P_x}, namely $g_{P_x} = i\sigma_3$ and $g_{P_x} = i\sigma_1$. For each of these expressions, the corresponding g_{P_y} is obtained by $g_{P_y} = \sigma_3 g_{P_x} \sigma_3$. The final results are

$$\boxed{g_\Theta = i\sigma_3 \quad g_{P_{xy}} = i\sigma_3 \quad g_{P_x} = i\sigma_3 \quad g_{P_y} = i\sigma_3} \tag{PSG11}$$

which implies $\varepsilon_{\Theta x} = \varepsilon_{\Theta y} = \varepsilon_P = 1$, and

$$\boxed{g_\Theta = i\sigma_3 \quad g_{P_{xy}} = i\sigma_3 \quad g_{P_x} = i\sigma_1 \quad g_{P_y} = -i\sigma_1} \tag{PSG12}$$

which implies $\varepsilon_{\Theta x} = \varepsilon_{\Theta y} = -1$ and $\varepsilon_P = 1$.

- The last case we consider is $\varepsilon_{xy} = -1$, $g_{P_{xy}} = i\sigma_1$, which implies $\varepsilon_{\Theta xy} = -1$. As a consequence of Eq. (T10), we observe that $g_{P_y} = \sigma_1 g_{P_x} \sigma_1$.

  Let us stress an important point here. Before finding an explicit expression for $g_{P_{xy}}$, our gauge freedom was made of $[U(1) \times Z_2]_3$ transformations, namely

$$W = W_3^\theta = e^{i\frac{\theta}{2}\sigma_3} \quad \text{and} \quad W = W_1^\pi W_3^\theta = i\sigma_1 e^{i\frac{\theta}{2}\sigma_3}, \tag{2.118}$$

  which respectively commute and anticommute with $g_\Theta = i\sigma_3$. Once the solution $g_{P_{xy}} = i\sigma_1$ is fixed, the residual gauge freedom is reduced by the additional constraint $[W, g_{P_{xy}}]_\pm = 0$, which imposes $\theta = \pi n$ ($n \in \mathbb{Z}$). As a result, the remaining freedom is reduced to the gauge transformations of the form $W = \pm i\sigma_a$ ($a = x, y, z$), and $W = \pm\mathbb{1}$.

  ▷ In the case $\varepsilon_{xx} = \varepsilon_{yy} = 1$ the only possible solution is $g_{P_x} = g_{P_y} = \mathbb{1}$, and we have

$$\boxed{g_\Theta = i\sigma_3 \quad g_{P_{xy}} = i\sigma_1 \quad g_{P_x} = \mathbb{1} \quad g_{P_y} = \mathbb{1}} \tag{PSG13}$$

  This solution necessarily requires that $\varepsilon_{\Theta x} = \varepsilon_{\Theta y} = \varepsilon_P = 1$.

  ▷ On the other hand, if $\varepsilon_{xx} = \varepsilon_{yy} = -1$ [Eq. (T8)], the expressions for g_{P_x} and g_{P_y} can take the generic form of Eq. (2.105). Here we face a new situation with respect to Scenarios 1 and 2, because the remaining gauge freedom is "too small" to fix a discrete number of solutions. However, as we will see, the parameters defining the form of g_{P_x} and g_{P_y} are constrained by the other PSG equations.

  For the sake of clarity, let us first concentrate on the solution for g_{P_x}, assuming $g_{P_x} = i(a_1\sigma_1 + a_2\sigma_2 + a_3\sigma_3)$. This matrix must satisfy Eq. (T14), namely $g_{P_x} = \varepsilon_{\Theta x}\sigma_3 g_{P_x}\sigma_3$. Depending on the value of $\varepsilon_{\Theta x}$, we get the following constraints:

$$\varepsilon_{\Theta x} = 1 \;\Rightarrow\; a_1 = a_2 = 0, \tag{2.119}$$

$$\varepsilon_{\Theta x} = -1 \;\Rightarrow\; a_3 = 0. \tag{2.120}$$

  → The first case, $\varepsilon_{\Theta x} = 1$, only allows for the solution $g_{P_x} = i\sigma_3$. As a consequence, $g_{P_y} = \sigma_1 g_{P_x} \sigma_1 = -i\sigma_3$ and $\varepsilon_P = 1$. The resulting PSG solution is

$$\boxed{g_\Theta = i\sigma_3 \quad g_{P_{xy}} = i\sigma_1 \quad g_{P_x} = i\sigma_3 \quad g_{P_y} = -i\sigma_3} \tag{PSG14}$$

  which is compatible with $\varepsilon_{\Theta y} = 1$.

  → In the second case, $\varepsilon_{\Theta x} = -1$, the solution for g_{P_x} can in general take the form $g_{P_x} = i(a_1\sigma_1 + a_2\sigma_2)$. Since $a_1^2 + a_2^2 = 1$, we can rewrite this expression using a compact notation:

$$g_{P_x} = i\sigma_1 \exp(i\phi\sigma_3), \tag{2.121}$$

where $\cos(\phi) = a_1$ and $\sin(\phi) = a_2$. In principle, there could be an infinite number of solutions labelled by a continuous parameter, however, it turns out that only some values of ϕ are allowed by the remaining PSG equations. Indeed, given the above expression for g_{P_x}, we can immediately compute

$$g_{P_y} = \sigma_1 g_{P_x} \sigma_1 = i\sigma_1 \exp(-i\phi\sigma_3), \tag{2.122}$$

which satisfies $g_{P_y}^2 = -\mathbb{1}$ and implies $\varepsilon_{\Theta y} = -1$. If we insert the two expressions for g_{P_x} and g_{P_y} into Eq. (T12), we obtain a constraint for ϕ:

$$\exp(4i\phi\sigma_3) = \varepsilon_P \mathbb{1} \;\Rightarrow\; \cos(4\phi) = \varepsilon_P,\ \sin(4\phi) = 0. \tag{2.123}$$

If $\varepsilon_P = 1$, the possible values of ϕ are

$$\phi = 0 \implies g_{P_x} = i\sigma_1,\ g_{P_y} = i\sigma_1 \tag{2.124}$$
$$\phi = \frac{\pi}{2} \implies g_{P_x} = i\sigma_2,\ g_{P_y} = -i\sigma_2 \tag{2.125}$$
$$\phi = \pi \implies g_{P_x} = -i\sigma_1,\ g_{P_y} = -i\sigma_1 \tag{2.126}$$
$$\phi = \frac{3}{2}\pi \implies g_{P_x} = -i\sigma_2,\ g_{P_y} = i\sigma_2 \tag{2.127}$$

We observe that the first solution is equivalent to the third, and the second is equivalent to the fourth (since we are always free to multiply any PSG solution by an element of the IGG, i.e. a minus sign). Therefore, we have two new PSG classes:

$$\boxed{g_\Theta = i\sigma_3 \quad g_{P_{xy}} = i\sigma_1 \quad g_{P_x} = i\sigma_1 \quad g_{P_y} = i\sigma_1} \tag{PSG15}$$

$$\boxed{g_\Theta = i\sigma_3 \quad g_{P_{xy}} = i\sigma_1 \quad g_{P_x} = i\sigma_2 \quad g_{P_y} = -i\sigma_2} \tag{PSG16}$$

On the other hand, if $\varepsilon_P = -1$, we can take

$$\phi = \frac{\pi}{4} \implies g_{P_x} = \frac{i}{\sqrt{2}}(\sigma_1 + \sigma_2),\ g_{P_y} = \frac{i}{\sqrt{2}}(\sigma_1 - \sigma_2) \tag{2.128}$$
$$\phi = \frac{3}{4}\pi \implies g_{P_x} = \frac{i}{\sqrt{2}}(-\sigma_1 + \sigma_2),\ g_{P_y} = \frac{i}{\sqrt{2}}(-\sigma_1 - \sigma_2) \tag{2.129}$$
$$\phi = \frac{5}{4}\pi \implies g_{P_x} = \frac{i}{\sqrt{2}}(-\sigma_1 - \sigma_2),\ g_{P_y} = \frac{i}{\sqrt{2}}(-\sigma_1 + \sigma_2) \tag{2.130}$$
$$\phi = \frac{7}{4}\pi \implies g_{P_x} = \frac{i}{\sqrt{2}}(\sigma_1 - \sigma_2),\ g_{P_y} = \frac{i}{\sqrt{2}}(\sigma_1 + \sigma_2) \tag{2.131}$$

Exploiting the freedom to multiply any PSG solutions by an element of the IGG, combined with gauge transformations of the form $G = \pm i\sigma_a$, one can easily prove that all the above expressions are gauge equivalent. Then, the last solution of the PSG equations is

$$\boxed{g_\Theta = i\sigma_3 \quad g_{P_{xy}} = i\sigma_1 \quad g_{P_x} = \frac{i}{\sqrt{2}}(\sigma_1 + \sigma_2) \quad g_{P_y} = \frac{i}{\sqrt{2}}(\sigma_1 - \sigma_2)} \tag{PSG17}$$

Once more, a schematic representation of the steps leading to the PSG solutions (PSG7-PSG17) is reported in Fig. 2.3.

In total, we found 17 PSG classes which, multiplied by the 16 possible choices for the

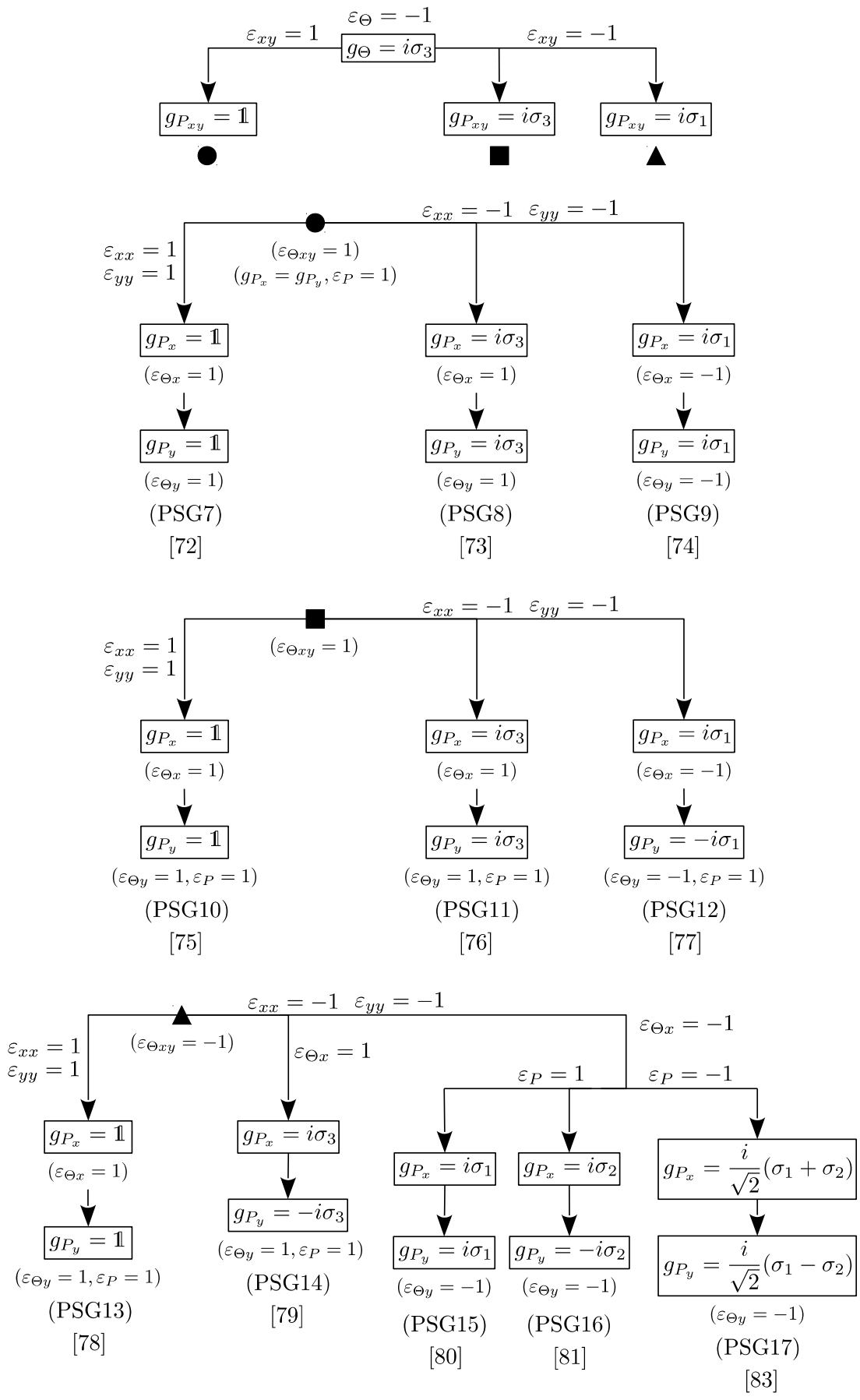

Figure 2.3: The same as Fig. 2.2 for the case $g_\Theta = i\sigma_3$.

parameters of $\mathcal{E}_s$, yield a total of 272 Z_2 spin liquids on the square lattice. However, some of these solutions correspond to trivial *Ansätze* in which all the matrices λ_i and $u_{i,j}$ are zero. This is the case, for example, of the $6 \times 8 = 48$ solutions with $g_\Theta = \mathbb{1}$ and $\varepsilon_\Theta = 1$, for which

$$\lambda_i = Q_\Theta(\lambda_i) = -\lambda_i \quad \text{and} \quad u_{i,j} = Q_\Theta(u_{i,j}) = -u_{i,j}. \tag{2.132}$$

According to Ref. [84], once the trivial solutions are ruled out, we are left with 196 possible Z_2 spin liquid states for the square lattice. In the following section we exemplify how the matrices $u_{i,j}$ and λ_i of an *Ansatz* can be explicitly determined from the PSG solutions. This is of fundamental importance for the construction of variational states fulfilling all the symmetries of the lattice model.

2.9 From the PSG solution to the spin liquid Ansatz: an example

For the purpose of describing the procedure through which a given fermionic *Ansatz* $(u_{i,j}, \lambda_i)$ is constructed starting from its algebraic PSG, we consider a specific case, taking the solution (PSG14), and assuming that $\varepsilon_T = \varepsilon_{\Theta T} = 1$ and $\varepsilon_A = \varepsilon_B = -1$. The variational wave function obtained by Gutzwiller-projecting the ground state of this *Ansatz*[9] is a gapless spin liquid with Dirac nodes, which yields the best variational energy for the highly frustrated region of the $J_1 - J_2$ Heisenberg model on the square lattice (see Section 4.2 for details) [97]. Before beginning to construct the matrices $(u_{i,j}, \lambda_i)$, let us choose a more convenient gauge by applying a transformation of the form $Q_W = (W, \mathcal{I})$, where

$$W(x,y) = (-)^x \exp\left(i\frac{\pi}{4}\sigma_1\right). \tag{2.133}$$

In the resulting gauge, the fermionic *Ansatz* only contains real hoppings and real pairings. Under the effect of the above gauge transformation, the PSG elements of the *Ansatz* change as follows:

$$\begin{cases} G_{T_x}(x,y) = \mathbb{1} \\ G_{T_y}(x,y) = \mathbb{1} \\ G_{P_{xy}}(x,y) = i\sigma_1 \\ G_{P_x}(x,y) = (-)^{x+y}(i\sigma_3) \\ G_{P_y}(x,y) = (-)^{x+y}(-i\sigma_3) \\ G_\Theta(x,y) = i\sigma_3 \end{cases} \Longrightarrow \begin{cases} G_{T_x}(x,y) = \mathbb{1} \quad (*) \\ G_{T_y}(x,y) = \mathbb{1} \\ G_{P_{xy}}(x,y) = (-)^{x+y}(i\sigma_1) \\ G_{P_x}(x,y) = (-)^{x+y}(i\sigma_2) \\ G_{P_y}(x,y) = (-)^{x+y}(i\sigma_2) \quad (*) \\ G_\Theta(x,y) = i\sigma_2 \end{cases} \tag{2.134}$$

Note that we manually changed the overall sign of the gauge transformations marked by $(*)$. This can always be achieved by a multiplication with the IGG element $Q_{\mathcal{I}}^-$.

As already pointed out, the trivial PSG gauge transformations associated to translations ensure that the fermionic Hamiltonian is translationally invariant, since

$$u_{i,j} = Q_{T_x}(u_{i,j}) = u_{T_x^{-1}(i,j)}, \qquad \lambda_i = Q_{T_x}(\lambda_i) = \lambda_{T_x^{-1}(i)}, \tag{2.135}$$

$$u_{i,j} = Q_{T_y}(u_{i,j}) = u_{T_y^{-1}(i,j)}, \qquad \lambda_i = Q_{T_y}(\lambda_i) = \lambda_{T_y^{-1}(i)}. \tag{2.136}$$

In general, the bond matrices $(u_{i,j})$ and onsite matrices (λ_i) can be expressed as a linear combination of $(i\mathbb{1}, \sigma_1, \sigma_2, \sigma_3)$ and $(\sigma_1, \sigma_2, \sigma_3)$, respectively:

$$u_{i,j} = it'_{i,j}\mathbb{1} + \Delta_{i,j}\sigma_1 + \Delta'_{i,j}\sigma_2 + t_{i,j}\sigma_3 \tag{2.137}$$

[9] We note that the chosen *Ansatz* corresponds to the PSG solution labelled as $Z2Azz13$ in Ref. [85].

$$\lambda_i = \zeta_i \sigma_1 + \zeta_i' \sigma_2 + \mu_i \sigma_3 \tag{2.138}$$

All the parameters of the above linear combinations are real. Because of PSG equations, some of the terms composing the *Ansatz* will be forced to be zero. We start by imposing the constraints due to time reversal [cf. Eqs. (2.45-2.46)],

$$u_{i,j} = -\sigma_2 u_{i,j} \sigma_2 \quad \text{and} \quad \lambda_i = -\sigma_2 \lambda_i \sigma_2, \tag{2.139}$$

which are satisfied only if $t'_{i,j} = \Delta'_{i,j} = \zeta'_i = 0$. Thus, as anticipated, the fermionic Hamiltonian only allows for real hoppings and real pairings.

Thanks to translational invariance, we can conveniently divide the definition of the parameters of the *Ansatz* by the range of the couplings, starting with onsite terms, and then moving to first neighbors, second neighbors, and so on.

Onsite terms

The onsite matrix λ_i does not depend on the site position, thanks to translational invariance. For simplicity, we consider the onsite matrix at the site $i = (0,0)$, $\lambda_{(0,0)} = \zeta\sigma_1 + \mu\sigma_3$, and we derive its final form, which can then be extended to all the sites of the lattice. We need to account for all the (non-trivial) symmetry transformations which leave site $(0,0)$ invariant, i.e. P_{xy}, P_x, P_y, and require that

$$\lambda_{(0,0)} = Q_{P_{xy}}\left(\lambda_{(0,0)}\right) \;\Rightarrow\; \lambda_{(0,0)} = (i\sigma_1)\lambda_{(0,0)}(-i\sigma_1), \tag{2.140}$$

$$\lambda_{(0,0)} = Q_{P_x}\left(\lambda_{(0,0)}\right) \;\Rightarrow\; \lambda_{(0,0)} = (i\sigma_2)\lambda_{(0,0)}(-i\sigma_2), \tag{2.141}$$

$$\lambda_{(0,0)} = Q_{P_y}\left(\lambda_{(0,0)}\right) \;\Rightarrow\; \lambda_{(0,0)} = (i\sigma_2)\lambda_{(0,0)}(-i\sigma_2). \tag{2.142}$$

If we take, for example, the last equation, we can write

$$\lambda_{(0,0)} = \zeta\sigma_1 + \mu\sigma_3 = \sigma_2\lambda_{(0,0)}\sigma_2 = -\zeta\sigma_1 - \mu\sigma_3, \tag{2.143}$$

which can be satisfied only if $\zeta = \mu = 0$. This means that the present *Ansatz* does not allow for any onsite term in the fermionic Hamiltonian.

First neighbors

For first-neighboring sites, we start by considering a representative bond for the "horizontal" terms $u_x = u_{i,T_x(i)}$, namely $u_{(0,0),(1,0)}$. In general, in two dimensions there is one (non-trivial) symmetry transformation which leaves the two sites of a bond invariant (a reflection on the line connecting the sites of the bond) and one symmetry transformation which exchanges them (a reflection with respect to the axis of the bond). For the representative bond we are considering, we have

$$\begin{cases} P_y(0,0) = (0,0) \\ P_y(1,0) = (1,0) \end{cases} \quad \text{and} \quad \begin{cases} T_x P_x(0,0) = (1,0) \\ T_x P_x(1,0) = (0,0), \end{cases} \tag{2.144}$$

whose corresponding PSG equations are $u_{(0,0),(1,0)} = Q_{P_y}\left(u_{(0,0),(1,0)}\right)$ and $u_{(0,0),(1,0)} = Q_{T_x}Q_{P_x}\left(u_{(0,0),(1,0)}\right)$. The explicit forms of the resulting constraints are:

$$u_{(0,0),(1,0)} = G_{P_y}(0,0)u_{P_y^{-1}(0,0),P_y^{-1}(1,0)}G^\dagger_{P_y}(1,0) = -\sigma_2 u_{(0,0),(1,0)}\sigma_2, \tag{2.145}$$

$$\begin{aligned} u_{(0,0),(1,0)} &= G_{T_x}(0,0)G_{P_x}[T_x^{-1}(0,0)]u_{P_x^{-1}T_x^{-1}(0,0),P_x^{-1}T_x^{-1}(1,0)}G^\dagger_{P_x}[T_x^{-1}(1,0)]G^\dagger_{T_x}(1,0) \\ &= G_{T_x}(0,0)G_{P_x}(-1,0)u_{(1,0),(0,0)}G^\dagger_{P_x}(0,0)G^\dagger_{T_x}(1,0) = -\sigma_2 u^\dagger_{(0,0),(1,0)}\sigma_2 \end{aligned} \tag{2.146}$$

In the last equation, we have used the fact that $u_{j,i} = u_{i,j}^\dagger$, and exploited the product rule of Eq. (2.31) to get $Q_{T_x}Q_{P_x} = (G_{T_x}T_xG_{P_x}T_x^{-1}, T_xP_x)$. If we set $u_{(0,0),(1,0)} = u_x = \Delta_1\sigma_1 + t_1\sigma_3 = u_x^\dagger$ (as required by the PSG constraint due to time reversal), we can easily convince ourselves that the above equations are automatically satisfied. Thus, we can use translational symmetry to conclude that all horizontal first-neighbor bonds of our *Ansatz* can contain a real hopping and a real pairing term.

Starting from the result for u_x, we can use reflections to construct the expression for u_y, i.e. the vertical bonds of the form $u_y = u_{i,T_y(i)}$. Indeed, we can consider the representative bond $u_{(0,0),(0,1)}$ and require that $u_{(0,0),(0,1)} = Q_{P_{xy}}\left(u_{(0,0),(0,1)}\right)$:

$$u_{(0,0),(0,1)} = G_{P_{xy}}(0,0)u_{P_{xy}^{-1}(0,0),P_{xy}^{-1}(0,1)}G_{P_{xy}}^\dagger(0,1). \tag{2.147}$$

Since $P_{xy}^{-1}(0,0) = (0,0)$ and $P_{xy}^{-1}(0,1) = (1,0)$, we find an equation connecting vertical and horizontal bonds:

$$u_{(0,0),(0,1)} = (i\sigma_1)u_{(0,0),(1,0)}(i\sigma_1) \;\Rightarrow\; u_y = -\sigma_1 u_x\sigma_1 = -\Delta_1\sigma_1 + t_1\sigma_3. \tag{2.148}$$

Thus, the fermionic *Ansatz* under construction allows for a first-neighbor real hopping with s-wave symmetry, and a first-neighbor real pairing with $d_{x^2-y^2}$-wave symmetry.

Second neighbors

We repeat the same procedure for bonds at second-neighbors, $u_{x+y} = u_{i,T_xT_y(i)}$ and $u_{x-y} = u_{i,T_xT_y^{-1}(i)}$. Let us consider first the former case, using the representative term $u_{(0,0),(1,1)} = \Delta_2\sigma_1 + t_2\sigma_3$, and the symmetry transformations

$$P_{xy} : (x,y) \mapsto (y,x) \quad \text{and} \quad T_yT_xP_yP_x : (x,y) \mapsto (1-x, 1-y). \tag{2.149}$$

The first one leaves the pair $(0,0),(1,1)$ invariant, while the second one swaps the two sites. The PSG constraint corresponding to the first symmetry reads

$$u_{(0,0),(1,1)} = G_{P_{xy}}(0,0)u_{(0,0),(1,1)}G_{P_{xy}}^\dagger(1,1) = \sigma_1 u_{(0,0),(1,1)}\sigma_1 = \Delta_2\sigma_1 - t_2\sigma_3, \tag{2.150}$$

and is satisfied only if $t_2 = 0$, thus implying $u_{(0,0),(1,1)} = \Delta_2\sigma_1$. The second constraint is obtained by applying the PSG element of the second transformation, which can be derived by the product rule (2.31):

$$Q_{T_y}Q_{T_x}Q_{P_y}Q_{P_x} = \left(G_{T_y}T_yG_{T_x}T_xG_{P_y}P_yG_{P_x}P_y^{-1}T_x^{-1}T_y^{-1}, T_yT_xP_yP_x\right). \tag{2.151}$$

We can write

$$\begin{aligned} u_{(0,0),(1,1)} &= Q_{T_y}Q_{T_x}Q_{P_y}Q_{P_x}\left(u_{(0,0),(1,1)}\right) \\ &= G_{T_y}(0,0)G_{T_x}(0,-1)G_{P_y}(-1,-1)G_{P_x}(-1,1)\cdot u_{(1,1),(0,0)} \\ &\quad \cdot G_{P_x}^\dagger(0,0)G_{P_y}^\dagger(0,0)G_{T_x}^\dagger(1,0)G_{T_y}^\dagger(1,1) = u_{(0,0),(1,1)}^\dagger. \end{aligned} \tag{2.152}$$

The above constraint is already satisfied by the bond matrix, so we can conclude that $u_{x+y} = \Delta_2\sigma_1$.

To get the other second-neighbor term, u_{x-y}, we consider the representative bond $(0,0),(1,-1)$ and we apply the PSG element for P_y. The resulting equation connects u_{x-y} to u_{x+y}:

$$\begin{aligned} u_{(0,0),(1,-1)} = Q_{P_y}(u_{(0,0),(1,-1)}) = G_{P_y}(0,0)u_{(0,0),(1,1)}G_{P_y}^\dagger(1,-1) \\ \Longrightarrow\; u_{x-y} = \sigma_2 u_{x+y}\sigma_2 = -\Delta_2\sigma_1. \end{aligned} \tag{2.153}$$

Therefore, at second neighbors, the auxiliary Hamiltonian contains a real pairing with d_{xy}-symmetry.

Third neighbors

The present *Ansatz* does not allow for any coupling at third neighbors. This can be understood if we consider the bond $u_{(0,0),(2,0)} = \Delta_3\sigma_1 + t_3\sigma_3$ as representative bond for the case $u_{2x} = u_{i,T_x^2(i)}$. Applying the PSG equation for P_y, we get,

$$u_{(0,0),(2,0)} = Q_{P_y}\left(u_{(0,0),(2,0)}\right) = \sigma_2 u_{(0,0),(2,0)}\sigma_2 = -u_{(0,0),(2,0)}, \tag{2.154}$$

which implies that $\Delta_3 = t_3 = 0$, i.e. $u_{2x} = 0$. Using P_{xy} reflection, one can easily prove that also $u_{2y} = u_{i,T_y^2(i)} = 0$.

Fourth neighbors

For what concerns fourth neighbors, we begin by considering the representative bond $u_{(0,0),(2,1)} = u_{2x+y} = \Delta_4\sigma_1 + t_4\sigma_3$. For this term only one constraint is available, coming from the symmetry transformation $T_x^2T_yP_xP_y$, that swaps the two sites. However, given the above form of u_{2x+y}, this constraint is automatically satisfied:

$$u_{(0,0),(2,1)} = Q_{T_x}^2 Q_{T_y} Q_{P_x} Q_{P_y}\left(u_{(0,0),(2,1)}\right) = \sigma_2^2 u_{(2,1),(0,0)}\sigma_2^2 = u^\dagger_{(0,0),(2,1)}. \tag{2.155}$$

Once the first bond is fixed, we can derive the other three inequivalent fourth-neighboring bonds by using the following equations:

$$u_{(0,0),(1,2)} = Q_{P_{xy}}\left(u_{(0,0),(1,2)}\right) = -\sigma_1 u_{(0,0),(2,1)}\sigma_1 \implies u_{x+2y} = -\Delta_4\sigma_1 + t_4\sigma_3, \tag{2.156}$$

$$u_{(0,0),(2,-1)} = Q_{P_y}\left(u_{(0,0),(2,-1)}\right) = -\sigma_2 u_{(0,0),(2,1)}\sigma_2 \implies u_{2x-y} = \Delta_4\sigma_1 + t_4\sigma_3, \tag{2.157}$$

$$u_{(0,0),(1,-2)} = Q_{P_y}\left(u_{(0,0),(1,-2)}\right) = -\sigma_2 u_{(0,0),(1,2)}\sigma_2 \implies u_{x-2y} = -\Delta_4\sigma_1 + t_4\sigma_3. \tag{2.158}$$

Therefore, at fourth neighbors, the *Ansatz* allows for a real hopping with s-wave symmetry and a real pairing with $d_{x^2-y^2}$-symmetry.

Fifth neighbors

We conclude the explicit construction of the *Ansatz* with fifth-neighbors, for which we take the representative bond $u_{(0,0),(2,2)} = u_{2x+2y} = \Delta_5\sigma_1 + t_5\sigma_3$. The situation here is very similar to the case of second-neighbors: the symmetry P_{xy} leaves the pair of sites $(0,0),(2,2)$ invariant, while the transformation $T_x^2T_y^2P_xP_y$ swaps the two sites. The corresponding constraints read:

$$u_{(0,0),(2,2)} = Q_{P_{xy}}\left(u_{(0,0),(2,2)}\right) = \sigma_1 u_{(0,0),(2,2)}\sigma_1, \tag{2.159}$$

$$u_{(0,0),(2,2)} = Q_{T_x}^2 Q_{T_y}^2 Q_{P_x} Q_{P_y}\left(u_{(0,0),(2,2)}\right) = \sigma_2^2 u_{(2,2),(0,0)}\sigma_2^2 = u^\dagger_{(0,0),(2,2)}, \tag{2.160}$$

and imply that $t_5 = 0$ (no hopping). Using P_y reflection, we can readily prove that the fifth-neighbor pairing has a d_{xy}-wave symmetry:

$$u_{(0,0),(2,-2)} = Q_{P_y}\left(u_{(0,0),(2,-2)}\right) = \sigma_2 u_{(0,0),(2,2)}\sigma_2 \implies u_{2x-2y} = -\Delta_5\sigma_1 \tag{2.161}$$

A summary of the different hopping and pairing terms forming the auxiliary Hamiltonian of the *Ansatz* considered here is presented in Fig. 2.4. It is interesting to look at the band structure of the fermionic Hamiltonian for different sets of parameters. For the sake of clarity, we concentrate only on first-, second- and fifth-neighbor terms. This choice is motivated by the fact that these couplings are the ones that play a major role in the definition of the optimal variational wave functions for the $J_1 - J_2$ Heisenberg model on the square lattice (see Section 4.2 for details). Limiting ourselves to the aforementioned

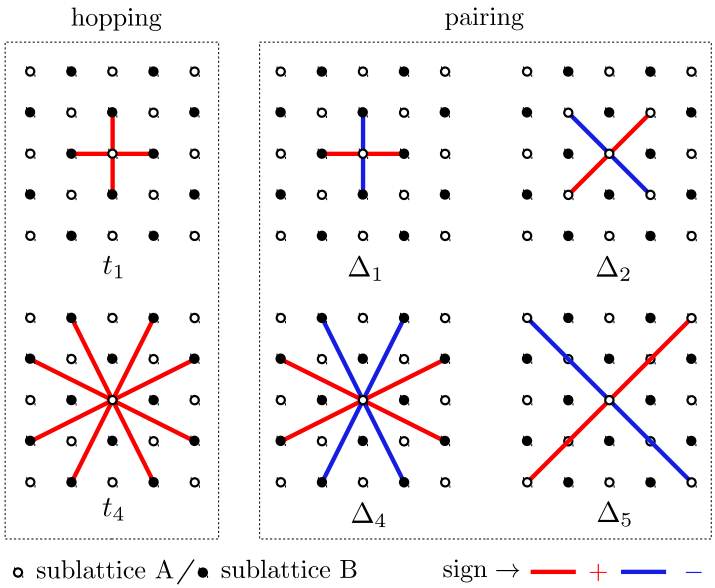

Figure 2.4: Hoppings and pairings forming the *Ansatz* considered in this section (up to fifth-neighbors). The hopping terms, which are rotationally invariant (s-wave symmetry), only involve sites of different sublattices; the pairing terms display $d_{x^2-y^2}$-wave symmetry when they connect two sites of opposite sublattices, and d_{xy}-wave symmetry when they connect two sites of the same sublattice [97].

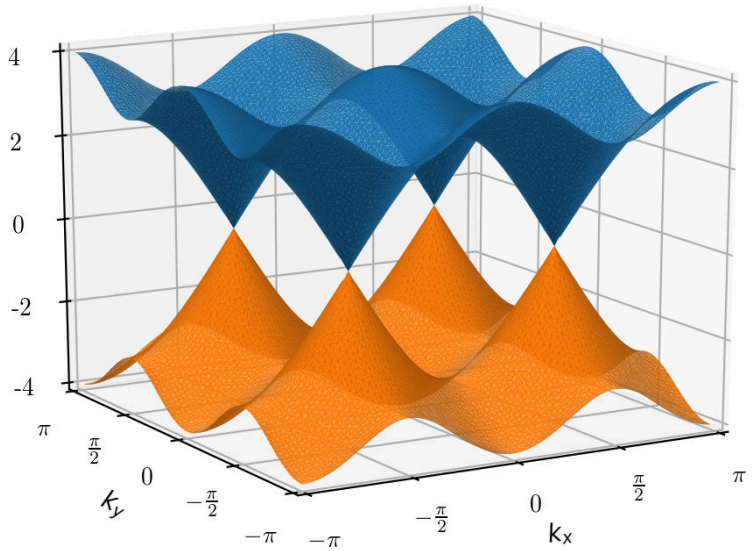

Figure 2.5: Band structure of the fermionic Hamiltonian $\mathcal{H}_0$ of the *Ansatz* considered in this section for $t_1 = \Delta_1 = 1$ (all the other couplings are set to zero). The energies $|E_k|$ and $-|E_k|$ [cf. Eq. (2.162)] are plotted in blue and orange, respectively. The dispersion shows Dirac cones at $k = (\pm\frac{\pi}{2}, \pm\frac{\pi}{2})$ and $k = (\pm\frac{\pi}{2}, \mp\frac{\pi}{2})$.

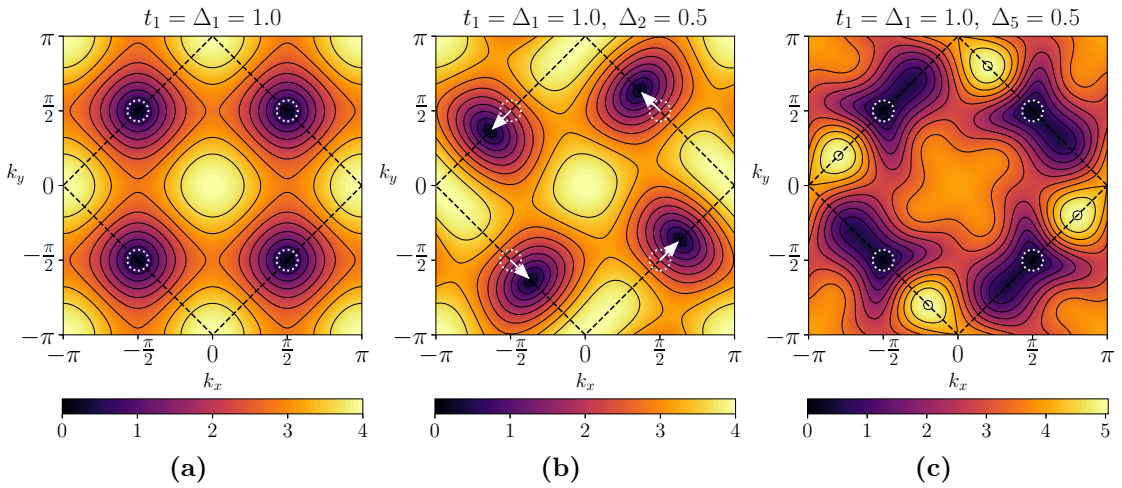

Figure 2.6: Colormap showing the positive branch of the single-particle energies of the spin liquid *Ansatz* considered in this section [$|E_k|$, cf. Eq. (2.162)], as a function of lattice momenta. The area of each picture covers the first Brillouin zone of the square lattice, while the black dashed line depicts the magnetic Brillouin zone. All the parameters whose values are not reported in the titles of the figures are taken to be zero. When only first-neighbor hoppings and pairings are included [panel (a)], the bands possess Dirac points at the momenta $k = (\pm\frac{\pi}{2}, \pm\frac{\pi}{2})$ and $k = (\pm\frac{\pi}{2}, \mp\frac{\pi}{2})$, which are marked by white dotted circles. The addition of a second-neighbor pairing Δ_2 causes the Dirac nodes to drift along the border of the magnetic Brillouin zone, as shown by the white arrows in panel (b). On the contrary, adding a fifth-neighbor pairing does not affect the position of the Dirac points [panel (c)].

terms, we can diagonalize the fermionic Hamiltonian $\mathcal{H}_0$ in momentum space [$k = (k_x, k_y)$] to obtain the following single-particle energies [38]:

$$E_k = \pm\sqrt{t_k^2 + \Delta_k^2}, \text{ where } \begin{cases} t_k = 2t_1 \left[\cos(k_x) + \cos(k_y)\right], \\ \Delta_k = \Delta_{1,k} + \Delta_{2,k} + \Delta_{5,k}, \\ \Delta_{1,k} = 2\Delta_1 \left[\cos(k_x) - \cos(k_y)\right], \\ \Delta_{2,k} = 2\Delta_2 \left[\cos(k_x + k_y) - \cos(k_x - k_y)\right], \\ \Delta_{5,k} = 2\Delta_5 \left[\cos(2k_x + 2k_y) - \cos(2k_x - 2k_y)\right]. \end{cases} \tag{2.162}$$

The fermionic spectrum of the system is gapless at the momenta k for which both t_k and Δ_k are equal to zero.

Let us focus on the case in which only first-neighbor couplings are nonzero ($t_1, \Delta_1 \neq 0$). As shown in Appendix E, when restricted to first-neighbor terms, the spin liquid *Ansatz* considered here is gauge equivalent to a Hamiltonian of pure hopping, which is characterized by a staggered magnetic flux piercing the elementary plaquettes of the square lattice [98]. The fermionic bands display Dirac nodes at $k = (\pm\frac{\pi}{2}, \pm\frac{\pi}{2})$ and $k = (\pm\frac{\pi}{2}, \mp\frac{\pi}{2})$ (see Figs. 2.5 and 2.6a). The position of the gapless points is affected by the addition of a second-neighbor pairing: as shown in Fig. 2.6b, the Dirac nodes migrate along the line delimiting the magnetic Brillouin zone when $\Delta_2 \neq 0$. On the contrary, if we add a fifth-neighbor pairing ($\Delta_5 \neq 0$) to the Hamiltonian with t_1 and Δ_1, we observe a deformation of the dispersion, but the positions of the Dirac points remain unchanged, as shown in Fig. 2.6c.

In conclusion, we refer the reader to Appendix E for a discussion on further PSG aspects related to the *Ansatz* considered in this section in the specific case in which its couplings are restricted to first-neighbors only.

3

Variational Monte Carlo methods

CONTENTS

3.1 The variational principle

Suppose we are faced with the problem of finding the solutions of the time-independent Schrödinger equation for a quantum model defined on a finite lattice and characterized by the generic Hamiltonian $\mathcal{H}$:

$$\mathcal{H}|\Upsilon_n\rangle = E_n|\Upsilon_n\rangle. \tag{3.1}$$

From a numerical point of view, the eigenvalues and the (normalized) eigenstates of Eq. (3.1), respectively denoted by E_n (in ascending order) and $|\Upsilon_n\rangle$, can be computed by diagonalizing the Hamiltonian within a certain basis set of the Hilbert space. However, in practice, this task becomes unfeasible when dealing with quantum many-body problems. Indeed, since the dimension of the Hilbert space grows exponentially with the number of degrees of freedom of the system, exact diagonalizations of Eq. (3.1) are usually limited to small clusters.

Instead of pursuing the exact solution of Eq. (3.1), we can try to follow another path and define a trial state $|\Psi_T\rangle$ to approximate one of the eigenstates of $\mathcal{H}$. Since, in general, $|\Psi_T\rangle$ is not an exact eigenstate of the system, we cannot associate an energy E_T to this state. However, we can introduce the following residual state [99]

$$|\phi\rangle = (\mathcal{H} - E_T)|\Psi_T\rangle, \tag{3.2}$$

whose norm is zero only when E_T and $|\Psi_T\rangle$ form an exact eigenvalue/eigenstate pair of $\mathcal{H}$. Therefore, the distance of our trial wave function $|\Psi_T\rangle$ from an exact eigenstate of $\mathcal{H}$ can be reduced by minimizing $\langle\phi|\phi\rangle$ with respect to E_T, namely by solving

$$\frac{\partial\langle\phi|\phi\rangle}{\partial E_T} = \frac{\partial}{\partial E_T}\left[\langle\Psi_T|\mathcal{H}^2|\Psi_T\rangle - 2E_T\langle\Psi_T|\mathcal{H}|\Psi_T\rangle + E_T^2\langle\Psi_T|\Psi_T\rangle\right] = 0. \tag{3.3}$$

The solution of this equation leads to the so-called Rayleigh's quotient [99], i.e. the expectation value of $\mathcal{H}$ with respect to the trial state:

$$E_T = \frac{\langle\Psi_T|\mathcal{H}|\Psi_T\rangle}{\langle\Psi_T|\Psi_T\rangle}. \tag{3.4}$$

This quantity is bounded from below by the exact ground state energy of $\mathcal{H}$, as can be easily proved by expanding the trial wave functions in terms of the eigenstates of the Hamiltonian:

$$E_T = \sum_n E_n \frac{|\langle \Upsilon_n | \Psi_T \rangle|^2}{\langle \Psi_T | \Psi_T \rangle} = E_0 + \sum_{n \neq 0} (E_n - E_0) \frac{|\langle \Upsilon_n | \Psi_T \rangle|^2}{\langle \Psi_T | \Psi_T \rangle} \geq E_0. \tag{3.5}$$

Here and in the following we assume that the ground state wave function is nondegenerate and the system is gapped (i.e. $E_1 > E_0$), as typically happens for finite-sized systems [86]. Eq. (3.5) constitutes the so-called *variational principle*, which defines a controlled way to approximate the ground state wave function of a given Hamiltonian. Indeed, within a variational approach, a particular guess for the trial wave function $|\Psi_T\rangle$ is formulated and its parameters are optimized in order to minimize the variational energy E_T. In general, one can compare the performances of different trial states (with different symmetries and physical properties), and select the one with the lowest energy as the best approximation for $|\Upsilon_0\rangle$.

To prove the validity of this approach, we can formulate an expression which relates the error of the variational energy, $\delta_E = E_T - E_0$, to the "distance" of the trial wave function from the exact ground state, which is measured by the following expectation value:

$$\delta_\Psi = \frac{\langle \Psi_T | \mathcal{P}_\perp | \Psi_T \rangle}{\langle \Psi_T | \Psi_T \rangle} = \left(1 - \frac{|\langle \Upsilon_0 | \Psi_T \rangle|^2}{\langle \Psi_T | \Psi_T \rangle} \right). \tag{3.6}$$

Here, $\mathcal{P}_\perp = (1 - |\Upsilon_0\rangle\langle\Upsilon_0|)$ is the projector onto the subspace orthogonal to $|\Upsilon_0\rangle$. We observe that $\delta_\Psi \geq 0$, and the equality holds only when the (normalized) trial state coincides with $|\Upsilon_0\rangle$. The relation between δ_E and δ_Ψ is proven by

$$\begin{aligned} \delta_E = \sum_{n \neq 0} (E_n - E_0) \frac{|\langle \Upsilon_n | \Psi_T \rangle|^2}{\langle \Psi_T | \Psi_T \rangle} &\geq (E_1 - E_0) \sum_{n \neq 0} \frac{|\langle \Upsilon_n | \Psi_T \rangle|^2}{\langle \Psi_T | \Psi_T \rangle} \\ &= (E_1 - E_0) \left(1 - \frac{|\langle \Upsilon_0 | \Psi_T \rangle|^2}{\langle \Psi_T | \Psi_T \rangle} \right) = (E_1 - E_0) \delta_\Psi, \end{aligned} \tag{3.7}$$

which implies that

$$\delta_\Psi \leq \frac{\delta_E}{(E_1 - E_0)}. \tag{3.8}$$

As a consequence, a sufficient condition to achieve an accurate estimate of the ground state wave function (i.e. $\delta_\Psi \ll 1$) is to obtain an error of the variational energy which is much smaller than the gap of the system [86].

3.2 Variational Monte Carlo

When dealing with many-body systems with a relatively large number of particles, the exact calculation of the variational energy (3.4) of a correlated trial wave function turns out to be an insurmountable task. Indeed, the evaluation of E_T requires a summation over all the configurations $|x\rangle$ spanning the Hilbert space of the model, which grows exponentially with the system size:

$$E_T = \frac{\sum_x \langle \Psi_T | x \rangle \langle x | \mathcal{H} | \Psi_T \rangle}{\sum_x \langle \Psi_T | x \rangle \langle x | \Psi_T \rangle}. \tag{3.9}$$

To overcome this difficulty, we can reformulate the above expression in a more convenient form:

$$E_T = \sum_x \frac{|\langle \Psi_T|x\rangle|^2}{\sum_x |\langle \Psi_T|x\rangle|^2} \frac{\langle x|\mathcal{H}|\Psi_T\rangle}{\langle x|\Psi_T\rangle} = \sum_x P(x) e_L(x). \tag{3.10}$$

The above equation can be interpreted as a statistical average of the so-called *local energy*, $e_L(x) = \frac{\langle x|\mathcal{H}|\Psi_T\rangle}{\langle x|\Psi_T\rangle}$, over the probability distribution

$$P(x) = \frac{|\langle \Psi_T|x\rangle|^2}{\sum_x |\langle \Psi_T|x\rangle|^2} = \frac{|\langle \Psi_T|x\rangle|^2}{\langle \Psi_T|\Psi_T\rangle}, \tag{3.11}$$

which is positive for all values of x and normalized. Thus, the calculation of the variational energy of a given trial state $|\Psi_T\rangle$ has been recast in a statistical problem which can be tackled by Monte Carlo sampling [86, 99]. Indeed, if we are able to generate a set X of N_X configurations distributed according to the probability function of Eq. (3.11), we can obtain a statistical estimate of the variational energy by computing

$$E_T \approx \frac{1}{N_X} \sum_{x \in X} e_L(x). \tag{3.12}$$

To evaluate the local energy for each sampled configuration $|x\rangle$ we can use the following expression,

$$e_L(x) = \sum_{x'} \langle x|\mathcal{H}|x'\rangle \frac{\langle x'|\Psi_T\rangle}{\langle x|\Psi_T\rangle}, \tag{3.13}$$

which has been obtained by inserting a resolution of the identity on the configurations $|x'\rangle$. Typically, the calculation of the above quantity is possible thanks to the locality of the couplings of the Hamiltonian $\mathcal{H}$, which implies that the number of configurations $|x'\rangle$ actually contributing to the sum scales linearly with the number of particles in the system. Concretely, for a fixed $|x\rangle$, the summation over $|x'\rangle$ is restricted to all the configurations that can be generated by applying the Hamiltonian to $|x\rangle$.

The production of statistical samples from the distribution $P(x)$ can be achieved by employing the Metropolis algorithm [100]. Starting with a given configuration $|x\rangle$, we propose a new trial configuration $|x'\rangle$, which is accepted with probability $W_{x\to x'} = \min[1, P(x')/P(x)]$. In practice, to decide whether the new configuration will be accepted or not, we extract a random number $0 < \eta \leq 1$ from the uniform distribution, and we accept the move $x \to x'$ if

$$\eta < \frac{P(x')}{P(x)} = \frac{|\langle \Psi_T|x'\rangle|^2}{|\langle \Psi_T|x\rangle|^2}. \tag{3.14}$$

The result of the Metropolis algorithm is a Markov chain of configurations which, after a transient *thermalization time*, are eventually distributed according to $P(x)$ [86]. We note that the crucial quantity which needs to be evaluated during the Monte Carlo sampling is the ratio of the amplitudes of the wave function in two different configurations, namely $\frac{\langle x'|\Psi_T\rangle}{\langle x|\Psi_T\rangle}$, which enters both the formula for the local energy and the criterion of acceptance of the Metropolis algorithm. As a consequence, the knowledge of the norm of the variational state is not required. This represents a serious advantage because the numerical calculation of $\langle \Psi_T|\Psi_T\rangle$ is generally unfeasible in the case of relatively large many-body systems.

Before moving to a detailed discussion regarding Gutzwiller-projected wave functions, let us highlight an important property of the variational Monte Carlo approach. If the trial wave function $|\Psi_T\rangle$ coincides with an exact eigenstate of the Hamiltonian, e.g. $|\Upsilon_n\rangle$, the local energy $e_L(x)$ is independent of the configuration and coincides with the relative

eigenvalue E_n. As a consequence, the statistical average of the random variable $e_L(x)$, see Eq. (3.12), has *zero variance*. Thus, in general, we can interpret a small value of the variance of the local energy as an indication that the trial wave function is close to an exact eigenstate of the system. This property is intimately connected to the argument used at the beginning of the chapter to introduce the variational principle. Indeed, the variance of the local energy can be written as

$$\sigma^2_{E_T} = \sum_x P(x)|e_L(x)|^2 - \left(\sum_x P(x)e_L(x)\right)^2 = \frac{\langle\Psi_T|(\mathcal{H}-E_T)^2|\Psi_T\rangle}{\langle\Psi_T|\Psi_T\rangle}, \tag{3.15}$$

which, a part for a normalization factor, is the norm of the residual state of Eq. (3.2), whose minimization led to the expression for the variational energy.

3.3 Jastrow-Slater wave functions for spin models

As pointed out in Chapter 1, the central topic of this thesis is the study of frustrated spin-$\frac{1}{2}$ models by a variational Monte Carlo approach based on a parton construction. We resort to the Abrikosov fermion representation of spins to introduce a trial wave function $|\Psi_0\rangle$ of the form of Eq. (1.22), which is made of the product of a symmetric spin-spin Jastrow factor[1] and a Gutzwiller-projected fermionic state. Since the fermionic part of the trial state, $|\Phi_0\rangle$, is a Slater determinant, the variational guess $|\Psi_0\rangle$ is often referred to as *Jastrow-Slater wave function*. Within the parton framework, the states $|x\rangle$ which are sampled by the Monte Carlo algorithm are fermionic configurations in real space (labelled by particle positions and spin components along z). Due to the presence of the Gutzwiller projector, only the configurations with no empty nor doubly occupied sites (i.e. the spin configurations) are considered. As emphasized in the previous section, the crucial quantity to compute in a variational Monte Carlo calculation is the ratio of the amplitudes of the wave function in two different configurations. We split the calculation of ratios in two parts, separately discussing the contributions coming from the Jastrow factor and the fermionic part of the variational state.

Jastrow factor

The Jastrow correlator included in the variational wave function is diagonal in the space of configurations, i.e. $\langle x|\mathcal{J}_s|x'\rangle = \mathcal{J}_s(x)\delta_{x,x'}$ A naive calculation of the ratio of two Jastrow factors, $\mathcal{J}_s(x')/\mathcal{J}_s(x)$, costs $O(N^2)$ operations. However, this computational burden can be reduced to $O(1)$ if the configurations $|x\rangle$ and $|x'\rangle$ differ only by few fermionic hoppings [86]. This favourable condition is always verified in the numerical calculations considered in this thesis, because the Monte Carlo moves employed in the simulations consist of spin-flipping processes of the form

$$|x'\rangle = S^+_i S^-_j |x\rangle = c^\dagger_{i,\uparrow}c_{i,\downarrow}c^\dagger_{j,\downarrow}c_{j,\uparrow}|x\rangle. \tag{3.16}$$

Therefore, the fast algorithm for the calculation of Jastrow ratios can be employed [86]. Without entering the details of this method, here we limit ourselves to observe that the implementation requires to store the following table at the beginning of the Monte Carlo run:

$$T_{\text{Jastrow}}(j) = \sum_i v_{i,j}S^z_i, \tag{3.17}$$

[1] In Chapter 5, the Jastrow factor is replaced by a neural network correlator.

where $v_{i,j}$ is the pseudopotential entering Eq. (1.21). Then, any ratio of Jastrow factors of the aforementioned form can be simply computed by reading out the appropriate element of T_{Jastrow} [86]. Since the above table needs to be updated every time a new configuration is accepted, the resulting computational cost per Monte Carlo move scales as $O(N)$.

The fermionic state

The fermionic part of the variational wave function is the ground state of a certain auxiliary Hamiltonian $\mathcal{H}_0$, defined in Eq. (1.15) and (1.20). If no pairing terms are included in $\mathcal{H}_0$, the total number of fermions is conserved and the ground state of the system is a Slater determinant. In order to construct this wave function, the auxiliary Hamiltonian is numerically diagonalized in real space to obtain a set of single-particle orbitals, whose creation operators are

$$\phi_I^\dagger = \sum_{i,\sigma} U_{i,\sigma;I} c_{i,\sigma}^\dagger. \tag{3.18}$$

Here, capital letters are used to label the aforementioned orbitals (in ascending order according to the corresponding energies) and the coefficients $U_{i,\sigma;I}$ are the entries of the unitary matrix that diagonalizes $\mathcal{H}_0$. If the system contains N spins, the ground state of $\mathcal{H}_0$ is built by filling the N single-particle orbitals with the lowest energies, i.e. $|\Phi_0\rangle = \prod_{I=1}^{N} \phi_I^\dagger |0\rangle$ [86]. The overlap of this state with a physical configuration $|x\rangle$ is the determinant of a $N \times N$ matrix. The numerical evaluation of such a Slater determinant has a computational cost that scales as $O(N^3)$. However, as already observed, the variational Monte Carlo technique involves the calculation of ratios of determinants, which can be performed with $O(N)$ operations by using the so-called *fast update* algorithm [86]. Since $O(N)$ ratios are required for the calculation of the local energy, the overall computational cost of the present variational Monte Carlo method scales as $O(N^2)$ [86].

We note that the numerical construction of $|\Phi_0\rangle$ requires the single-particle spectrum of $\mathcal{H}_0$ to be a closed shell, in order to avoid ambiguities when filling up the lowest orbitals. This condition, which ensures that the ground state of the system is uniquely defined, trivially occurs in the case of gapped auxiliary Hamiltonians. On the contrary, if $\mathcal{H}_0$ is gapless in the thermodynamic limit, its diagonalization on finite size clusters could return an open-shell spectrum. In this case, we can try to impose different (periodic or antiperiodic) boundary conditions to the fermionic degrees of freedom in order to open a finite-size gap. This is usually possible in the situations in which the fermionic spectrum displays gapless Dirac nodes: playing with the size and the shape of the finite cluster, and with the boundary conditions of the fermions, it is possible to avoid the k-points of the Brillouin in which the spectrum is gapless. On the other hand, if $\mathcal{H}_0$ is characterized by an extended Fermi surface, the situation becomes more complicated and a closed-shell spectrum is not always achievable.

If the Hamiltonian $\mathcal{H}_0$ contains pairing terms, the number of particles of the system is no more conserved and the fermionic ground state is generally represented by a Pfaffian wave function [86]. However, in the particular case in which only hopping and pairing terms are included (i.e., no magnetic field in the xy-plane), we can exploit a formal trick to reduce all the couplings of the Hamiltonian to hoppings, thus restoring the conservation of particles. This trick is based upon the definition of a different set of fermionic operators (labelled by d), which are related to the original Abrikosov fermions by a particle-hole transformation on down spins:

$$d_{i,\uparrow} = c_{i,\uparrow} \qquad d_{i,\downarrow} = c_{i,\downarrow}^\dagger. \tag{3.19}$$

We strongly emphasize that this particle-hole transformation **is not** a gauge transformation, because it does not preserve the original form of the spin operators. The single-site

configurations of d-fermions are related to the ones of the c-fermions by the following equations:

$$\begin{aligned} |0_c\rangle &= d^\dagger_\downarrow |0_d\rangle, & c^\dagger_\uparrow c^\dagger_\downarrow |0_c\rangle &= d^\dagger_\uparrow |0_d\rangle, \\ c^\dagger_\downarrow |0_c\rangle &= |0_d\rangle, & c^\dagger_\uparrow |0_c\rangle &= d^\dagger_\uparrow d^\dagger_\downarrow |0_d\rangle. \end{aligned} \tag{3.20}$$

Here $|0_c\rangle$ and $|0_d\rangle$ label the vacuum states of the c- and d-fermions, respectively. The Monte Carlo sampling of d-fermions is ruled by the transformed Gutzwiller projector,

$$\mathcal{P}^d_G = \prod_i \left(1 + d^\dagger_{i,\uparrow} d_{i,\uparrow} - d^\dagger_{i,\downarrow} d_{i,\downarrow}\right) \left(1 - d^\dagger_{i,\uparrow} d_{i,\uparrow} + d^\dagger_{i,\downarrow} d_{i,\downarrow}\right), \tag{3.21}$$

which kills all the configurations containing singly-occupied sites. As a consequence of the particle-hole transformation of Eq. (3.19), the pairing terms of $\mathcal{H}_0$ are transformed into spin-flipping hoppings (i.e. $c_{i,\downarrow} c_{j,\uparrow} \mapsto d^\dagger_{i,\downarrow} d_{j,\uparrow}$), and the resulting Hamiltonian conserves the total number of d-fermions. Therefore, in the new fermionic language, the ground state of the system can be expressed as a Slater determinant, and the computational machinery previously described can be applied [86].

All the numerical results presented in this thesis are obtained by using a Slater wave function for the fermionic part of the variational state. In other words, no auxiliary Hamiltonians involving both the in-plane magnetic field and singlet pairing terms are considered. This limitation does not affect significatively the accuracy of the variational calculations since, in general, the energy gain provided by pairing couplings is small within magnetically ordered phases.

3.4 Optimization of the parameters

The Jastrow-Slater wave function contains several variational parameters, which need to be optimized in order to minimize the variational energy. For this purpose, we employ the *stochastic reconfiguration* technique [101, 102], whose main ingredients are briefly summarized in this section.

Let us denote by $|\Psi^\alpha_T\rangle$ the variational wave function, with the superscript α indicating its dependence on a set of p variational parameters, $\{\alpha_k\}_{k=1,\dots,p}$. We can compute the derivative of the variational energy (3.4) with respect to a certain parameter α_k and define the corresponding *force* f_k as follows

$$f_k = -\frac{\partial}{\partial \alpha_k} \left[\frac{\langle \Psi^\alpha_T | \mathcal{H} | \Psi^\alpha_T \rangle}{\langle \Psi^\alpha_T | \Psi^\alpha_T \rangle} \right]. \tag{3.22}$$

In order to provide a more explicit formula for f_k, we introduce the operator $\mathcal{O}_k$, that is related to the logarithmic derivative of the trial state. Its definition is given in terms of its (diagonal) matrix elements between two generic configurations, i.e. $\langle x | \mathcal{O}_k | x' \rangle = \mathcal{O}_k(x) \delta_{x,x'}$, where

$$\mathcal{O}_k(x) = \frac{\partial \log\left[\langle x | \Psi^\alpha_T \rangle\right]}{\partial \alpha_k} = \frac{1}{\langle x | \Psi^\alpha_T \rangle} \frac{\partial \langle x | \Psi^\alpha_T \rangle}{\partial \alpha_k}. \tag{3.23}$$

Performing a linear expansion of the trial state for small variations of the parameter α_k,

we can derive the following expression for the force [86]:

$$f_k = -2\,\mathrm{Re}\left(\frac{\langle\Psi_T^\alpha|\mathcal{H}(\mathcal{O}_k-\overline{\mathcal{O}}_k)|\Psi_T^\alpha\rangle}{\langle\Psi_T^\alpha|\Psi_T^\alpha\rangle}\right)$$
$$= -2\,\mathrm{Re}\left[\sum_x P(x)e_L^*(x)O_k(x) - \left(\sum_x P(x)e_L(x)\right)\times\left(\sum_x P(x)O_k(x)\right)\right]. \quad (3.24)$$

In the above formula $\overline{\mathcal{O}}_k$ represents the expectation value of the logarithmic derivative operator, i.e.

$$\overline{\mathcal{O}}_k = \frac{\langle\Psi_T^\alpha|\mathcal{O}_k|\Psi_T^\alpha\rangle}{\langle\Psi_T^\alpha|\Psi_T^\alpha\rangle} = \sum_x P(x)O_k(x). \quad (3.25)$$

If we are able to write down explicit expressions for the logarithmic derivatives of $|\Psi_T^\alpha\rangle$, we can compute the forces f_k by Monte Carlo sampling, and exploit them to update the parameters α_k so that the variational energy is minimized. For this purpose, the simplest minimization algorithm is the standard *steepest descent* method [103], in which the parameters are updated following the direction of the gradients, namely

$$\alpha_k' = \alpha_k + \eta f_k. \quad (3.26)$$

Here, α_k' is the new value of the k-th parameter after the update and η is an arbitrary small constant. The drawback of this simple scheme lies in the fact that it treats all the variational parameters on the same footing, ignoring their "weight" on the amplitudes of the wave function. Specifically, the method works efficiently only when small variations of the different parameters yield a similar impact on the amplitudes of the variational state. This condition is typically violated by correlated wave functions, which display a highly nonlinear dependence on the variational parameters. For instance, correlated states may contain parameters which strongly affect their amplitudes, together with parameters whose variations produce marginal effects [86].

To cure the deficiencies of the steepest descent, we can introduce a more refined method, named stochastic reconfiguration technique. Within this approach, the update of the parameter is performed according to the following rule:

$$\alpha_k' = \alpha_k + \eta\sum_{k'}\mathcal{S}^{-1}_{k,k'}f_{k'}, \quad (3.27)$$

where $\mathcal{S}^{-1}$ is the inverse of the covariance matrix

$$\mathcal{S}_{k,k'} = \mathrm{Re}\left[\frac{\langle\Psi_T^\alpha|(\mathcal{O}_k^\dagger-\overline{\mathcal{O}}_k^*)(\mathcal{O}_{k'}-\overline{\mathcal{O}}_{k'})|\Psi_T^\alpha\rangle}{\langle\Psi_T^\alpha|\Psi_T^\alpha\rangle}\right]$$
$$= \mathrm{Re}\left[\sum_x P(x)(\mathcal{O}_k^*(x)-\overline{\mathcal{O}}_k^*)(\mathcal{O}_{k'}(x)-\overline{\mathcal{O}}_{k'})\right], \quad (3.28)$$

which can be computed by Monte Carlo sampling, and η is once more an arbitrary small constant. We note that both the steepest descent and the stochastic reconfiguration techniques rely on the fact that the updated parameters, α_k', should be close to the initial ones, α_k, in terms of a specific metric. The metric of the steepest descent method, which is defined by the Euclidean distance between the vectors α_k and α_k', does not retain any information on the dependence of the trial state on the variational parameters. On the contrary, the metric of the stochastic reconfiguration method is provided by the $\mathcal{S}$-matrix, and is connected to the difference of the variational wave functions $|\Psi_T^\alpha\rangle$ and $|\Psi_T^{\alpha'}\rangle$ (before and after the update). For this reason, the stochastic reconfiguration method proves to be more efficient for the optimization of correlated wave functions with a large number of variational parameters [86].

3.5 Dynamical variational Monte Carlo

As previously discussed, the fermionic parton construction represents a versatile framework for the definition of variational *Ansätze* for the ground state wave functions of spin systems, through the application of a Gutzwiller projector. The idea of splitting the spin operators into fermionic (or bosonic) partons is motivated by the possible emergence of fractional quasiparticles as elementary excitations of frustrated magnets. Therefore, it is plausible to think about extending the ground state method outlined above in order to target the excited states of spin systems by specifically tailored variational *Ansätze*. This extension, which is one of the main topics of this thesis, is presented in the remainder of the chapter.

Concretely, we introduce a variational method for the calculation of the spin dynamical structure factor. This quantity provides fundamental insights into the nature of the excitations of a spin system, and is directly measured by inelastic neutron scattering experiments (cf. Section 1.3). The *dynamical variational Monte Carlo* technique described below is based on the theoretical proposal by Li and Yang [104], who devised a recipe to approximate the excited states of spin-$\frac{1}{2}$ models from a parton perspective. Within this approach, once the optimal variational wave function for the ground state of the system is determined, the definition of the excited states does not require any other optimization. Moreover, at variance with other quantum Monte Carlo techniques, the present variational method does not require any analytic continuation from time to frequency domain and does not suffer of sign problem.

Let us begin our discussion by providing an "operative" definition of the dynamical structure factor for a spin model on a finite lattice.

3.5.1 The dynamical structure factor

We consider a spin model on a finite-sized periodic lattice formed by an underlying Bravais lattice of N_C unit cells (with periodic boundary conditions) and a repeated basis of N_B sites. The positions of the unit cells are labelled by the Bravais vectors R, while the position of the site a of the basis within each unit cell is specified by the vector δ_a. Therefore, the $N = N_C N_B$ sites of the system are labelled by pairs of indices of the form (R, a), whose coordinates are given by $R + \delta_a$. Let us focus on a translationally invariant spin Hamiltonian $\mathcal{H}$ defined on the aforementioned lattice. The ground state of $\mathcal{H}$, named $|\Upsilon_0\rangle$, has a well-defined momentum Q, i.e.

$$T_R|\Upsilon_0\rangle = \exp(-iQ \cdot R)|\Upsilon_0\rangle \qquad (\forall R), \tag{3.29}$$

with T_R indicating a generic Bravais lattice translation operator[2] ($T_R : R_0 \mapsto R_0 + R$).

To introduce the dynamical structure factor, we start by considering the expectation value of the spin-spin correlation as a function of space and time[3]. For the sake of clarity, we concentrate on the S^z-S^z contribution, namely

$$S^{zz}_{a,b}(R, t) = \langle \Upsilon_0 | S^z_{0,a}(0) S^z_{R,b}(t) | \Upsilon_0 \rangle, \tag{3.30}$$

but the various steps of the definition can be straightforwardly generalized to any other

[2] We note that the choice for the sign of the argument of the phase factor is connected to the Fourier transform convention adopted in this chapter, see Appendix F.1.

[3] Here we resort to the Heisenberg picture of quantum mechanics, in which time dependent operators are defined as $O(t) = \exp(-i\mathcal{H}t) O \exp(i\mathcal{H}t)$ (with O being the time-independent operator in the Schrödinger picture).

pair of spin components. Exploiting the translational invariance of the ground state wave function (3.30) we can write

$$S^{zz}_{a,b}(R,t) = \frac{1}{N_C}\sum_{R'}\langle\Upsilon_0|S^z_{R',a}(0)S^z_{R+R',b}(t)|\Upsilon_0\rangle. \tag{3.31}$$

We can insert a resolution of the identity on the eigenstates of $\mathcal{H}$, i.e. $\mathcal{I} = \sum_n |\Upsilon_n\rangle\langle\Upsilon_n|$, between the two spin operators, getting:

$$S^{zz}_{a,b}(R,t) = \frac{1}{N_C}\sum_{n}\sum_{R'} e^{-i(E_n-E_0)t}\langle\Upsilon_0|S^z_{R',a}|\Upsilon_n\rangle\langle\Upsilon_n|S^z_{R+R',b}|\Upsilon_0\rangle. \tag{3.32}$$

The dynamical structure factor tensor is defined by performing the Fourier transform of $S^{zz}_{a,b}(R,t)$ with respect to space and time:

$$\begin{aligned} S^{zz}_{a,b}(q,\omega) &= \sum_R e^{iq\cdot R}\int dt e^{i\omega t} S^{zz}_{a,b}(R,t) \\ &= \sum_n \langle\Upsilon_0|S^z_{-q,a}|\Upsilon_n\rangle\langle\Upsilon_n|S^z_{q,b}|\Upsilon_0\rangle\delta(\omega - E_n + E_0). \end{aligned} \tag{3.33}$$

Here, we have implicitly introduced the definition of the Fourier-transformed spin operators, i.e. $S^z_{q,a} \equiv \frac{1}{\sqrt{N_C}}\sum_R e^{iq\cdot R}S^z_{R,a}$, which satisfy the property $(S^z_{q,a})^\dagger = S^z_{-q,a}$. The total structure factor, which is measured in neutron scattering experiments, is obtained by averaging over the sites of the basis with the appropriate Fourier factors:

$$S^z(q,\omega) \equiv \frac{1}{N_B}\sum_{a,b} e^{iq\cdot(\delta_b-\delta_a)}S^{zz}_{a,b}(q,\omega). \tag{3.34}$$

Adopting a variational perspective, we can compute the dynamical structure factor tensor of Eq. (3.33) by finding suitable approximate expressions for both the ground state, $|\Upsilon_0\rangle$, and the excited states, $\{|\Upsilon_n\rangle\}_{n>0}$, of the model. For what concerns the former, we employ the optimal Jastrow-Slater state $|\Psi_0\rangle$ (1.22) resulting from energy minimization. Then, starting from $|\Phi_0\rangle$, i.e. the fermionic ground state of the auxiliary Hamiltonian $\mathcal{H}_0$, we construct an approximate set of excited states, which consist of Gutzwiller-projected particle-hole excitations. For this purpose, we follow the variational scheme introduced by Li and Yang in Ref. [104], which is outlined in the remainder of the chapter.

3.5.2 Gutzwiller-projected particle-hole states

We aim at introducing a basis set of excitations with momentum q which will be employed for the construction of approximate excited states for the spin system. In the fermionic space, we consider a generic *local* particle-hole excitation on top of the ground state, $c^\dagger_{R,a,\sigma}c_{0,b,\sigma}|\Phi_0\rangle$, in which a fermion with spin σ jumps from the site $(0,b)$ to the site (R,a). In order to construct a translationally invariant excitation out of this local state, we can apply the projector

$$\mathcal{L}_q = \frac{1}{\sqrt{N_C}}\sum_{R'} e^{iq\cdot R'}T_{R'}, \tag{3.35}$$

which yields a fermionic particle-hole excitation with momentum[4] q:

$$\mathcal{L}_q c^\dagger_{R,a,\sigma} c_{0,b,\sigma} |\Phi_0\rangle = \frac{1}{\sqrt{N_C}} \sum_{R'} e^{iq\cdot R'} c^\dagger_{R+R',a,\sigma} c_{R',b,\sigma} |\Phi_0\rangle \tag{3.36}$$

Strictly speaking, the above equation is valid only when periodic boundary conditions for the fermions are considered. A little modification is required when fermions are subject to antiperiodic boundary conditions. For instance, let us suppose that $c_{R+T,a,\sigma} \equiv -c_{R,a,\sigma}$, where T is the lattice vector along which antiperiodic boundary conditions are imposed. In this case, when the projector (3.35) is applied, we need to add an extra minus sign to the terms of the summation (3.36) in which the translation $T_{R'} : R \mapsto R + R'$ causes the original site R to cross the edge of the finite cluster along the direction T.

Example. *Let us consider a chain of $N_C = 4$ sites ($N_B = 1$, $R \in \{0,1,2,3\}$) with antiperiodic boundary conditions. Dropping the spin labels for simplicity, we can apply $\mathcal{L}_q$ to the excitation $c^\dagger_2 c_0$, getting*

$$\begin{aligned}
&\mathcal{L}_q c^\dagger_2 c_0 |\Phi_0\rangle \\
&\quad = \frac{1}{2}\left(c^\dagger_{2+0} c_{0+0} + e^{iq} c^\dagger_{2+1} c_{0+1} + e^{2iq} c^\dagger_{2+2} c_{0+2} + e^{3iq} c^\dagger_{2+3} c_{0+3} \right) |\Phi_0\rangle \\
&\quad = \frac{1}{2}\left(c^\dagger_2 c_0 + e^{iq} c^\dagger_3 c_1 - e^{2iq} c^\dagger_0 c_2 - e^{3iq} c^\dagger_1 c_3 \right) |\Phi_0\rangle .
\end{aligned} \tag{3.37}$$

We note that two extra minus signs appear in the above formula because, upon translation, some sites have crossed the border with antiperiodic boundary conditions.

If we perform the Gutzwiller projection of the fermionic state of Eq. (3.36), we obtain a variational *Ansatz* for the excitations of the spin model under investigation:

$$|q; R, a; b; \sigma\rangle = \mathcal{P}_{S^z_{tot}} \mathcal{J}_s \mathcal{P}_G \frac{1}{\sqrt{N_C}} \sum_{R'} e^{iq\cdot R'} c^\dagger_{R+R',a,\sigma} c_{R',b,\sigma} |\Phi_0\rangle . \tag{3.38}$$

Here, in addition to projectors, the optimal spin-spin Jastrow factor for the ground state variational wave function has been included (cf. Section 1.5). Since we are interested in computing the S^z-S^z component of the dynamical structure factor, we can limit ourselves to $S_z = 0$ triplet excitations:

$$\begin{aligned}
|q; R, a; b\rangle &= \frac{1}{2}\left(|q; R, a; b; \uparrow\rangle - |q; R, a; b; \downarrow\rangle \right) \\
&= \mathcal{P}_{S^z_{tot}} \mathcal{J}_s \mathcal{P}_G \frac{1}{2} \frac{1}{\sqrt{N_C}} \sum_{R'} e^{iq\cdot R'} \left(c^\dagger_{R+R',a,\uparrow} c_{R',b,\uparrow} - c^\dagger_{R+R',a,\downarrow} c_{R',b,\downarrow} \right) |\Phi_0\rangle ,
\end{aligned} \tag{3.39}$$

which are the only terms giving a finite contribution to the spectral weight. On the contrary, singlet excitations can be defined by replacing the minus sign in the above equation with a plus.

For a fixed momentum q, $\{|q; R, a; b\rangle\}$ represents a non-orthogonal basis set that we exploit to approximate the low-energy excitations of the spin system. Concretely, our

[4] More precisely, the excited state of Eq. (3.36) has momentum q with respect to the ground state $|\Phi_0\rangle$, which has momentum q_0 (i.e. $T_R|\Phi_0\rangle = e^{-iq_0\cdot R}|\Phi_0\rangle$). Indeed,

$$T_{\bar{R}} \mathcal{L}_q c^\dagger_{R,a,\sigma} c_{0,b,\sigma} |\Phi_0\rangle = \mathcal{L}_q c^\dagger_{R+\bar{R},a,\sigma} c_{\bar{R},b,\sigma} T_{\bar{R}} |\Phi_0\rangle = e^{-i(q+q_0)\cdot\bar{R}} \mathcal{L}_q c^\dagger_{R,a,\sigma} c_{0,b,\sigma} |\Phi_0\rangle .$$

variational *Ansätze* for the excited states of $\mathcal{H}$ (with momentum q) are expressed as linear combinations of the elements of $\{|q;R,a;b\rangle\}$:

$$|\Psi_n^q\rangle = \sum_{R,a,b} A_{R,a;b}^{n,q} |q;R,a;b\rangle. \tag{3.40}$$

Given the number of states of the basis set (3.39), it is clear that we can construct at most $N_C N_B^2$ linearly independent excited states $|\Psi_n^q\rangle$ for any given momentum q. However, as we will point out in the following, some of the excitations of $\{|q;R,a;b\rangle\}$ turn out to be linearly dependent, thus reducing the effective number of linear combinations which can be defined. Still, in general, we can say that the present method is able to provide a number of approximate low-energy excitations which scales linearly with the number of sites of the lattice [$O(N)$ states].

For each value of q, the optimal coefficients of the expansion of Eq. (3.40) are the ones which minimize Rayleigh's quotient

$$E_n^q = \frac{\langle \Psi_n^q | \mathcal{H} | \Psi_n^q \rangle}{\langle \Psi_n^q | \Psi_n^q \rangle}, \tag{3.41}$$

where E_n^q is the variational energy associated to the excitation $|\Psi_n^q\rangle$ [99]. The result of the minimization yields a generalized eigenvalue problem in which the spin Hamiltonian is restricted to the subspace generated by $\{|q;R,a;b\rangle\}$:

$$\sum_{R',a',b'} H_{R,a;b|R',a';b'}^q A_{R',a';b'}^{n,q} = E_n^q \sum_{R',a',b'} O_{R,a;b|R',a';b'}^q A_{R',a';b'}^{n,q}. \tag{3.42}$$

The label n runs over the distinct eigenvalues/eigenstates resulting from the solution of the problem (with $n = 0$ indicating the lowest-lying excited state). In the above formula we have introduced two matrices,

$$H_{R,a;b|R',a';b'}^q = \langle q;R,a;b|\mathcal{H}|q;R',a';b'\rangle \quad \text{(Hamiltonian matrix)}, \tag{3.43}$$

$$O_{R,a;b|R',a';b'}^q = \langle q;R,a;b|q;R',a';b'\rangle \quad \text{(overlap matrix)}, \tag{3.44}$$

whose entries are computed by Monte Carlo sampling, as described in the following. The strategy adopted for the solution of the generalized eigenvalue problem of Eq. (3.42) is outlined in Appendix F.2. In a nutshell, it is necessary to restrict Eq. (3.42) to the subspace of eigenvectors of the overlap matrix that have nonzero eigenvalues in order to get rid of the linear dependence which may affect the set $\{|q;R,a;b\rangle\}$.

Once the generalized eigenvalue problem is solved, the dynamical structure factor tensor is approximated by taking:

$$S_{a,b}^{zz}(q,\omega) = \sum_n \langle \Psi_0 | S_{-q,a}^z | \Psi_n^q \rangle \langle \Psi_n^q | S_{q,b}^z | \Psi_0 \rangle \delta(\omega - E_n^q + E_0^{\text{var}}). \tag{3.45}$$

where, compared to the exact form of Eq. (3.33), the variational states $|\Psi_0\rangle$ and $\{|\Psi_n^q\rangle\}$ are considered[5] (instead of the exact eigenstates), and the variational energies E_0^{var} (corresponding to $|\Psi_0\rangle$) and $\{E_n^q\}$ are taken (instead of the exact ones). Most importantly, the

[5]Without loss of generality, let us assume that both the variational ground state, $|\Psi_0\rangle$, and all the excitations coming from the solutions of the generalized eigenvalue problem, $\{|\Psi_n^q\rangle\}$, are normalized. As already observed for ground state quantities, the norm of the variational states does not play any relevant role in the variational Monte Carlo approach.

sum over excited states runs over $O(N)$ states (instead of an exponentially large number). Using the definition of $|\Psi_0\rangle$ of Eq. (1.22), we can observe that

$$\begin{aligned} S^z_{q,b}|\Psi_0\rangle &= \frac{1}{\sqrt{N_C}} \sum_R e^{iq\cdot R} S^z_{R,b} \left(\mathcal{P}_{S^z_{tot}} \mathcal{J}_s \mathcal{P}_G |\Phi_0\rangle \right) \\ &= \mathcal{P}_{S^z_{tot}} \mathcal{J}_s \mathcal{P}_G \frac{1}{2} \frac{1}{\sqrt{N_C}} \sum_R e^{iq\cdot R} \left(c^\dagger_{R,b,\uparrow} c_{R,b,\uparrow} - c^\dagger_{R,b,\downarrow} c_{R,b,\downarrow} \right) |\Phi_0\rangle = |q,0,b,b\rangle, \quad (3.46) \end{aligned}$$

where we have exploited the fact that the S^z-operators commute with both projectors, and with the Jastrow factor. As a consequence, the amplitudes of Eq. (3.45) can be readily computed in terms of the coefficients of the expansion of Eq. (3.40), and the elements of the overlap matrix:

$$\langle \Psi^q_n | S^z_{q,b} | \Psi_0 \rangle = \sum_{R',a',b'} [A^{n,q}_{R',a';b'}]^* O^q_{R',a';b'|0,b;b}, \quad (3.47)$$

$$\langle \Psi_0 | S^z_{-q,a} | \Psi^q_n \rangle = \sum_{R',a';b'} O^q_{0,a;a|R',a';b'} A^{n,q}_{R',a';b'}. \quad (3.48)$$

Therefore, computing the Hamiltonian and overlap matrices by Monte Carlo directly provides all the necessary ingredients to assess the dynamical structure factor.

We emphasize that, within this procedure, once the ground-state wave function is optimized, the only remaining parameters are the coefficients $\{A^{n,q}_{R',a;b}\}$, which are completely determined by solving Eq. (3.42). In other words, the particle-hole excitations are applied to a *fixed* reference state, i.e. $|\Phi_0\rangle$, which is optimized, once for all, to minimize the ground-state variational energy.

In conclusion of this discussion, let us point out that the basis set $\{|q;R,a;b\rangle\}$ of the present variational approach constitutes a natural generalization of the well-known *single-mode approximation* [48]. Indeed, if we consider a lattice with one site per unit cell (for which no a,b labels are needed), we can easily convince ourselves that the single-mode approximation is recovered by restricting to consider only one element of the basis of excitations, namely $|q,0\rangle = S^z_q|\Psi_0\rangle$. In this case, the Hamiltonian and overlap matrices reduce to numbers, and only a single excitation for each momentum q can be defined.

Which Bravais lattice?

Before entering the next section, dedicated to the Monte Carlo sampling of the Hamiltonian and overlap matrices, let us make an important remark concerning the translational symmetry of the variational wave functions, which determines the way the dynamical structure factor is computed.

The definition of the translationally invariant excitations of Eq. (3.39) is based on the periodicity of the auxiliary Hamiltonian $\mathcal{H}_0$, which may be different from the one of the spin Hamiltonian $\mathcal{H}$ under investigation. We can distinguish two different cases in which $\mathcal{H}_0$ breaks the translational symmetry of the spin model:

- VBS wave functions, in which both $|\Phi_0\rangle$ (unprojected state) and $|\Psi_0\rangle$ (projected state) do not fulfill the periodicity of the spin model (e.g. dimer VBS);
- spin liquid states defined by a fermionic state $|\Phi_0\rangle$ with a reduced periodicity (e.g. the Z_2 spin liquids on the square lattice which require an auxiliary Hamiltonian $\mathcal{H}_0$ with a doubled unit cell, see Section 2.7); in this case, the Gutzwiller projection restores the full translational symmetry, and so $|\Psi_0\rangle$ is symmetric.

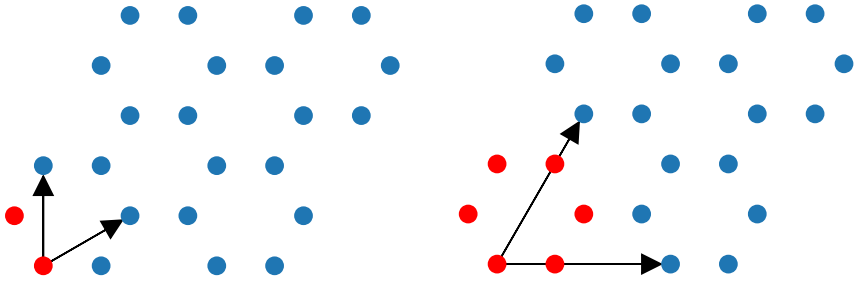

Figure 3.1: Left panel: honeycomb lattice, formed by a triangular Bravais lattice, whose unit vectors are indicated by black arrows, and a repeated basis of $N_B = 2$ sites (shown in red). Right panel: the same lattice shown on the left is represented by combining a different Bravais lattice (with a larger lattice spacing), and a repeated basis of $N_B = 6$ sites. While the superexchange couplings of $J_1 - J_2$ model on the honeycomb lattice are periodic with respect to the Bravais translations shown on the left panel, the fermionic Hamiltonian $\mathcal{H}_0$ defining the plaquette VBS *Ansatz* for this model has the periodicity of the Bravais lattice depicted on the right [105].

As an example of a VBS state, we can consider the $J_1 - J_2$ Heisenberg model on the honeycomb lattice. The exchange couplings characterizing the Hamiltonian $\mathcal{H}$ fulfill the periodicity of the honeycomb lattice, which is formed by a triangular Bravais lattice and a repeated unit cell of $N_B = 2$ sites (see left panel of Fig. 3.1). However, in the region $0.23 \lesssim J_2/J_1 \lesssim 0.36$ of the phase diagram, the optimal variational wave function for the aforementioned model is a plaquette VBS state, which breaks the translational symmetry [105]. Indeed, the auxiliary Hamiltonian $\mathcal{H}_0$ for this variational *Ansatz* has a 6-sites unit cell and is periodic with respect to a different Bravais lattice, which is triangular as the previous one, but possesses a larger lattice spacing (see right panel of Fig. 3.1). When computing the dynamical structure factor with the methods outlined above, we need to consider excitations (3.39) which are periodic with respect to the Bravais lattice of $\mathcal{H}_0$. As a consequence, the dynamical structure factor tensor of Eq. (3.33) is a 6×6 matrix. Once this tensor is computed, the total dynamical structure factor for the original spin model is recovered by averaging $S^{zz}_{a,b}(q,\omega)$ over the positions of the sites of the enlarged unit cell, as done in Eq. (3.34).

For what concern spin liquid states which break the translational symmetry *before* projection, we can adopt two different strategies. For simplicity, let us focus on the case of Z_2 spin liquid *Ansätze* on a Bravais lattice. As shown by the classification of Section 2.7, the translationally invariant PSG solutions can be divided in two broad classes, depending on whether the PSG elements of translations T_x and T_y commute ($\varepsilon_T = 1$) or anticommute ($\varepsilon_T = -1$). In the latter case, the auxiliary Hamiltonian $\mathcal{H}_0$ breaks the translational symmetry along one direction, thus requiring a doubled unit cell. The simplest option to compute the dynamical structure factor of these spin liquids is adopting the same strategy employed for VBS states, i.e. constructing a set of excitations $\{|q; R, a; b\rangle\}$ which fulfill the reduced translational symmetry of $\mathcal{H}_0$. On the other hand, a more elegant solution is achieved by taking advantage of the gauge transformations of the PSG classification to directly construct particle-hole excitations which satisfy the translational symmetry of the original lattice model. This second option is discussed in Appendix F.3.

3.5.3 Monte Carlo sampling

The Hamiltonian and overlap matrices which are required for the calculation of the dynamical structure factor can be computed by Monte Carlo sampling:

$$H^q_{R,a;b|R',a';b'} = \sum_x \langle q;R,a;b|x\rangle\langle x|\mathcal{H}|q;R',a';b'\rangle, \tag{3.49}$$

$$O^q_{R,a;b|R',a';b'} = \sum_x \langle q;R,a;b|x\rangle\langle x|q;R',a';b'\rangle. \tag{3.50}$$

Due to the presence of the projectors $\mathcal{P}_G$ and $\mathcal{P}_{S^z_{tot}}$ in the definition of $\{|q;R,a;b\rangle\}$ [cf. Eq. (3.39)], the sum over $|x\rangle$ is restricted to spin configurations with $S^z_{tot}=0$. These set of states can be sampled by using the variational ground state wave function as probability distribution:

$$H^q_{R,a;b|R',a';b'} = \sum_x \left[\frac{\langle q;R,a;b|x\rangle}{\langle\Psi_0|x\rangle}\frac{\langle x|\mathcal{H}|q;R',a';b'\rangle}{\langle x|\Psi_0\rangle}\right]|\langle x|\Psi_0\rangle|^2, \tag{3.51}$$

$$O^q_{R,a;b|R',a';b'} = \sum_x \left[\frac{\langle q;R,a;b|x\rangle}{\langle\Psi_0|x\rangle}\frac{\langle x|q;R',a';b'\rangle}{\langle x|\Psi_0\rangle}\right]|\langle x|\Psi_0\rangle|^2. \tag{3.52}$$

Here, $|\langle x|\Psi_0\rangle|^2 = P(x)$ is the probability distribution employed in the Metropolis algorithm (remember that, for simplicity, we have assumed that $\langle\Psi_0|\Psi_0\rangle = 1$). At this stage, it is worth making some remarks. First of all, our sampling procedure is possible because both the ground-state wave function, $|\Psi_0\rangle$, and the particle-hole excitations of Eq. (3.39) have $S^z_{tot}=0$ and, therefore, the set of configurations $\{|x\rangle\}$ can be chosen to also have $S^z_{tot}=0$. This would not be possible whenever considering excitations involving a spin flip. For this case, a different sampling procedure has been proposed in Ref. [104], in which the spin configurations are sampled according to a probability distribution which is defined by combining the amplitudes of all the different excitations of the basis set. This alternative scheme was employed in Refs. [47, 106] to compute the S^+-S^- component of the dynamical structure factor. The most important advantage of our approach is that all the values of the momentum q can be computed with a *single* Monte Carlo simulation, at variance with the original technique of Ref. [104], in which each q requires a separate calculation. Since, in general, we are interested in computing the dynamical structure factor for a set of $O(N)$ momenta, our technique allows us to reduce the numerical effort by a factor $\sim N$.

However, one drawback of our formulation is the fact that, in principle, the sampling of Eqs. (3.51-3.52) is correct only when the ground-state wave function is nonzero for all the configurations $|x\rangle$ (which satisfy the projectors); otherwise, the sampling procedure neglects the contributions from these "vanishing" configurations. Indeed, Eqs. (3.51-3.52) have been obtained by multiplying and dividing Eqs. (3.49-3.50) by $|\langle x|\Psi_0\rangle|^2$, and this is correct only if $|\langle x|\Psi_0\rangle|^2 \neq 0$. From the practical point of view, before performing any calculation of the dynamical structure factor, it is important to check whether the number of zero configurations is negligible or if it constitutes a relevant portion of the Hilbert space. In the latter case, the above sampling scheme turns out to be incorrect.

A possible workaround to overcome this problem is trying to eliminate the zeros of the wave functions by slightly breaking the symmetries of the state. For this purpose, one can apply a *random smearing* to the auxiliary Hamiltonian by adding a small site-dependent chemical potential, i.e.

$$\mathcal{H}_0 \;\mapsto\; \mathcal{H}_0 + \sum_{i,\sigma} r_i \mu_s c^\dagger_{i,\sigma} c_{i,\sigma}. \tag{3.53}$$

Here, r_i is a site-dependent random number taken from a normal distribution or a uniform

distribution between $[-1,1]$, and μ_s is the amplitude of the smearing term. In order not to spoil the original form of the variational wave function, the value of μ_s needs to be considerably smaller than the other parameters forming $\mathcal{H}_0$. In most cases, this simple trick is sufficient to ensure that $|\langle x|\Psi_0\rangle|^2 > 0$ for almost all configurations, without significantly affecting the variational energy of the wave function.

To compute the entries of the overlap and Hamiltonian matrices by means of Eqs. (3.51-3.52), we need to evaluate the following quantities,

$$\frac{\langle x|q;R,a;b\rangle}{\langle x|\Psi_0\rangle} = \frac{1}{\sqrt{N_C}}\sum_{R'} e^{iq\cdot R'}\sum_{\sigma}\sigma\frac{\langle x|c^{\dagger}_{R+R',a,\sigma}c_{R',b,\sigma}|\Phi_0\rangle}{\langle x|\Phi_0\rangle}, \tag{3.54}$$

$$\frac{\langle x|\mathcal{H}|q;R,a;b\rangle}{\langle x|\Psi_0\rangle} = \frac{1}{\sqrt{N_C}}\sum_{R'} e^{iq\cdot R'}\sum_{\sigma}\sigma\frac{\langle x|\mathcal{H}c^{\dagger}_{R+R',a,\sigma}c_{R',b,\sigma}|\Phi_0\rangle}{\langle x|\Phi_0\rangle}, \tag{3.55}$$

for each sampled configuration $|x\rangle$ (which satisfies the Gutzwiller projection and $S^z_{tot}=0$). This boils down to computing the matrices

$$G^{\sigma}_{R,a|R',a'}(x) = \frac{\langle x|c^{\dagger}_{R,a,\sigma}c_{R',a',\sigma}|\Phi_0\rangle}{\langle x|\Phi_0\rangle}, \tag{3.56}$$

$$\Gamma^{\sigma}_{R,a|R',a'}(x) = \frac{\langle x|\mathcal{H}c^{\dagger}_{R,a,\sigma}c_{R',a',\sigma}|\Phi_0\rangle}{\langle x|\Phi_0\rangle} \tag{3.57}$$

whose indices run over all pairs of sites of the lattice, $(R,a|R',a')$. The calculation of the G-matrix (3.56) reduces to the evaluation of wave function ratios between two configurations differing by a single hopping, i.e. $|x\rangle$ and $c^{\dagger}_{R',a',\sigma}c_{R,a,\sigma}|x\rangle$. On the other hand, to compute Γ we can use the following expression:

$$\begin{aligned}\Gamma^{\sigma}_{R,a|R',a'}(x) &= \sum_{x'}\langle x|\mathcal{H}|x'\rangle\frac{\langle x'|c^{\dagger}_{R,a,\sigma}c_{R',a',\sigma}|\Phi_0\rangle}{\langle x|\Phi_0\rangle}\\ &= \sum_{x'}\langle x|\mathcal{H}|x'\rangle\frac{\langle x'|\Phi_0\rangle}{\langle x|\Phi_0\rangle}\frac{\langle x'|c^{\dagger}_{R,a,\sigma}c_{R',a',\sigma}|\Phi_0\rangle}{\langle x'|\Phi_0\rangle}\\ &= \sum_{x'}\langle x|\mathcal{H}|x'\rangle\frac{\langle x'|\Phi_0\rangle}{\langle x|\Phi_0\rangle}G^{\sigma}_{R,a|R',a'}(x').\end{aligned} \tag{3.58}$$

In the second equality above we have divided and multiplied by $\langle x'|\Phi_0\rangle$, using the same procedure employed to introduce the sampling of Eqs. (3.51-3.52), which is valid only when the ground state wave function has a negligible number of vanishing configurations (see previous discussion). Analogously to the case of the local energy [cf. Eq. (3.13)], the sum over x' runs over only $O(N)$ configurations. Once more, all the quantities needed to evaluate the Γ-matrix are ratios of amplitudes of $|\Psi_0\rangle$.

During the Monte Carlo run, we store the N^2 entries of G and Γ for every sampled configuration. At the end of the simulation, the overlap and Hamiltonian matrices for any desired value of q are obtained by first computing the elements of Eqs. (3.54-3.55), namely

$$\frac{\langle x|q;R,a;b\rangle}{\langle x|\Psi_0\rangle} = \frac{1}{2}\frac{1}{\sqrt{N_C}}\sum_{R'} e^{iq\cdot R'}\left[G^{\uparrow}_{R+R',a|R',b}(x) - G^{\downarrow}_{R+R',a|R',b}(x)\right], \tag{3.59}$$

$$\frac{\langle x|\mathcal{H}|q;R,a;b\rangle}{\langle x|\Psi_0\rangle} = \frac{1}{2}\frac{1}{\sqrt{N_C}}\sum_{R'} e^{iq\cdot R'}\left[\Gamma^{\uparrow}_{R+R',a|R',b}(x) - \Gamma^{\downarrow}_{R+R',a|R',b}(x)\right], \tag{3.60}$$

and then averaging over all sampled configurations x.

4

Dynamical structure factor of frustrated spin models

CONTENTS

4.1 The $J_1 - J_2$ model in one dimension

In this section, we report variational Monte Carlo (VMC) results for the dynamical properties of the frustrated $S = 1/2$ Heisenberg model in one dimension [107]. The Hamiltonian of the model contains first-neighbor ($J_1 > 0$) and second-neighbor ($J_2 > 0$) antiferromagnetic exchange couplings:

$$\mathcal{H} = J_1 \sum_R \mathbf{S}_R \cdot \mathbf{S}_{R+1} + J_2 \sum_R \mathbf{S}_R \cdot \mathbf{S}_{R+2}, \tag{4.1}$$

Here, $R = 1, 2, \ldots, N$ are the (integer) coordinates of the N sites of the chain, and the system is assumed to have periodic boundary conditions ($\mathbf{S}_{N+1} \equiv \mathbf{S}_1$).

The phase diagram of the one-dimensional $J_1 - J_2$ model (4.1) is well-known [108]: for small values of the frustrating ratio, the system is gapless (i.e., a Luttinger fluid) with power-law spin-spin correlations, while for large values of J_2/J_1, the system is in a gapped phase characterized by long-range dimer order. In addition, (short-ranged) spin-spin correlations show an incommensurate periodicity for $J_2/J_1 \gtrsim 0.5$. The critical point that separates gapless and gapped phases has been estimated with high accuracy, $(J_2/J_1)^c = 0.241167 \pm 0.000005$ [109].

The purpose of our study is performing a systematic benchmark of the variational method for the calculation of the dynamical structure factor described in Chapter 3. Since the variational wave functions employed for this model do not break the $SU(2)$ symmetry of the Hamiltonian (4.1) (see the following section), any component of the dynamical structure factor gives the same result. Therefore, computing $S^z(q, \omega)$ [Eqs. (3.33) and (3.34)] does not represent a limitation. The VMC results are compared with Lanczos diagonalizations on a small $N = 30$ cluster in order to show the accuracy of the method for different values of the frustrating ratio J_2/J_1. Then, calculations are reported for large systems, illustrating how the various features of the dynamical structure factor evolve from the gapless to the gapped phase, also entering in the incommensurate region with $J_2/J_1 \gtrsim 0.5$.

Previous results for the dynamical spectrum of this model were obtained by exact

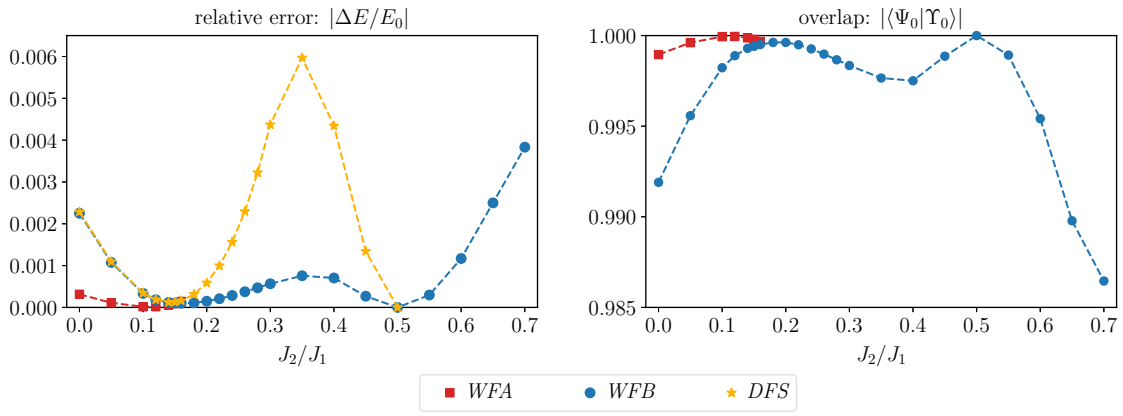

Figure 4.1: Left panel: accuracy of the *DFS*, *WFA*, and *WFB* wave functions for a chain of $N = 30$ sites. ΔE is the difference between the variational energy ($E_0^{\rm var}$) and the exact ground-state energy (E_0), obtained with Lanczos diagonalizations. For $J_2/J_1 \lesssim 0.35$, the optimal *DFS* state reduces to the uniform hopping *Ansatz*, dubbed *UFS*. For large values of the frustrating ratio, i.e. $J_2/J_1 > 0.5$, the accuracy of the *DFS* state is not shown since it rapidly deteriorates. Right panel: overlap $|\langle\Psi_0|\Upsilon_0\rangle|$ between the variational wave functions, either *WFA* or *WFB*, and the exact one.

diagonalizations on relatively small clusters [110], semi-analytical calculations [111], and matrix product states [112]. More recently, a variational scheme based on neural network quantum states has been employed [113]. Moreover, for what concerns the unfrustrated Heisenberg chain (i.e. $J_2 = 0$), very accurate approximations of the dynamical structure factor based on Bethe Ansatz results were achieved [72–74]. Finally, the spectrum of the Heisenberg model was also computed by DMRG [114], and its lowest-energy spinon excitations were tackled by Gutzwiller-projected *Ansätze* in Ref. [115].

4.1.1 Variational wave functions

As discussed in Ref. [38], Gutzwiller-projected fermionic wave functions provide very accurate estimates of the ground state of the one-dimensional $J_1 - J_2$ model. Here, we consider three different fermionic *Ansätze*, which are defined by the auxiliary BCS Hamiltonians presented below[1]. Let us note that all the parameters of the various choices of $\mathcal{H}_0$, i.e., hopping and pairing amplitudes, are taken to be real and fully optimized by means of the stochastic reconfiguration technique, in order to minimize the variational energy of $|\Psi_0\rangle$ [102]. We must emphasize the fact that both periodic boundary conditions (PBC) and antiperiodic boundary conditions (APBC) are allowed within the auxiliary BCS Hamiltonian (leading to a real wave function). However, while in the presence of a gapped fermionic spectrum either options will lead to a *unique* ground state, the same may not be true for a gapless spectrum. For example, if there are gapless points at $k = \pm\pi/2$, the ground state is unique if PBC (APBC) are considered for $N = 4n+2$ ($N = 4n$), where n is an integer.

The simplest *Ansatz* that can be used to describe both the gapless and the gapped (dimerized) phase of the model is obtained from a pure hopping Hamiltonian with broken translational symmetry. This can be achieved by doubling the unit cell and taking different

[1]We note that no Jastrow factor is applied to the Gutzwiller-projected *Ansätze* for this model, since it provides a negligible energy gain. Therefore, all the variational wave functions described in this section fulfill the spin $SU(2)$ symmetry.

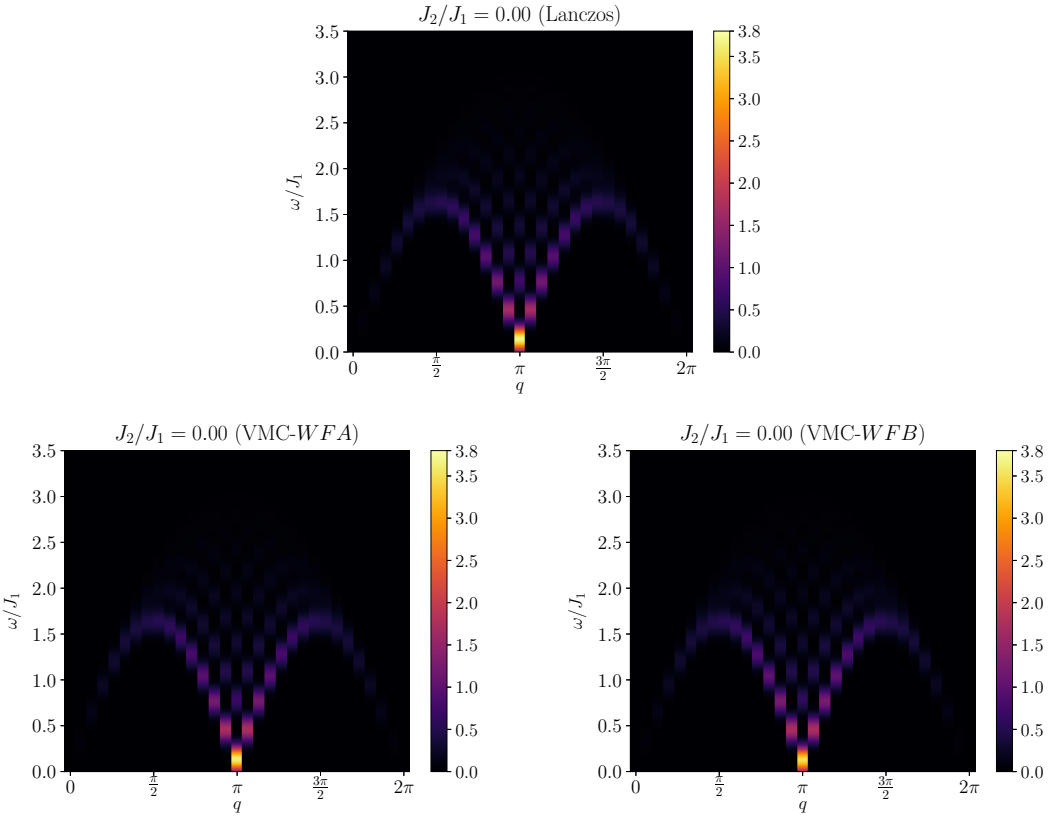

Figure 4.2: Dynamical structure factor for $N = 30$ and $J_2 = 0$. The Lanczos results are reported in the top panel. The variational calculations in the bottom left and bottom right panels were obtained using the *Ansätze* *WFA* and *WFB*, respectively. Here, the *WFB* wave function coincides with the *UFS* state, because the optimal onsite (ζ) and second-neighbor (Δ_2) pairings reduce to zero for $J_2/J_1 \lesssim 0.1$. The delta-functions in Eqs. (3.33) and (3.45) have been replaced by normalized Gaussians with $\sigma = 0.1 J_1$.

intra-cell (t_1) and inter-cell (t_1') hoppings, namely

$$\mathcal{H}_0^{DFS} = \left(t_1 \sum_{R \text{ odd}} \sum_{\sigma} c^\dagger_{R,\sigma} c_{R+1,\sigma} + t_1' \sum_{R \text{ even}} \sum_{\sigma} c^\dagger_{R,\sigma} c_{R+1,\sigma} \right) + H.c. \tag{4.2}$$

When $t_1 = t_1'$, $\mathcal{H}_0^{DFS}$ recovers translational invariance and reduces to the case of free fermions in one dimension, which have a Fermi sea ground state and gapless excitations. Instead, when $t_1' \neq t_1$, there are two fermionic bands separated by a finite gap. The uniform and dimerized states are dubbed *UFS* and *DFS*, respectively. The accuracy for a cluster with $N = 30$ sites is shown in the top panel of Fig. 4.1. For $J_2/J_1 \lesssim 0.35$ the optimal wave function does not break the translational symmetry (i.e., $t_1' = t_1$); by contrast, for larger values of the frustrating ratio, $t_1' \neq t_1$. At the Majumdar-Ghosh point ($J_2/J_1 = 0.5$), one of the two hopping parameters is equal to zero, indicating that the wave function is a product of nearest-neighbor singlets. Here, the variational state becomes exact. Actually, the fully dimerized *DFS* wave function remains the optimal solution for $J_2/J_1 > 0.5$, but its accuracy quickly worsens, since its energy is independent on J_2.

More accurate wave functions can be built from translationally invariant *Ansätze*, which include both hopping and pairing terms (with $t_{R,R'} = t_{|R-R'|}$ and $\Delta_{R,R'} = \Delta_{|R-R'|}$). Nonetheless, even by considering translational symmetry, a "spontaneous symmetry breaking" mechanism is possible after Gutzwiller projection is included, leading, for example,

to dimer order [38, 116]. Within a gapless regime, an extremely accurate state, dubbed *WFA* is constructed from a fermionic Hamiltonian that contains first- and third-neighbor hoppings (t_1 and t_3), as well as first-neighbor pairing (Δ_1), namely

$$\mathcal{H}_0^{WFA} = \left[t_1 \sum_{R,\sigma} c^\dagger_{R,\sigma} c_{R+1,\sigma} + t_3 \sum_{R,\sigma} c^\dagger_{R,\sigma} c_{R+3,\sigma} + \Delta_1 \sum_R \left(c_{R,\downarrow} c_{R+1,\uparrow} + c_{R+1,\downarrow} c_{R,\uparrow} \right) \right] + H.c. \tag{4.3}$$

This choice gives a gapless fermionic band at $k = \pm\pi/2$ and can be stabilized up to $J_2/J_1 \approx 0.15$. For larger values of the frustrating ratio, the pairing term goes to zero and the wave function coincides with the *UFS* state. A different possibility, which allows the existence of a gap in the fermionic spectrum, is given by taking first-neighbor hopping and both onsite (ζ) and second-neighbor (Δ_2) pairings:

$$\mathcal{H}_0^{WFB} = \left[t_1 \sum_{R,\sigma} c^\dagger_{R,\sigma} c_{R+1,\sigma} + \Delta_2 \sum_R \left(c_{R,\downarrow} c_{R+2,\uparrow} + c_{R+2,\downarrow} c_{R,\uparrow} \right) + \zeta \sum_R c_{R,\downarrow} c_{R,\uparrow} \right] + H.c. \tag{4.4}$$

This *Ansatz*, which is dubbed *WFB*, is gapped unless $\zeta = -\Delta_2$. Optimizing the parameters of this wave function for $N = 30$ sites, we find that it reduces to the simple *UFS* state (i.e., $\zeta = \Delta_2 = 0$) for $J_2/J_1 \lesssim 0.1$. Then, the optimal pairing terms become non-zero and the wave function proves to be more accurate than the *DFS* state and stable for all the values of the frustrating ratios (see Fig. 4.1).

We expect that, in the thermodynamic limit, the gap in the fermionic spectrum will open in the vicinity of the exact transition point $(J_2/J_1)^c$ and will follow the behavior of the spin gap. However, it is extremely hard to locate this point by performing a finite size-scaling analysis, since the gap is exponentially small in an extended region after the critical point.

4.1.2 Numerical results

Here, we present the numerical results for the spin dynamical structure factor $S^z(q,\omega)$. Let us start by considering a small cluster with $N = 30$ sites, where exact diagonalizations are possible by using the Lanczos method. First of all, we demonstrate that the variational results do not change appreciably when considering the wave function *WFA* or *WFB* to compute the dynamical structure factor (see Fig. 4.2). Indeed, even though the latter state is about five times less accurate than the former one for $J_2 = 0$ (see Fig. 4.1), the actual differences between the two dynamical calculations are negligible (and either option gives an excellent description of the exact results). Therefore, in the following, we consider only the *WFB* wave function to compute the dynamical structure factor.

In order to best quantify the agreement between the variational and the exact calculations, we directly report $S^z(q,\omega)$ for several momenta q as a function of the frequency ω for two values of the frustrating ratio (see Figs. 4.3). The agreement is very good, not only for the unfrustrated case with $J_2 = 0$ (left panel of Fig. 4.3), but also in the presence of a sizable frustration, $J_2/J_1 = 0.45$ (right panel of Fig. 4.3). Similar results are also obtained for larger values of the ratio J_2/J_1 (see below). Therefore, it is expected that, within this approach, both gapless and gapped regimes are correctly described. The accuracy of the variational method is highlighted in Fig. 4.4, where we report the overlaps between the variational excited states of Eq. (3.40) and the exact ones. In particular, whenever the excited states are well separated in energy, it is easy to match each exact excitation with a corresponding variational one (in this case, the overlap is very large, as for $J_2 = 0$). Instead, when two or even more excitations are close in energy, this correspondence is

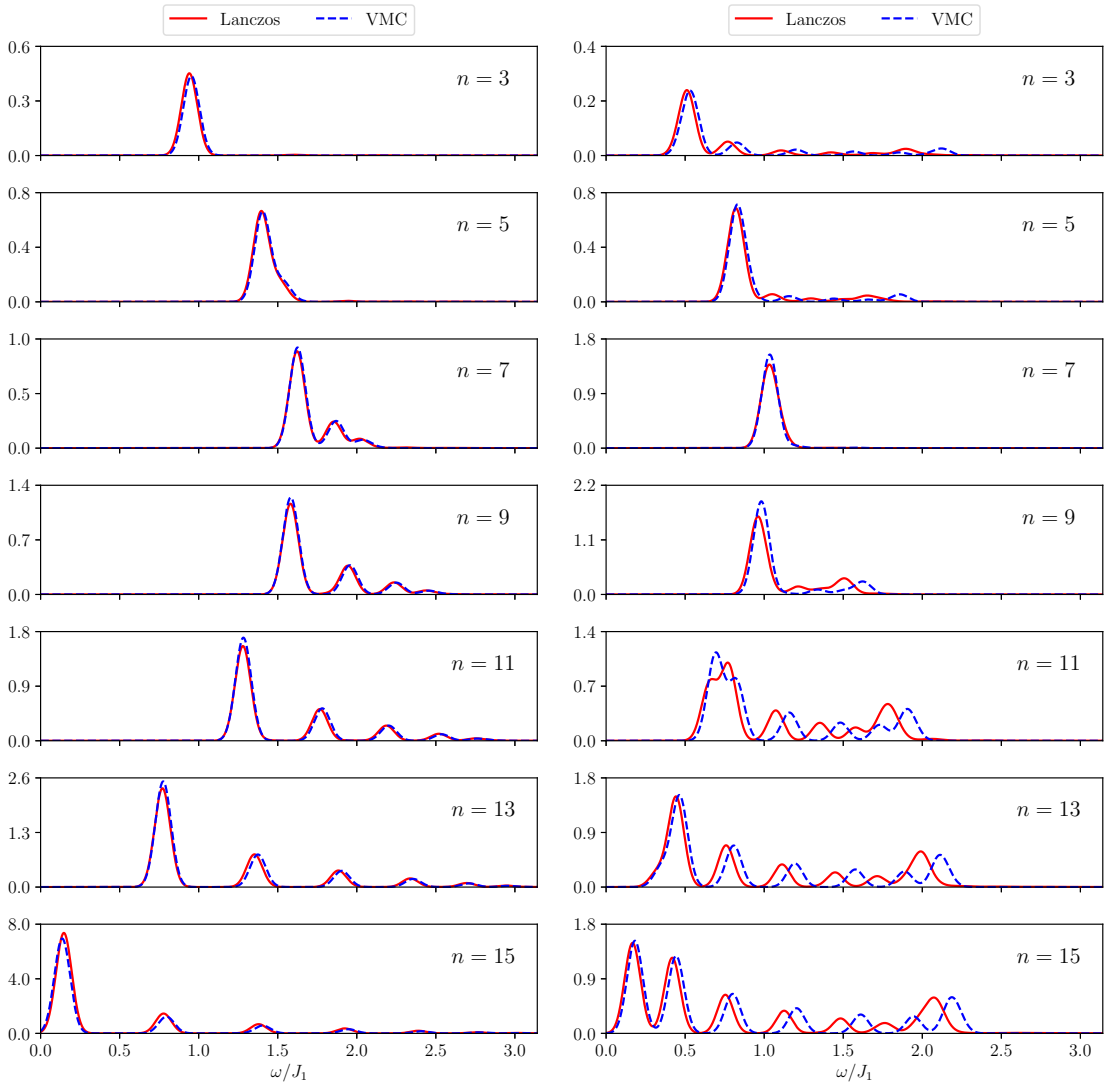

Figure 4.3: Comparison between Lanczos and variational calculations for $S^z(q,\omega)$ at different momenta $q = 2\pi/N \times n$, with n being an integer specified in the figure. Here, we consider $N = 30$ and two values of the frustrating ratio, namely $J_2 = 0$ (left) and $J_2/J_1 = 0.45$ (right). The delta-functions in Eqs. (3.33) and (3.45) have been replaced by normalized Gaussians with $\sigma = 0.05J_1$. Statistical errors are negligible within the present scale.

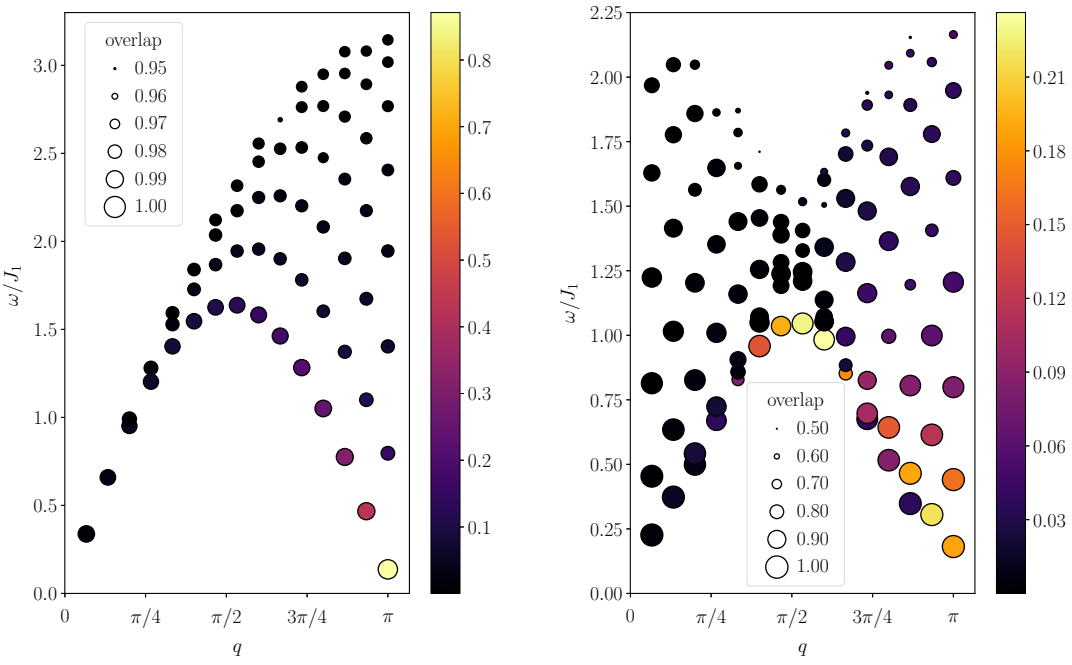

Figure 4.4: The overlaps between the exact and the variational excitations are reported for a chain of $N = 30$ sites. The cases with $J_2 = 0$ (left panel) and $J_2/J_1 = 0.45$ (right panel) are shown. The size of the circles indicates the magnitude of the overlap, while their colors represent the value of the variational spectral weights $|\langle\Psi_n^q|S_q^z|\Psi_0\rangle|^2$. For a detailed description of the calculations of the overlaps, see the main text.

not easy to resolve and, for each variational state, we computed the overlap with all the exact states and plotted the maximum value. In this case, a reduction in the overlap is observed, as for a number of cases at $J_2/J_1 = 0.45$. Nevertheless, in all cases, the relevant excitations, which carry sizable spectral weight, are well reproduced by the variational approach, and a reduced overlap is detected for states which do not contribute much to the whole intensity of the dynamical structure factor.

Finally, the results obtained with the exact and variational approaches are compared in Fig. 4.5, where $S^z(q,\omega)$ of a chain of $N = 30$ sites is represented using color maps for $J_2/J_1 = 0.2$, 0.45, 0.7 and 1. In all the cases, the variational results follow the exact ones, including the development of incommensurate features when $J_2/J_1 > 0.5$. In fact, by increasing the frustrating ratio, the intensity progressively shifts from $q = \pi$ (low energies) to $q = \pm\pi/2$ (high energies). At even larger values of J_2/J_1, the modes at $q = \pm\pi/2$ soften and eventually become gapless for $J_2 \to \infty$ (in this limit, the spin Hamiltonian consists of two decoupled Heisenberg models, one for each sublattice, and J_2 represents a nearest-neighbor superexchange on each sublattice). Remarkably, the variational approach is able to perfectly reproduce all the relevant features of the dynamical structure factor. We mention the fact that the only case where our Monte Carlo sampling technique fails is at the Majumdar-Ghosh point $J_2/J_1 = 0.5$, where the number of vanishing configurations in the ground-state wave function (exactly reproduced by our Gutzwiller-projected fermionic state) is exponentially large (cf. the discussion of Section 3.5.3).

The results for a large cluster with $N = 198$ sites are reported in Fig. 4.6 for $J_2/J_1 = 0$, 0.2, 0.4, 0.45, 0.7, and 1. In the unfrustrated case, it is known [72], that most of the total intensity of the dynamical structure factor is carried by the two-spinon contributions. For

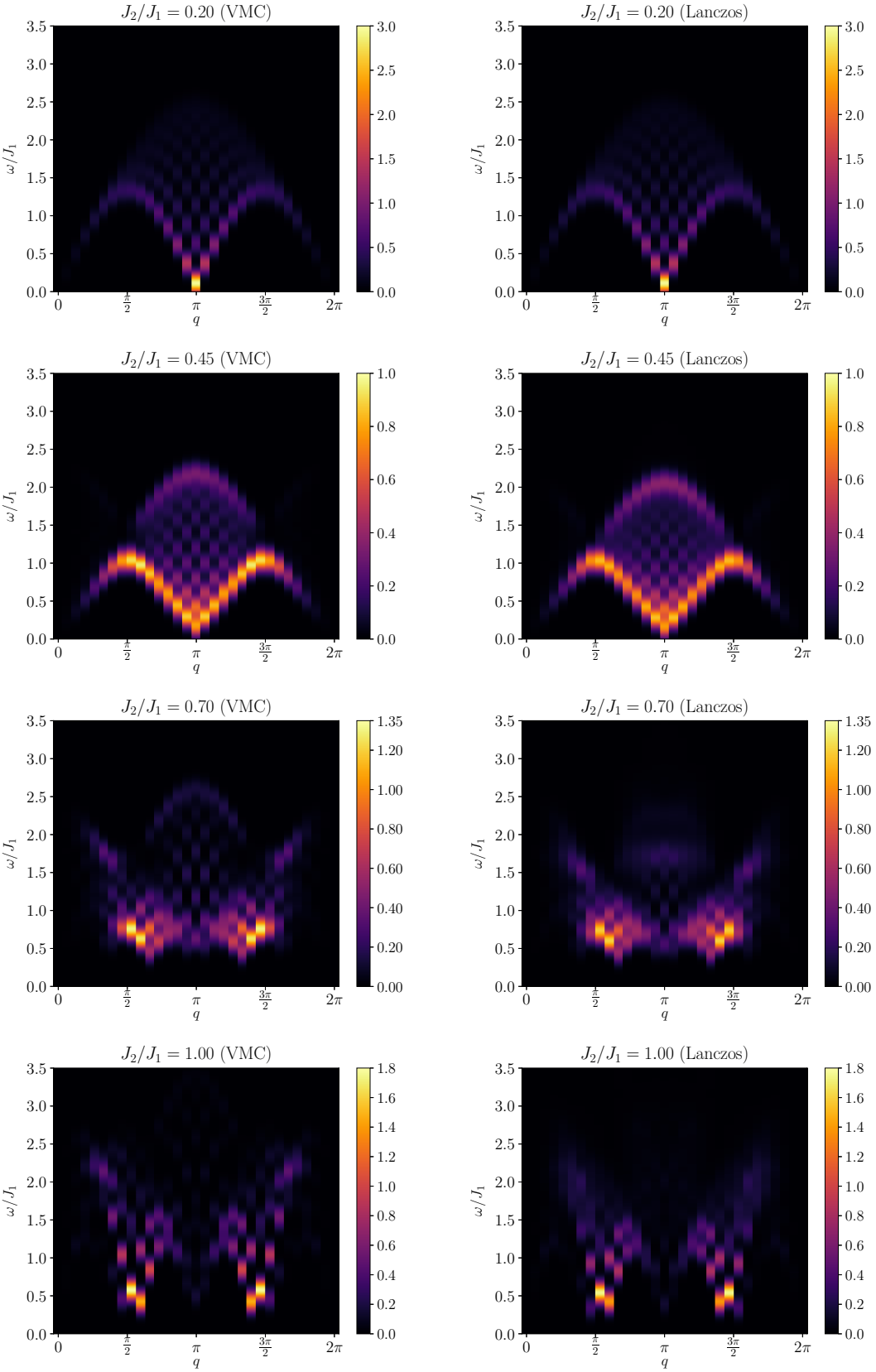

Figure 4.5: Dynamical spin structure factor $S^z(q,\omega)$ for a chain of $N = 30$ sites: comparison of variational (left) and Lanczos (right) results for different values of the frustrating ratio. The delta-functions in Eqs. (3.33) and (3.45) have been replaced by normalized Gaussians with $\sigma = 0.1J_1$.

these excitations the lower and upper energy limits are given by [117]:

$$\omega_{\text{lower}} = \frac{\pi}{2} \left|\sin(q)\right|, \tag{4.5}$$

$$\omega_{\text{upper}} = \pi \left|\sin\left(\frac{q}{2}\right)\right|. \tag{4.6}$$

Indeed, we find that our dynamical structure factor is bounded by these limits and closely resembles the one obtained with a Bethe *Ansatz* approach [74, 118].

It should be stressed that, for a relatively large region within the gapped phase, the value of the spin gap remains very small, since the transition from the gapless to the dimerized phase belongs to the Kosterlitz-Thouless universality class. Therefore, even for a relatively large system size, it is very hard to detect the presence of a finite gap in the excitation spectrum: for example, the dynamical structure factors at $J_2/J_1 = 0.2$ and 0.4 (see Fig. 4.6) look very similar, even though the former case corresponds to a gapless phase and the latter corresponds to a gapped spectrum. On this large cluster, the gradual shift of the intensity from $q = \pi$ to $q = \pm\pi/2$ is evident, as well as the presence of a "rounding" around $q = \pi$ within the gapped phase for $J_2/J_1 < 0.5$. Within such a large size, incommensurate features appear clearly for $J_2/J_1 > 0.5$; namely, the excitations with the lowest energy move from $q = \pi$ to $q = \pm\pi/2$, giving rise to a non-trivial form of the spectral function. These effects are determined by the gapped BCS spectrum, whose minima lie at incommensurate momenta. The rich structure of $S^z(q, \omega)$ is related to the fact that, in the limit $J_2/J_1 \to \infty$, the system decouples into two independent Heisenberg chains with coupling constant J_2. The Brillouin zone is then halved with respect to the case with $J_2 = 0$, and the dynamical structure factor is given by the repetition of the one of the pure Heisenberg model between $[0, \pi]$ and $[\pi, 2\pi]$, scaled by J_2/J_1. For finite values of J_2/J_1 in the incommensurate phase, the spectral features at high energies are related to the lower and upper bounds of the two-spinon continuum that develops in the aforementioned limit.

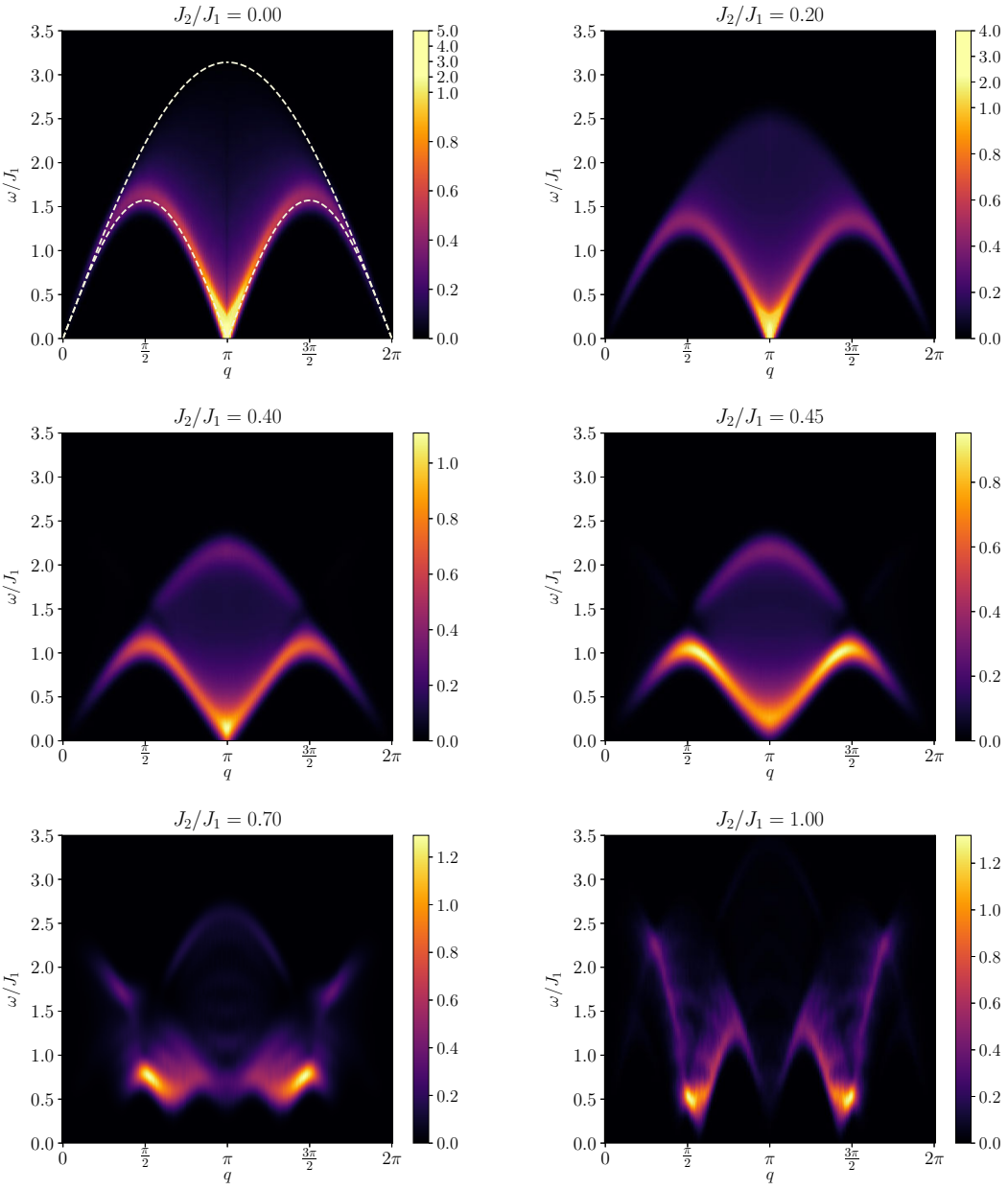

Figure 4.6: Dynamical spin structure factor $S^z(q,\omega)$ for different values of the frustrating ratio and $N = 198$ sites. The delta-functions in Eq. (3.45) have been replaced by normalized Gaussians with $\sigma = 0.1J_1$. The white dashed lines for $J_2 = 0$ indicate the lower and upper limits of the two-spinon contributions, Eqs. (4.5) and (4.6).

4.2 The $J_1 - J_2$ model on the square lattice

In this section, we discuss VMC results for the dynamical structure factor of the frustrated Heisenberg model on the square lattice, with first-neighbor ($J_1 > 0$) and second-neighbor ($J_2 > 0$) exchange couplings (see Fig. 4.7) [61]:

$$\mathcal{H} = J_1 \sum_i (\mathbf{S}_i \cdot \mathbf{S}_{i+y} + \mathbf{S}_i \cdot \mathbf{S}_{i+x}) + J_2 \sum_i (\mathbf{S}_i \cdot \mathbf{S}_{i+x+y} + \mathbf{S}_i \cdot \mathbf{S}_{i+x-y}) \,. \tag{4.7}$$

Here, $x = (1, 0)$ and $y = (0, 1)$ are the unit vectors of the square lattice, and the system is assumed to have periodic boundary conditions. For $J_2 = 0$, the above Hamiltonian reduces to the one of the square lattice Heisenberg model, whose ground state is Néel ordered, as shown by quantum Monte Carlo calculations [119, 120]; on the other hand, for $J_2 \gg J_1$, the system develops a columnar magnetic order with pitch vector $Q = (\pi, 0)$ or $Q = (0, \pi)$ [121]. In the classical phase diagram, a direct transition between the Néel phase and the columnar one takes place at $J_2/J_1 = 0.5$. However, at the quantum level, in the intermediate phase of maximal frustration the nature of the ground state is unknown and represents a long standing problem in the context of frustrated magnetism. Different numerical techniques suggested the existence of a quantum critical point at $J_2/J_1 \approx 0.5$, separating the Néel antiferromagnet from a non-magnetic phase [97, 122–128], whose precise nature is still under debate. Within the variational approach of this thesis, the system undergoes a continuous phase transition from the Néel phase to a gapless $\mathbb{Z}_2$ spin liquid state (at $J_2/J_1 \approx 0.48$). The VMC phase diagram of the $J_1 - J_2$ model is reported in the right panel of Fig. 4.7. At $J_2/J_1 \approx 0.6$, we observe a first order transition from the $\mathbb{Z}_2$ spin liquid to the magnetic phase with columnar order.

As briefly discussed in Section 1.3.1, the spectral properties of the square lattice antiferromagnet have been heavily investigated both from the theoretical and the experimental point of view. In particular, recent neutron-scattering experiments on $Cu(DCOO)_2{\cdot}4D_2O$ (CFTD), revealed the presence of a very broad spectrum around the wave vector $q = (\pi, 0)$ [and $(0, \pi)$] together with a strong magnon peak around $q = (\pi, \pi)$ (see Fig. 1.6). The combination of the experimental results with a theoretical analysis based upon the variational method employed in this thesis and the unfrustrated Heisenberg model ($J_2 = 0$), suggested the possibility of the coexistence of almost deconfined spinons and conventional $S = 1$ magnon excitations [47]. However, the theoretical description was not fully satisfactory, since the magnon branch in the whole Brillouin zone was recovered by a variational state including magnetic order, while a broad continuum of deconfined excitations was

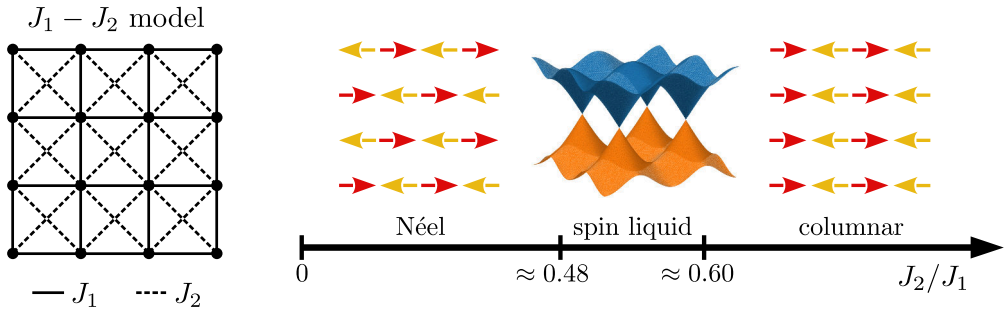

Figure 4.7: Left panel: exchange couplings of the $J_1 - J_2$ model on the square lattice [Eq. (4.7)]. Right panel: schematic representation of the variational phase diagram of the $J_1 - J_2$ model. The intermediate phase is a gapless Z_2 spin liquid [97].

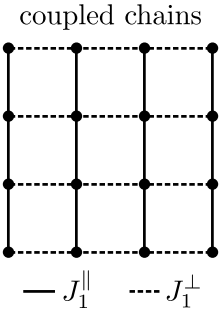

Figure 4.8: Exchange couplings of the anisotropic Heisenberg model of Eq. (4.8).

obtained by using a *non optimal* spin liquid wave function. As already pointed out in Chapter 1, an alternative interpretation of the anomalous spectral features of the square lattice Heisenberg model brings into play the effects of strong magnon-magnon interactions [62, 63].

More recently, quantum Monte Carlo calculations for a square lattice antiferromagnet with four-spin interactions ($J-Q$ model) [60] revived the idea that nearly-deconfined spinons may exist in the unfrustrated Heisenberg model. The phase diagram of the $J-Q$ model is characterized by a phase transition between the Néel ordered phase to a dimerized VBS state [129, 130]. According to the numerical results of Ref. [60], the magnon pole of the Heisenberg model at $q=(\pi,0)$ is destroyed by the addition of a coupling Q which is *smaller* than the one required to drive the phase transition. On the contrary, the magnon branch at $q=(\pi/2,\pi/2)$ remains a well-defined excitation for larger values of Q/J, up to the critical point of the system. In light of this results, the anomalous spectral features of $Cu(DCOO)_2{\cdot}4D_2O$ were interpreted as a signature of the proximity to a quantum critical point, and the physical origin of the fragility of the magnon branch at $q=(\pi,0)$ was described by a simple model of magnons decaying into spinons [60].

In this section, we explore the possibility of destabilizing the magnon branch of the Heisenberg model by a different frustrating coupling, namely the second-neighbor exchange J_2. For this purpose, we study how the dynamical structure factor of the J_1-J_2 model evolves across the continuous transition from the Néel antiferromagnet to the spin liquid phase. Upon increasing the frustrating ratio J_2/J_1, the magnon branch of the Heisenberg model is gradually replaced by a broad continuum of excitations, suggesting that deconfined spinons are released when approaching the quantum critical point.

In addition to the J_1-J_2 model, we consider also an anisotropic Hamiltonian, in which L Heisenberg chains of L sites, and coupling constant $J_1^{\parallel}$, are coupled to form a $L\times L$ square lattice by a transverse exchange interaction $J_1^{\perp}$ (see Fig. 4.8):

$$\mathcal{H}=J_1^{\parallel}\sum_i \mathbf{S}_i\cdot\mathbf{S}_{i+y}+J_1^{\perp}\sum_i \mathbf{S}_i\cdot\mathbf{S}_{i+x}. \tag{4.8}$$

The above Hamiltonian interpolates between the one-dimensional ($J_1^{\perp}=0$) and the two-dimensional ($J_1^{\perp}=J_1^{\parallel}$) Heisenberg models. Due to the bipartite nature of the square lattice, antiferromagnetic Néel order develops as soon as $J_1^{\perp}$ is "turned on"[2] [131, 132]. Our purpose is investigating how the dynamical structure factor reflects the crossover from a bunch of Heisenberg chains with fractionalized excitations, to a two-dimensional system possessing long-range magnetic order.

[2]Here the situation is different from what we discussed in Section 1.3.2 for the anisotropic Heisenberg model on the triangular lattice, which has a nonmagnetic ground state for weak inter-chain couplings.

4.2.1 Variational wave functions

The optimal variational wave function for the Néel phase of the $J_1 - J_2$ Heisenberg model is defined by the following auxiliary Hamiltonian

$$\mathcal{H}_0 = \sum_{\langle i,j \rangle} \sum_{\sigma} t_{i,j} c^{\dagger}_{i,\sigma} c_{j,\sigma} + h \sum_i \left(e^{iQ \cdot R_i} c^{\dagger}_{i,\uparrow} c_{i,\downarrow} + e^{-iQ \cdot R_i} c^{\dagger}_{i,\downarrow} c_{i,\uparrow} \right), \tag{4.9}$$

where $\langle \cdots \rangle$ restricts the summation over nearest-neighboring sites. The above Hamiltonian contains a staggered magnetic field pointing along x [with pitch vector $Q = (\pi, \pi)$], and a complex first-neighbor hopping, generating a staggered magnetic flux on elementary (square) plaquettes [98]. For a detailed description of the phases of the hopping parameters $t_{i,j}$ we refer to Appendix E, Eq. (E.3) and Fig. E.1 in particular. The Gutzwiller-projected fermionic state is supplemented by a long-range spin-spin Jastrow factor (1.21). All the parameters inside $\mathcal{H}_0$, as well as the Jastrow pseudo-potential ($v_{i,j}$) are optimized by means of the stochastic reconfiguration technique [102].

The wave function defined by the Hamiltonian of Eq. (4.9) is the optimal variational state up to $J_2/J_1 \approx 0.48$, where the magnetic order melts ($h \to 0$). Within our approach, the system undergoes a phase transition to a Z_2 spin liquid state defined by the fermionic Hamiltonian

$$\begin{aligned} \mathcal{H}_0 = \Bigg[& t_1 \sum_{i,j} \sum_{\sigma} c^{\dagger}_{i,\sigma} c_{j,\sigma} (\delta_{j,i+x} + \delta_{j,i+y}) + \Delta_1 \sum_{i,j} \left(c_{i,\downarrow} c_{j,\uparrow} + c_{j,\downarrow} c_{i,\uparrow} \right) (\delta_{j,i+x} - \delta_{j,i+y}) \\ & + \Delta_5 \sum_{i,j} \left(c_{i,\downarrow} c_{j,\uparrow} + c_{j,\downarrow} c_{i,\uparrow} \right) (\delta_{j,i+2x+2y} - \delta_{j,i+2x-2y}) \Bigg] + H.c. \end{aligned} \tag{4.10}$$

This *Ansatz* has been explicitly constructed in Section 2.9, starting from the PSG classification of Z_2 spin liquids on the square lattice. Here, referring to Fig. 2.4, we limit ourselves to the s-wave hopping ($t_1 \in \mathbb{R}$) and $d_{x^2-y^2}$-wave pairing ($\Delta_1 \in \mathbb{R}$) at first neighbors, together with the d_{xy}-wave pairing at fifth neighbors[3] ($\Delta_5 \in \mathbb{R}$). As discussed in Appendix E, the first-neighbor terms of Eq. (4.10) are gauge equivalent to the flux phase hoppings of Eq. (4.9). We note that, within the spin liquid phase, we do not include the Jastrow factor in the variational wave function in order to preserve the $SU(2)$ rotational invariance of the *Ansatz*. This choice does not significantly affect the energy of our variational state, since the Jastrow factor provides a negligible energy gain in absence of magnetic order.

The spin liquid phase ends at $J_2/J_1 \approx 0.6$, where columnar magnetic order develops. The best variational state in this regime is determined by the auxiliary Hamiltonian

$$\begin{aligned} \mathcal{H}_0 = & \left[(t_1 + it_1') \sum_{i,\sigma} c^{\dagger}_{i,\sigma} c_{i+x,\sigma} + it_2 \sum_{i,j} \sum_{\sigma} c^{\dagger}_{i,\sigma} c_{j,\sigma} e^{iQ \cdot R_i} (\delta_{j,i+x+y} - \delta_{j,i+x-y}) \right] + H.c. \\ & + h \sum_i \left(e^{iQ \cdot R_i} c^{\dagger}_{i,\uparrow} c_{i,\downarrow} + e^{-iQ \cdot R_i} c^{\dagger}_{i,\downarrow} c_{i,\uparrow} \right), \end{aligned} \tag{4.11}$$

where h is a columnar magnetic field with pitch vector $Q = (\pi, 0)$, $t_1 + it_1'$ is a first-neighbor complex hopping along x (i.e. along the antiferromagnetic direction of the columnar order), and it_2 is a second-neighbor imaginary hopping[4]. For the columnar phase, we apply a

[3] Given the range of the Hamiltonian (4.7), the most natural choice would be to take the d_{xy}-pairing at second-neighbors. However, in order to have gapless (Dirac) points located at the commensurate momenta $q = (\pm\frac{\pi}{2}, \pm\frac{\pi}{2})$, and achieve a more stable optimization, we consider the d_{xy}-pairing at fifth-neighbors (cf. Fig. 2.6). We emphasize that the variational energy is not significantly altered by this choice.

[4] The it_2 hopping connects sites belonging to the same sublattice, and its sign structure generates a flux phase with $\phi = \frac{\pi}{2}$ on second-neighbor links [cf. Appendix E]. The staggering factor $e^{iQ \cdot R_i} = (-)^{x_i}$ determines the relation between the signs of the hoppings on AA and BB plaquettes.

Jastrow factor with a pseudopotential $v_{i,j}$ which breaks the C_4 rotational symmetry of the square lattice (as also $\mathcal{H}_0$ does).

Finally, for the anisotropic Heisenberg model of coupled chains (4.8), with $J_1^\perp \neq J_1^\parallel$, we consider the same wave function as the one for the Heisenberg model, but we allow the hoppings of the Hamiltonian (4.9) to take different values along the x- and y-directions[5]. We note that in the limit of decoupled chains, i.e. $J_1^\perp/J_1^\parallel \to 0$, the optimal values of the hopping parameters along x and the magnetic field h vanish. As a consequence, the wave function becomes equivalent to the UFS *Ansatz* discussed in Section 4.1.

Before moving to the discussion of the numerical results, let us stress an important point. In this thesis, we compute the S^z-component of the dynamical structure factor. When h is finite in the auxiliary Hamiltonian, the resulting variational state breaks the spin $SU(2)$ symmetry and possesses a finite magnetization along x. Therefore, $S^z(q,\omega)$ probes *transverse* fluctuations. Instead, in the spin liquid phase, where no fictitious magnetic field nor Jastrow factor are present, the spin $SU(2)$ symmetry is preserved and all the components of the dynamical structure factor give the same contribution.

4.2.2 Numerical results

Anisotropic Heisenberg model of coupled chains

We first discuss the case of the anisotropic Heisenberg model (4.8) with $J_1^\perp \neq J_1^\parallel$. For $J_1^\perp = 0$, the lattice is decoupled into L copies of a one-dimensional chain with L sites. As discussed in Section 4.1, the system does not possess long-range magnetic order and the elementary excitations are spinons, which form a broad signal in the dynamical structure factor. As soon as $J_1^\perp$ takes a finite value, the ground state develops Néel magnetic order and the optimal magnetic field h of our variational *Ansatz* becomes finite. VMC calculations show that the spinon excitations, which characterize the spectrum of the one-dimensional Heisenberg model, are gradually pushed to a narrow region at higher energies when $J_1^\perp/J_1^\parallel$ is increased, and progressively lose their spectral weight. Concurrently, at low energies, a strong magnon branch sets in. The results for different values of the inter-chain exchange coupling $J_1^\perp$ are shown in Fig. 4.9 for a 22×22 cluster. For $J_1^\perp/J_1^\parallel = 0.1$, the dynamical structure factor still resembles the one of a pure Heisenberg chain (cf. Fig. 4.2). However, at variance with $J_1^\perp = 0$, where the spectrum does not depend upon q_x, here there is already a sensible difference in the intensity of the lowest-energy excitations for different q_x: for example, at $q_y = \pi$, the strongest signal is found at $q_x = \pi$, due to the presence of the (weak) Néel order. As $J_1^\perp/J_1^\parallel$ is raised, the gap at $(\pi, 0)$ and $(0, \pi)$ increases. In addition, the former one gains spectral weight, while the latter one loses it, until the limit of $J_1^\perp/J_1^\parallel = 1$ is reached (isotropic Heisenberg model), where the rotational symmetry of the square lattice is recovered and the two momenta become equivalent (see Fig. 4.10). Remarkably, the broad continuum that characterizes the quasi-one-dimensional spectrum gradually disappears when approaching the two-dimensional limit. Here, above the magnon branch, a weak signal is observed in the transverse channel, which does not reproduce the actual multi-magnon continuum obtained by quantum Monte Carlo calculations [56, 60], especially at low energies.

The lack of multi-magnon features could be ascribed to the nature of the variational excitations employed in our approach. Before Gutzwiller projection, the excited states of the VMC construction are particle-hole excitations in the fermionic spectrum, which we identify as two-spinon terms. Therefore, it is natural to expect that our VMC approach is suited to describe excited states of deconfined phases, as we have seen for the one-

[5] More precisely, using the notation of Eq. (E.3), we consider different values of t and Δ along x and y.

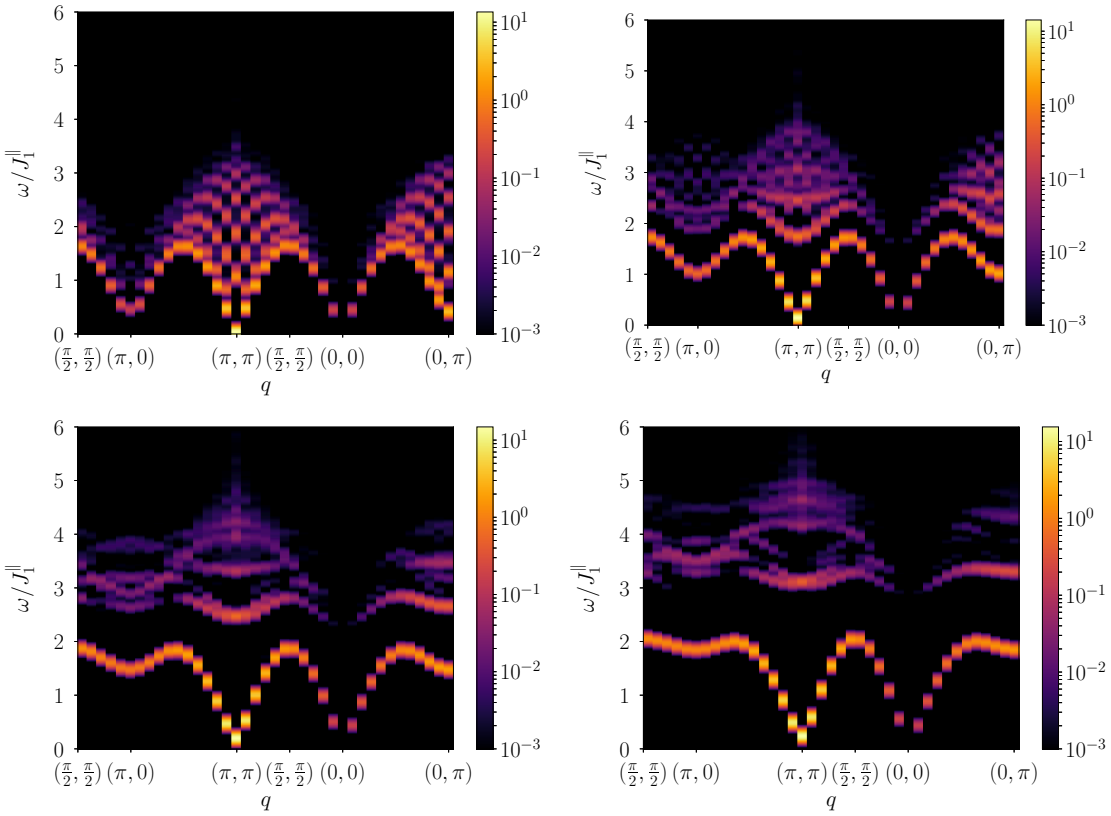

Figure 4.9: Dynamical spin structure factor of the spatially anisotropic Heisenberg model of coupled chains (4.8). Different values of the inter-chain couplings are reported: $J_1^{\perp}/J_1^{\parallel} = 0.1$ (upper left), 0.3 (upper right), 0.5 (lower left), and 0.7 (lower right). The square cluster contains $N = 22 \times 22$ sites. Spectral functions have been convoluted with normalized Gaussians with standard deviation $0.05 J_1^{\parallel}$.

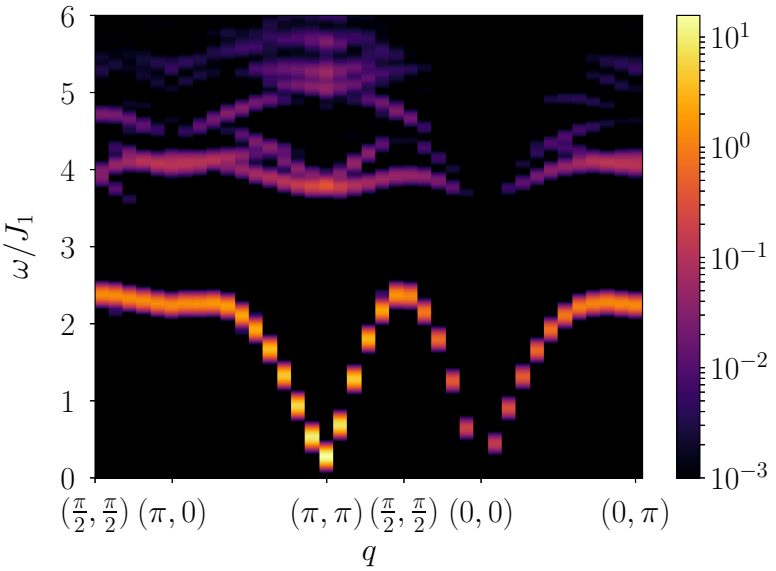

Figure 4.10: Dynamical spin structure factor of the isotropic Heisenberg model on the 22×22 square lattice. The variational wave function employed here is the one defined by the Hamiltonian (4.9) (with the inclusion of a Jastrow factor). The spectral function has been convoluted with a normalized Gaussian with standard deviation $0.05J_1$.

dimensional $J_1 - J_2$ model in Section 4.1. Nonetheless, bound states of two spinons can be also obtained, such as single-magnon excitations, as shown by the well-defined branch which dominates the spectrum of the Heisenberg model (Fig. 4.10) [47]. However, the possibility to capture multi-magnon features is more problematic. In this sense, it would be tantalizing to discriminate between two possible channels for the magnon decay, one driven by a magnon-magnon interaction, leading to a multi-magnon decay, and another one in which the magnon splits into two spinons. While the latter one can be captured by the variational *Ansätze* of Eq. (3.40), the former one may go beyond our description.

The isotropic Heisenberg model

Focusing on the case of the isotropic Heisenberg model, it is worth asking ourselves how the different components of the variational wave function contribute to the results of the dynamical structure factor shown in Fig. 4.10. For this purpose, we can imagine building the optimal variational state one brick at a time.

The simplest possible variational *Ansatz* we can consider is obtained by Gutzwiller-projecting the ground state of the fermionic Hamiltonian (4.9) in the case in which only the Néel magnetic field is present (i.e. the flux phase hopping $t_{i,j}$ is set to zero). The resulting wave function gives rise to a single-mode excitation spectrum with a trivially flat branch (see upper-left panel of Fig. 4.11), which reflects the non-interacting band structure of fermions. In this case, the spins are frozen in the Néel configuration, and the gap of the excitation at every momentum q is given by the cost of a spin flip ($E = 2J_1$). Remarkably, it is sufficient to add a Jastrow factor on top of this Néel state to obtain a reasonable magnon mode, whose dispersion is compatible with linear spin wave results (see upper-right and lower panels of Fig. 4.11). However, while the variational magnon branch is clearly gapless at $q = (0, 0)$, a considerably large gap is observed at the ordering vector $q = (\pi, \pi)$.

If we then restore also the flux phase hopping of the auxiliary Hamiltonian (4.9), we recover the optimal variational *Ansatz*, which includes also a Jastrow factor and produces

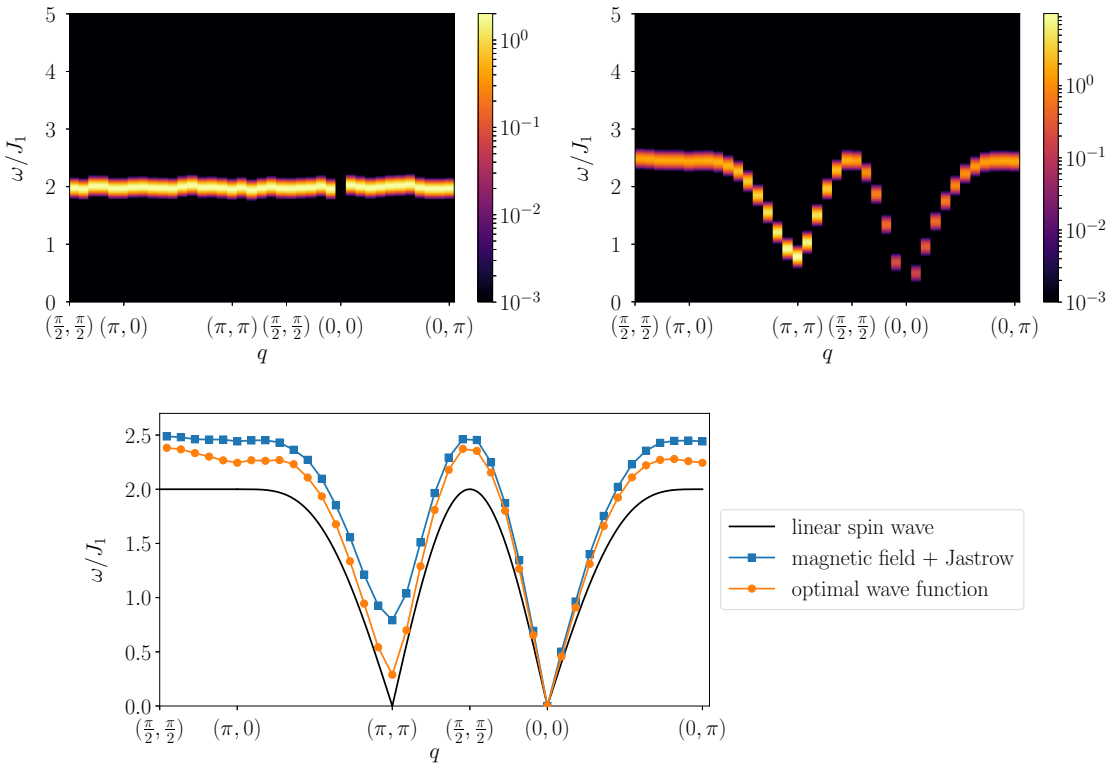

Figure 4.11: In the two upper panels, we report the dynamical spin structure factor of the isotropic Heisenberg model on the square lattice ($N = 22 \times 22$ sites). The results have been obtained employing different variational wave functions. In both cases, the auxiliary Hamiltonian defining the fermionic *Ansatz* is the one of Eq. (4.9) with only the Néel magnetic field h, and no hopping terms (i.e. $t_{i,j} = 0$). However, for the spectrum of the upper-right panel a Jastrow factor has been applied to the Gutzwiller-projected state, while for the one of the upper-left panel only the projected fermionic *Ansatz* has been considered. We note how the inclusion of the Jastrow factor gives rise to a dispersive magnon branch. Both spectral functions have been convoluted with normalized Gaussians with standard deviation $0.05J_1$. Lower-panel: magnon dispersion of the isotropic Heisenberg model on the square lattice ($N = 22 \times 22$ sites). The blue squares correspond to the magnon branch of the spectrum in the upper-right panel [variational wave function: fermionic *Ansatz* (4.9) with $t_{i,j} = 0$, plus Jastrow factor]. The orange circles represent the results obtained with the optimal variational state (see Fig. 4.10), in which the full auxiliary Hamiltonian (4.9) is considered, together with a Jastrow factor. In both cases the error bars are smaller than the size of the dots. We note that the inclusion of the flux phase hopping in the auxiliary Hamiltonian causes the magnon branch to bend downward at $q = (\pi, 0)$. Finally, the black line shows the magnon dispersion of the linear spin wave theory, which is flat between $q = (\pi/2, \pi/2)$ and $q = (\pi, 0)$.

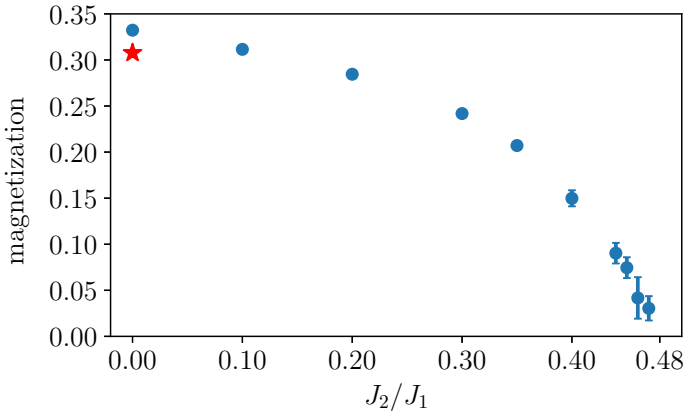

Figure 4.12: Variational estimates of the ground-state magnetization of the $J_1 - J_2$ Heisenberg model. The results are obtained in the thermodynamic limit, by extrapolating the isotropic spin-spin correlations at the maximum distance in the $L \times L$ clusters with L ranging from 10 to 22. The exact result for the unfrustrated Heisenberg model, obtained by quantum Monte Carlo [119, 120], is also reported for comparison (red star).

the spectrum of Fig. 4.10. In this case, several excited states for each momentum q can be constructed. We note that the finite-size gap of the magnon branch at $q = (\pi, \pi)$ is markedly reduced by the addition of the hopping term, and a weak multi-magnon continuum appears at higher energies. Moreover, we recover the well-known result that the lowest-energy excitation at $q = (\pi, 0)$ [and $q = (0, \pi)$] is slightly lower than the one at $q = (\pm\pi/2, \pm\pi/2)$ [52, 54–56, 60, 62, 63, 133]. Within our variational scheme, the appearance of the roton mode at $q = (\pi, 0)$, which has been observed also experimentally [47] (see Fig. 1.6), is caused by the presence of the flux phase hopping in the auxiliary Hamiltonian (4.9), as shown in the lower panel of Fig. 4.11. However, we mention that our variational approach is not able to fully capture the asymmetry between the weights of the magnon pole at $q = (\pm\pi/2, \pm\pi/2)$ and $q = (\pi, 0)$.

$J_1 - J_2$ Heisenberg model

We now move to the frustrated case of the $J_1 - J_2$ Heisenberg model. First of all, to locate the quantum phase transition from the Néel to the magnetically disordered phase, we compute the staggered magnetization using the isotropic spin-spin correlation at maximum distance for different lattice size, and we extrapolate to the thermodynamic limit. The results, reported in Fig. 4.12, show that the magnetization drops to zero at $J_2/J_1 \approx 0.48$, as suggested by recent variational calculations on the spin gap [97]. The disappearance of the order parameter is related to the fact that $h \to 0$ in the auxiliary Hamiltonian (4.9). In the region where $h = 0$ ($0.48 \lesssim J_2/J_1 \lesssim 0.6$), no energy gain is obtained by allowing translational symmetry breaking in hopping or pairing terms, thus implying that no valence-bond order is present.

A comparison with exact results on the 6×6 lattice provides the degree of accuracy of our VMC approach for both the unfrustrated regime, $J_2 = 0$ (see Fig. 4.13), and the highly-frustrated one, $J_2/J_1 = 0.5$ (see Fig. 4.14). We note that in the former case, the variational spectrum reported in Fig. 4.13 corresponds to the transverse component of the dynamical structure factor, since the variational wave function explicitly breaks the $SU(2)$ symmetry of the Heisenberg model (due to $h \neq 0$). On the other hand, the spectrum obtained through Lanczos diagonalization is symmetric under $SU(2)$ rotations, since no spontaneous symmetry breaking is possible on finite clusters. At $J_2 = 0$, our

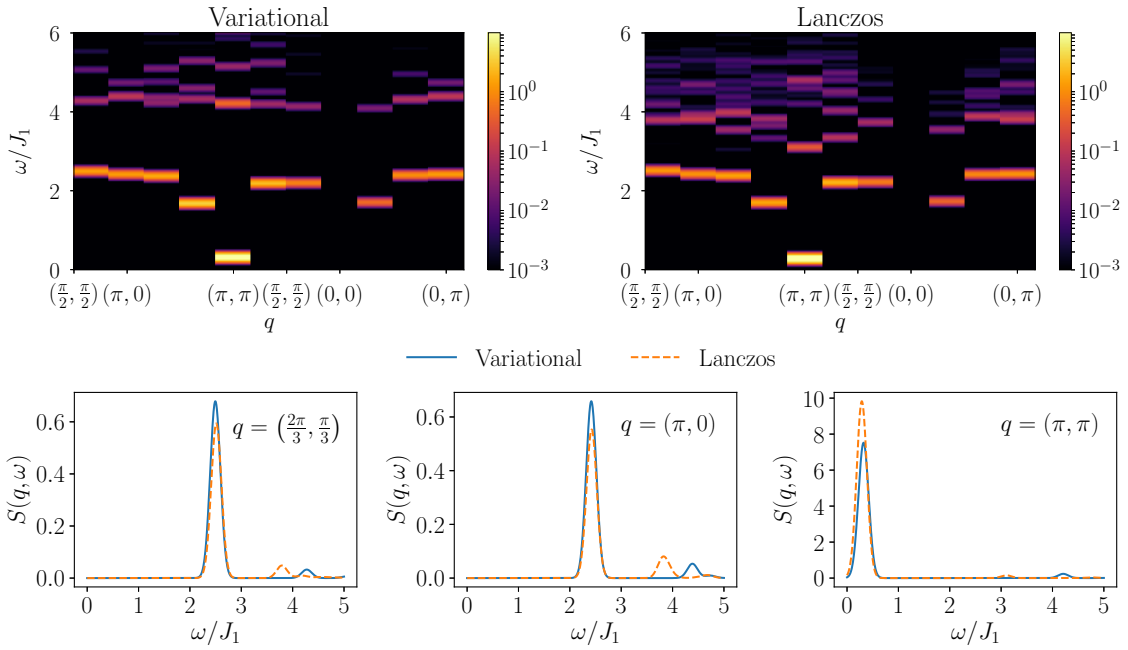

Figure 4.13: Dynamical spin structure factor of the unfrustrated Heisenberg model on the 6×6 square lattice. The VMC results are compared to the exact ones obtained by Lanczos diagonalization. Upper panels: Color maps of the dynamical structure factor along a given path in the Brillouin zone. Lower panels: Dynamical structure factor for three selected momenta. Spectral functions have been convoluted with normalized Gaussians with standard deviation $0.05J_1$ (upper panels) and $0.1J_1$ (lower panels).

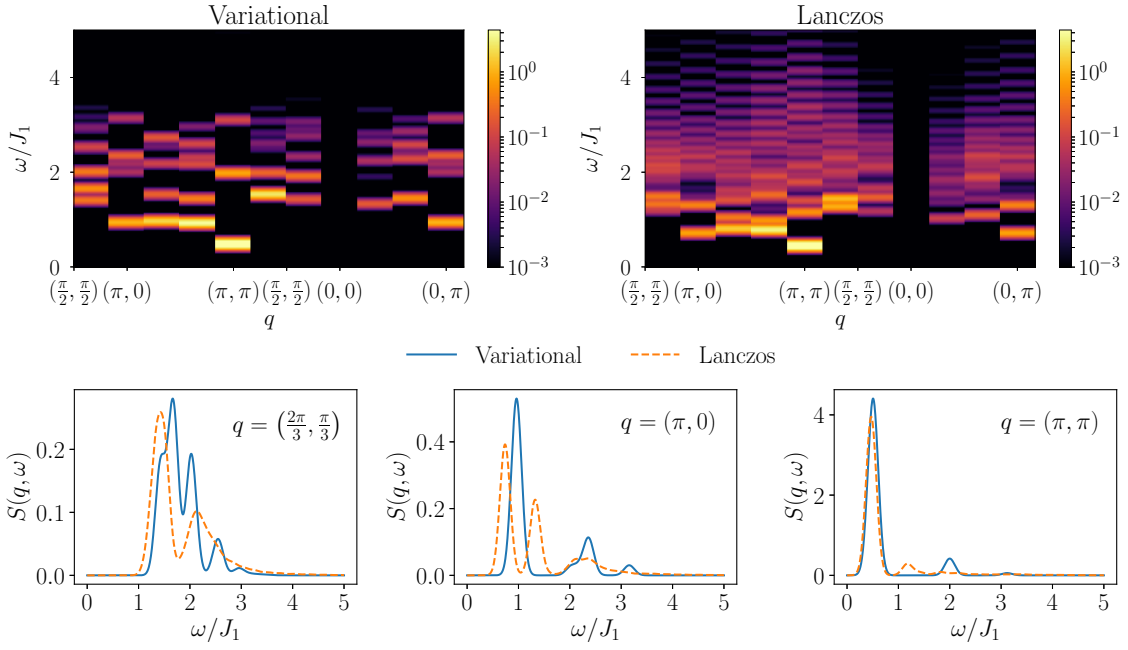

Figure 4.14: The same as Fig. 4.13 for the $J_1 - J_2$ Heisenberg model with $J_2/J_1 = 0.5$.

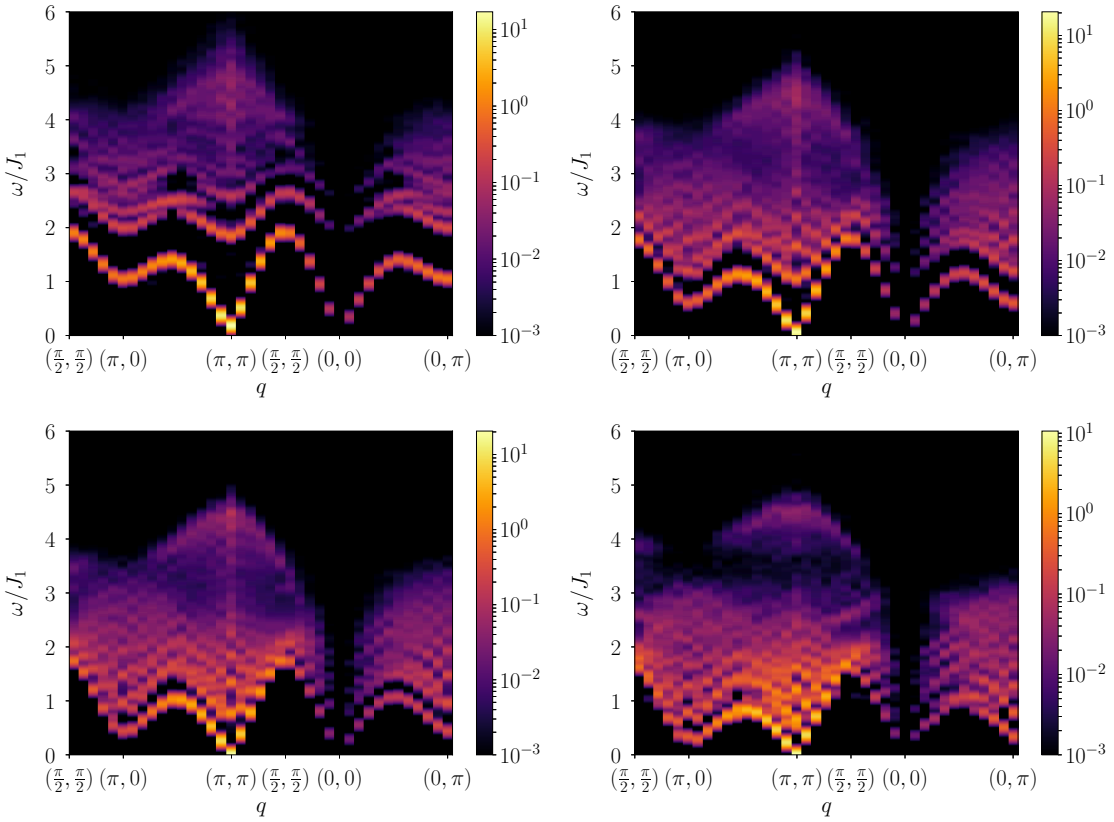

Figure 4.15: Dynamical spin structure factor of the $J_1 - J_2$ Heisenberg model. Different values of the frustrating ratio are reported: $J_2/J_1 = 0.3$ (upper left), 0.4 (upper right), 0.45 (lower left), and 0.55 (lower right). For the first three cases we have employed the variational wave function defined by the Hamiltonian (4.9), while for $J_2/J_1 = 0.55$ we have considered the Z_2 spin liquid state constructed from the Hamiltonian of Eq. (4.10). The square cluster contains $N = 22 \times 22$ sites. Spectral functions have been convoluted with normalized Gaussians with standard deviation $0.05J_1$.

approach yields a good estimate of the location and intensity of the lowest excitation (i.e. the magnon branch), while slightly overestimating the energies of the higher states. At $J_2/J_1 = 0.5$, where the Z_2 spin liquid *Ansatz* (4.10) is employed, the $O(N)$ variational states of our method are not sufficient to capture the full continuum of excitations found by Lanczos diagonalization. Nevertheless, a good approximation of the low-lying states is achieved, and the most relevant features of the spectrum are correctly captured. We note that, in general, the accuracy of the variational spectra is less satisfactory than the one observed for the $J_1 - J_2$ model on the chain (cf. Section 4.1). A possible explanation for the better performances of the VMC method in the one-dimensional case is the higher accuracy of the ground state variational *Ansätze* [38].

The VMC results for the dynamical structure factor of the $J_1 - J_2$ model on the 22×22 square lattice are reported in Fig. 4.15, for different values of the frustrating ratio. Remaining within the ordered phase, two principal effects are visible when increasing J_2/J_1. The first one is a clear reduction of the lowest-energy excitation at $q = (\pi, 0)$, as already suggested in Ref. [97]. The second one is a gradual broadening of the spectrum, with the formation of a wide continuum close to the magnon branch. For weak frustrations, the presence of a broad continuum in the dynamical spectra suggests the possibility of having an unconventional antiferromagnetic state in which magnons and nearly-deconfined spinons coexist [134] (in agreement with the results of Refs. [47, 60]). We observe also that

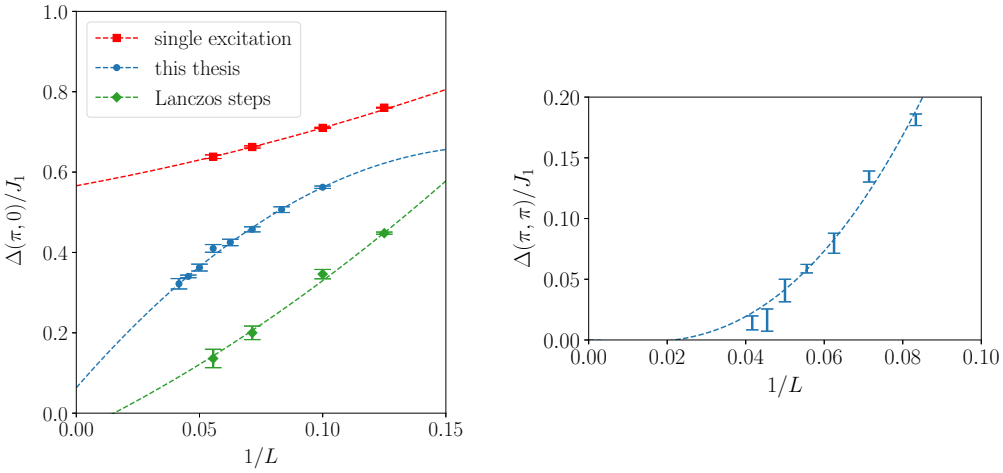

Figure 4.16: Left panel: finite-size scaling of the variational gap at $q = (\pi, 0)$ within the spin liquid phase at $J_2/J_1 = 0.55$ (blue circles). For comparison, we report two sets of results taken from Ref. [97]. The red squares represent an approximation of the gap obtained by a single Gutzwiller-projected particle-hole excitation. We note that the method employed in the present thesis makes use of a larger basis of excitations and, therefore, yields an improved finite-size scaling of the gap. Within our method, the gap is computed by the difference between the energy of the lowest excitation of Eq. (3.42) at $q = (\pi, 0)$ and the ground state energy. However, a gapless excitation in the thermodynamic limit is obtained only by a variance extrapolation within the Lanczos step procedure (green diamonds) [97]. Right panel: finite-size scaling of the variational gap at $q = (\pi, \pi)$ within the spin liquid phase ($J_2/J_1 = 0.55$). The gap is computed by the difference between the energy of the lowest excitation of Eq. (3.42) at $q = (\pi, \pi)$ and the ground state energy. The value of the gap is rapidly decreasing to zero, suggesting a vanishing value in the thermodynamic limit. The dashed line is a guide to the eye.

the magnon branch gradually loses its spectral weight around $q = (\pi, 0)$ when approaching the critical point. Then, when the system enters the spin liquid regime, $0.48 \lesssim J_2/J_1 \lesssim 0.6$, fully deconfined spinon excitations dominate the dynamical structure factor.

Within the spin liquid phase, the spectrum is expected to be gapless not only at $q = (0, 0)$, (π, π) (as in the Néel phase), but also at $(\pi, 0)$ and $(0, \pi)$, as a consequence of the BCS spectrum of the auxiliary Hamiltonian (4.10) (before Gutzwiller projection), which displays four Dirac points at $q = (\pm\pi/2, \pm\pi/2)$ (cf. Fig. 2.6). In presence of the Gutzwiller projection, the spectrum is clearly gapless at (π, π), while the gap at $(\pi, 0)$ and $(0, \pi)$ may possess much larger size effects, as shown in Fig. 4.16. A similar situation appeared within the single-mode approximation of Ref. [97], where a variance extrapolation was necessary to prove the existence of gapless excitations at $(\pi, 0)$ and $(0, \pi)$. We note that also the model studied in Ref. [135] displays four gapless excitations at $q = (0, 0)$, (π, π), $(\pi, 0)$ and $(0, \pi)$, but their origin is different because it can be traced back to an emergent $O(4)$ symmetry (involving Néel and VBS order parameters).

In conclusion, let us complete our discussion on the spectral properties of the $J_1 - J_2$ model by presenting the VMC results for the magnetically ordered phase with columnar order (see Fig. 4.7). We emphasize that the best variational wave function for $J_2/J_1 \gtrsim 0.6$ is defined by the auxiliary Hamiltonian (4.11), which contains a fictitious magnetic field with pitch vector $Q = (\pi, 0)$. This causes neighboring spins to order antiferromagnetically along the x-direction and ferromagnetically along the y-direction. For this kind of columnar order, the linear spin wave theory predicts the existence of four gapless points at $q = (0, 0)$, $q = (\pi, 0)$, $q = (0, \pi)$, $q = (\pi, \pi)$. However, the latter two points turn out to be pseudo-

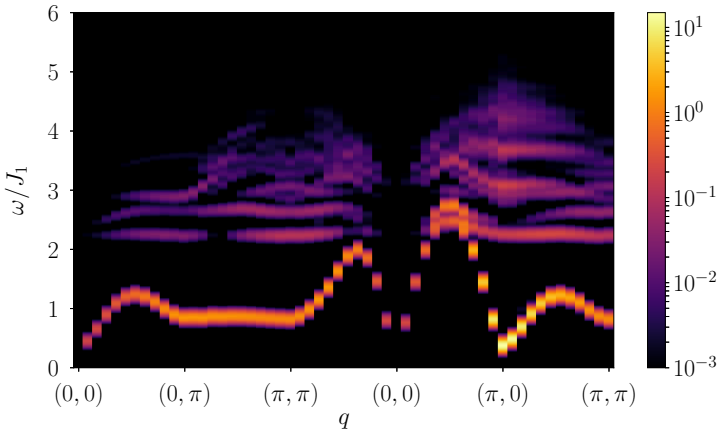

Figure 4.17: Dynamical spin structure factor of the $J_1 - J_2$ Heisenberg model on the 22×22 square lattice for $J_2/J_1 = 0.7$ (columnar magnetic phase). The spectral function has been convoluted with a normalized Gaussian with standard deviation $0.05J_1$.

Goldstone modes [136], whose existence is caused by accidental degeneracies which are lifted by an order-by-disorder effect when further quantum fluctuations are included [136–138]. Indeed, the variational spectrum for $J_2/J_1 = 0.7$, which is shown in Fig. 4.17, is gapless only at $q = (0,0)$ and $q = (\pi,0)$ (i.e. the ordering vector). The variational results are in good agreement with the outcome of previous series expansion calculations [139], and show a magnon branch which possesses different velocities in the x and y directions around the $q = (\pi,0)$ point. We also note that the continuum which was observed in the spin liquid phase has been replaced by a less intense signal at higher energies, characterized by relatively dispersionless features.

4.3 The $J_1 - J_2$ model on the triangular lattice

In this section, we present VMC results for the dynamical structure factor of the frustrated Heisenberg model on the triangular lattice, with first-neighbor ($J_1 > 0$) and second-neighbor ($J_2 > 0$) exchange couplings [70]:

$$\begin{aligned}\mathcal{H} = J_1 \sum_i \left(\mathbf{S}_i \cdot \mathbf{S}_{i+a_1} + \mathbf{S}_i \cdot \mathbf{S}_{i+a_2} + \mathbf{S}_i \cdot \mathbf{S}_{i+a_1-a_2}\right) \\ + J_2 \sum_i \left(\mathbf{S}_i \cdot \mathbf{S}_{i+a_1+a_2} + \mathbf{S}_i \cdot \mathbf{S}_{i+2a_1-a_2} + \mathbf{S}_i \cdot \mathbf{S}_{i-a_1+2a_2}\right).\end{aligned} \tag{4.12}$$

Here, $a_1 = (1,0)$ and $a_2 = (\frac{1}{2}, \frac{\sqrt{3}}{2})$ are the primitive vectors of the lattice, and the system is assumed to have periodic boundary conditions. For $J_2 = 0$, the above Hamiltonian reduces to the one of the Heisenberg model on the triangular lattice, whose ground state displays a noncollinear magnetization with 120° order [25, 26]. Due to the strong effect of quantum fluctuations, small perturbations on top of the nearest-neighbor model have been shown to drive the system into magnetically disordered phases [140, 141]. In this sense, the addition of the second neighbor exchange J_2 represents the simplest way to introduce further frustration while preserving the spin $SU(2)$ symmetry. Therefore, the $J_1 - J_2$ model (4.12) has been intensively investigated by different numerical approaches,

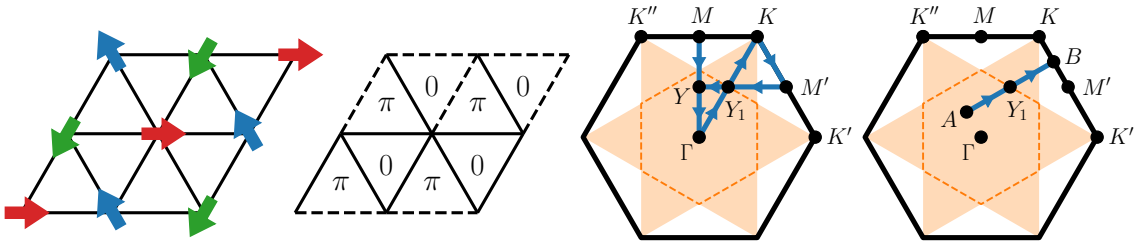

Figure 4.18: First panel from the left: the classical spin configuration (in the xy plane) that is determined by the fictitious magnetic field h in the Hamiltonian (4.13) with $Q = (2\pi/3, 2\pi/\sqrt{3})$. Second panel from the left: pattern $s_{i,j}$ for the sign structure of the first-neighbor hopping of Eq. (4.13), $s_{i,j} = +1$ (-1) for solid (dashed) lines; notice the the amplitude of the kinetic terms is chosen to be $t > 0$. Third panel from the left: the path in the Brillouin zone that is used to plot the results of the dynamical structure factor of the 30×30 triangular lattice (blue arrows), see Figs. 4.19, 4.20, 4.21, 4.24, and 4.25. Fourth panel from the left: the path in the Brillouin zone that is used to plot the dynamical structure factor of the 84×6 cylinder (blue arrows), see Fig. 4.23. In the last two panels the orange shaded area corresponds to the region of the Brillouin zone in which magnon decay is predicted by the spin-wave approximation [49, 64] and the dashed line delimits the magnetic Brillouin zone.

which identified a nonmagnetic phase developing at $J_2/J_1 \approx 0.07(1)$, whose nature is not settled down, with evidences for either a gapped [142, 143] or a gapless [144] spin liquid.

The spectral properties of the Heisenberg model are strongly affected by the instability of magnons. Indeed, semi-classical approaches, based upon the large-S expansion, suggested that the excitation spectrum obtained within the leading order (i.e., within the linear spin-wave approximation) is subjected to significant corrections when interactions between spin waves are taken into account [145]. This fact is mainly due to the non-collinearity of the magnetization, which allows for three-magnon interactions [65]. Then, despite the presence of long-range order, the Goldstone modes are not stable but they may decay in a large part of the Brillouin zone (see Fig. 4.18); in particular, the existence of more than one Goldstone mode, with different velocities, immediately causes that magnons may be kinematically unstable, decaying into two magnons with lower energy [49, 64]. A detailed analysis, which includes interactions among spin waves, corroborated this outcome, also showing roton-like minima at $M = (0, 2\pi/\sqrt{3})$ and symmetry-related points (i.e., midpoints of the edges of the Brillouin zone) [49, 64, 65]. The latter aspect shares similarities with the Heisenberg model on the square lattice, where minima of the magnon dispersion are present around $(\pi, 0)$ and $(0, \pi)$ [52, 54]. As far as the triangular lattice is concerned, aspects of the strong renormalization of the magnon dispersion at high energies have been confirmed by series expansions [146]. Moreover, within these numerical calculations, a huge downward renormalization of the one-magnon excitations is recovered, in stark contrast with the case of the square lattice antiferromagnet, where the linear spin wave spectrum is (slightly) shifted upward when magnon interactions are brought into play [54].

As previously mentioned (cf. Section 1.3.1), recent experimental measurements supported the idea that $Ba_3CoSb_2O_9$ could be described by a $S = 1/2$ Heisenberg model on the triangular lattice with predominant nearest-neighbor super-exchange couplings (a small easy-plane anisotropy is present, in addition to a small interlayer coupling) [68]. Inelastic neutron scattering experiments showed that, even if $Ba_3CoSb_2O_9$ is magnetically ordered at low temperatures, several aspects of the magnon dispersion and the multi-magnon continuum reveal an unconventional behavior (see also Fig. 1.8), which can only be partly ex-

plained within semi-classical approaches [67, 147]. First of all, at low-energies, the magnon dispersion is strongly renormalized with respect to the linear spin-wave approximation; an anomalous line broadening has also been detected, leading to the conclusion that magnon decay may be plausible; finally, the continuum presents unexpected dispersive features at high energies. It should be noticed that, since the neutron scattering data of Ref. [67] are sensitive to the full dynamical spin structure factor, three copies of the magnon dispersion (translated by the ordering vectors) are visible in the spectra of Fig. 1.8. Motivated by these experimental findings, there have been a few attempts to investigate the Heisenberg model on the triangular lattice (also including small perturbations) with both analytical and numerical tools [69, 148–150]. In particular, by using DMRG calculations, Verresen and collaborators [69] claimed that the magnon decay does not take place (in some parts of the Brillouin zone), because of the strong interactions between quasi-particles (i.e., magnons) in the Heisenberg model[6]. As a result of the avoided decay, the midpoint of the edge of the *magnetic* Brillouin zone (dubbed Y_1, cf. Fig. 4.18) displays a minimum of the magnon dispersion, possibly explaining the high-energy features seen around the M point in the inelastic neutron scattering spectra of Fig. 1.8 [67].

Other magnetic materials described by effective $S = 1/2$ spins on a triangular lattice have been recently discovered, such as $YbMgGaO_4$ [151, 152] and $NaYbO_2$ [153, 154]. In both cases, no signatures of magnetic order appear down to very low temperatures, suggesting the existence of a quantum spin liquid phase. Even if the actual low-energy Hamiltonians for these materials may be more complicated than the $SU(2)$-invariant one of Eq. (4.12), their physical properties can share many similarities with the ground state of the $J_1 - J_2$ model, as suggested in Ref. [140].

4.3.1 Variational wave functions

The variational phase diagram for the $J_1 - J_2$ model on the triangular lattice has been determined in Ref. [144]: the system undergoes a phase transition from the magnetically ordered phase to a gapless spin liquid at $J_2/J_1 \approx 0.08$. For this model, the optimal variational wave functions are constructed from the following auxiliary Hamiltonian:

$$\mathcal{H}_0 = t \sum_{\langle i,j \rangle} s_{i,j} c^\dagger_{i,\sigma} c_{j,\sigma} + h \sum_i \left(e^{iQ\cdot R_i} c^\dagger_{i,\uparrow} c_{i,\downarrow} + e^{-iQ\cdot R_i} c^\dagger_{i,\downarrow} c_{i,\uparrow} \right), \tag{4.13}$$

where $\langle \cdots \rangle$ restricts the summation over nearest-neighboring sites. Here t is a real hopping with a non-trivial sign structure ($s_{i,j} = \pm 1$) which generates a pattern of alternating 0 and π fluxes through the triangular plaquettes of the lattice, see Fig. 4.18; h is a fictitious magnetic field which displays the classical 120° order with $Q = (2\pi/3, 2\pi/\sqrt{3})$, see Fig. 4.18 (considering $Q = (4\pi/3, 0)$ would not change the physical content of the ground state wave function). All the parameters included in $\mathcal{H}_0$, and the pseudopotential $v_{i,j}$ entering the Jastrow factor, are optimized to minimize the variational energy. While in the magnetic phase of the system the optimal value for the ratio h/t is finite, for $J_2/J_1 \gtrsim 0.08$ the system enters the spin liquid phase and the magnetic field parameter vanishes in the thermodynamic limit [144].

Below, we discuss the results for the dynamical structure factor of the $J_1 - J_2$ model on the 30×30 triangular lattice. For $J_2 = 0$, we first consider the crudest approximation for the ground state, which consists in setting the hopping term t to zero. The resulting wave function is equivalent to the state of Ref. [155], with only a two-body Jastrow factor. Much more accurate results are then achieved by restoring the hopping term in the Hamiltonian

[6] In Ref. [69], a small easy-axis anisotropy has been considered in order to have a gapped spectrum and tractable numerical simulations.

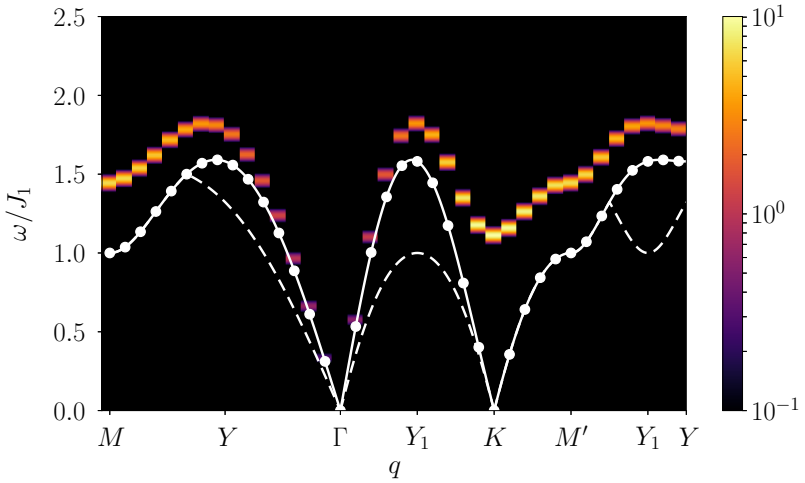

Figure 4.19: Dynamical structure factor of the nearest-neighbor Heisenberg model on the 30×30 triangular lattice obtained by using the variational wave function (1.22) with the auxiliary Hamiltonian (4.13) with $t = 0$. The path along the Brillouin zone is shown in Fig. 4.18. A Gaussian broadening of the spectrum has been applied ($\sigma = 0.02J_1$). The spin-wave energies of the magnon branch (ϵ_q), on the same cluster size, are represented by the white dots connected with a solid line. The dashed line corresponds to the bottom of the continuum within linear spin waves, i.e. $E_q = \min_k\{\epsilon_{q-k} + \epsilon_k\}$. Notice that $E_q < \epsilon_q$ in most of the Brillouin zone, as obtained in Ref. [49, 64].

and optimizing all the variational parameters, for the cases $J_2 = 0$ and $J_2/J_1 = 0.07$. In this cases, $S^z(q, \omega)$ corresponds to the out-of-plane dynamical structure factor. On the other hand, when the system is in the spin liquid regime ($J_2/J_1 = 0.09$ and $J_2/J_1 = 0.125$), h is vanishing and the Jastrow factor is not considered, because of its negligible effects on the variational results. Thus, the variational wave function, which corresponds to a fully symmetric $U(1)$ spin liquid according to the PSG classification [156], is $SU(2)$-invariant, and all the components of the dynamical structure factor are equal.

4.3.2 Numerical results

The nearest-neighbor Heisenberg model

Let us start our analysis by considering the pure Heisenberg model with only first-neighbor exchange ($J_2 = 0$). We first consider the simplest variational guess, in which the auxiliary Hamiltonian (4.13) contains only the fictitious magnetic field ($t = 0$). In this case, the Abrikosov fermions are completely localized (e.g., the eigenvalues of $\mathcal{H}_0$ define flat bands), and transverse fluctuations are included by the Jastrow factor (1.21). The results for the dynamical structure factor on the 30×30 cluster are shown in Fig. 4.19. Here, the spectrum consists of a *single* mode, which is identified as the magnon excitation. Notice that only one magnon branch is visible, related to the magnon dispersion ϵ_q, since we consider the out-of-plane dynamical structure factor (the *folded* branches $\epsilon_{q\pm K}$ do not contribute to the signal). As already observed in the square lattice case, the dispersion of the magnon branch is possible thanks to the Jastrow factor, since the wave function without it would give rise to a trivially flat spectrum. By contrast, the long-range Jastrow term is able to produce a reasonable magnon mode, which agrees fairly well with the spin-wave calculations. In particular, the spectrum is gapless at $\Gamma = (0, 0)$ (with a vanishingly small weight). Instead, in contrast to spin waves, which correctly predict gapless magnons at K and K' due to the coplanar 120° order, this simple wave function leads to a gapped

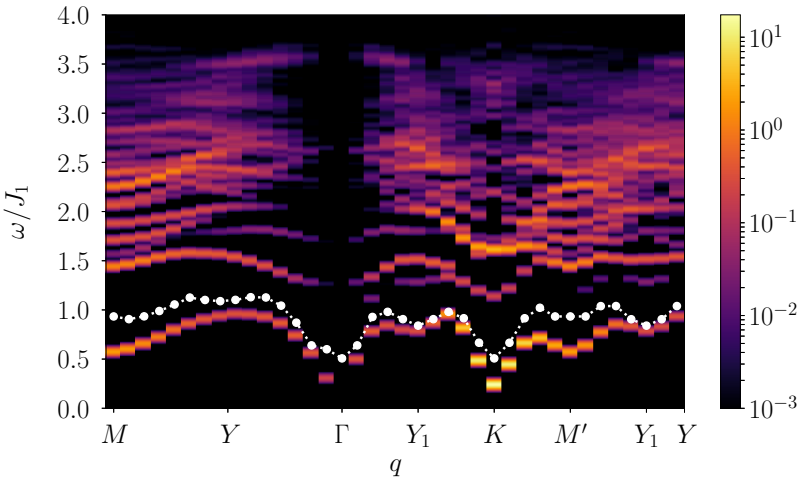

Figure 4.20: The same as Fig. 4.19 but for the optimal variational wave function with both hopping t and fictitious magnetic field h. The path along the Brillouin zone is shown in Fig. 4.18. The dotted line denotes the bottom of the continuum $E_q = \min_k\{E_0^{q-k}+E_0^k\}$, where E_0^q is the lowest energy for a given momentum q obtained within our variational approach. Since the spectrum is gapless at the Γ point, we exclude the cases $k = (0, 0)$ and $k = q$ in the search of the minimum, because the resulting E_q would simply coincide with the energy of the magnon branch E_0^q all over the Brillouin zone. The purpose of this kinematic analysis is to show that no magnon decay can yield an energy E_q which is lower than the one of the magnon branch E_0^q (in contrast with spin wave results).

spectrum at the corners of the Brillouin zone. In connection to that, the out-of-plane static structure factor $S^z(q) = \int d\omega S^z(q, \omega)$ does not diverge at K or K' when $N \to \infty$, showing only a maximum.

A much more realistic spectrum is obtained when considering a finite fermion hopping t (with the π-flux pattern shown in Fig. 4.18), as well as the optimized value of the fictitious magnetic field h (and the Jastrow factor). The results for the 30×30 lattice are reported in Fig. 4.20. In this case, there are several excitations with a finite weight for each momentum, thus reproducing the existence of a broad continuum, which extends up to relatively large energies. We would like to mention that, with respect to the square lattice Heisenberg model (Section 4.2, Fig. 4.10 in particular), here many more excitations for each momentum possess a visible spectral weight. Within this calculation, we identify the lowest-energy excitation E_0^q as the magnon peak [cf. Eq. (3.42)]. The validity of this assumption is corroborated by the results shown in Fig. 4.21, where the variational energies E_0^q closely follow the magnon branch obtained by series expansions. Instead, identifying the lowest-energy peak as the bottom of the continuum is not very plausible, since a much broader signal should be present in this case.

In order to discuss the issue of magnon decay, we apply a kinematic argument (as done both in the linear spin-wave approach [49, 64] and within DMRG [69]) and we consider all the possible two-magnons decays, which fulfill the conservation of momenta, i.e., $E_q = \min_k\{E_0^{q-k} + E_0^k\}$. For this purpose, we computed the magnon energies E_0^k for all the k-vectors in the Brillouin zone on the 30×30 lattice. The outcome is that the bottom of the two-magnon continuum, defined by the kinematic analysis, lies above the magnon branch (see Fig. 4.20). These results clearly indicate an avoided decay in a large part of the Brilloiun zone, as suggested by DMRG calculations, which considered certain (high-energy) parts of the magnon dispersion [69]. Still, we cannot exclude the existence of small regions where the magnon decay may persist, especially close to the gapless points. In this respect, within the linear spin-wave approach, the different velocities of the excitation

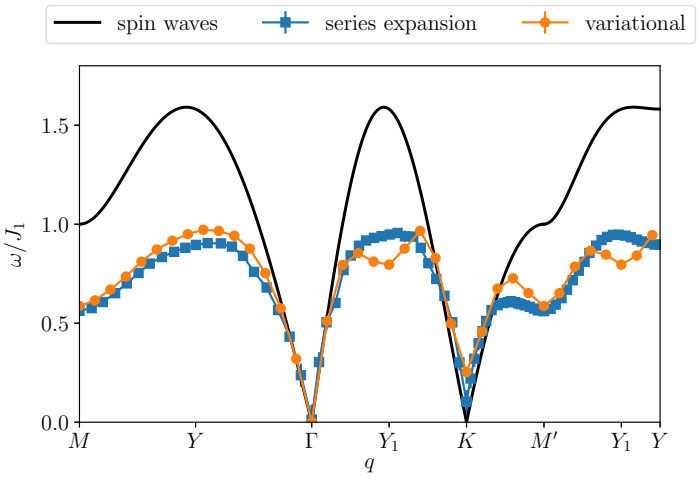

Figure 4.21: Energies of the magnon branch for the nearest-neighbor Heisenberg model on the triangular lattice obtained with different methods. The path in the Brillouin zone is shown in Fig. 4.18. The black line corresponds to linear spin wave, the blue squares to series expansion [146], and the orange circles to our variational energies E_0^q (on the 30×30 cluster). We note the appearance of an additional roton mode at Y_1 in the VMC magnon branch (in agreement with DMRG results [69]).

spectrum at Γ and K immediately lead to an unstable magnon branch close to the Γ point [49, 64]. Should this aspect be a genuine feature of the model, the magnon would be unstable in a small part around the center of the Brillouin zone. Unfortunately, given the finiteness of the cluster used in our numerical calculations, we cannot reliably estimate the slope of the magnon spectrum at Γ and K and, therefore, make definitive statements for this issue.

Here, we would like to notice the strong renormalization of the magnon branch with respect to spin-wave calculations, see Fig. 4.21. Most importantly, we emphasize that, within the VMC calculation, the magnon branch shows a roton-like minimum not only at M, but also at Y_1, i.e., the midpoint of the edge of the magnetic Brillouin zone (see also Fig. 4.22), as already detected by neutron scattering measurements in $Ba_3CoSb_2O_9$ [67]. This feature was not captured by the previous series expansion calculations [146] but, instead, has been observed by recent DMRG calculations on an infinitely long cylinder (with a small circumference $L = 6$) [69] and has been interpreted as the hallmark of the absence of magnon decay. In order to make a closer comparison with DMRG data, we perform the variational calculations on a long cylinder (84×6) along the same path in the Brillouin zone as the one that has been considered in Ref. [69]. The results are shown in Fig. 4.23. Here, the large number of lattice points along the cylinder allows us to have a detailed resolution of the magnon branch, which closely follows the one obtained by DMRG. In particular, we can estimate the bottom of the continuum by evaluating $E_q = \min\{E_0^{q-K} + E_0^K, E_0^{q+K} + E_0^{-K}\}$, where we consider the possible decays involving a magnon at K and $-K$. In doing so, we find that the lowest-energy excitation E_0^q is always below E_q, indicating that well defined branch exists and magnon decay is avoided. We finally remark that a roton minimum is detected along the same path as the one studied by Verresen and collaborators [69], strongly suggesting that this is a genuine feature of the Heisenberg model.

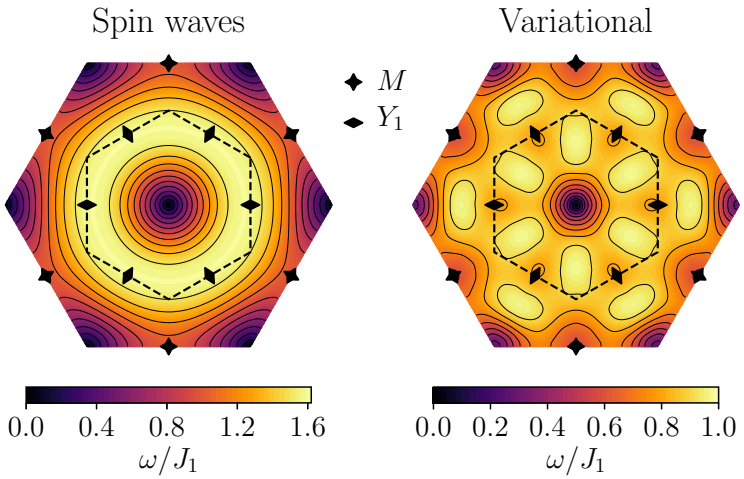

Figure 4.22: Dispersion relation of the magnon branch E_0^q as obtained within our variational approach (on the 30×30 cluster). The linear spin-wave results are also reported for comparison. Dashed lines represent the edges of the magnetic Brillouin zone. The presence of the roton minima at the M and Y_1 points in the variational spectrum is evident.

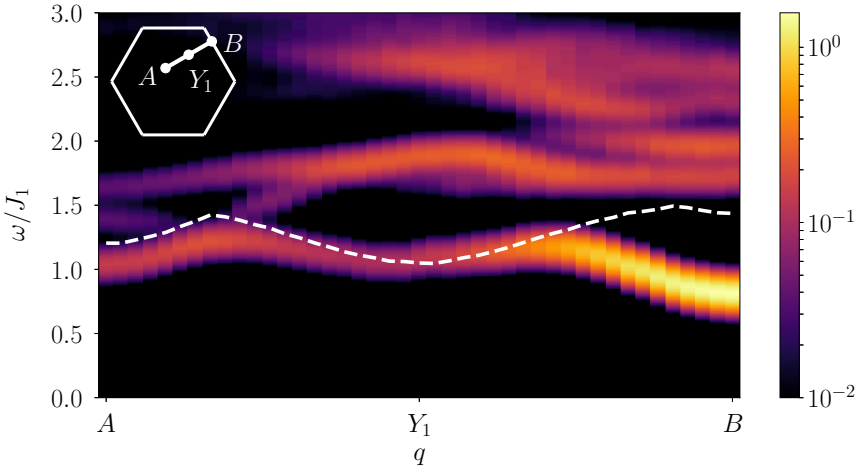

Figure 4.23: The dynamical structure factor for the nearest-neighbor Heisenberg model on a cylindrical geometry (84×6), to make a close comparison with DMRG calculations by Verresen and collaborators [69]. We apply a Gaussian broadening to the spectrum which is equivalent to the one of the aforementioned DMRG result ($\sigma = 0.077 J_1$). The path in the Brillouin zone is shown in the inset and in Fig.4.18 (the point A lies at 1/4 of the $\Gamma - K''$ line, where $K'' = (-2\pi/3, 2\pi/\sqrt{3})$; the point B lies at 1/4 of the $K - K'$ line). The dashed line denotes the bottom of the continuum, which is evaluated by taking $E_q = \min\{E_0^{q-K} + E_0^K, E_0^{q+K} + E_0^{-K}\}$, where E_0^q is the lowest energy for a given momentum q obtained within our variational approach and $K = (2\pi/3, 2\pi/\sqrt{3})$.

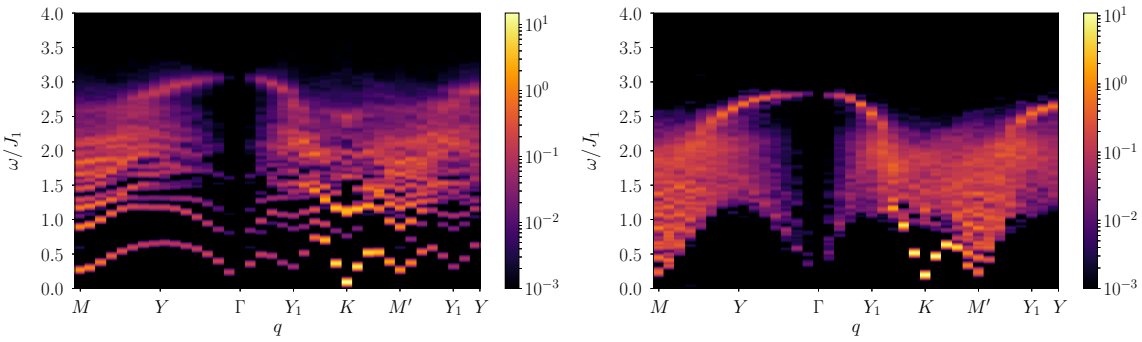

Figure 4.24: The dynamical structure factor for the $J_1 - J_2$ Heisenberg model on the 30×30 cluster with $J_2/J_1 = 0.07$ (left) and $J_2/J_1 = 0.09$ (right). The path along the Brillouin zone is shown in Fig. 4.18 and a Gaussian broadening of the spectrum has been applied ($\sigma = 0.02 J_1$).

The frustrated $J_1 - J_2$ model

We now move to the case in which also the second-neighbor coupling J_2 is present. Within our variational approach, a gapless spin liquid phase is stabilized for $0.08 \lesssim J_2/J_1 \lesssim 0.16$; here, the fictitious magnetic field vanishes in the thermodynamic limit and the best wave function only contains fermionic hopping (with π-flux threading half of the triangular plaquettes) [144]. On a finite size, a small value of h can be stabilized, as well as a tiny Jastrow pseudopotential. Still, we verified that these ingredients do not cause sensible differences in the dynamical structure factor. In Fig. 4.24, we show the results for the 30×30 cluster and for two values of J_2/J_1, which are very close to the transition point, one still inside the magnetic phase ($J_2/J_1 = 0.07$) the other one in the spin liquid region ($J_2/J_1 = 0.09$). By approaching the quantum phase transition, the major modification of the spectrum comes from the softening of the magnon excitation at the M points. This feature closely resembles the case of the frustrated $J_1 - J_2$ model on the square lattice (Section 4.2), where a softening is clearly detected for $q = (\pi, 0)$ and $(0, \pi)$ (cf. Fig. 4.15). In this latter case, this fact has been connected to the progressive deconfinement of spinons that have gapless (Dirac) points at $q = (\pm\pi/2, \pm\pi/2)$. On the triangular lattice, the softening of the spectrum at the M points is a direct consequence of the Dirac points at $q = (0, \pm\pi/\sqrt{3})$ in the spinon band structure. Therefore, since the spectrum of the magnetically ordered phase is gapless at K, we expect both M and K points to be gapless at the critical point (as well as Y_1, which can be obtained by combining M and K vectors), as required by the continuous nature of the phase transition [144]. However, let us remark an important difference with respect to the square lattice case. Here, the spectrum of the π-flux hopping included in the auxiliary Hamiltonian (4.13) is gapped at the momentum corresponding to the 120° magnetic order (i.e. K). On the contrary, in the case of the $J_1 - J_2$ model on the square lattice, the flux phase hopping of the auxiliary Hamiltonian (4.9) is gapless (also) at the Néel ordering vector $q = (\pi, \pi)$.

In Fig. 4.25, we report the dynamical structure factor for $J_2/J_1 = 0.125$. The spin liquid state is characterized by a broad continuum that extends up to relatively large energies. In particular, around the M points, the magnon roton-like minima of the ordered phase fractionalize into an incoherent set of excitations at low energies. This feature is compatible with the existence of Dirac points in the unprojected spectrum of the auxiliary Hamiltonian $\mathcal{H}_0$, see Fig. 4.25. By contrast, a strong signal in the lowest-energy part of the spectrum is detected around the K points, where the unprojected spinon spectrum is instead gapped. In this respect, the Gutzwiller projection is fundamental to include interaction among spinons in a non-perturbative way and give a drastic modification of

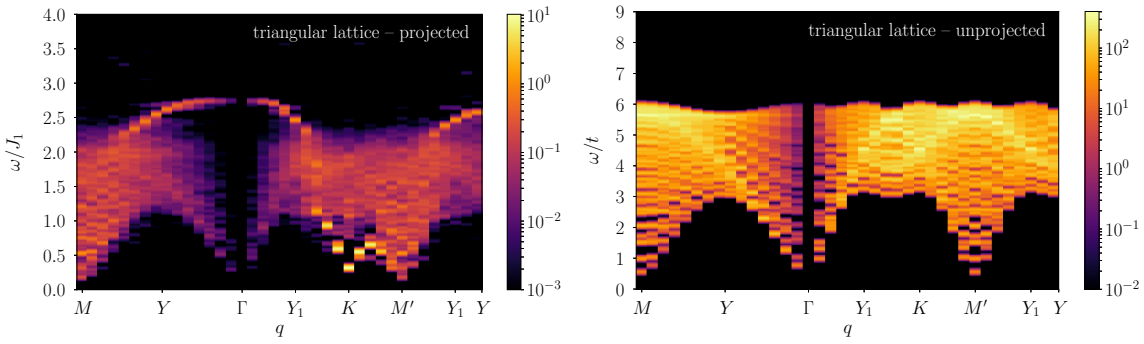

Figure 4.25: The dynamical structure factor for the $J_1 - J_2$ Heisenberg model on the 30×30 triangular lattice with $J_2/J_1 = 0.125$. The variational results (left panel) are compared to the ones obtained from the unprojected Abrikosov fermion Hamiltonian $\mathcal{H}_0$ of Eq. (4.13) with $t = 1$ and $h = 0$ (right panel). The path along the Brillouin zone is shown in Fig. 4.18. We applied a Gaussian broadening of $\sigma = 0.02J_1$ to the variational results. Notice that, for the unprojected data, the energy scale is given by the hopping amplitude t of the fermionic Hamiltonian (4.13), instead of J_1. Therefore, the broadening of the unprojected spectrum has been rescaled in order to account for the larger bandwidth.

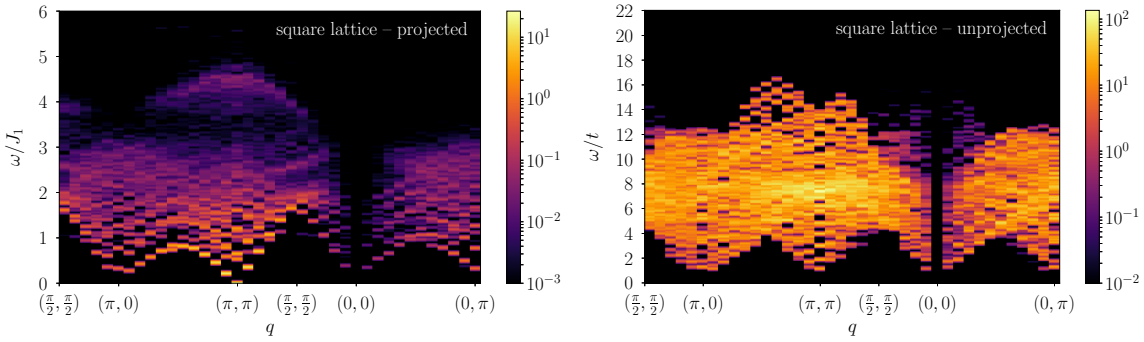

Figure 4.26: The dynamical structure factor for the $J_1 - J_2$ Heisenberg model on the square lattice (22×22) with $J_2/J_1 = 0.55$ (the same as in Fig. 4.15). The variational results (left panel) are compared to the ones obtained from the unprojected Abrikosov fermion Hamiltonian (4.10) for the gapless Z_2 spin liquid discussed in Section 4.2 (right panel). We applied a Gaussian broadening of $\sigma = 0.02J_1$ to the variational results. Notice that, for the unprojected data, the energy scale is given by the hopping amplitude t of the fermionic Hamiltonian of Eq. (4.10), instead of J_1. Therefore, the broadening of the unprojected spectrum has been rescaled in order to account for the larger bandwidth.

the low-energy features. This is a distinctive aspect of the triangular lattice, since, on the square lattice, all the low-energy (gapless) points observed in presence of the Gutzwiller projector [i.e. $q = (0,0)$, (π,π), $(\pi,0)$ and $(0,\pi)$] already exist in the non-interacting picture [97], see Fig. 4.26. We would like to emphasize that, in contrast to the magnetically ordered phase, where no visible spectral weight is present right above the magnon branch (see Fig. 4.20), in the spin liquid phase the continuum is not separated from the lowest-energy excitation. This outcome corroborates the fact of having deconfined spinons in the magnetically disordered phase. The intense signal at K points immediately implies strong (but short-range) antiferromagnetic correlations in the variational wave function, which are absent in the unprojected π-flux state (by contrast, on the square lattice, the π-flux state has already significant antiferromagnetic correlations built in it).

The presence of low-energy spectral weight at the corners of the Brillouin zone could be ascribed to the existence of critical monopole excitations, as suggested by the analysis of Ref. [157]. In fact, the Gutzwiller projector introduces temporal fluctuations of the gauge fields that are completely frozen within the non-interacting picture (i.e., within the unprojected wave function) [84]. Even though we cannot exclude a more conventional picture where a bound state of spinons is responsible for the intense signal around K, it is plausible that this feature originates from the existence of gauge fields, which emerge in the field-theoretical description of spin liquids [15]. Certainly, our VMC calculations provide an indisputable evidence of the fact that the non-interacting (i.e., unprojected) spinon spectrum is not sufficient to fully explain the low-energy spectrum detected by the dynamical structure factor.

Remarkably, on the 30×30 cluster, the lowest-energy excitation at K is slightly higher inside the spin liquid phase (i.e., for $J_2/J_1 = 0.125$) than close to the critical point (i.e., for $J_2/J_1 \approx 0.08$), see Figs. 4.24 and 4.25. This fact may suggest the possibility that this kind of excitation may be slightly gapped in the spin liquid region, while being gapless at the critical point. We finally highlight the existence of an unexpected high-energy dispersing mode, which bends from the Γ point down into the continuum, being seemingly connected to the low-energy excitation at K. A comparison with other numerical techniques will be needed to clarify whether this feature is a genuine aspect of the model or an artifact of the present variational approach.

5

Neural Gutzwiller-projected wave functions

CONTENTS

5.1 Introduction

In the previous chapters, we largely discussed how variational wave functions based on Gutzwiller-projected fermionic states can be employed to compute static and dynamical properties of frustrated spin models. The main virtue of this class of variational *Ansätze* is their physical transparency: the variational parameters of the trial state are the fermionic couplings forming the auxiliary Hamiltonian $\mathcal{H}_0$, which have a clear physical meaning that simplifies the interpretation of the results. For example, some properties of the variational states can be immediately inferred from the parameters of $\mathcal{H}_0$, e.g. the presence of symmetry breaking or magnetic order. On the other hand, the major drawback of this variational approach is the lack of a systematic way of improving the quality of the approximation. First of all, the Gutzwiller projector reintroduces only the temporal fluctuations of the gauge fields (neglecting the spatial ones), and this may not be sufficient to capture important long wavelength properties [84, 158]. Moreover, the number of variational parameters contained in $\mathcal{H}_0$ is limited, and, typically, the addition of long-range hoppings or pairings does not provide a sensible improvement of the variational energy. The situation is different with respect to other numerical approaches, such as DMRG and tensor network techniques, in which a certain parameter (i.e. the bond dimension) controls the degree of accuracy of the method [39].

Recently, in the quest for an efficient representation of the ground state wave function of many-body systems, artificial neural networks have emerged as an alternative to more traditional methods. Generally speaking, neural networks constitute a powerful approach to approximate multi-variable functions. The pioneering work of Carleo and Troyer [159] introduced a neural network variational *Ansatz*, specifically a *restricted Boltzmann machine* (RBM, see Section 5.2), for the ground state wave functions of spin systems. RBMs have been extensively used in condensed matter physics and quantum information [160–167] contexts because, due to the nature of their non-local structure, they can represent some highly-entangled many-body states using a relatively small number of parameters [160, 163, 164, 168].

Notably, neural networks can be easily combined with Gutzwiller-projected fermionic states, in order to improve the variational energy of the latter [166]. Within this hybrid scheme, the simple two-body Jastrow factor of Eq. (1.21) is replaced by a neural network

factor, which introduces many-body spin-spin correlations at all distances. The neural network correlator offers the possibility of systematically improving the variational energy of the wave function by increasing the number of parameters of the network. Variational methods based on neural networks have been proven to provide extremely accurate results for the Heisenberg model on the square lattice [159, 166]. However, a comprehensive study of the performances of these variational *Ansätze* in the case of frustrated spin models is lacking. Here, we aim at filling this gap by tackling several prototypical frustrated models by a RBM-fermionic wave function.

The definition of our hybrid variational scheme is presented in the following section. In order to put emphasis on the role of the neural network correlator, which replaces the Jastrow factor, in this chapter we adopt a notation which is slightly different from the one used in the rest of the thesis.

5.2 Definition of the wave function

We consider a generic variational wave function which is written as a product of a Gutzwiller-projected fermionic state, $|\Psi_f\rangle = \mathcal{P}_{S^z_{tot}}\mathcal{P}_G|\Phi_0\rangle$ (cf. Section 1.5), and a certain correlator, $\hat{\mathcal{C}}$:

$$|\Psi_{\mathcal{C}}\rangle = \hat{\mathcal{C}}|\Psi_f\rangle = \sum_{\sigma} \mathcal{C}(\sigma)\langle\sigma|\Psi_f\rangle|\sigma\rangle. \tag{5.1}$$

In the above formula we have inserted a resolution of the identity ($\mathcal{I} = \sum_\sigma |\sigma\rangle\langle\sigma|$) and exploited the fact that $\hat{\mathcal{C}}$ is taken to be diagonal in the many-body computational basis for spins $\{|\sigma\rangle\} = \{|\sigma^z_1, ..., \sigma^z_N\rangle\}$ (where σ^z_i indicates the z-component of the ith spin). The fermionic part of the *Ansatz* is obtained by Gutzwiller-projecting the ground state $|\Phi_0\rangle$ of a given auxiliary Abrikosov fermion Hamiltonian $\mathcal{H}_0$ [which takes, in general, the form displayed in Eqs. (1.14) and (1.20)]. For what concerns the correlator $\hat{\mathcal{C}}$, we have seen that the two-body spin-spin Jastrow factor [Eq. (1.21)] is a valid choice to increase the accuracy of the fermionic *Ansatz*, especially in the case of magnetically ordered phases. In this chapter we aim at exploring the possibility of improving Gutzwiller-projected fermionic wave functions by applying a stronger many-body correlator than the two-body Jastrow factor. For this purpose, a neural network is employed in the form of a *restricted Boltzmann machine*. This network is defined by introducing a set of auxiliary Ising variables, $\{h^\alpha\}_{\alpha=1,...,N_\alpha}$, which are referred to as *hidden* units and form the so-called *hidden* layer (see Fig. 5.1). These variables are coupled to the z-components of the spins of the lattice (dubbed as *visible* layer, $\{\sigma^z_i\}_{i=1,...,N}$) through a classical energy functional of the form:

$$E_{\mathrm{RBM}} = \sum_{i=1}^{N}\sum_{\alpha=1}^{N_\alpha} h^\alpha W^\alpha_i \sigma^z_i + \sum_{\alpha=1}^{N_\alpha} b^\alpha h^\alpha + \sum_{i=1}^{N} a_i \sigma^z_i. \tag{5.2}$$

The RBM correlator is then obtained by computing the Boltzmann factor $e^{E_{\mathrm{RBM}}}$ and taking its trace over the hidden variables degrees of freedom. This operation can be performed exactly due to the particular form of the classical energy functional of Eq. (5.2), which only contains interactions between variables belonging to the two different layers (i.e., no intralayer couplings are allowed). If we assume to be interested in translationally invariant states with $S^z_{tot} = 0$, we can set $a_i = 0$ and obtain the final form of the RBM correlator [159]:

$$\mathcal{C}_{\mathrm{RBM}}(\sigma) = \exp\left[\sum_\alpha \log\cosh\left(b^\alpha + \sum_i W^\alpha_i \sigma^z_i\right)\right]. \tag{5.3}$$

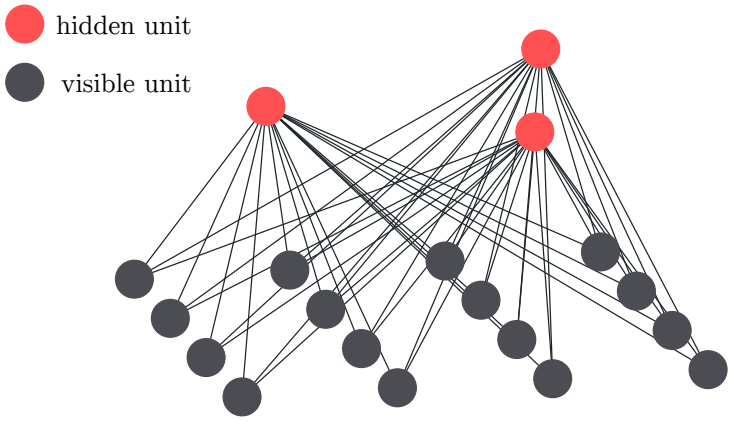

Figure 5.1: Schematic representation of the restricted Boltzmann machine. The visible units (grey dots) correspond to the lattice sites of the spin model (here a 4×4 square lattice). The $N_\alpha = 3$ hidden units (red dots) are coupled to all the visible ones through the weights W_i^α (forming a fully connected network).

The parameters of $\hat{\mathcal{C}}_{\mathrm{RBM}}$ are called *biases* (b^α) and *weights* (W_i^α), and are assumed to be complex numbers, unless otherwise stated. The complex parametrization of the RBM allows the correlator to change both the amplitudes and the phases of the fermionic wave function to which it is applied. The expression of Eq. (5.3) can be regarded as a sort of many-body Jastrow factor, since a series expansion of the $\log\cosh(\dots)$ function contains all the n-body terms of the σ^z variables. Unlike the Jastrow factor, the RBM correlator not only breaks the $SU(2)$ symmetry of spin, but also the Z_2 symmetry $\sigma^z \mapsto -\sigma^z$. This happens if the biases b^α are nonzero, since the aforementioned expansion can contain products of odd numbers of spins.

When studying lattice models, an important question to address is the implementation of lattice symmetries in the correlator $\hat{\mathcal{C}}$. As already pointed out in Section 1.5, a symmetric two-body Jastrow factor is obtained by simply taking a symmetric pseudopotential, e.g., $v_{i,j} = v(|R_i - R_j|)$. This procedure, however, cannot be applied to the RBM correlator, since its parameters depend upon the index α (labelling the hidden units), which doesn't have any physical meaning. Therefore, the most straightforward way of including symmetries is to implement them *a posteriori*. Concretely, if we want to enforce translational symmetry, we symmetrize the RBM correlator through a product over all possibile Bravais lattice translations $\{T_R\}$:

$$\mathcal{C}_{\mathrm{tRBM}}(\sigma) = \prod_R C_{\mathrm{RBM}}[T_R(\sigma)] = \exp\left[\sum_R \sum_\alpha \log\cosh\left(b^\alpha + \sum_i W_i^\alpha \sigma^z_{i+_R}\right)\right]. \tag{5.4}$$

The above expression is translationally invariant with momentum $\mathbf{K} = 0$. In addition, the point group symmetries $\{\Sigma\}$ of the lattice can be implemented on top of the translationally invariant correlator. The procedure is the same as the one employed in Eq. (5.4):

$$\begin{aligned}\mathcal{C}_{\mathrm{sRBM}}(\sigma) &= \prod_\Sigma \prod_R C_{\mathrm{RBM}}[\Sigma T_R(\sigma)] \\ &= \exp\left[\sum_\Sigma \sum_R \sum_\alpha \log\cosh\left(b^\alpha + \sum_i W_i^\alpha \sigma^z_{\Sigma(i+_R)}\right)\right],\end{aligned} \tag{5.5}$$

where $\Sigma(j)$ indicates the position of the site obtained by applying the symmetry Σ to the site j. The quantum numbers of the above correlator, which are associated to the different point group symmetries, are all zero by construction. A more general strategy to implement symmetries with the desired quantum numbers is outlined in Ref. [169].

The main advantage of the RBM correlator with respect to the Jastrow factor comes from the fact that its accuracy can be, in principle, systematically improved by increasing the number of hidden variables N_α. This is due to the fact that a RBM is a universal function approximator [170], which means that it can approximate any function with arbitrary accuracy if the number of variables in the hidden layer is allowed to grow arbitrarily large. In addition, the non-local structure of this neural network makes it capable of capturing highly-entangled phases of matter. On the other hand, the disadvantage of employing the RBM correlator in relation to the simpler two-body Jastrow factor mainly resides in its higher computational cost. Crucial for an efficient variational Monte Carlo, computing ratios of translationally invariant RBMs has a cost which scales linearly with the number of sites and the number of hidden units $[O(N \times N_\alpha)]$, while computing ratios of two-body Jastrow factors simply scales as $O(1)$ (cf. Section 3.3) [86]. Finally, another disadvantage of the RBM is the lack of straightforward physical interpretability of its variational parameters, which are associated to many-body spin-spin correlations at all distances. Instead, the pseudopotential $v_{i,j}$ of the Jastrow factor clearly accounts for the two-body correlation of spins i and j, and typically shows a clear physical behavior [171], decaying with the distance $|R_i - R_j|$.

5.3 Spin models

We investigate the accuracy gain obtained by augmenting the fermionic wave function with the addition of the RBM correlator, and we assess its performances for different spin models on a lattice. We focus mainly on the $J_1 - J_2$ Heisenberg model on the square lattice (4.7), studying two different values of the frustrating ratio J_2/J_1. First we consider the case $J_2 = 0$, i.e. the (unfrustrated) Heisenberg model, where a pure RBM wave function has been shown to yield very accurate energies with a large systematic accuracy gain when the number of hidden units is increased [159]. The results of Ref. [159] were obtained by fixing the sign structure of the variational *Ansatz* to the one of the exact ground state (Marshall-Peierls sign rule [38, 172]) and taking a real-valued RBM correlator. One of the questions we want to address is to which degree the knowledge of the exact sign of the ground state plays a role in providing accurate RBM variational energies and how the RBM-fermionic *Ansatz* performs when the sign structure is unknown. For this reason, we consider the case $J_2/J_1 = 0.5$, where the nature of the ground state of the model is a long standing problem [173, 174] and the sign structure of the ground state is expected to be very complicated due to frustration.

Another model we tackle is the XY model on the square lattice, whose Hamiltonian is given by

$$\mathcal{H} = J \sum_{\langle i,j \rangle} (S_i^x S_j^x + S_i^y S_j^y), \tag{5.6}$$

where $\langle \cdots \rangle$ indicates first-neighboring sites. In this case, the ground state exhibits Néel order with the spins aligned in the xy plane. A fundamental difference between the XY and the Heisenberg models comes from their symmetries: while the Heisenberg exchange interaction is invariant under global spin rotations around any axis (i.e., it exhibits $SU(2)$ symmetry), the XY coupling is invariant only under global rotations around S_z (leading

to a $U(1)$ symmetry). The purpose of considering the XY model is understanding whether the RBM correlator performs better for a model whose exact ground state breaks the spin $SU(2)$ symmetry.

Finally, we consider the Heisenberg model on the triangular lattice (4.12), whose ground state is magnetically ordered [25, 26], but, at variance with the case of the square lattice, displays a nontrivial sign structure and strong deviations from the semiclassical limit (cf. Section 4.3). This scenario gives us the possibility to evaluate the performance of the RBM-fermionic wave function for a magnetically ordered model which is characterized by strong frustration effects.

5.4 Numerical results

5.4.1 The $J_1 - J_2$ model on the square lattice

We first discuss the variational Monte Carlo results for the $J_1 - J_2$ model on a 6×6 square lattice. For $J_2 = 0$, the auxiliary fermionic Hamiltonian $\mathcal{H}_0$ which defines the variational *Ansatz* is the one of Eq. (4.9), which contains a Néel magnetic field and the flux phase hopping [98]. We emphasize that this fermionic wave function possesses the sign structure of the exact ground state of the Heisenberg model, i.e., it follows the Marshall-Peierls sign rule [38, 172]. Therefore, it is sufficient to use a RBM correlator with real parameters, so that $C_{\mathrm{RBM}}(\sigma) \geq 0$. On the contrary, in the frustrated regime, the sign structure of the exact ground state is unknown. For $J_2/J_1 = 0.5$ we combine a complex-valued RBM correlator and the Z_2 spin liquid state defined by the auxiliary Hamiltonian of Eq. (4.10). Once more, we point out that all the parameters of the variational states, i.e., the weights and biases of the RBM and the couplings included in $\mathcal{H}_0$, are fully optimized through the stochastic reconfiguration technique [86, 102].

We aim at evaluating the accuracy gain provided by the application of the RBM correlator to the fermionic wave function. In the magnetically ordered phase ($J_2 = 0$), where the fermionic state of reference breaks the $SU(2)$ symmetry because of the presence of a nonzero magnetic field inside $\mathcal{H}_0$, we compare the results obtained by applying the RBM correlator and the two-body Jastrow factor to the same fermionic state $|\Psi_f\rangle$. Indeed, in this case, the presence of the Jastrow factor plays the important role of including transverse quantum fluctuations which considerably improve the variational energy. Instead, within the non-magnetic phase ($J_2/J_1 = 0.5$), the best fermionic state does not break the $SU(2)$ symmetry and the Jastrow factor typically gives a negligible contribution. In this case, we choose to compare the accuracy of the combined RBM-fermionic wave function to the pure Gutzwiller-projected fermionic state. In both cases, the RBM correlator is expected to yield an improvement of the accuracy when all the parameters are properly optimized, since it can be shown that the Jastrow factor can be represented exactly as a RBM [166, 168]. The underlying question we address is understanding to which extent the application of the RBM correlator improves the accuracy and the physical content of the variational wave function. For the $J_1 - J_2$ model, we consider both the translationally invariant [$\hat{\mathcal{C}}_{\mathrm{tRBM}}$, Eq. (5.4)] and the fully symmetric [$\hat{\mathcal{C}}_{\mathrm{sRBM}}$, Eq. (5.5)] RBM correlators.

In Fig. 5.2 we report the relative error of the variational energy of the $J_1 - J_2$ model on the 6×6 lattice with respect to the exact value, obtained by Lanczos diagonalization. This quantity is defined as

$$\Delta E = \left| \frac{E_{\mathcal{C}} - E_0}{E_0} \right|, \tag{5.7}$$

where $E_{\mathcal{C}}$ is the energy of a given variational *Ansatz* and E_0 is the exact ground-state energy. The results clearly show that the variational wave function is overall more accurate in the unfrustrated regime than in the frustrated one. In particular, at $J_2 = 0$ the inclusion of the RBM provides a large energy gain with respect to the fermionic reference state (for which $\Delta E \approx 0.4\%$): the relative error of the energy improves by a factor ≈ 8 when applying the translationally invariant RBM ($\Delta E \approx 0.05\%$ for $N_\alpha = 12$) and a factor of ≈ 20 when applying the fully symmetric RBM ($\Delta E \approx 0.02\%$ for $N_\alpha = 12$). In general, for each value of N_α we observe that the inclusion of the point group symmetries in the RBM correlator halves the relative error of the variational energy. By contrast, at $J_2/J_1 = 0.5$ the accuracy gain is considerably smaller: the relative error of the energy changes from $\Delta E \approx 0.6\%$ to $\Delta E \approx 0.3\%$ by applying a translationally invariant RBM correlator, and the addition of point group symmetries is far less effective than what we observe for the unfrustrated case. In Fig. 5.2 the variational energies obtained with the RBM-fermionic wave functions are compared to the ones of Ref. [175], in which a convolutional neural network (CNN) quantum state is employed: the CNN wave function is more accurate in the unfrustrated phase, while the RBM-fermionic *Ansatz* gives better energies in the frustrated regime.

The overall better performance of the RBM-fermionic state in the unfrustrated regime is supported by the results of Appendix G, where we report the results of a regression analysis in which the amplitudes and the sign structure of the ground state wave function on a small cluster are separately fitted by RBM functions.

To further elucidate the ability of the RBM-fermionic wave functions in capturing the ground state properties of the model, we compute the spin-spin correlations at different distances on the lattice. Whereas the exact ground state wave function of the $J_1 - J_2$ model on finite cluster possesses all the symmetries of its Hamiltonian, most of the variational *Ansätze* used in our calculations break the spin $SU(2)$ symmetry of the model due to the presence of the RBM correlator, the Jastrow factor, or the fictitious magnetic field h. Therefore, to investigate the spin symmetry properties of the resulting states, we separate the computation of the spin-spin correlations at distance R into the in-plane part,

$$\mathcal{S}_R^{xy} \equiv \frac{1}{2N} \sum_{i=1}^{N} \left(S_i^x S_{i+R}^x + S_i^y S_{i+R}^y \right), \tag{5.8}$$

and the out-of-plane part,

$$\mathcal{S}_R^{z} \equiv \frac{1}{N} \sum_{i=1}^{N} S_i^z S_{i+R}^z. \tag{5.9}$$

We then compare the variational estimates of the two contributions separately with the exact value $\langle \mathcal{S}_R \rangle_0 \equiv 1/3 \langle \mathbf{S}_0 \cdot \mathbf{S}_R \rangle_0 = \langle S_0^a S_R^a \rangle_0$, $a = x, y, z$. Here $\langle \dots \rangle_0$ indicates the expectation value over the exact ground state $|\Upsilon_0\rangle$, obtained by Lanczos diagonalization. Thus, the relative error of the spin-spin correlations at distance R is computed as

$$\Delta \mathcal{S}_R^{\alpha} = \frac{\langle \mathcal{S}_R^{\alpha} \rangle_{\mathcal{C}} - \langle \mathcal{S}_R \rangle_0}{\langle \mathcal{S}_R \rangle_0}, \tag{5.10}$$

where $\langle \dots \rangle_{\mathcal{C}}$ indicates the expectation value over a given variational wave function, and $\alpha = xy, z$ refer to the in-plane, Eq. (5.8), and out-of plane, Eq. (5.9), estimators.

In Fig. 5.3, we show the in-plane and out-of-plane variational correlations as a function of distance, in comparison to the exact value. The results are obtained with the fully symmetric RBM-fermionic wave function $\hat{\mathcal{C}}_{\mathrm{sRBM}} |\Psi_f\rangle$ ($N_\alpha = 1$) for $J_2 = 0$. Due to the presence of the antiferromagnetic parameter h, which induces magnetic ordering in the xy plane, the in-plane correlations overestimate the exact ones in absolute value, while the out-of-plane correlations underestimates them. This tendency is observed for the spin-spin

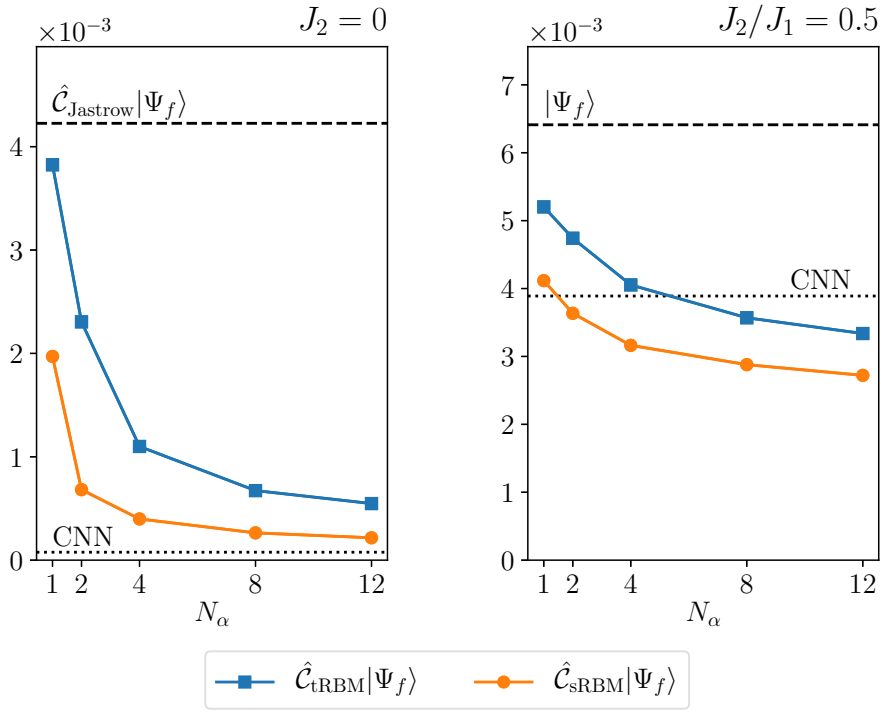

Figure 5.2: Relative error of the VMC energies ΔE [see Eq. (5.7)] with respect to the exact ones for the $J_1 - J_2$ model on the 6×6 square lattice. The results for the unfrustrated case ($J_2 = 0$) and the frustrated one ($J_2/J_1 = 0.5$) are shown on the left and on the right panel, respectively. The relative error of the RBM-fermionic wave function is plotted as a function of the number of hidden units: blue squares refer to the case of translationally invariant RBM correlator $\hat{\mathcal{C}}_{\text{tRBM}}$, while orange circles correspond to the fully symmetric RBM correlator $\hat{\mathcal{C}}_{\text{sRBM}}$. The error bars are smaller than the size of the dots. The dashed line represents the relative error of the fermionic wave function of reference, which includes a Jastrow factor in the unfrustrated case ($J_2 = 0$). The dotted line refers to the relative error of the CNN quantum state of Ref. [175].

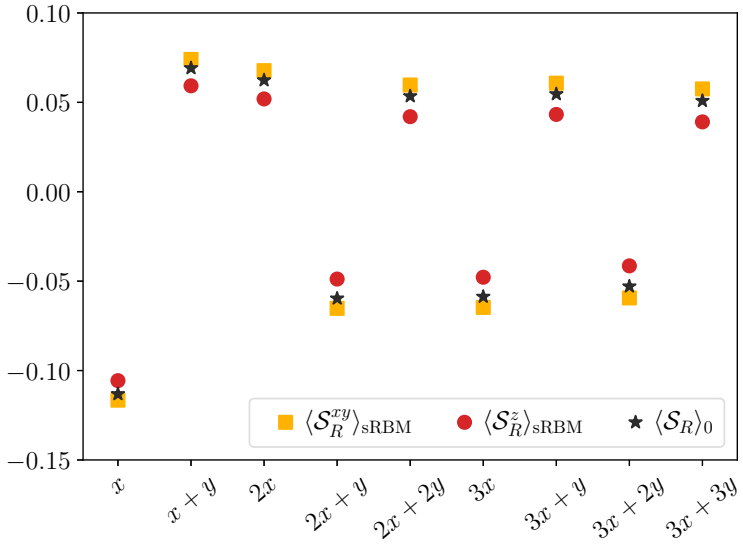

Figure 5.3: Spin-spin correlations for the Heisenberg model ($J_2 = 0$) on the 6×6 square lattice, as a function of distance R. Here, $x = (1, 0)$ and $y = (0, 1)$ are the lattice unit vectors. The set of data represented with yellow squares (red circles) corresponds to the expectation value of $\mathcal{S}^{xy}_R$ ($\mathcal{S}^{z}_R$) on the RBM-fermionic wave function with the fully symmetric correlator $\hat{\mathcal{C}}_{\text{sRBM}}$ ($N_\alpha = 1$). The error bars are smaller than the size of the dots. The black stars represent the exact values of the spin-spin correlations, i.e., $\langle \mathcal{S}_R \rangle_0 = 1/3 \langle \mathbf{S}_0 \cdot \mathbf{S}_R \rangle_0$.

correlations at any distance and for any value of N_α. The results obtained by increasing the number of hidden units are shown in Fig. 5.4, where the relative error of the variational estimates of the correlations with respect to the exact value is reported for some selected distances R. We observe a systematic improvement of the accuracy when the number of hidden units is increased, with both the in-plane and the out-of-plane correlations approaching the exact value. The fact that these two terms tend to get closer to each other when N_α is increased indicates that the RBM correlator tries to restore the anticipated spin $SU(2)$ symmetry in the wave function. As expected, since the optimal wave function is computed by minimizing the ground state energy, the most accurate values for the correlations are obtained at first-neighbors. We note also that, at any distance, the RBM correlator systematically provides a more accurate estimation of the spin-spin correlations than the simple Jastrow factor.

Before moving to the frustrated case, we explain the motivation of our choice to consider the accuracy of $\mathcal{S}^{xy}_R$ and $\mathcal{S}^{z}_R$ *separately*, instead of using the isotropic spin-spin correlation, $(\mathcal{S}^{z}_R + 2\mathcal{S}^{xy}_R)/3$. When performing the optimization of the variational parameters of the wave function, we observed that the final set of weights and biases of the RBM can depend on their initial values. Indeed, the parametrization of the RBM displays a considerable degree of redundancy, as indicated by the presence of zero eigenvalues of the covariance matrix of the stochastic reconfiguration technique [Eq. (3.28)] [86]. Therefore, the optimization procedure can end into different local minima which can have equivalent energies and slightly different in-plane and out-of-plane spin-spin correlations. However, this small difference, which is typically negligible in the unfrustrated regime, can be enhanced or reduced in a random fashion by cancellation of error when the isotropic correlation is computed. Therefore, we argue that a study of the separate components of the correlation

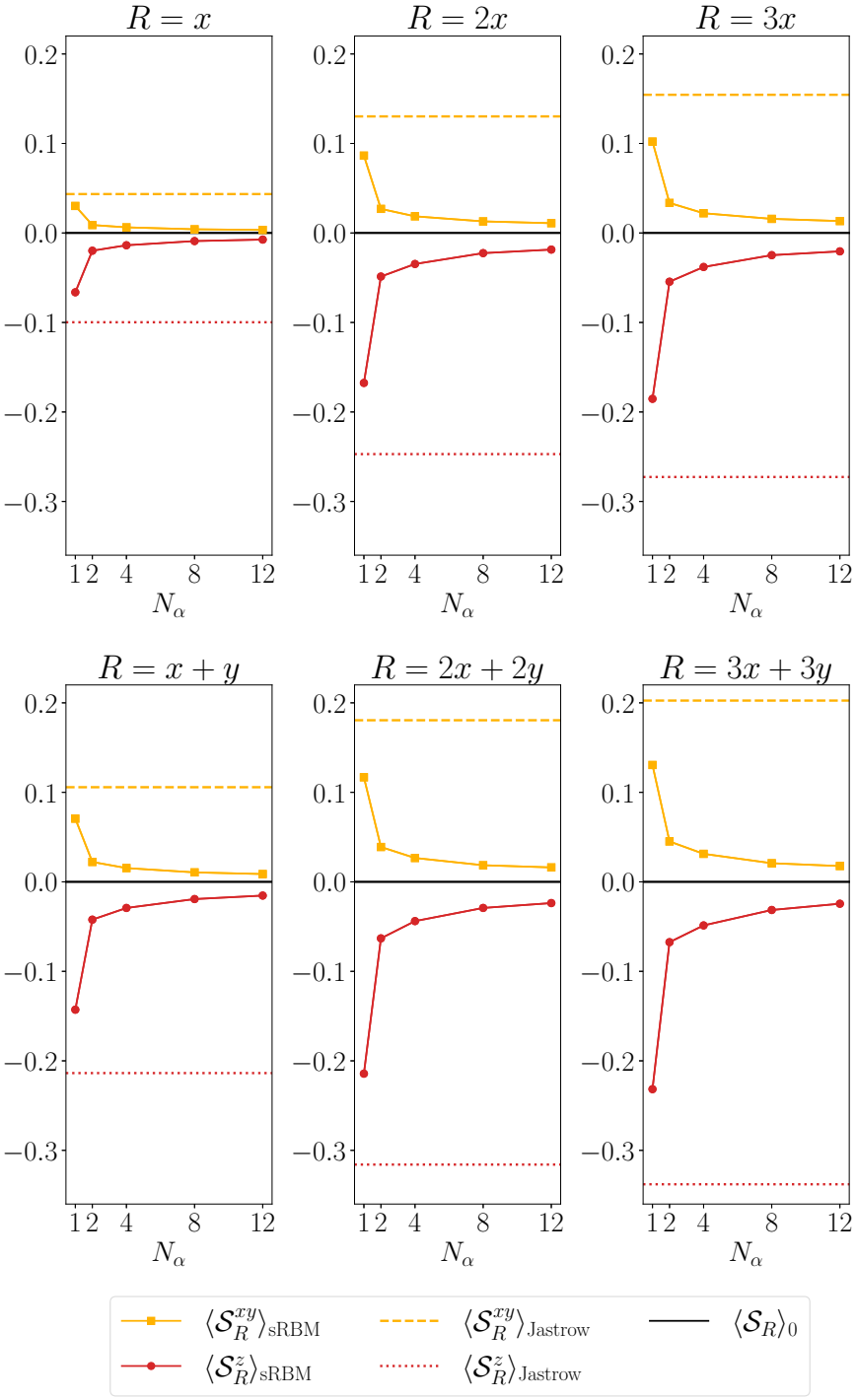

Figure 5.4: Relative error of the spin-spin correlations [see Eq. (5.10)] for the Heinseberg model ($J_2 = 0$) on the 6×6 square lattice, as a function of the number of hidden units. The correlations are evaluated at different distances R, which are expressed in terms of the lattice unit vectors $x = (1, 0)$ and $y = (0, 1)$. The set of data represented with yellow squares (red circles) corresponds to the relative error of the expectation value of $\mathcal{S}^{xy}_R$ ($\mathcal{S}^{z}_R$), computed by employing the RBM-fermionic wave function with the fully symmetric correlator $\hat{\mathcal{C}}_{\text{sRBM}}$. The yellow dashed (red dotted) line, instead, refers to the relative error of the expectation value of $\mathcal{S}^{xy}_R$ ($\mathcal{S}^{z}_R$) computed by employing the Jastrow correlator instead of the RBM. Finally, the black line indicates the zero of the vertical axis, i.e. the position of the exact value in the relative error scale.

function, rather than the isotropic counterpart, provides a better characterization of the symmetry properties of our *Ansatz*.

At $J_2/J_1 = 0.5$, the situation is considerably different from the unfrustrated case, as demonstrated in Fig. 5.5. The accuracy of the variational correlations does not show a systematic improvement with the number of hidden units. Indeed, even if in general the results are more accurate for $N_\alpha = 12$ than $N_\alpha = 1$, the behavior of the relative error is not as smooth as the respective one observed in Fig. 5.4 for $J_2 = 0$. Moreover, in some cases the relative error obtained by applying the RBM correlator is larger than the one obtained from the use of the simple Jastrow factor. A regular improvement is observed only at first and second neighbors, which are the correlations contributing to the value of the energy. Most importantly, the role of the RBM correlator regarding the expected $SU(2)$ symmetry is not clear; we find that the out-of-plane correlations display a better improvement than the in-plane ones when N_α is increased. We argue that this irregular behaviour of the accuracy of the spin-spin correlations is a consequence of the presence of several local minima in the optimization of the variational parameters of the RBM correlator, which leads to states with markedly different energies and correlation functions. While the effect is already present in the unfrustrated Heisenberg model, it is enhanced in the highly-frustrated regime of the $J_1 - J_2$ model.

To investigate this issue, we performed 40 distinct optimizations of the $\hat{\mathcal{C}}_{\mathrm{tRBM}}|\Psi_f\rangle$ *Ansatz* with $N_\alpha = 4$ at $J_2/J_1 = 0.5$, choosing different values of the RBM parameters as starting point. The relative error of the spin-spin correlations obtained by the 40 resulting wave functions is plotted as a function of the relative error of the variational energy in Fig. 5.6. We observe that the accuracy of the results show considerably large fluctuations. In particular, while the out-of-plane correlations seem to be more accurate when the variational energy is lower, an opposite effect is observed for the in-plane terms at some distances. The RBM correlator, which is a function of the σ_z degrees of freedom, tends to "sacrifice" the accuracy of the in-plane correlations for the sake of improving the variational energy. This numerical experiment suggests that the complexity of the optimization landscape of RBM in the presence of frustration is significantly different from the unfrustrated case: while in the unfrustrated case all the local minima display similar energies and correlation functions, the highly frustrated regime exhibits a wide array of local minima with similar variational energy but strikingly different correlation functions. We speculate that these minima are due to the presence of a possible glassy phase in the optimization induced by frustration [176].

We conclude our analysis of the $J_1 - J_2$ model by presenting the variational energies for the 10×10 square lattice. The wave functions we employ have the same form of the ones used for the 6×6 lattice. However, while the number of parameters entering $\mathcal{H}_0$ is the same, the number of weights of the RBM increases linearly with the size. For the Heisenberg model ($J_2 = 0$), in Fig. 5.7 we show the relative error of the variational energy with respect to the exact one, computed by quantum Monte Carlo [119, 120]. The relative error of the RBM-fermionic wave function is of the same order of magnitude of the one obtained on the 6×6 lattice and shows a remarkable energy gain with respect to the Jastrow-fermionic state. However, the accuracy gain provided by the inclusion of the point group symmetries is slightly smaller than the one observed for the 6×6 lattice. We note that the variational energy of the CNN quantum state of Ref. [175] is lower than our best RBM-fermionic energy. Here, we emphasize the fact that the CNN state employs a larger number of variational parameters (3838 complex numbers [175]) than the RBM-fermionic wave function with $N_\alpha = 8$ (810 real numbers). However, the local structure of the CNN is advantageous in the process of optimization, because the optimal parameters obtained for a smaller lattice constitute a good a starting point for the optimization of the wave

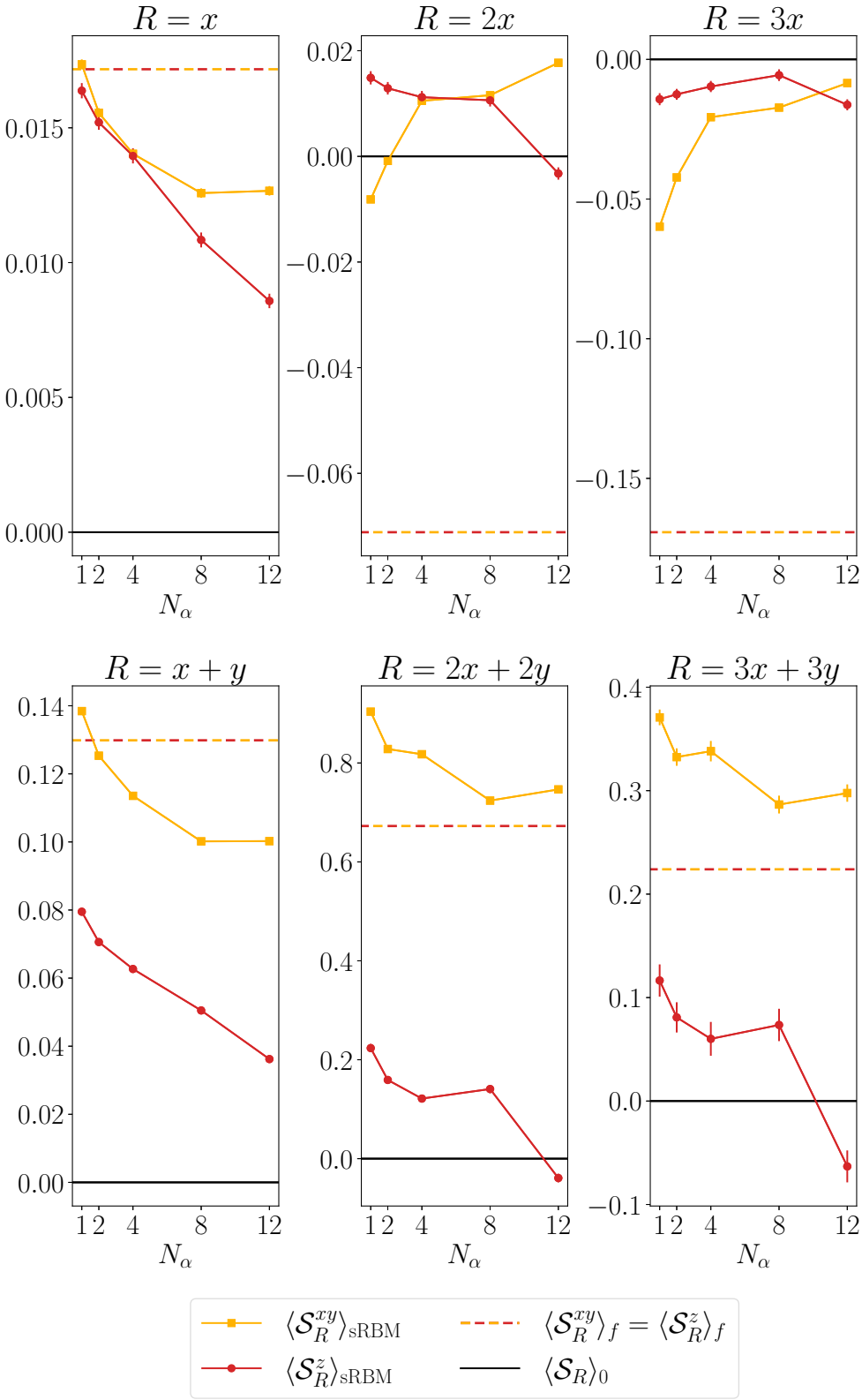

Figure 5.5: The same as in Fig. 5.4 for $J_2/J_1 = 0.5$. The only difference is given by the fact that the fermionic state (without Jastrow factor) is spin $SU(2)$-invariant and, therefore, in-plane and out-of-plane correlations are equal (and denoted by the bicolor dashed line).

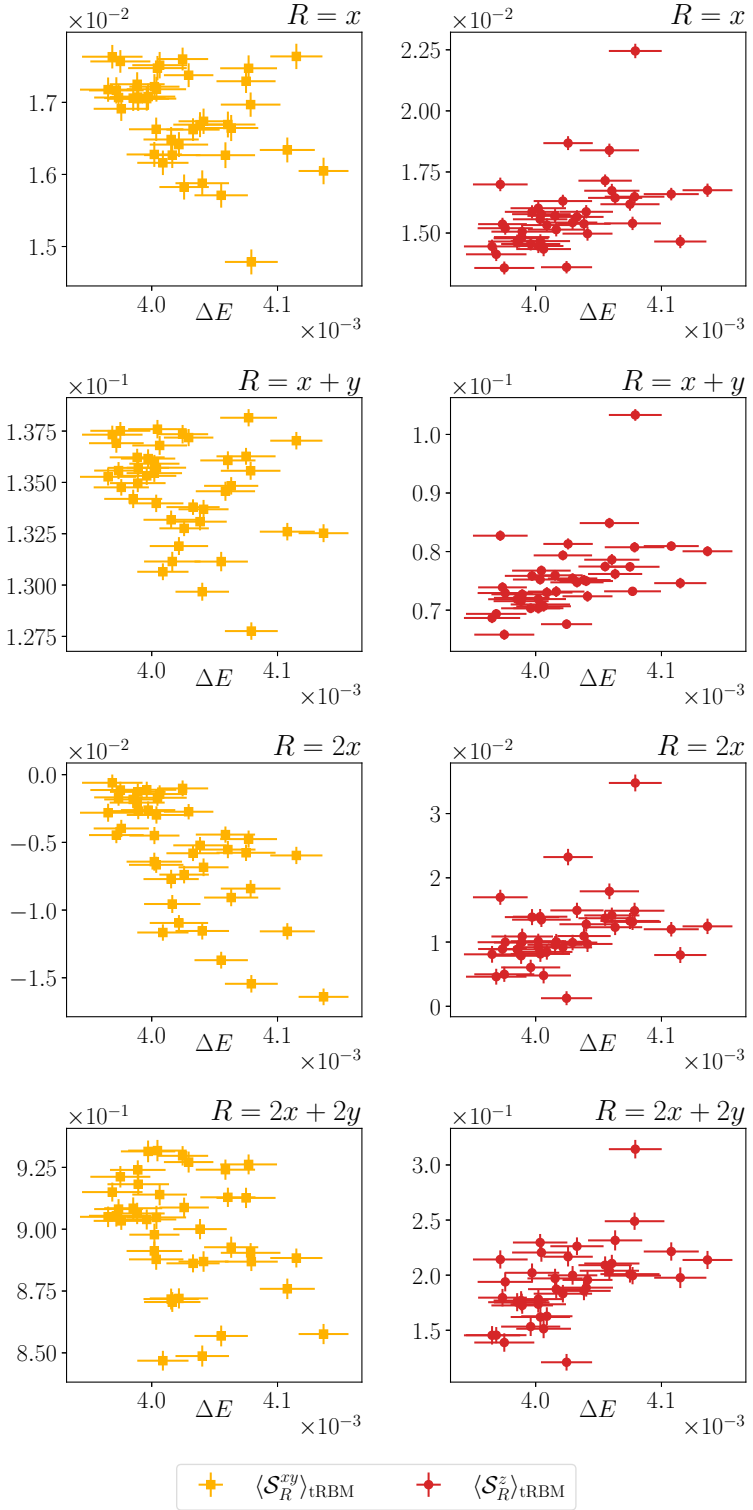

Figure 5.6: Relative error of the spin-spin correlations as a function of ΔE [see Eq. (5.7)] for the $J_1 - J_2$ model on the 6×6 square lattice in the frustrated regime, $J_2/J_1 = 0.5$. The correlations are computed at different distances R, which are expressed in terms of the lattice unit vectors $x = (1, 0)$ and $y = (0, 1)$. The wave function employed in the calculations is a RBM-fermionic *Ansatz* with a translational invariant correlator ($N_\alpha = 4$). Different points correspond to the results of different optimizations of the variational parameters. The set of data represented with yellow squares (red circles) corresponds to the relative error of the expectation value of the in-plane (out-of-plane) correlations.

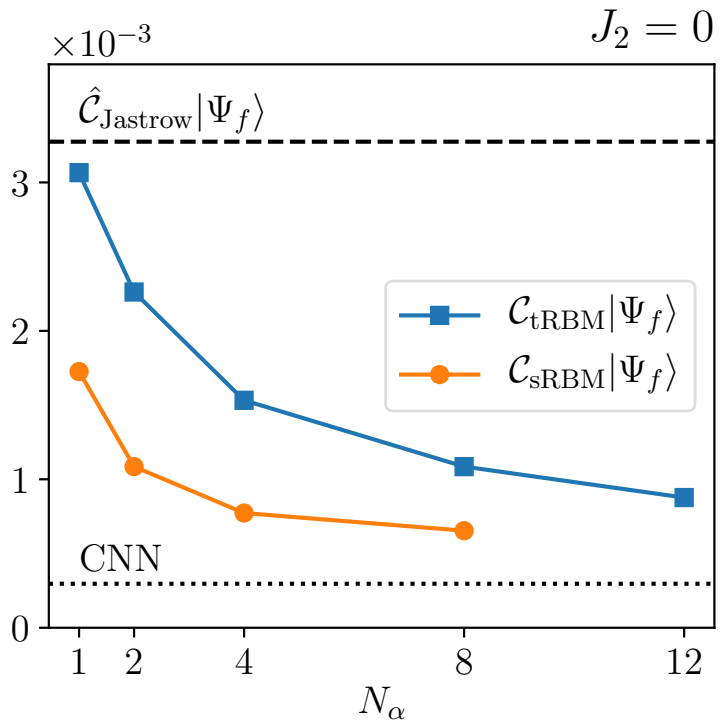

Figure 5.7: Relative error of the VMC energies for the Heisenberg model on the 10×10 square lattice, computed with respect to the exact result of quantum Monte Carlo [119, 120]. The relative error of the RBM-fermionic wave function is plotted as a function of the number of hidden units: blue squares refer to the case of translationally invariant RBM correlator $\hat{\mathcal{C}}_{\text{tRBM}}$, while orange circles correspond to the fully symmetric RBM correlator $\hat{\mathcal{C}}_{\text{sRBM}}$. The error bars are smaller than the size of the dots. The dotted line refers to the relative error of the CNN quantum state of Ref. [175].

function on a larger lattice [175]. The same procedure cannot be applied in the case of the RBM correlator, due to its highly nonlocal structure, which implies that the optimization of the parameters of this network necessarily becomes harder when the size of the system increases.

In Fig. 5.8 we compare our variational energies in the frustrated phase, $J_2/J_1 = 0.5$, with several different results from literature. Here, at variance with the unfrustrated case, the variational energies obtained by using the RBM-fermionic wave function are better than the ones of the CNN of Ref. [175], and are very close to the best DMRG estimates of Ref. [123]. However, a considerably lower variational energy is obtained in Ref. [97], where a fermionic wave function, defined by an auxiliary Hamiltonian $\mathcal{H}_0$ which contains two additional $d_{x^2-y^2}$ pairings (at fourth- and sixth-neighbors) with respect to the one of Eq. (4.10), is improved by the application of few Lanczos steps. The relative energy gain provided by two Lanczos steps, which require the addition of only two variational parameters, is remarkably larger than the improvement which is obtained by the application of the RBM correlator, which contains more than 2000 parameters for $N_\alpha = 12$. In general, as already observed for the 6×6 lattice, in the frustrated regime the RBM correlator yields a much smaller energy gain with respect to the unfrustrated case.

In summary, these results suggest that the RBM correlator provides a systematic way of improving the description of magnetically ordered phases beyond the Jastrow factor, where the RBM effectively induces out-of-plane fluctuations that counterbalance the in-

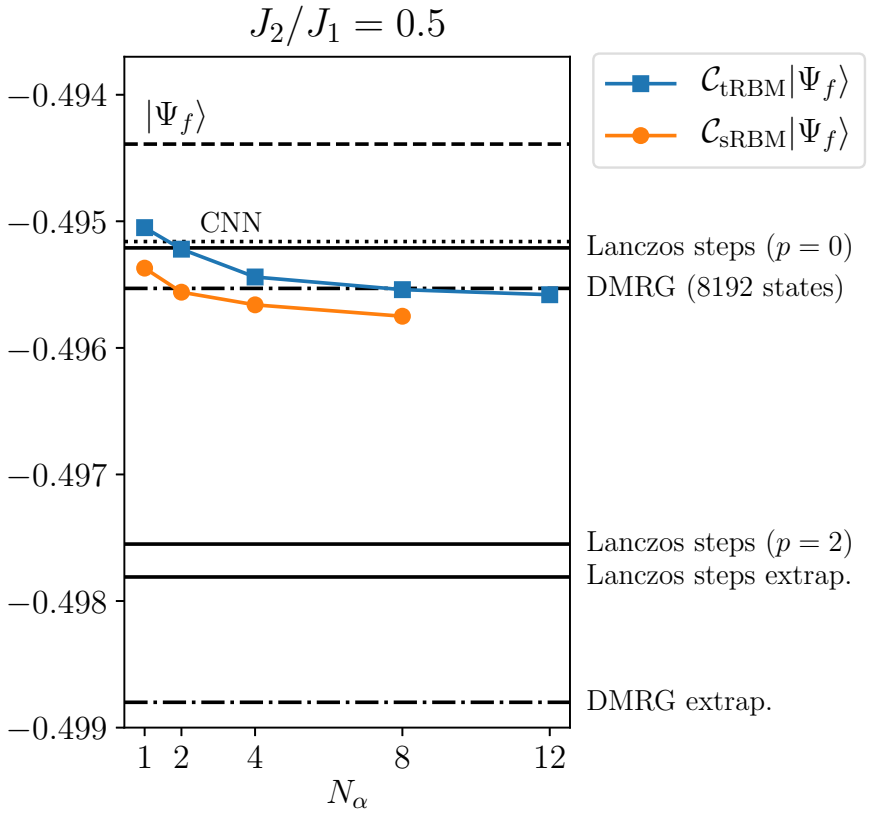

Figure 5.8: VMC energies for the $J_1 - J_2$ model on the 10×10 square lattice in the frustrated regime ($J_2/J_1 = 0.5$). The variational energies of the RBM-fermionic wave function are plotted as a function of the number of hidden units: blue squares refer to the case of translationally invariant RBM correlator $\hat{\mathcal{C}}_{\text{tRBM}}$, while orange circles correspond to the fully symmetric RBM correlator $\hat{\mathcal{C}}_{\text{sRBM}}$. The error bars are smaller than the size of the dots. As a comparison we report several different results. The dashed line indicates the energy of the fermionic wave function of reference. DMRG energies from Ref. [123] are plotted with a dotted-dashed line: the highest energy corresponds to the most accurate result obtained by a DMRG calculation (using 8192 $SU(2)$ states), while the lowest one corresponds to the value which was obtained by extrapolating DMRG data with respect to the truncation error. Full lines represent the results of Ref. [97], in which Lanczos steps were applied to a fermionic wave function in order to improve its accuracy. Three values are reported here: the highest energy is obtained with the pure fermionic wave function ($p = 0$, i.e., no Lanczos steps), the middle one by the application of two Lanczos steps ($p = 2$), while the lowest one is the result of the variance extrapolation. Finally, the variational energy obtained with the CNN quantum state of Ref. [175] is depicted with a dotted line.

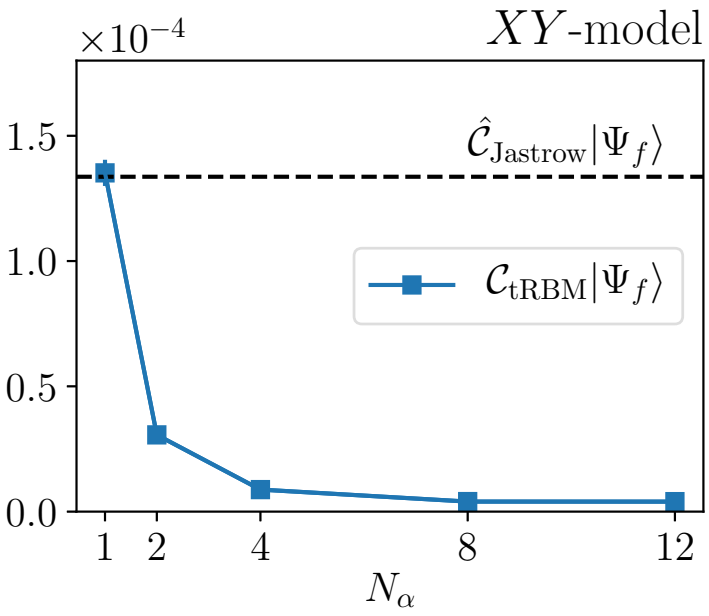

Figure 5.9: Relative error of the VMC energies ΔE [see Eq. (5.7)] with respect to the exact ones for the XY model on the 6×6 square lattice. The blue squares correspond to the relative error of the RBM-fermionic wave function as a function of the number of hidden units (N_α). The error bars are smaller than the size of the dots. The dashed line represents the relative error of the fermionic wave function of reference, which includes a Jastrow factor.

plane magnetic order induced by the fictitious magnetic field h [cf. Eq. (4.9)]. In the frustrated regime, even though the application of the RBM leads to better variational energies, it generally does not improve the description of the correlation functions beyond nearest neighbors. Apart from their numerically expensive training procedure, the RBM's energetic enhancement comes at the price of breaking of the $SU(2)$ symmetry of the fermionic wave function. The symmetry breaking we observe is especially evident in the correlation functions beyond nearest neighbors, which do not directly affect the variational energy during the optimization procedure. All these issues could be addressed in the future by using a recently introduced parametrization of the RBM correlator, which by construction satisfies the spin $SU(2)$ symmetry of the models considered in our study [177].

5.4.2 The XY model on the square lattice

As already pointed out, one of the main drawbacks of the introduction of the RBM correlator is the breaking of the spin $SU(2)$ symmetry of the wave function. For this reason, we evaluate the accuracy of the RBM-fermionic construction for a model whose Hamiltonian has lower symmetry, i.e., the XY model of Eq. (5.6). The exact ground state of the XY model has the same sign structure of the one of the Heisenberg model, i.e. it follows the Marshall-Peierls rule [172]. Thus, we employ an analogous RBM-fermionic wave function like the one used for the Heisenberg model (with real weights and biases). The variational results are reported in Fig. 5.9 for the translationally invariant correlator $\hat{\mathcal{C}}_{\text{tRBM}}$. The relative error of the variational energy with respect to the exact one is at least a factor of 10 smaller than the one obtained for the Heisenberg model and the accuracy gain provided by the RBM correlator is remarkable ($\Delta E \approx 0.0004\%$ for $N_\alpha = 12$). The higher accuracy

of the wave function is related to the fact that here the symmetry of the variational *Ansatz* is consistent with the spin symmetry of the model.

5.4.3 The Heisenberg model on the triangular lattice

Our previous results suggest the idea that the application of the RBM correlator is more effective for magnetically ordered phases, as exemplified in the Heisenberg and XY model, rather than for non-magnetic ones, as in the frustrated region of the $J_1 - J_2$ model. However, in the Néel phases considered above, the exact sign structure of the wave function is particularly simple and exactly captured by the fermionic part of the variational *Ansatz*. To try to disentangle whether the successes observed in our simulations are related to the special structure of the sign or to the presence of magnetic order, we consider a model whose ground state is magnetically ordered but displays a non-trivial sign structure: the Heisenberg model on the triangular lattice (4.12). In this case, the fermionic part of the *Ansatz* is constructed via the auxiliary Hamiltonian of Eq. (4.13), which features a magnetic field h with 120° order and a real nearest-neighbor hopping t, which generates an alternation of 0 and π fluxes threading the triangular plaquettes (see Fig. 4.18) [144]. While in the square lattice a real parametrization on top of the fermionic state already gives an accurate representation for both signs and amplitudes of the exact ground state, we anticipate that the triangular lattice Heisenberg model requires a complex-valued correlator to approximate the unknown sign structure of the wave function induced by the geometric frustration of the problem. Thus, on top of the fermionic state, we apply a translationally invariant RBM correlator with complex parameters ($\hat{\mathcal{C}}_{\text{tRBM}}$).

In Fig. 5.10, we compare the accuracy of the RBM-fermionic wave function for the Heisenberg model on the 6×6 square and triangular lattices. The energy gain provided by the application of the RBM correlator is considerably larger in the case of the square lattice, where the relative error of the energy decreases of a factor ≈ 8, with respect to the case of the triangular lattice, where it decreases of a factor ≈ 1.5 (from $\Delta E \approx 2.2\%$ to $\Delta E \approx 1.4\%$). Overall, the variational energy is more accurate on the square lattice than on the triangular lattice, and the relative errors differ by an order of magnitude.

In Fig. 5.10, we also compare the results of the aforementioned RBM-fermionic wave functions to the ones obtained by simpler *Ansätze*, which are constructed by setting the hopping terms to zero and considering an auxiliary fermionic Hamiltonian with only magnetic field ($\mathcal{H}_0 = \mathcal{H}_{\text{AF}}$). In this way, the fermionic degrees of freedom are localized and $|\Psi_f\rangle$ reduces to a (projected) product state $|\Psi_Q\rangle = \mathcal{P}_{S^z_{tot}=0} \prod_{i=1}^{N} (|\uparrow\rangle_i + e^{iQR_i} |\downarrow\rangle_i)$, which displays "classical" order in the xy-plane. This wave function can be employed as a reference state for the application of a Jastrow factor [178] or the RBM correlator. Here, we apply a translationally invariant RBM correlator to $|\Psi_Q\rangle$. We observe that the energy gain provided by the presence of the hopping term in the fermionic *Ansatz* is remarkably large when the simple Jastrow factor is applied to the reference state. However, when the RBM correlator is employed, the contribution of the hopping term becomes less important, decreasing considerably with the number of hidden units, which suggests that the RBM replaces the effect of the fermionic hopping term in the state.

Finally, in Fig. 5.11 we present the variational energies obtained for the Heisenberg model on the 12×12 triangular lattice. For a large enough N_α, the variational energy of the RBM-fermionic wave function is more accurate than the Green's function Monte Carlo (GFMC) result of Ref. [25]. To summarize our numerical experiments, we surmise that the high accuracy of the results for the unfrustrated square lattice Heisenberg model is due to having an exact representation of the sign structure built in the *Ansatz*, while the lower accuracy in the triangular lattice is presumably due to the approximate nature of the sign structure imposed by the complex-valued RBM in conjunction with the fermionic

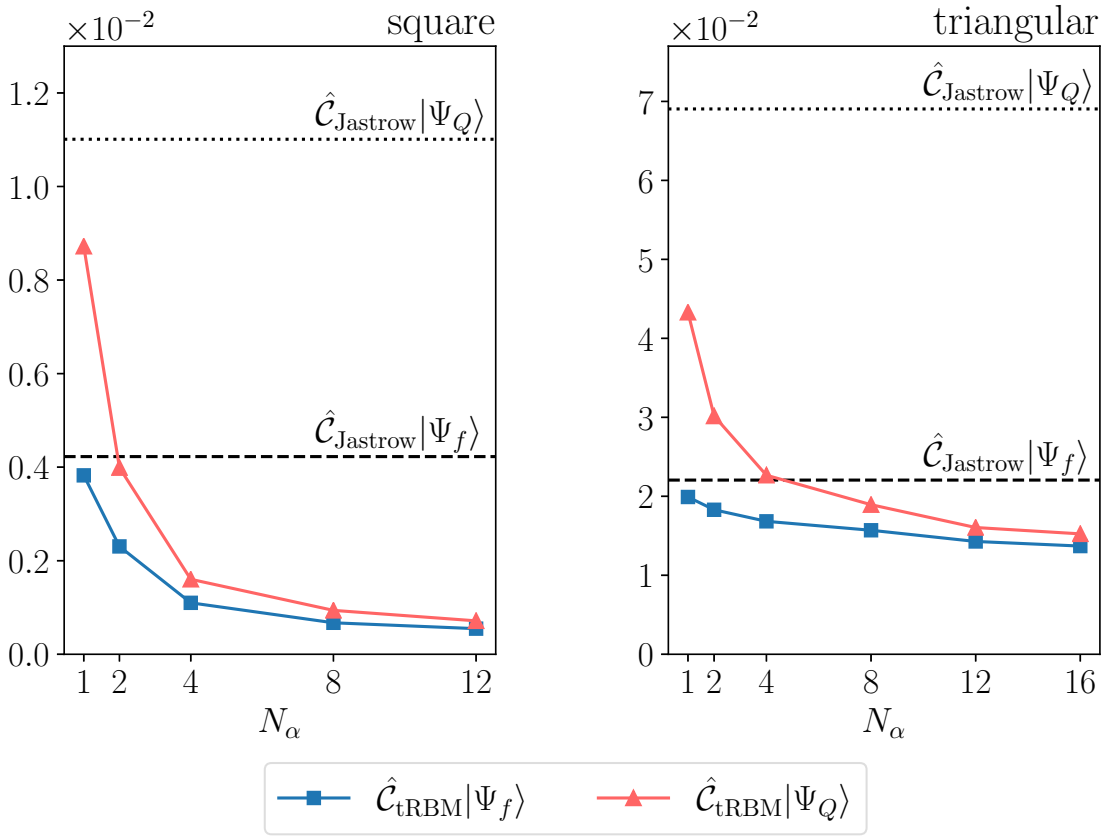

Figure 5.10: Relative error of the VMC energies ΔE [see Eq. (5.7)] with respect to the exact ones for the Heisenberg model on the 6×6 square (left) and triangular (right) lattices. The blue squares (pink triangles) correspond to the relative error of the wave function obtained by applying a translationally invariant RBM correlator to $|\Psi_f\rangle$ ($|\Psi_Q\rangle$), as a function of the number of hidden units N_α. The error bars are smaller than the size of the dots. The dashed lines represent the relative error of the Jastrow-fermionic wave function $\hat{\mathcal{C}}_{\text{Jastrow}}|\Psi_f\rangle$, while the dotted ones correspond to $\hat{\mathcal{C}}_{\text{Jastrow}}|\Psi_Q\rangle$.

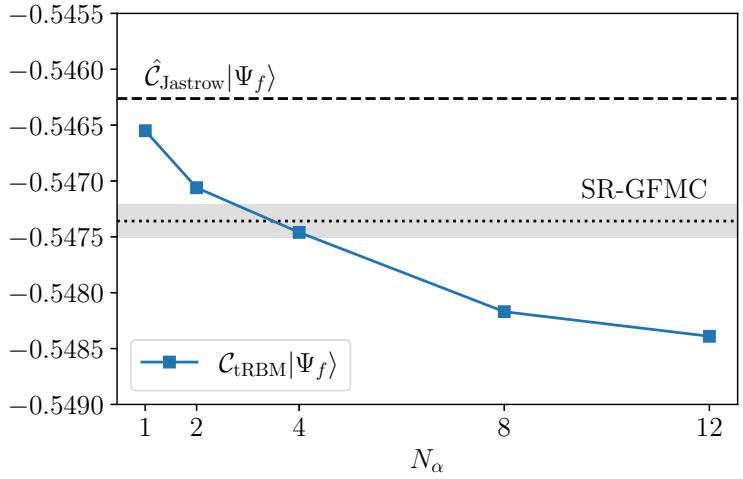

Figure 5.11: VMC energies for the Heisenberg model on the 12×12 triangular lattice. The variational energies of the RBM-fermionic wave function are plotted as a function of the number of hidden units (blue squares). The error bars are smaller than the size of the dots. The dashed line indicates the energy of the Jastrow-fermionic wave function of reference. The dotted line corresponds to the Green's function Monte Carlo result of Ref. [25], whose error bar is represented by the grey shaded area.

state. Since magnetically ordered states are pervasive in frustrated magnetism, it remains an important issue to unequivocally establish whether the origin of the high accuracy of the results for the Heisenberg model on the square lattice is only due to the absence of frustration or to the fact that the sign structure is exactly known in the unfrustrated case.

6

Conclusions

In this thesis, we employed a variational Monte Carlo approach to tackle ground state and dynamical properties of frustrated spin models. Our variational scheme is based on Gutzwiller-projected fermionic wave functions, which are supplemented by the addition of a spin-spin Jastrow factor or a neural network correlator.

6.1 Dynamical variational Monte Carlo

In Chapter 3, we discussed how the dynamical structure factor of spin models can be computed with a variational Monte Carlo technique. This spectral function yields valuable information on the nature of the elementary excitations of magnetic systems. Most importantly, the dynamical structure factor is directly related to the results of inelastic neutron scattering experiments, which constitute the method of choice for the detection of exotic phases of matter in frustrated magnets, e.g. the spin liquid phase.

Within the variational technique applied in this thesis, the dynamical structure factor is evaluated by constructing a set of approximate excited states for the spin model under investigation. Specifically, the low-energy part of the spectrum is described in terms of projected particle-hole excitations on top of the optimal fermionic ground state [104]. All the quantities that define the dynamical structure factor can be computed within a variational Monte Carlo scheme, thus avoiding any sign problem and the need for analytic continuation. Our dynamical spectra turned out to agree quite well with previous results from DMRG and quantum Monte Carlo calculations. This leads us to believe that our variational approach can provide reliable estimates of the dynamical structure factor of frustrated models for which there are no numerical results available in the literature.

To benchmark the accuracy of the variational Monte Carlo approach, we computed the dynamical structure factor of the one-dimensional $J_1 - J_2$ Heisenberg model (Section 4.1) [107], and compared the results for a small chain of 30 sites with the data from Lanczos diagonalizations. The variational spectra display an excellent accuracy both in the gapless and in the gapped phase of the model, and the most relevant excitations of the system are well reproduced by the approximate wave functions. Furthermore, calculations on a large cluster showed how the spectral features evolve when increasing the frustrating ratio, with the appearance of incommensurate structures for large values of J_2/J_1.

After having assessed its accuracy, we applied the dynamical variational method to two-dimensional spin systems, beginning with the antiferromagnetic $J_1 - J_2$ Heisenberg model on the square lattice (Section 4.2) [61]. We computed the dynamical structure factor for a relatively large cluster, tracking the spectral changes across the phase transition between the Néel ordered phase and a gapless Z_2 spin liquid. In the unfrustrated regime ($J_2 = 0$), the variational results correctly reproduce the magnon dispersion, including the anomalous roton mode at $q = (\pi, 0)$ and $q = (0, \pi)$ which had been previously detected by inelastic neutron scattering experiments [47] and numerical calculations [56, 60, 62, 63]. On the other hand, multimagnon features are not fully captured by our variational spectra and

only a weak signal is observed above the magnon branch. When increasing the frustrating ratio J_2/J_1, we observe a further softening of the magnon excitation at $q = (\pi, 0)$ and $q = (0, \pi)$, together with the appearance of a broad continuum of states, which suggests the possible coexistence of magnons and nearly-deconfined spinons. In the spin liquid phase, the spectrum is characterized by a diffuse signal, with gapless excitations at $q = (0, 0)$, $q = (\pi, 0)$, $q = (0, \pi)$, $q = (\pi, \pi)$, which can be traced back to the four Dirac points at $q = \left(\pm\frac{\pi}{2}, \pm\frac{\pi}{2}\right)$ and $q = \left(\pm\frac{\pi}{2}, \mp\frac{\pi}{2}\right)$ of the single-particle spectrum of the unprojected fermionic *Ansatz*.

Then, in Section 4.3 we presented variational estimates of the dynamical structure factor of the $J_1 - J_2$ Heisenberg model on the triangular lattice. At $J_2 = 0$, where 120° magnetic order develops, the variational spectrum confirms large deviations of the magnon dispersion from linear spin-wave results. In addition to the strong downward renormalization of the magnon branch, we detect the concomitant appearance of roton modes at the M and Y_1 points of the Brillouin zone, which are compatible with the outcome of inelastic neutron scattering experiments. In agreement with recent DMRG calculations [69], the presence of the roton mode at Y_1 is interpreted as a signature of avoided magnon decay (in contrast to semiclassical predictions [49, 64]). Adding a second-neighbor coupling J_2, we drove the system across a phase transition to a gapless spin liquid. By increasing the frustrating ratio J_2/J_1, we observe a clear softening of the spectrum around the M points, similarly to what happens in the square lattice case. However, on the triangular lattice the low-energy physics of the spin liquid phase cannot be fully described by the unprojected spinon picture. Indeed, besides the gapless excitations at M and M', which are related to the Dirac points of the fermionic bands, the variational spectra exhibit anomalous low-energy states appearing around the K points. These excitations may be connected to the effect of emergent gauge fields, or simply indicate the formation of a bound state of spinons.

In summary, the dynamical variational method employed in this thesis proved to be an efficient numerical technique to assess spectral properties of frustrated spin models, both within magnetically ordered phases, characterized by conventional magnon excitations, and within more exotic ones, in which deconfined spinons may appear. This fact suggests that Gutzwiller-projected fermionic wave functions not only can accurately reproduce the ground-state properties of frustrated spin models, but also constitute a good framework to generate low-energy excitations.

For what concerns future extensions of the present work, the dynamical variational scheme employed here could be generalized to tackle spin Hamiltonians with bond-directional interactions. These models describe the physics of the so-called Kitaev materials [34, 35], which are characterized by strong spin-orbit coupling effects [36]. Inspired by the exact solution of the Kitaev model [32], the competition of bond-anisotropic couplings is regarded as an alternative method to induce frustration and stabilize a spin liquid phase. Due to the broken spin $SU(2)$ symmetry, a comprehensive variational study of these systems involves the use of Pfaffian wave functions [86]. Moreover, in order to compute the quantities needed for the evaluation of the dynamical structure factor, a more general scheme for the Monte Carlo sampling is required [104]. An interesting question to address is whether Gutzwiller-projected states can reproduce the dynamical spectra of Kitaev-like models, which are strongly affected by the presence of vison excitations [82].

6.2 Neural Gutzwiller-projected wave functions

In Chapter 5, we explored the possibility of systematically improving the accuracy of Gutzwiller-projected fermionic wave functions by the application of a neural network correlator, namely a complex-valued restricted Boltzmann machine (RBM) [159]. We evaluated the accuracy of the RBM-fermionic *Ansatz* by studying different spin models, mainly focusing our attention on the $J_1 - J_2$ model on the square lattice.

In agreement with other results based upon neural networks alone [159, 175], our calculations showed that RBM-fermionic *Ansätze* are very effective for the unfrustrated square lattice Heisenberg model ($J_2 = 0$), where the knowledge of the exact sign structure of the ground state allowed us to use a real-valued RBM. Here, a few hidden units in the neural network are sufficient to reach a striking accuracy. Moreover, we emphasize the remarkable ability of the RBM correlator to systematically recover the spin $SU(2)$ symmetry upon increasing the number of hidden units, as inferred by looking at spin-spin correlations. On the contrary, in the highly frustrated regime ($J_2/J_1 = 0.5$), where the exact ground state sign is not known *a priori*, the addition of the RBM correlator to a Gutzwiller-projected spin liquid wave function provides a considerably smaller energy gain. Here, at variance with the unfrustrated limit, the broken $SU(2)$ symmetry is hardly recovered when increasing the number of hidden units: the S^z correlations are clearly more accurate than the S^{xy} ones, highlighting the "asymmetry" of the RBM correlator, which is defined in terms of the z-component of the local spin.

We also investigated the accuracy of the RBM-fermionic state for the triangular lattice Heisenberg model, whose ground state is magnetically ordered, but possesses a nontrivial sign structure. Although the RBM correlator provides a substantial energy gain with respect to the original parton wave function, the variational procedure does not yield the same accuracy as in the square lattice Heisenberg model, even for a relatively large number of hidden units.

We surmise that the application of neural network variational states to frustrated spin systems requires an extensive investigation of the intricate relation between the representation power of neural networks to capture highly-entangled states of matter, and the complexity of the optimization landscape of the problem induced by frustration. The disentangling of these factors could be approached through a clustering analysis of the trained RBM parameters and their associated spin-spin correlation functions.

Finally, different directions can be pursued to improve the accuracy of the RBM-fermionic *Ansätze* studied in this thesis. On the one hand, deep neural network architectures may be employed instead of the RBM, e.g. convolutional [175] or feed-forward [169] neural networks. On the other hand, the recent proposal to generalize the RBM to fulfill the $SU(2)$ symmetry [177] may pave the way for the definition of fully symmetric neural-network wave functions.

Acknowledgements

First of all, I want to thank Federico for having guided me all along my PhD years. I am truly grateful for his precious (and patient) help, his every-day (sometimes every-hour) support, and his capability of providing simple and enlightening explanations and advices. Most of the physics I learnt during my four years at SISSA is due to him.

Special thanks go to Sandro Sorella for his kind availability to discuss, his technical support and for having given me access to his computational resources. I want to thank also Alberto Parola for our collaboration, made of stimulating discussions and exchange of ideas (and numerical data). I am also thankful to Samuel Bieri, for his explanations on different aspects of the projective symmetry group approach. His notes have been fundamental for the preparation of Chapter 2 of this thesis.

A special thank goes to Juan Carrasquilla, for having given me the great opportunity of spending two months at the Vector Institute for Artificial Intelligence in Toronto, to work with him on neural network quantum states. I am grateful to Juan for his supervision, made of friendly help and encouragement, and invaluable ideas. In addition, I also acknowledge the kind hospitality and financial support of the Vector Institute.

I want to thank also my colleagues and friends for making my time in Trieste unforgettable. After four years spent here, I won't be able to leave this town without a lump in my throat. Special thanks go to my office mates, Jacopo, Juraj and Luca, for useful and useless discussions, and to Milo (i.e. Paolo), our "CM student in-law". I'd like to thank also all SISSA people with whom I spent a wonderful time here in Trieste.

Finally, I thank my family, for always supporting me. And Giulia, for everything.

List of publications

Most of the results presented in this thesis are adapted from the following publications:

- F. Ferrari, A. Parola, S. Sorella, and F. Becca, *Dynamical structure factor of the J_1-J_2 Heisenberg model in one dimension: The variational Monte Carlo approach*, Phys. Rev. B **97**, 235103 (2018).
- F. Ferrari and F. Becca, *Spectral signatures of fractionalization in the frustrated Heisenberg model on the square lattice*, Phys. Rev. B **98**, 100405(R) (2018).
- F. Ferrari and F. Becca, *Dynamical Structure Factor of the J_1-J_2 Heisenberg Model on the Triangular Lattice: Magnons, Spinons, and Gauge Fields*, Phys. Rev. X **9**, 031026 (2019).
- F. Ferrari, F. Becca, and J. Carrasquilla, *Neural Gutzwiller-projected variational wave functions*, Phys. Rev. B **100**, 125131 (2019).

My PhD work led also to the following publication, whose results have not been reported in this thesis:

- F. Ferrari, S. Bieri, and F. Becca, *Competition between spin liquids and valence-bond order in the frustrated spin-$\frac{1}{2}$ Heisenberg model on the honeycomb lattice*, Phys. Rev. B **96**, 104401 (2017).

A

Generic mean field Hamiltonian

In this appendix we provide explicit formulae for the mean field Hamiltonian of Eqs. (2.9-2.12), which we report here for the sake of clarity:

$$H_{\mathrm{MF}} = H_0 + H_x + H_y + H_z \tag{A.1}$$

$$H_0 = \frac{1}{2}\sum_{i,j} \mathrm{Tr}\left[\Psi_i^\dagger u_{i,j}^0 \Psi_j\right], \tag{A.2}$$

$$H_x = \frac{1}{2}\sum_{i,j} \mathrm{Tr}\left[\sigma_x \Psi_i^\dagger u_{i,j}^x \Psi_j\right], \tag{A.3}$$

$$H_y = \frac{1}{2}\sum_{i,j} \mathrm{Tr}\left[\sigma_y \Psi_i^\dagger u_{i,j}^y \Psi_j\right], \tag{A.4}$$

$$H_z = \frac{1}{2}\sum_{i,j} \mathrm{Tr}\left[\sigma_z \Psi_i^\dagger u_{i,j}^z \Psi_j\right]. \tag{A.5}$$

The complex-valued matrices $u_{i,j}^a$ entering the above expression are conveniently written in the following form[90]:

$$u_{i,j}^0 = i\alpha_{i,j}^{0,0}\mathbb{1} + \left(\alpha_{i,j}^{0,1}\sigma_1 + \alpha_{i,j}^{0,2}\sigma_2 + \alpha_{i,j}^{0,3}\sigma_3\right), \tag{A.6}$$

$$u_{i,j}^x = \alpha_{i,j}^{x,0}\mathbb{1} + i\left(\alpha_{i,j}^{x,1}\sigma_1 + \alpha_{i,j}^{x,2}\sigma_2 + \alpha_{i,j}^{x,3}\sigma_3\right), \tag{A.7}$$

$$u_{i,j}^y = \alpha_{i,j}^{y,0}\mathbb{1} + i\left(\alpha_{i,j}^{y,1}\sigma_1 + \alpha_{i,j}^{y,2}\sigma_2 + \alpha_{i,j}^{y,3}\sigma_3\right), \tag{A.8}$$

$$u_{i,j}^z = \alpha_{i,j}^{z,0}\mathbb{1} + i\left(\alpha_{i,j}^{z,1}\sigma_1 + \alpha_{i,j}^{z,2}\sigma_2 + \alpha_{i,j}^{z,3}\sigma_3\right), \tag{A.9}$$

where $\alpha_{i,j}^{a,b}$ ($a = 0, x, y, z$ and $b = 0, 1, 2, 3$) are 16 real-valued parameters which completely determine the mean field couplings for the bond i, j. The condition for Hermiticity, $u_{j,i}^a = [u_{i,j}^a]^\dagger$, immediately implies that

$$\alpha_{j,i}^{0,0} = -\alpha_{i,j}^{0,0}, \qquad \alpha_{j,i}^{0,b} = \alpha_{i,j}^{0,b} \quad (\text{for } b = 1, 2, 3); \tag{A.10}$$

$$\alpha_{j,i}^{a,0} = \alpha_{i,j}^{a,0}, \qquad \alpha_{j,i}^{a,b} = -\alpha_{i,j}^{a,b} \quad (\text{for } a = x, y, z \text{ and } b = 1, 2, 3). \tag{A.11}$$

In the following, we explicitly write down the full form of the various terms composing the mean field Hamiltonian.

We begin by considering the so-called singlet Hamiltonian:

$$\begin{aligned} H_0 = \frac{1}{2}\sum_{i,j} & i\alpha_{i,j}^{0,0}\left(c_{i,\uparrow}^\dagger c_{j,\uparrow} + c_{i,\downarrow}^\dagger c_{j,\downarrow} - c_{j,\uparrow}^\dagger c_{i,\uparrow} - c_{j,\downarrow}^\dagger c_{i,\downarrow}\right) \\ & + \alpha_{i,j}^{0,1}\left(c_{i,\downarrow} c_{j,\uparrow} + c_{i,\uparrow}^\dagger c_{j,\downarrow}^\dagger + c_{j,\downarrow} c_{i,\uparrow} + c_{j,\uparrow}^\dagger c_{i,\downarrow}^\dagger\right) \\ & + i\alpha_{i,j}^{0,2}\left(c_{i,\downarrow} c_{j,\uparrow} - c_{i,\uparrow}^\dagger c_{j,\downarrow}^\dagger + c_{j,\downarrow} c_{i,\uparrow} - c_{j,\uparrow}^\dagger c_{i,\downarrow}^\dagger\right) \\ & + \alpha_{i,j}^{0,3}\left(c_{i,\uparrow}^\dagger c_{j,\uparrow} + c_{i,\downarrow}^\dagger c_{j,\downarrow} + c_{j,\uparrow}^\dagger c_{i,\uparrow} + c_{j,\downarrow}^\dagger c_{i,\downarrow}\right), \end{aligned} \tag{A.12}$$

which contains singlet hopping terms, having the same coupling constant for ↑ and ↓ spins ($c^\dagger_{i,\uparrow}c_{j,\uparrow} + c^\dagger_{i,\downarrow}c_{j,\downarrow}$), and singlet pairing terms of the form $c^\dagger_{i,\uparrow}c^\dagger_{j,\downarrow} + c^\dagger_{j,\uparrow}c^\dagger_{i,\downarrow}$ (symmetric under the exchange of sites $i \leftrightarrow j$). H_0 is the only contribution which is invariant under any global spin $SU(2)$ rotation, while the remaining three terms, named triplet Hamiltonians, mix with each other under rotations. The H_z part is the $S_z = 0$ triplet term

$$\begin{aligned} H_z = \frac{1}{2}\sum_{i,j} & \alpha^{z,0}_{i,j}\left(c^\dagger_{i,\uparrow}c_{j,\uparrow} - c^\dagger_{i,\downarrow}c_{j,\downarrow} + c^\dagger_{j,\uparrow}c_{i,\uparrow} - c^\dagger_{j,\downarrow}c_{i,\downarrow}\right) \\ & + i\alpha^{z,1}_{i,j}\left(c_{i,\downarrow}c_{j,\uparrow} + c^\dagger_{i,\uparrow}c^\dagger_{j,\downarrow} - c_{j,\downarrow}c_{i,\uparrow} - c^\dagger_{j,\uparrow}c^\dagger_{i,\downarrow}\right) \\ & + \alpha^{z,2}_{i,j}\left(-c_{i,\downarrow}c_{j,\uparrow} + c^\dagger_{i,\uparrow}c^\dagger_{j,\downarrow} + c_{j,\downarrow}c_{i,\uparrow} - c^\dagger_{j,\uparrow}c^\dagger_{i,\downarrow}\right) \\ & + i\alpha^{z,3}_{i,j}\left(c^\dagger_{i,\uparrow}c_{j,\uparrow} - c^\dagger_{i,\downarrow}c_{j,\downarrow} - c^\dagger_{j,\uparrow}c_{i,\uparrow} + c^\dagger_{j,\downarrow}c_{i,\downarrow}\right), \end{aligned} \tag{A.13}$$

which contains a triplet hopping with opposite signs for ↑ and ↓ spins ($c^\dagger_{i,\uparrow}c_{j,\uparrow} - c^\dagger_{i,\downarrow}c_{j,\downarrow}$) and a triplet pairing which is antisymmetric under the exchange of sites $i \leftrightarrow j$ ($c^\dagger_{i,\uparrow}c^\dagger_{j,\downarrow} - c^\dagger_{j,\uparrow}c^\dagger_{i,\downarrow}$). Finally, the H_x and H_y Hamiltonians contain $S_z = \pm 1$ terms, such as spin flipping hoppings ($c^\dagger_{i,\downarrow}c_{j,\uparrow},\ c^\dagger_{i,\uparrow}c_{j,\downarrow}$) and pairings with parallel spin ($c^\dagger_{i,\uparrow}c^\dagger_{j,\uparrow},\ c^\dagger_{i,\downarrow}c^\dagger_{j,\downarrow}$):

$$\begin{aligned} H_x = \frac{1}{2}\sum_{i,j} & \alpha^{x,0}_{i,j}\left(c^\dagger_{i,\downarrow}c_{j,\uparrow} + c^\dagger_{i,\uparrow}c_{j,\downarrow} + c^\dagger_{j,\downarrow}c_{i,\uparrow} + c^\dagger_{j,\uparrow}c_{i,\downarrow}\right) \\ & + i\alpha^{x,1}_{i,j}\left(c_{i,\downarrow}c_{j,\downarrow} + c^\dagger_{i,\downarrow}c^\dagger_{j,\downarrow} + c_{j,\uparrow}c_{i,\uparrow} + c^\dagger_{j,\uparrow}c^\dagger_{i,\uparrow}\right) \\ & + \alpha^{x,2}_{i,j}\left(-c_{i,\downarrow}c_{j,\downarrow} + c^\dagger_{i,\downarrow}c^\dagger_{j,\downarrow} - c_{j,\uparrow}c_{i,\uparrow} + c^\dagger_{j,\uparrow}c^\dagger_{i,\uparrow}\right) \\ & + i\alpha^{x,3}_{i,j}\left(c^\dagger_{i,\downarrow}c_{j,\uparrow} + c^\dagger_{i,\uparrow}c_{j,\downarrow} - c^\dagger_{j,\downarrow}c_{i,\uparrow} - c^\dagger_{j,\uparrow}c_{i,\downarrow}\right), \end{aligned} \tag{A.14}$$

$$\begin{aligned} H_y = \frac{1}{2}\sum_{i,j} & i\alpha^{y,0}_{i,j}\left(-c^\dagger_{i,\downarrow}c_{j,\uparrow} + c^\dagger_{i,\uparrow}c_{j,\downarrow} - c^\dagger_{j,\downarrow}c_{i,\uparrow} + c^\dagger_{j,\uparrow}c_{i,\downarrow}\right) \\ & + \alpha^{y,1}_{i,j}\left(-c_{i,\downarrow}c_{j,\downarrow} + c^\dagger_{i,\downarrow}c^\dagger_{j,\downarrow} + c_{j,\uparrow}c_{i,\uparrow} - c^\dagger_{j,\uparrow}c^\dagger_{i,\uparrow}\right) \\ & + i\alpha^{y,2}_{i,j}\left(-c_{i,\downarrow}c_{j,\downarrow} - c^\dagger_{i,\downarrow}c^\dagger_{j,\downarrow} + c_{j,\uparrow}c_{i,\uparrow} + c^\dagger_{j,\uparrow}c^\dagger_{i,\uparrow}\right) \\ & + \alpha^{y,3}_{i,j}\left(c^\dagger_{i,\downarrow}c_{j,\uparrow} - c^\dagger_{i,\uparrow}c_{j,\downarrow} - c^\dagger_{j,\downarrow}c_{i,\uparrow} + c^\dagger_{j,\uparrow}c_{i,\downarrow}\right). \end{aligned} \tag{A.15}$$

B

Gauge transformation on a single site

In Section 2.2 we have discussed the $SU(2)$ gauge structure of the Abrikosov fermion representation of spins. In this appendix, we want to observe how the various fermionic configurations change under the effect of a gauge transformation. Let us consider a single-site system, whose Hilbert space contains four configurations:

$$|0\rangle, \qquad |\uparrow\rangle = c_\uparrow^\dagger|0\rangle, \qquad |\downarrow\rangle = c_\downarrow^\dagger|0\rangle, \qquad |\uparrow\downarrow\rangle = c_\uparrow^\dagger c_\downarrow^\dagger|0\rangle. \tag{B.1}$$

Here, $|0\rangle$ is the vacuum of the Abrikosov fermions. In general, a gauge transformation is defined by a 2×2 $SU(2)$ matrix of the form

$$G^\dagger = \begin{pmatrix} A & B \\ -B^* & A^* \end{pmatrix} \quad \text{with } |A|^2 + |B|^2 = 1. \tag{B.2}$$

Under the effect of G, the fermionic operators transform according to Eq. (2.6), namely

$$\tilde\Psi = G^\dagger \Psi \;\Rightarrow\; \begin{cases} \tilde c_\uparrow = A c_\uparrow + B c_\downarrow^\dagger \\ \tilde c_\downarrow = A c_\downarrow - B c_\uparrow^\dagger \end{cases} \tag{B.3}$$

Here, the tilde symbol indicates the fermionic operators (and the configurations) after the gauge transformation. We want to determine the vacuum of the $\tilde c$-fermions, which can be generally expressed as a linear combination of the configurations of Eq. (B.1),

$$|\tilde 0\rangle = \alpha|0\rangle + \beta|\uparrow\rangle + \gamma|\downarrow\rangle + \delta|\uparrow\downarrow\rangle \qquad (\text{with } \alpha,\beta,\gamma,\delta\in\mathbb{C}). \tag{B.4}$$

By definition, $|\tilde 0\rangle$ is annihilated by $\tilde c_\uparrow$ and $\tilde c_\downarrow$. This yields the following constraints

$$\begin{aligned} \tilde c_\uparrow|\tilde 0\rangle = 0 \;\Rightarrow\; & \left(A c_\uparrow + B c_\downarrow^\dagger\right)\left(\alpha + \beta c_\uparrow^\dagger + \gamma c_\downarrow^\dagger + \delta c_\uparrow^\dagger c_\downarrow^\dagger\right)|0\rangle \\ & = \left(A\beta c_\uparrow c_\uparrow^\dagger + A\delta c_\uparrow c_\uparrow^\dagger c_\downarrow^\dagger + B\alpha c_\downarrow^\dagger + B\beta c_\downarrow^\dagger c_\uparrow^\dagger\right)|0\rangle \\ & = A\beta|0\rangle + (A\delta + B\alpha)|\downarrow\rangle - B\beta|\uparrow\downarrow\rangle = 0, \end{aligned} \tag{B.5}$$

$$\begin{aligned} \tilde c_\downarrow|\tilde 0\rangle = 0 \;\Rightarrow\; & \left(A c_\downarrow - B c_\uparrow^\dagger\right)\left(\alpha + \beta c_\uparrow^\dagger + \gamma c_\downarrow^\dagger + \delta c_\uparrow^\dagger c_\downarrow^\dagger\right)|0\rangle \\ & = \left(A\gamma c_\downarrow c_\downarrow^\dagger + A\delta c_\downarrow c_\uparrow^\dagger c_\downarrow^\dagger - B\alpha c_\uparrow^\dagger - B\gamma c_\uparrow^\dagger c_\downarrow^\dagger\right)|0\rangle \\ & = A\gamma|0\rangle - (A\delta + B\alpha)|\uparrow\rangle - B\gamma|\uparrow\downarrow\rangle = 0, \end{aligned} \tag{B.6}$$

which are satisfied only if all the coefficients of the expansions are identical to zero. This implies that $\beta = \gamma = 0$ and $A\delta + B\alpha = 0$, so we can write that

$$|\tilde 0\rangle = e^{i\phi}\left(A - B c_\uparrow^\dagger c_\downarrow^\dagger\right)|0\rangle. \tag{B.7}$$

The new vacuum is normalized and defined modulo a global phase $e^{i\phi}$, which is arbitrary.

At this point, we are interested in discovering how the singly occupied configurations

transform. Indeed, $|\uparrow\rangle$ and $|\downarrow\rangle$ correspond to physical configurations of spin, and are the only ones surviving the Gutzwiller projection. We have

$$|\tilde{\uparrow}\rangle = \tilde{c}^{\dagger}_{\uparrow}|\tilde{0}\rangle = e^{i\phi}\left(A^{*}c^{\dagger}_{\uparrow} + B^{*}c_{\downarrow}\right)\left(A - Bc^{\dagger}_{\uparrow}c^{\dagger}_{\downarrow}\right)|0\rangle = e^{i\phi}\left(|A|^{2} + |B|^{2}\right)c^{\dagger}_{\uparrow}|0\rangle = e^{i\phi}|\uparrow\rangle \quad \text{(B.8)}$$

$$|\tilde{\downarrow}\rangle = \tilde{c}^{\dagger}_{\downarrow}|\tilde{0}\rangle = e^{i\phi}\left(A^{*}c^{\dagger}_{\downarrow} - B^{*}c_{\uparrow}\right)\left(A - Bc^{\dagger}_{\uparrow}c^{\dagger}_{\downarrow}\right)|0\rangle = e^{i\phi}\left(|A|^{2} + |B|^{2}\right)c^{\dagger}_{\downarrow}|0\rangle = e^{i\phi}|\downarrow\rangle \quad \text{(B.9)}$$

As expected, physical configurations of spins are invariant under gauge transformations (modulo an irrelevant global phase).

C

Product of PSG elements

In this appendix, we derive the rule of Eq. (2.31) for the product between two PSG elements, $Q_{T_2} = (G_{T_2}, T_2)$ and $Q_{T_1} = (G_{T_1}, T_1)$, by observing their consecutive actions on the auxiliary Hamiltonian

$$\mathcal{H}_0 = \frac{1}{2}\sum_{i,j} \mathrm{Tr}\left[\Psi_i^\dagger u_{i,j} \Psi_j\right] + \sum_i \mathrm{Tr}\left[\Psi_i^\dagger \lambda_i \Psi_i\right]. \tag{C.1}$$

First we apply the symmetry transformation T_2 to the fermionic operators of the matrices Ψ_i,Ψ_j and we redefine the indices of summation $(T_2(i), T_2(j) \mapsto i, j)$:

$$\mathcal{H}_0 = \frac{1}{2}\sum_{i,j} \mathrm{Tr}\left[\Psi_i^\dagger u_{T_2^{-1}(i,j)} \Psi_j\right] + \sum_i \mathrm{Tr}\left[\Psi_i^\dagger \lambda_{T_2^{-1}(i)} \Psi_i\right], \tag{C.2}$$

Then, the symmetry is complemented by the associated gauge transformation G_{T_2}:

$$\mathcal{H}_0 = \frac{1}{2}\sum_{i,j} \mathrm{Tr}\left[\Psi_i^\dagger G_{T_2}(i) u_{T_2^{-1}(i,j)} G_{T_2}^\dagger(j) \Psi_j\right] + \sum_i \mathrm{Tr}\left[\Psi_i^\dagger G_{T_2}(i) \lambda_{T_2^{-1}(i)} G_{T_2}^\dagger(i) \Psi_i\right]. \tag{C.3}$$

Now we apply the second symmetry operation T_1 to Ψ_i,Ψ_j:

$$\begin{aligned}\mathcal{H}_0 = \frac{1}{2}\sum_{i,j} &\mathrm{Tr}\left[\Psi_{T_1(i)}^\dagger G_{T_2}(i) u_{T_2^{-1}(i,j)} G_{T_2}^\dagger(j) \Psi_{T_1(j)}\right] \\ &+ \sum_i \mathrm{Tr}\left[\Psi_{T_1(i)}^\dagger G_{T_2}(i) \lambda_{T_2^{-1}(i)} G_{T_2}^\dagger(i) \Psi_{T_1(i)}\right]\end{aligned} \tag{C.4}$$

Redefining the indices of summation $(T_1(i), T_1(j) \mapsto i, j)$ we have:

$$\begin{aligned}\mathcal{H}_0 = \frac{1}{2}\sum_{i,j} &\mathrm{Tr}\left[\Psi_i^\dagger \; G_{T_2}(T_1^{-1}(i)) u_{T_2^{-1}T_1^{-1}(i,j)} G_{T_2}^\dagger(T_1^{-1}(j)) \; \Psi_j\right] \\ &+ \sum_i \mathrm{Tr}\left[\Psi_i^\dagger \; G_{T_2}(T_1^{-1}(i)) \lambda_{T_2^{-1}T_1^{-1}(i)} G_{T_2}^\dagger(T_1^{-1}(i)) \; \Psi_i\right]\end{aligned} \tag{C.5}$$

Finally we apply the gauge transformation G_{T_1}:

$$\begin{aligned}\mathcal{H}_0 = \frac{1}{2}\sum_{i,j} &\mathrm{Tr}\left[\Psi_i^\dagger \; G_{T_1}(i) G_{T_2}(T_1^{-1}(i)) u_{T_2^{-1}T_1^{-1}(i,j)} G_{T_2}^\dagger(T_1^{-1}(j)) G_{T_1}^\dagger(j) \; \Psi_j\right] \\ &+ \sum_i \mathrm{Tr}\left[\Psi_i^\dagger \; G_{T_1}(i) G_{T_2}(T_1^{-1}(i)) \lambda_{T_2^{-1}T_1^{-1}(i)} G_{T_2}^\dagger(T_1^{-1}(i)) G_{T_1}^\dagger(i) \; \Psi_i\right]\end{aligned} \tag{C.6}$$

From the above formula, we can read out the rules for products

$$Q_{T_1} Q_{T_2}(u_{i,j}) = G_{T_1}(i) G_{T_2}(T_1^{-1}(i)) u_{T_2^{-1}T_1^{-1}(i,j)} G_{T_2}^\dagger(T_1^{-1}(j)) G_{T_1}^\dagger(j) \tag{C.7}$$

$$Q_{T_1} Q_{T_2}(\lambda_i) = G_{T_1}(i) G_{T_2}(T_1^{-1}(i)) \lambda_{T_2^{-1}T_1^{-1}(i)} G_{T_2}^\dagger(T_1^{-1}(i)) G_{T_1}^\dagger(i) \tag{C.8}$$

Following the notation of Ref. [89], the product rule is written in a more compact form in terms of PSG elements:

$$Q_{T_1} Q_{T_2} = (G_{T_1}, T_1)(G_{T_2}, T_2) = (G_{T_1} T_1 G_{T_2} T_1^{-1}, T_1 T_2) \tag{C.9}$$

where $T_1 G_{T_2} T_1^{-1} = T_1 \left[\otimes_i G_{T_2}(i)\right] T_1^{-1} = \otimes_i G_{T_2}(T_1^{-1}(i))$.

D

Time reversal

D.1 Definition of time reversal

In quantum mechanics, time reversal is represented by an antiunitary operator Θ, which, by definition, satisfies the following properties [179]:

$$\langle \Theta\phi|\Theta\psi\rangle = \langle\psi|\phi\rangle = \langle\phi|\psi\rangle^* \qquad \Theta \text{ is antiunitary,} \tag{D.1}$$

$$\Theta\left(\alpha|\phi\rangle + \beta|\psi\rangle\right) = \alpha^*\Theta|\phi\rangle + \beta^*\Theta|\psi\rangle \qquad \Theta \text{ is antilinear.} \tag{D.2}$$

Here $|\phi\rangle$ and $|\psi\rangle$ are generic quantum states and α, β are complex coefficients. Being an antiunitary operator, time reversal can be expressed as the product of a unitary operator U and the conjugation operator $\mathcal{K}$ [179]. The definition of the latter depends on the choice of a given basis set $\{|\phi_n\rangle\}$, whose elements are invariant under the action of $\mathcal{K}$, i.e. $\mathcal{K}|\phi_n\rangle = |\phi_n\rangle$. Then, the effect of $\mathcal{K}$ on a generic wave function $|\psi\rangle$ can be understood by expanding the state over the elements of the basis set $\{|\phi_n\rangle\}$. If we denote by $\alpha_n = \langle\phi_n|\psi\rangle$ the various expansion coefficients, we can write

$$\mathcal{K}|\psi\rangle = \mathcal{K}\left(\sum_n \alpha_n|\phi_n\rangle\right) = \sum_n \alpha_n^*|\phi_n\rangle. \tag{D.3}$$

From this equation, we can also conclude that $\mathcal{K}^2 = 1$ and $\mathcal{K}^{-1} = \mathcal{K}$. However, one must be careful when a change of basis is performed, because $\mathcal{K}$ and U needs to be changed accordingly in order to keep a consistent definition of the time reversal operator $\Theta = U\mathcal{K}$ [179].

For our purposes, which are connected to the Abrikosov representation of spins, we select a single-particle basis set of fermionic orbitals specified by a lattice position and a spin orientation (along S_z), i.e. $|i,\sigma\rangle$, which remain unchanged under the effect of $\mathcal{K}$. Within a second quantization formalism, this means that

$$|i,\sigma\rangle = \mathcal{K}|i,\sigma\rangle \implies c^\dagger_{i,\sigma}|0\rangle = \mathcal{K}c^\dagger_{i,\sigma}|0\rangle = \mathcal{K}c^\dagger_{i,\sigma}\mathcal{K}^{-1}\mathcal{K}|0\rangle. \tag{D.4}$$

Assuming that $\mathcal{K}|0\rangle = |0\rangle$ (and using $\mathcal{K}^{-1} = \mathcal{K}$), we conclude that $c^\dagger_{i,\sigma} = \mathcal{K}c^\dagger_{i,\sigma}\mathcal{K}$, i.e. the conjugation operator does not affect the fermionic creators. As a consequence, a generic one-body operator O transforms as follows:

$$\mathcal{K}O\mathcal{K} = \mathcal{K}\left(\sum_{i,j}\sum_{\alpha,\beta} c^\dagger_{i,\alpha}O^{\alpha,\beta}_{i,j}c_{j,\beta}\right)\mathcal{K} = \sum_{i,j}\sum_{\alpha,\beta} c^\dagger_{i,\alpha}\left(O^{\alpha,\beta}_{i,j}\right)^* c_{j,\beta}, \tag{D.5}$$

where $O^{\alpha,\beta}_{i,j} = \langle i,\alpha|O|j,\beta\rangle$. Therefore, if we apply the conjugation operator to the Hamiltonian $\mathcal{H}_0$, only the coefficients of the *Ansatz*, namely the entries of $u_{i,j}$ and λ_i, are affected.

Once the action of $\mathcal{K}$ is set, the definition of the time reversal operator requires the introduction of an appropriate unitary transformation U which, acting in the space of

the 2×2 matrices Ψ_j [cf. Eq. (2.4)], reverses all spins ($\mathbf{S}_j \mapsto -\mathbf{S}_j$). This is achieved by choosing [89]

$$\Theta : \Psi_j \mapsto \mathcal{K}\Psi_j(i\sigma_y). \tag{D.6}$$

Indeed, using the definition (2.2), we can prove that:

$$\begin{aligned}\Theta : S_j^a = -\frac{1}{4}\,\mathrm{Tr}\left[\Psi_j \sigma_a^* \Psi_j^\dagger\right] \mapsto & -\frac{1}{4}\,\mathrm{Tr}\left[\mathcal{K}\Psi_j(i\sigma_y)\sigma_a^*(-i\sigma_y)\Psi_j^\dagger\mathcal{K}\right] \\ &= -\frac{1}{4}\,\mathrm{Tr}\left[\Psi_j \mathcal{K}\sigma_y\sigma_a^*\sigma_y\mathcal{K}\Psi_j^\dagger\right] \\ &= \frac{1}{4}\,\mathrm{Tr}\left[\Psi_j \mathcal{K}\sigma_a\mathcal{K}\Psi_j^\dagger\right] \\ &= \frac{1}{4}\,\mathrm{Tr}\left[\Psi_j \sigma_a^*\Psi_j^\dagger\right] = -S_j^a. \end{aligned} \tag{D.7}$$

For the first equality on the right we have used the fact that $\mathcal{K}\Psi_j = \Psi_j\mathcal{K}$ (in agreement with the above definition of $\mathcal{K}$); for the second equality we have exploited the property $\sigma_y\sigma_a^*\sigma_y = -\sigma_a$; and for the third equality we have applied the conjugation operator to the Pauli matrix, i.e. $\mathcal{K}\sigma_a\mathcal{K} = \sigma_a^*$.

D.2 A more convenient definition of time reversal

Following the intuition of Wen [85], within the context of PSG it is convenient to redefine the time reversal transformation, supplementing it with a global gauge transformation $W = -i\sigma_y$:

$$\Theta : \Psi_j \mapsto W^\dagger\mathcal{K}\Psi_j(i\sigma_y) = (i\sigma_y)\mathcal{K}\Psi_j(i\sigma_y) = -\mathcal{K}\sigma_y\Psi_j\sigma_y. \tag{D.8}$$

The above definition[1] does not change the effect of Θ in the physical space of spins. However, the "new" time reversal operator has the nice property of commuting with gauge transformations [89]. This can be proven by considering a generic 2×2 $SU(2)$ matrix G, which can be always expressed as a linear combination of the identity $\mathbb{1}$ and the set $i\boldsymbol{\sigma} = (i\sigma_x, i\sigma_y, i\sigma_z)$ (with real coefficients). Exploiting the properties of Pauli matrices, we observe that any gauge transformation G commutes with the operator $\mathcal{K}\sigma_y$

$$\begin{aligned}\mathcal{K}\sigma_y G &= \mathcal{K}\sigma_y(a_0\mathbb{1} + ia_x\sigma_x + ia_y\sigma_y + ia_z\sigma_z) \\ &= \mathcal{K}(a_0\mathbb{1} - ia_x\sigma_x + ia_y\sigma_y - ia_z\sigma_z)\sigma_y \\ &= (a_0\mathbb{1} + ia_x\sigma_x + ia_y\sigma_y + ia_z\sigma_z)\mathcal{K}\sigma_y = G\mathcal{K}\sigma_y. \end{aligned} \tag{D.9}$$

So, we can directly conclude that Θ commutes with all gauge transformations.

Let us apply the definition (D.8) of time reversal to $\mathcal{H}_0$, to understand how the fermionic *Ansätze* transform. For the $u_{i,j}$ terms, we have

$$\begin{aligned}\mathrm{Tr}\left[\Psi_i^\dagger u_{i,j}\Psi_j\right] \mapsto & \,\mathrm{Tr}\left[\sigma_y\Psi_i^\dagger\sigma_y\mathcal{K}u_{i,j}\mathcal{K}\sigma_y\Psi_j\sigma_y\right] \\ &= \mathrm{Tr}\left[\Psi_i^\dagger\sigma_y u_{i,j}^*\sigma_y\Psi_j\right] = -\,\mathrm{Tr}\left[\Psi_i^\dagger u_{i,j}\Psi_j\right], \end{aligned} \tag{D.10}$$

[1] With a little abuse of notation, Eq. (D.8) is sometimes written as $\Theta : \Psi_j \mapsto \mathcal{K}\Psi_j^*$, with

$$\Psi_j^* = \begin{pmatrix} c_{j,\uparrow}^\dagger & c_{j,\downarrow}^\dagger \\ c_{j,\downarrow} & -c_{j,\uparrow} \end{pmatrix}.$$

where we have exploited the cyclic property of the trace and the fact that $\sigma_y u^*_{i,j}\sigma_y = -u_{i,j}$ ($u_{i,j}$ is a linear combination, with real coefficients, of $i\mathbb{1}$ and the Pauli matrices). The case of the onsite matrix λ_i is completely analogous. Therefore, the net effect of time reversal (D.8) is to change sign to the parameters of the *Ansatz*, i.e. $\Theta : (u_{i,j}, \lambda_i) \mapsto (-u_{i,j}, -\lambda_i)$.

D.3 Product rule for time reversal PSG elements

Since time reversal is a particular symmetry, which does not act directly on the lattice positions, we have to understand if the product rule of Eq. (2.31) is still valid when the PSG elements $Q_\Theta = (G_\Theta, \Theta)$ are involved. In analogy to what is done in Appendix C, we first apply Q_Θ to the *Ansatz* defining $\mathcal{H}_0$:

$$\mathcal{H}_0 = -\frac{1}{2}\sum_{i,j} \mathrm{Tr}\left[\Psi_i^\dagger G_\Theta(i) u_{i,j} G_\Theta^\dagger(j)\Psi_j\right] - \sum_i \mathrm{Tr}\left[\Psi_i^\dagger G_\Theta(i)\lambda_i G_\Theta^\dagger(i)\Psi_i\right]. \tag{D.11}$$

Then, we apply a generic symmetry T, and we redefine the indices of summation $(T(i), T(j) \mapsto i, j)$:

$$\begin{aligned}\mathcal{H}_0 = &-\frac{1}{2}\sum_{i,j} \mathrm{Tr}\left[\Psi_i^\dagger G_\Theta(T^{-1}(i)) u_{T^{-1}(i,j)} G_\Theta^\dagger(T^{-1}(j))\Psi_j\right] \\ &- \sum_i \mathrm{Tr}\left[\Psi_i^\dagger G_\Theta(T^{-1}(i))\lambda_{T^{-1}(i)} G_\Theta^\dagger(T^{-1}(i))\Psi_i\right].\end{aligned} \tag{D.12}$$

Finally, we perform the corresponding gauge transformation G_T:

$$\begin{aligned}\mathcal{H}_0 = &-\frac{1}{2}\sum_{i,j} \mathrm{Tr}\left[\Psi_i^\dagger G_T(i) G_\Theta(T^{-1}(i)) u_{T^{-1}(i,j)} G_\Theta^\dagger(T^{-1}(j)) G_T^\dagger(j)\Psi_j\right] \\ &- \sum_i \mathrm{Tr}\left[\Psi_i^\dagger G_T(i) G_\Theta(T^{-1}(i))\lambda_{T^{-1}(i)} G_\Theta^\dagger(T^{-1}(i)) G_T^\dagger(i)\Psi_i\right],\end{aligned} \tag{D.13}$$

Thus we obtain $Q_T Q_\Theta = (G_T, T)(G_\Theta, \Theta) = (G_T T G_\Theta T^{-1}, T\Theta)$, which fits in the product rule (2.31). If we reverse the order of the two operations, we first get

$$\mathcal{H}_0 = \frac{1}{2}\sum_{i,j} \mathrm{Tr}\left[\Psi_i^\dagger G_T(i) u_{T^{-1}(i,j)} G_T^\dagger(j)\Psi_j\right] + \sum_i \mathrm{Tr}\left[\Psi_i^\dagger G_T(i)\lambda_{T^{-1}(i)} G_T^\dagger(i)\Psi_i\right]. \tag{D.14}$$

Then, we apply the time reversal operator. Exploiting the fact that $[\mathcal{K}\sigma_y, G_T] = 0$, one can readily prove that $\Theta :\ \mathcal{H}_0 \mapsto -\mathcal{H}_0$. Finally, we insert the gauge transformation G_Θ,

$$\begin{aligned}\mathcal{H}_0 = &-\frac{1}{2}\sum_{i,j} \mathrm{Tr}\left[\Psi_i^\dagger G_\Theta(i) G_T(i) u_{T^{-1}(i,j)} G_T^\dagger(j) G_\Theta^\dagger(j)\Psi_j\right] \\ &- \sum_i \mathrm{Tr}\left[\Psi_i^\dagger G_\Theta(i) G_T(i)\lambda_{T^{-1}(i)} G_T^\dagger(i) G_\Theta^\dagger(i)\Psi_i\right],\end{aligned} \tag{D.15}$$

reading out the product of PSG elements: $Q_\Theta Q_T = (G_\Theta, \Theta)(G_T, T) = (G_\Theta G_T, \Theta T)$. After a long detour, we have arrived to a formula which can be framed in the context of the product rule of Eq. (2.31), once we observe that $\Theta G_T \Theta^{-1} = G_T$, i.e. that time reversal and gauge transformations commute. Wrapping everything up, we conclude that Eq. (2.31) is valid also for the PSG elements of time reversal [thanks to the definition (D.8)].

E

Flux phase on the square lattice

E.1 The staggered flux phase

In Section 2.9, we derived the explicit form of the fermionic *Ansatz* corresponding to the PSG solution (PSG14) with $\varepsilon_T = \varepsilon_{\Theta T} = 1$ and $\varepsilon_A = \varepsilon_B = -1$. If we restrict the range of the couplings to first-neighbor, we obtain a fermionic Hamiltonian with a s-wave hopping and a $d_{x^2-y^2}$-pairing (cf. Fig. 2.4), namely

$$\begin{cases} u_{i,T_x(i)} = u_x = t\sigma_3 + \Delta\sigma_1 \\ u_{i,T_y(i)} = u_y = t\sigma_3 - \Delta\sigma_1 \end{cases} \qquad (t + \Delta_{x^2-y^2}\ \textit{Ansatz})\,. \tag{E.1}$$

As a consequence of this restriction, we are left with a $U(1)$ spin liquid. Indeed, the IGG of the $t + \Delta_{x^2-y^2}$ *Ansatz* is made of global $U(1)$ transformations, as can be proven by an analysis of the $SU(2)$ fluxes [89]. The situation in which the actual IGG of an *Ansatz* turns out to be larger than the IGG chosen for the classification is not uncommon, especially when the couplings of the Hamiltonian are restricted to a limited range.

Being the $t + \Delta_{x^2-y^2}$ *Ansatz* a $U(1)$ spin liquid, there must exist a gauge in which its Hamiltonian is expressed in terms of pure hopping. This gauge is attained by performing the following transformation

$$W(x,y) = (-)^{xy}(-)^{\frac{x(x+1)}{2}}(-)^{\frac{y(y+1)}{2}}(-i\sigma_1)^{x+y}\exp\left(-i\frac{\pi}{4}\sigma_1\right)(i\sigma_3). \tag{E.2}$$

If we denote by sublattice A (sublattice B) the set of sites $i = (x, y)$ for which $x + y$ is even (odd), after the above gauge transformation we have

$$\begin{cases} u_{i,T_x(i)} = t\sigma_3 + i\Delta\mathbb{1} \\ u_{i,T_y(i)} = t\sigma_3 - i\Delta\mathbb{1} \end{cases} \quad \text{if } i \in A,$$
$$\begin{cases} u_{i,T_x(i)} = t\sigma_3 - i\Delta\mathbb{1} \\ u_{i,T_y(i)} = t\sigma_3 + i\Delta\mathbb{1} \end{cases} \quad \text{if } i \in B. \tag{E.3}$$

A more convenient formulation of the *Ansatz* is obtained by introducing an amplitude, $\rho = \sqrt{t^2 + \Delta^2}$, and a phase, ϕ, such that $\tan(\phi/4) = \Delta/t$. Then we can write

$$\begin{cases} u_{(x,y),(x+1,y)} = \rho\sigma_3 \exp\left[i(-)^{x+y}\frac{\phi}{4}\sigma_3\right], \\ u_{(x,y),(x,y+1)} = \rho\sigma_3 \exp\left[-i(-)^{x+y}\frac{\phi}{4}\sigma_3\right]. \end{cases} \tag{E.4}$$

The resulting *Ansatz* is the so-called *staggered flux phase*, in which the plaquettes of the square lattice are threaded by alternating $\pm\phi$ fluxes[1] (see Fig. E.1).

[1] Strictly speaking, the $SU(2)$ flux of an elementary square plaquette (with base site j) is computed as $P_j = u_{j,j+x}u_{j+x,j+x+y}u_{j+x+y,j+y}u_{j+y,j} = \rho^4\exp(\pm i\phi\sigma_3)$ [89]. The sign of the exponent depends on the sublattice of j (+ for sublattice A, − for sublattice B).

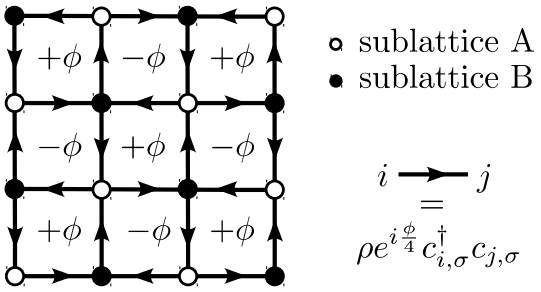

Figure E.1: The staggered flux phase on the square lattice, see Eq. (E.4).

E.2 The π-flux state

Let us consider the particular case in which $\phi = \pi$, the so-called π-flux state, which in the original gauge corresponds to the $t + \Delta_{x^2-y^2}$ *Ansatz* with $\Delta = t$:

$$\begin{cases} u_{i,T_x(i)} = t\,(\sigma_3 + \sigma_1)\,, \\ u_{i,T_y(i)} = t\,(\sigma_3 - \sigma_1)\,. \end{cases} \tag{E.5}$$

As already mentioned, the above *Ansatz* was constructed from the PSG solution (PSG14), with the specific choice $\varepsilon_T = 1$. This implies that its algebraic PSG is characterized by trivial gauge transformations for the translations, namely $Q_{T_x} = (\mathbb{1}, T_x)$ and $Q_{T_y} = (\mathbb{1}, T_y)$ ($Q_{T_x} Q_{T_y} = Q_{T_y} Q_{T_x}$). In simple terms, this spin liquid *Ansatz* is translationally invariant even before projection.

We can start from this *Ansatz* and perform the following gauge transformation:

$$\begin{cases} W(x,y) = (-)^y (i\sigma_2) W_0 & \text{if } x \text{ is even}, \\ W(x,y) = W_0 & \text{if } x \text{ is odd}, \end{cases} \tag{E.6}$$

where $W_0 = \exp\left(-i\frac{\pi}{8}\sigma_2\right)$. For the horizontal bonds we have

- even $x \Rightarrow \tilde{u}_{(x,y),(x+1,y)} = (-)^y (i\sigma_2) W_0\; t(\sigma_3 + \sigma_1)\; W_0^\dagger = (-)^y \sqrt{2} t \sigma_3$,
- odd $x \Rightarrow \tilde{u}_{(x,y),(x+1,y)} = W_0\; t(\sigma_3 + \sigma_1)\; W_0^\dagger (-)^y (-i\sigma_2) = (-)^y \sqrt{2} t \sigma_3$,

while for the vertical ones

- even $x \Rightarrow \tilde{u}_{(x,y),(x,y+1)} = (-)^y (i\sigma_2) W_0\; t(\sigma_3 - \sigma_1)\; W_0^\dagger (-)^{y+1} (-i\sigma_2) = \sqrt{2} t \sigma_3$,
- odd $x \Rightarrow \tilde{u}_{(x,y),(x,y+1)} = W_0\; t(\sigma_3 - \sigma_1)\; W_0^\dagger = \sqrt{2} t \sigma_3$.

The result is a pure hopping *Ansatz* which requires a doubled unit cell in the y direction:

$$\begin{cases} \tilde{u}_{i,T_x(i)} = (-)^y \tilde{t} \sigma_3, \\ \tilde{u}_{i,T_y(i)} = \tilde{t} \sigma_3, \end{cases} \tag{E.7}$$

where we have defined $\tilde{t} = \sqrt{2} t$ (see Fig. E.2). The above *Ansatz* $\tilde{u}$ has been obtained by gauge transforming the one of Eq. (E.5). Therefore, we can compute the PSG elements $\tilde{Q}_{T_x}$ and $\tilde{Q}_{T_y}$ by applying the same gauge transformation to the PSG elements of the original *Ansatz* [as in Eq. (2.37)]:

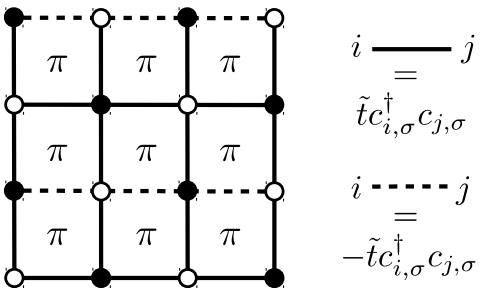

Figure E.2: The π-flux phase on the square lattice (with a 1×2 unit cell), see Eq. (E.7).

- even x
$$\begin{cases}\tilde{G}_{T_x}(x,y) = W(x,y)G_{T_x}(x,y)W^\dagger(x-1,y) = (-)^y(i\sigma_2),\\ \tilde{G}_{T_y}(x,y) = W(x,y)G_{T_y}(x,y)W^\dagger(x,y-1) = -\mathbb{1},\end{cases}$$

- odd x
$$\begin{cases}\tilde{G}_{T_x}(x,y) = W(x,y)G_{T_x}(x,y)W^\dagger(x-1,y) = (-)^y(-i\sigma_2),\\ \tilde{G}_{T_y}(x,y) = W(x,y)G_{T_y}(x,y)W^\dagger(x,y-1) = \mathbb{1}.\end{cases}$$

In conclusion, we obtain $\tilde{G}_{T_x} = (-)^{x+y}(i\sigma_2)$ and $\tilde{G}_{T_y} = (-)^{x+1}\mathbb{1}$. Even if they are no more trivial, the two PSG elements commute, as in the original gauge. This can be seen by observing that the following equations provide the same result:

$$\tilde{Q}_{T_x}\tilde{Q}_{T_y} \;\Rightarrow\; \tilde{G}_{T_x}(x,y)\tilde{G}_{T_y}(x-1,y) = (-)^{x+y}(-)^x(i\sigma_2) = (-)^y(i\sigma_2), \tag{E.8}$$
$$\tilde{Q}_{T_y}\tilde{Q}_{T_x} \;\Rightarrow\; \tilde{G}_{T_y}(x,y)\tilde{G}_{T_x}(x,y-1) = (-)^{x+1}(-)^{x+y-1}(i\sigma_2) = (-)^y(i\sigma_2). \tag{E.9}$$

However, the *Ansatz* of Eq. (E.7), which requires a doubled unit cell in the y direction, is also invariant under another pair of PSG elements, $\tilde{Q}'_{T_x}$ and $\tilde{Q}'_{T_y}$, which are defined by

$$\tilde{G}'_{T_x}(x,y) = \mathbb{1} \;\text{ and }\; \tilde{G}'_{T_y}(x,y) = (-)^x\mathbb{1}. \tag{E.10}$$

As already observed in Chapter 2, these two PSG elements anticommute, namely $\tilde{Q}'_{T_x}\tilde{Q}'_{T_y} = -\tilde{Q}'_{T_y}\tilde{Q}'_{T_x}$. At this point, we can apply the inverse of the gauge transformation (E.6) to work out the PSG elements for the original *Ansatz* (E.5) which are equivalent to the ones of Eq. (E.10):

- even x
$$\begin{cases}G'_{T_x}(x,y) = W^\dagger(x,y)\tilde{G}'_{T_x}(x,y)W(x-1,y) = (-)^y(-i\sigma_2),\\ G'_{T_y}(x,y) = W^\dagger(x,y)\tilde{G}'_{T_y}(x,y)W(x,y-1) = -\mathbb{1},\end{cases}$$

- odd x
$$\begin{cases}G'_{T_x}(x,y) = W^\dagger(x,y)\tilde{G}'_{T_x}(x,y)W(x-1,y) = (-)^y(i\sigma_2),\\ G'_{T_y}(x,y) = W^\dagger(x,y)\tilde{G}'_{T_y}(x,y)W(x,y-1) = -\mathbb{1}.\end{cases}$$

As expected, the resulting PSG elements anticommute:

$$\begin{cases}Q'_{T_x} = \left[(-)^{x+y+1}(i\sigma_2), T_x\right]\\ Q'_{T_y} = [-\mathbb{1}, T_y]\end{cases} \Rightarrow\; Q'_{T_x}Q'_{T_y} = [(-)^{x+y}(i\sigma_2), T_xT_y] = -Q'_{T_y}Q'_{T_x} \tag{E.11}$$

At first sight, the present scenario may look counterintuitive. We performed a PSG classification whose solutions can be divided into two broad classes, according to the value

of ε_T: in one class the PSG elements associated to translations commute ($\varepsilon_T = 1$), in the other class they anticommute ($\varepsilon_T = -1$), and the two classes cannot be connected by any gauge transformation[2]. Then we explicitly constructed the *Ansatz* (E.5) starting from a PSG solution with **commuting** Q_{T_x} and Q_{T_y}. However, after some calculations, we found that this *Ansatz* is invariant under another pair of PSG elements, Q'_{T_x} and Q'_{T_y}, which **anticommute**. In this example we observe a situation in which the invariant PSG of an *Ansatz* is larger than its algebraic PSG [85]. In other words, there are some elements $Q_T = (G_T, T)$ (symmetry+gauge transformation) under which the *Ansatz* of Eq. (E.5) is invariant, which do not belong to the PSG solution of the classification from which we started. In general, these extra PSG elements do not fulfill the algebraic relations with the other symmetries of the lattice.

This situation is a consequence of the restriction of the couplings of the Hamiltonian to first neighbors, which "simplifies" the *Ansatz*[3]. Indeed, one can easily prove that the second-neighbor pairing allowed by the PSG solution (cf. Section 2.9) is not invariant under the effect of Q'_{T_x}.

[2]As we have seen, gauge transformations do not affect the algebraic relations between PSG elements.

[3]Having fixed $\Delta = t$ is not relevant, since one can verify *a posteriori* that also the generic $t + \Delta_{x^2-y^2}$ *Ansatz* is invariant under the PSG elements of Eq. (E.11).

F

Dynamical variational Monte Carlo: miscellanea

F.1 Fourier transform convention

We adopt the following convention for the Fourier transforms of fermionic operators:

$$\begin{cases} c_{k,a,\sigma} = \frac{1}{\sqrt{N_C}} \sum_R e^{-ik\cdot R} c_{R,a,\sigma}, \\ c_{R,a,\sigma} = \frac{1}{\sqrt{N_C}} \sum_k e^{ik\cdot R} c_{k,a,\sigma}. \end{cases} \tag{F.1}$$

With this choice, the state $|k,a,\sigma\rangle = c^\dagger_{k,a,\sigma}|0\rangle$, which has momentum k by definition, is an eigenstate of translations $\{T_R\}$ with eigenvalues $\{\exp(-ik\cdot R)\}$:

$$\begin{aligned} T_R|k,a,\sigma\rangle &= T_R \frac{1}{\sqrt{N_C}} \sum_{R'} e^{ik\cdot R'} c_{R',a,\sigma}|0\rangle \\ &= \frac{1}{\sqrt{N_C}} \sum_{R'} e^{ik\cdot R'} c_{R'+R,a,\sigma}|0\rangle = e^{-ik\cdot R}|k,a,\sigma\rangle. \end{aligned} \tag{F.2}$$

F.2 Solution of the generalized eigenvalue problem

For the sake of simplicity, let us rewrite the generalized eigenvalue problem of Eq. (3.42) using a shorthand notation in which the label of momentum is dropped and the indices of the basis set of excitations (3.39), $(R,a;b)$, are grouped in a single label, simply denoted by R. We have:

$$|\Psi_n\rangle = \sum_R A^n_R |R\rangle \implies \sum_{R'} H_{R,R'} A^n_{R'} = E_n \sum_{R'} O_{R,R'} A^n_{R'}. \tag{F.3}$$

Due to the possible linear dependence between the excitations of the basis set $\{|R\rangle\}$, the overlap matrix can display several zero eigenvalues. Since the generalized eigenvalue problem is well-defined only for a strictly positive definite $O_{R,R'}$, we need to get rid of the aforementioned linear dependence. Therefore, as first step we diagonalize the overlap matrix:

$$\tilde{O} = \Lambda^\dagger O \Lambda \;\Leftrightarrow\; \tilde{O}_{\alpha,\beta} = \tilde{O}_\alpha \delta_{\alpha,\beta} = \sum_{R,R'} (\Lambda^\dagger)_{\alpha,R} O_{R,R'} \Lambda_{R',\beta}. \tag{F.4}$$

Here $\tilde{O}$ is diagonal and Λ is a matrix whose columns are the eigenvectors of the overlap matrix, ordered according to the magnitudes of the corresponding eigenvalues: the first N_0 columns contain the eigenvectors with zero eigenvalue, while the following $N_{>0}$ columns contain the eigenvectors corresponding to positive eigenvalues. Using the matrix Λ, we can perform a change of basis for the full problem. Employing a matrix notation, we can write:

$$HA^n = E_n O A^n \;\Rightarrow\; (\Lambda^\dagger H \Lambda)(\Lambda^\dagger A^n) = E_n (\Lambda^\dagger O \Lambda)(\Lambda^\dagger A^n) \;\Rightarrow\; \tilde{H}\tilde{A}^n = E_n \tilde{O}\tilde{A}^n. \tag{F.5}$$

We note that the tilde symbol is used to denote matrices/vectors expressed in the basis of the eigenvectors of O, whose entries are labeled by greek letters. After the above change of basis, we are left with the block matrices $\tilde{O}$ and $\tilde{H}$:

$$\tilde{O} = \begin{pmatrix} 0_{N_0 \times N_0} & 0_{N_0 \times N_{>0}} \\ 0_{N_{>0} \times N_0} & \overline{O} \end{pmatrix}, \qquad \tilde{H} = \begin{pmatrix} 0_{N_0 \times N_0} & 0_{N_0 \times N_{>0}} \\ 0_{N_{>0} \times N_0} & \overline{H} \end{pmatrix}, \tag{F.6}$$

which are all zero except for the $N_{>0} \times N_{>0}$ blocks denoted by a bar, $\overline{O}$ and $\overline{H}$. As a consequence, the eigenvalue problem can be restricted to these blocks, namely

$$\overline{H}\,\overline{A}^n = E_n \overline{O}\,\overline{A}^n. \tag{F.7}$$

The above equation is a well-defined generalized eigenvalue problem, being the matrix $\overline{O}$ positive definite by construction. We note that $\overline{A}^n$ is a vector containing the last $N_{>0}$ elements of $\tilde{A}^n$. The solutions of the restricted eigenvalue problem (F.7) are sufficient to compute the spectral weights of the dynamical structure factor. Indeed, let us take, for instance, the amplitude of Eq. (3.48), which can be rewritten in the shorthand notation defined before and expressed in the basis of eigenvectors of the overlap matrix:

$$\sum_R O_{R_0,R} A^n_R = [OA^n]_{R_0} = [(\Lambda \tilde{O} \Lambda^\dagger)(\Lambda \tilde{A}^n)]_{R_0} = (\Lambda \tilde{O} \tilde{A}^n)_{R_0}. \tag{F.8}$$

Since $\tilde{O}_{\alpha\beta} = \tilde{O}_\alpha \delta_{\alpha,\beta}$ is nonzero only for $\alpha > N_0$ (i.e., in the $\overline{O}$ block), we can write

$$(\Lambda \tilde{O} \tilde{A}^n)_{R_0} = \sum_\alpha \Lambda_{R_0,\alpha} \tilde{O}_\alpha \tilde{A}^n_\alpha = \sum_{\alpha > N_0} \Lambda_{R_0,\alpha} \tilde{O}_\alpha \tilde{A}^n_\alpha. \tag{F.9}$$

From the above formula, it is clear that the coefficients solving the restricted eigenvalue problem of Eq. (F.7), namely $\overline{A}_n$, are sufficient to determine the amplitude of Eq. (3.48). Indeed, the summation over α involves only the last $N_{>0}$ elements of $\tilde{A}^n$, which are the ones forming $\overline{A}_n$.

From the practical point of view, the overlap matrix is computed stochastically by Monte Carlo sampling and then diagonalized by numerical routines. The resulting spectrum is employed to restrict the generalized eigenvalue problem to the set of eigenstates of the overlap matrix with nonzero eigenvalues, cf. Eq. (F.7). In practice, due to machine finite precision, we discard the eigenvectors whose eigenvalues are smaller than an arbitrary cutoff (λ). One may wonder whether it could be difficult to distinguish eigenvalues which are small (and should be exactly zero) because of the linear dependence of the basis set, from the eigenvalues which are small for other reasons. Fortunately, this is not the case: the typical scenario is always quite clear, with the almost zero eigenvalues well separated from the other ones, as exemplified in Fig. F.1. So, in essentially all situations, one can safely choose to discard the eigenvalues of the overlap matrix which are smaller than $\lambda \approx 10^{-8}$.

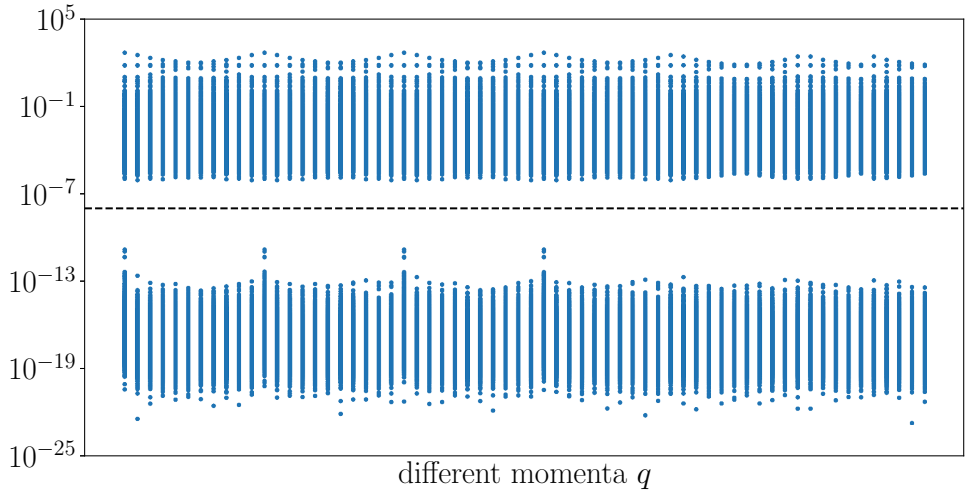

Figure F.1: Example of the distribution of the eigenvalues of the overlap matrix for different momenta q. The results are obtained for the Heisenberg model on the 22×22 square lattice (cf. Section 4.2). The dashed line corresponds to the cutoff value $\lambda = 10^{-8}$. The figure shows that the zero eigenvalues of the overlap matrix can be easily identified.

F.3 A particular case: spin liquids with a doubled unit cell

Let us consider a generic spin model on a two-dimensional lattice with one site per unit cell, whose primitive vectors are denoted by a_x and a_y. As discussed in Chapter 2, knowing the symmetries of the lattice, we can perform a full classification of the possible spin liquid phases of the model. In particular, if we restrict our analysis to Z_2 spin liquids, and we consider only translational symmetries, two classes of states emerge, as shown in the first two paragraphs of Section 2.7. The first class of solution is trivial, since it corresponds to symmetric spin liquids which are obtained by Gutzwiller-projecting the ground state wave functions of translationally invariant fermionic Hamiltonians $\mathcal{H}_0$. However, quite unexpectedly, another class of translationally invariant spin liquids is obtained by starting from fermionic Hamiltonians which break the translational symmetry along one direction (a_y, in our case). Indeed, referring to the results of Chapter 2, one can construct a fermionic Hamiltonian $\mathcal{H}_0$ that is invariant under the combined application of a translation, T_x or T_y, and the corresponding gauge transformation,

$$G_{T_x}(R) = \mathbb{1} \quad \text{or} \quad G_{T_y}(R) = (-)^{R_x}\mathbb{1}. \tag{F.10}$$

Here, $R = R_x a_x + R_y a_y$ is a lattice vector and R_x, R_y are its integer coordinates. Since the gauge transformation associated to T_x is trivial, $\mathcal{H}_0$ must be translationally invariant along a_x. On the contrary, in the a_y-direction a doubled unit cell is required by the staggered form of the gauge transformation G_{T_y}. As examples of a spin liquid states of this kind, we can mention the π-flux states on the square (cf. Appendix E.2 and Fig. E.2) and triangular (cf. Section 4.3.1 and second panel of Fig. 4.18) lattices.

Let us focus on a generic spin liquid *Ansatz* defined by a Hamiltonian $\mathcal{H}_0$ that belongs to the class of states requiring a doubled unit cell along a_y ($\varepsilon_T = -1$, cf. Section 2.7). We can denote by $\tilde{T}_x$ and $\tilde{T}_y$ the operators which result from the combination of the translations T_x and T_y with their corresponding gauge transformations (F.10):

$$\tilde{T}_x c_{R,\sigma} \tilde{T}_x^{-1} = c_{R+a_x,\sigma} \quad \text{and} \quad \tilde{T}_y c_{R,\sigma} \tilde{T}_y^{-1} = (-)^{R_x} c_{R+a_y,\sigma}. \tag{F.11}$$

The fermionic Hamiltonian under concern is invariant under the effect of $\tilde{T}_x$ and $\tilde{T}_y$, i.e. $[\tilde{T}_x, \mathcal{H}_0] = [\tilde{T}_y, \mathcal{H}_0] = 0$. On the other hand, we note that $\tilde{T}_x$ and $\tilde{T}_y$ anticommute between themselves by construction (cf. Section 2.7). Denoting the ground state of $\mathcal{H}_0$ as $|\Phi_0\rangle$, we can write:

$$\mathcal{H}_0|\Phi_0\rangle = \mathcal{E}_0|\Phi_0\rangle \implies \begin{cases} \tilde{T}_x\mathcal{H}_0|\Phi_0\rangle = \mathcal{H}_0\left(\tilde{T}_x|\Phi_0\rangle\right) = \mathcal{E}_0\left(\tilde{T}_x|\Phi_0\rangle\right), \\ \tilde{T}_y\mathcal{H}_0|\Phi_0\rangle = \mathcal{H}_0\left(\tilde{T}_y|\Phi_0\rangle\right) = \mathcal{E}_0\left(\tilde{T}_y|\Phi_0\rangle\right), \end{cases} \tag{F.12}$$

If we assume that the ground state of the system is unique[1], we can conclude that

$$\tilde{T}_x|\Phi_0\rangle = e^{-i2\pi q_x^0}|\Phi_0\rangle \quad \text{and} \quad \tilde{T}_y|\Phi_0\rangle = e^{-i2\pi q_y^0}|\Phi_0\rangle \tag{F.13}$$

Then, exploiting the fact that the application of gauge transformations before Gutzwiller projection does not change the physical wave function, we can write

$$T_a|\Psi_0\rangle = T_a\mathcal{P}_G|\Phi_0\rangle = \mathcal{P}_G T_a|\Phi_0\rangle = \mathcal{P}_G\tilde{T}_a|\Phi_0\rangle = \mathcal{P}_G e^{-i2\pi q_a^0}|\Phi_0\rangle = e^{-i2\pi q_a^0}|\Psi_0\rangle, \tag{F.14}$$

where $a = x, y$. This result shows that the Gutzwiller-projected wave function $|\Psi_0\rangle = \mathcal{P}_G|\Phi_0\rangle$ has momentum $q^0 = q_x^0 b_x + q_y^0 b_y$, where b_x and b_y are the primitive vectors of the reciprocal lattice.

Suppose we want to define a set of projected particle-hole excitations with momentum q with respect to $|\Psi_0\rangle$. In this case, the definition of Eq. (3.39) is not suitable, because the fermionic Hamiltonian $\mathcal{H}_0$ breaks the translational symmetry along a_y. However, exploiting the knowledge of the gauge transformations (F.10), we can introduce a generalized version of the projector of Eq. (3.35), replacing the bare translations, T_x and T_y, with $\tilde{T}_x$ and $\tilde{T}_y$:

$$\tilde{\mathcal{L}}_q = \frac{1}{\sqrt{N_C}} \sum_{R'} e^{iq\cdot R'} (\tilde{T}_x)^{R'_x} (\tilde{T}_y)^{R'_y}. \tag{F.15}$$

Here, $R'_x = R' \cdot a_x$ and $R'_y = R' \cdot a_y$ are integer numbers. Then, following the same ideas of Section 3.5, we apply the operator $\tilde{\mathcal{L}}_q$ to a local (triplet) excitation and we perform the Gutzwiller-projection, obtaining[2]:

$$\begin{aligned} |q; R\rangle &= \frac{1}{2}\mathcal{P}_G\tilde{\mathcal{L}}_q \left(c^\dagger_{R,\uparrow}c_{0,\uparrow} - c^\dagger_{R,\downarrow}c_{0,\downarrow}\right) \\ &= \frac{1}{2}\frac{1}{\sqrt{N_C}}\mathcal{P}_G \sum_{R'} e^{iq\cdot R'}(-)^{R_x R'_y} \left(c^\dagger_{R+R',\uparrow}c_{R',\uparrow} - c^\dagger_{R+R',\downarrow}c_{R',\downarrow}\right)|\Phi_0\rangle. \end{aligned} \tag{F.16}$$

Compared to the definition of Eq. (3.39), the above expression contains an extra term, $(-)^{R_x R'_y}$, which is a consequence of the fact that G_{T_y} has been applied R'_y times to the creation operator [cf. Eq. (F.11)].

To prove the validity of our construction, we can explicitly show that the excitations of Eq. (F.16) have momentum q with respect to the ground state. Indeed, if we apply the translation T_x, we get

$$\begin{aligned} T_x|q; R\rangle &= \frac{1}{\sqrt{N_C}}\mathcal{P}_G \sum_{R'}\sum_{\sigma} e^{iq\cdot R'}(-)^{R_x R'_y}\sigma \left(\tilde{T}_x c^\dagger_{R+R',\sigma}\tilde{T}_x^{-1}\right)\left(\tilde{T}_x c_{R',\sigma}\tilde{T}_x^{-1}\right)\tilde{T}_x|\Phi_0\rangle \\ &= \frac{1}{\sqrt{N_C}}\mathcal{P}_G \sum_{R'}\sum_{\sigma} e^{iq\cdot R'}(-)^{R_x R'_y}\sigma\ c^\dagger_{R+R'+a_x,\sigma}c_{R'+a_x,\sigma}\left(e^{-i2\pi q_x^0}|\Phi_0\rangle\right) \\ &= e^{-i(q+q^0)\cdot a_x}|q; R\rangle, \end{aligned} \tag{F.17}$$

[1] From the variational point of view of this thesis, this assumption is always true, because actual calculations on finite lattices require the single-particle spectrum of $\mathcal{H}_0$ to be a closed shell, which implies that $|\Phi_0\rangle$ is unique.

[2] We note that, for simplicity, the $S^z_{tot} = 0$ projector and the spin-spin Jastrow factor have been ignored, since their presence would not change the content of the present discussion.

where the last equality is justified by the redefinition of the summation index $R' + a_x \mapsto R'$. This proves that $|q; R\rangle$ is an eigenstate of T_x with total momentum $(q + q^0) \cdot a_x$. On the other hand, if we apply T_y and we account for the effect of the gauge transformation G_{T_y} ("on the right" of the Gutzwiller projector), we get

$$\begin{aligned} T_y|q; R\rangle &= \frac{1}{\sqrt{N_C}} \mathcal{P}_G \sum_{R'} \sum_{\sigma} e^{iq\cdot R'} (-)^{R_x R'_y} \sigma \left(\tilde{T}_y c^\dagger_{R+R',\sigma} \tilde{T}_y^{-1} \right) \left(\tilde{T}_y c_{R',\sigma} \tilde{T}_y^{-1} \right) \tilde{T}_y |\Phi_0\rangle \\ &= \frac{1}{\sqrt{N_C}} \mathcal{P}_G \sum_{R'} \sum_{\sigma} e^{iq\cdot R'} (-)^{R_x (R'_y+1)} \sigma \; c^\dagger_{R+R'+a_y,\sigma} c_{R'+a_y,\sigma} \left(e^{-i2\pi q^0_y} |\Phi_0\rangle \right) \\ &= e^{-i(q+q^0)\cdot a_y} |q; R\rangle. \end{aligned} \tag{F.18}$$

At variance with the previous case, the redefinition of the summation index, $R' + a_y \mapsto R'$, leading to the last equality not only affects the exponential $e^{iq\cdot R'}$, but also the staggered minus sign, causing $(-)^{R_x(R'_y+1)} \mapsto (-)^{R_x R'_y}$. After this relabelling, we recover the state $|q; R\rangle$, which is then an eigenstate of T_y with total momentum $(q+q^0)\cdot a_y$. Thus, in conclusion, $|q; R\rangle$ is an eigenstate of translations and represents an excitation with momentum q (relative to the ground state).

G

Regression analysis of the RBM wave function

As a complement to the variational results obtained with the RBM-fermionic wave function in Chapter 5, we perform a regression analysis to further evaluate the accuracy of the neural network. In particular, we address the capability of the RBM to capture I) the amplitudes and II) the phases of the ground state wave function, as if they were two separate quantities. For this purpose, we consider the $J_1 - J_2$ Heisenberg model on the 4×4 square lattice, and we compute its ground state $|\Upsilon_0\rangle$ by Lanczos diagonalization, for $J_2 = 0$ and $J_2/J_1 = 0.5$. We can expand $|\Upsilon_0\rangle$ on the basis set of the $S^z_{tot} = 0$ sector,

$$|\Upsilon_0\rangle = \sum_\sigma |\sigma\rangle\langle\sigma|\Upsilon_0\rangle = \sum_\sigma \Big[|\langle\sigma|\Upsilon_0\rangle| \times \mathrm{sign}\left(\langle\sigma|\Upsilon_0\rangle\right) \Big] |\sigma\rangle, \tag{G.1}$$

and regard the amplitudes ($|\langle\sigma|\Upsilon_0\rangle|$) and the signs [$\mathrm{sign}\left(\langle\sigma|\Upsilon_0\rangle\right)$] as two independent functions of the configurations σ. Our purpose is fitting each of them separately using RBM functions (or closely related expressions, see below).

The motivation for this regression analysis comes from two sides. On the one hand, the results of Section 5.4.1 may suggest that the better performances of the RBM correlator in the unfrustrated regime ($J_2 = 0$), with respect to the frustrated one ($J_2/J_1 = 0.5$), could be due to the knowledge of the exact sign structure in the former case. Indeed, as already pointed out, the fermionic part of the *Ansatz* for $J_2 = 0$ already possesses the Marshall-Peierls sign [38, 172], and so the role of the (real) RBM is limited to adjusting the amplitudes of the variational state. Thus, we want to isolate the problem of reproducing only the amplitudes of $|\Upsilon_0\rangle$, to understand whether the frustrated regime is more problematic only because of its sign, or because of a combination of signs and amplitudes. On the other hand, we question the capability of a *complex-valued* RBM correlator to efficiently capture a function like the sign of $|\Upsilon_0\rangle$, which takes only values ± 1.

Regression of the amplitudes

First we consider the regression of the amplitudes of the ground state, i.e. $|\langle\sigma|\Upsilon_0\rangle|$. Our fitting functions, which are labelled generically as $\mathcal{C}_{\mathrm{fit}}(\sigma)$, take the form of the RBM without symmetries of Eq. (5.3) [$\mathcal{C}_{\mathrm{RBM}}(\sigma)$], of the translationally invariant RBM of Eq. (5.4) [$\mathcal{C}_{\mathrm{tRBM}}(\sigma)$], and of the fully symmetric RBM of Eq. (5.5) [$\mathcal{C}_{\mathrm{sRBM}}(\sigma)$]. Since the amplitudes of the ground state are real and positive numbers, it is sufficient to take real biases and weights for the fitting functions. The regression analysis is performed by minimizing the following *loss function*[1]:

$$\mathcal{L}_A = 1 - \sum_\sigma |\mathcal{C}_{\mathrm{fit}}(\sigma)| \times |\langle\sigma|\Upsilon_0\rangle|. \tag{G.2}$$

Thanks to the relatively small dimension of the Hilbert space of the model (12870 configurations in the $S^z_{tot} = 0$ sector), the sum over σ can be performed exactly. Minimizing the loss function essentially corresponds to maximizing the overlap between the RBM fitting

[1] For the calculations of this appendix we employed the open-source library TensorFlow [180] and its implementation of the Adam optimizer [181].

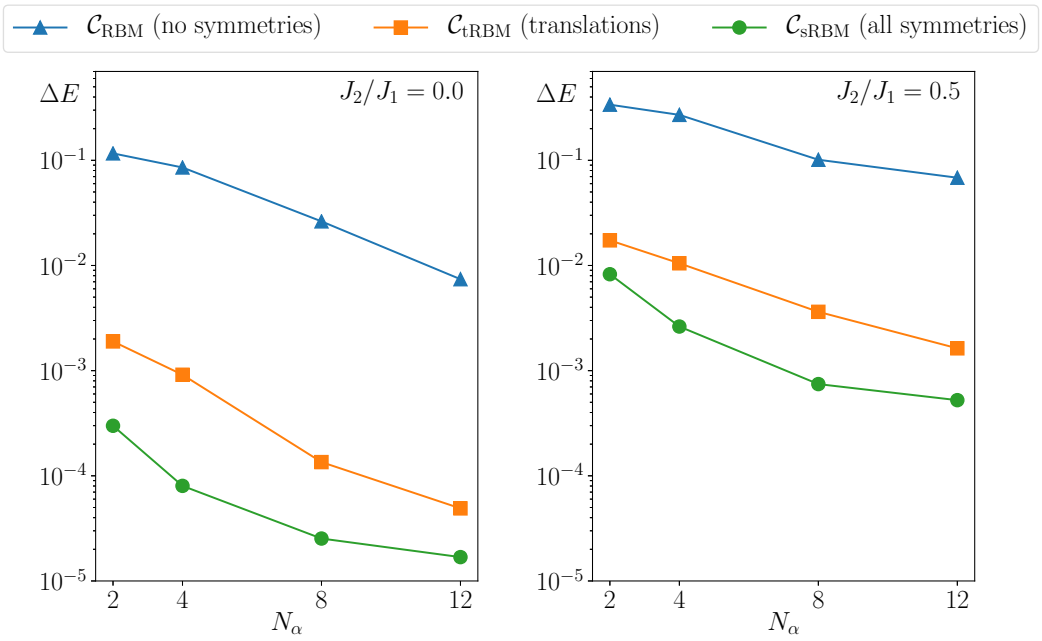

Figure G.1: Relative error of the energies E_{fit} with respect to the exact ground state value E_0 of the $J_1 - J_2$ Heisenberg model on the 4×4 square lattice. The values of E_{fit} are obtained by employing a variational wave function with the exact sign structure of the ground state, whose amplitudes are optimized by a regression analysis. The different RBM fitting functions are reported in the legend and their energies are plotted as a function of the number of hidden units N_α, for the unfrustrated regime ($J_2 = 0$, left panel) and the frustrated one ($J_2/J_1 = 0.5$, right panel).

function and $|\Upsilon_0\rangle$, as if they were two wave functions with identical sign structure. When the optimal parameters are determined, we can construct a physical wave function multiplying $\mathcal{C}_{\text{fit}}(\sigma)$ by the exact ground state sign. Once normalized, this wave function is then employed to compute the expectation value of the ground state energy:

$$E_{\text{fit}} = \sum_{\sigma,\sigma'} \langle \sigma' | \mathcal{H} | \sigma \rangle \times \mathcal{C}_{\text{fit}}(\sigma) \mathcal{C}_{\text{fit}}(\sigma') \times \text{sign}\left(\Upsilon_0(\sigma')\Upsilon_0(\sigma)\right) . \tag{G.3}$$

The relative error of the energies obtained following the above procedure is reported in Fig. G.1. The data clearly show how the inclusion of lattice symmetries significantly improves the accuracy of the results, both in the unfrustrated and in the frustrated regimes. However, the relative error is from 10 to almost 100 times smaller in the $J_2 = 0$ case. This outcome suggests that not only the sign structure of the ground state is more complicated in the frustrated regime, but also the distribution of the amplitudes of the wave function. This conclusion is confirmed by the data shown in Fig. G.2, where the value of the amplitudes is reported, as a function of the number of frustrated bonds with respect to the Néel configurations. In the unfrustrated phase, the main contribution to the wave function clearly comes from the Néel configurations, with few other states contributing. On the other hand, in the frustrated regime, many more configurations contribute to the wave function with a significant weight.

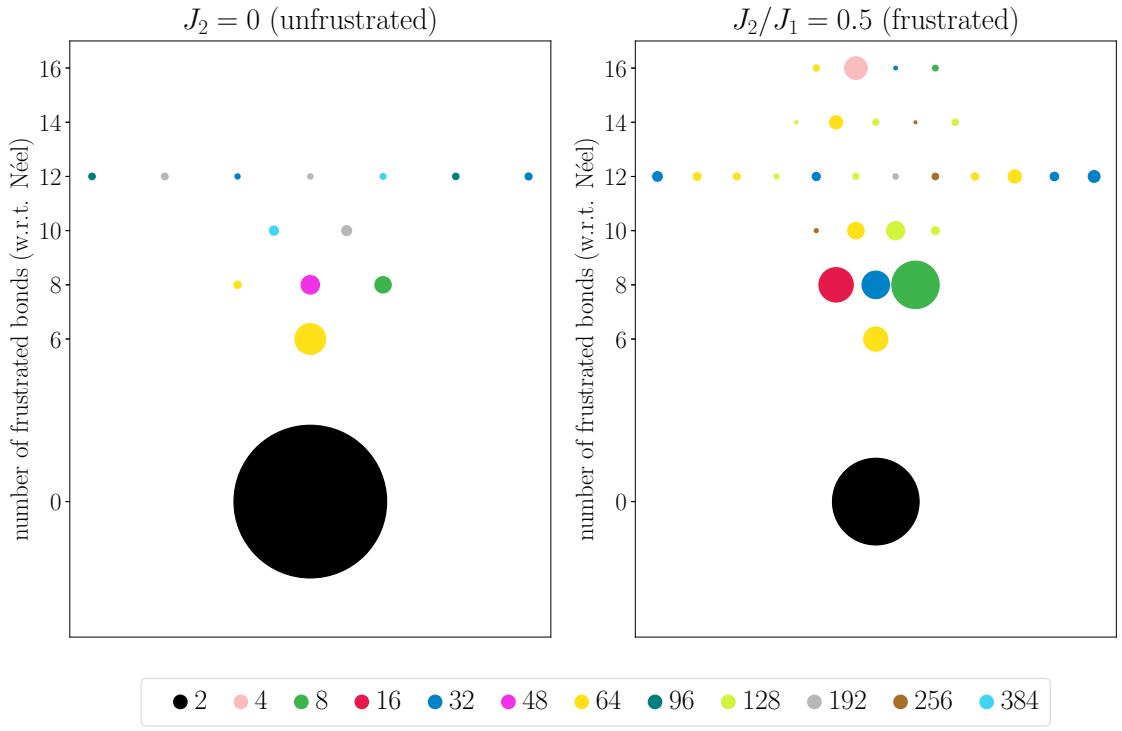

Figure G.2: Distribution of the amplitudes of the exact ground state wave function of the $J_1 - J_2$ Heisenberg model on the 4×4 square lattice. The cases $J_2 = 0$ and $J_2/J_1 = 0.5$ are shown in the left and right panel, respectively. The diameter of the dots is proportional to the value of the amplitude $|\Upsilon_0(\sigma)|$, and, for the sake of clarity, only the configurations σ such that $|\Upsilon_0(\sigma)|^2 > \max_\sigma \left(|\Upsilon_0(\sigma)|^2\right)/1000$ have been reported. The configurations are ordered on the y-axis by counting the number of frustrated bonds with respect to the Néel configurations. The colors of the dots indicate the number of equivalent configurations that are connected by the symmetries of the lattice.

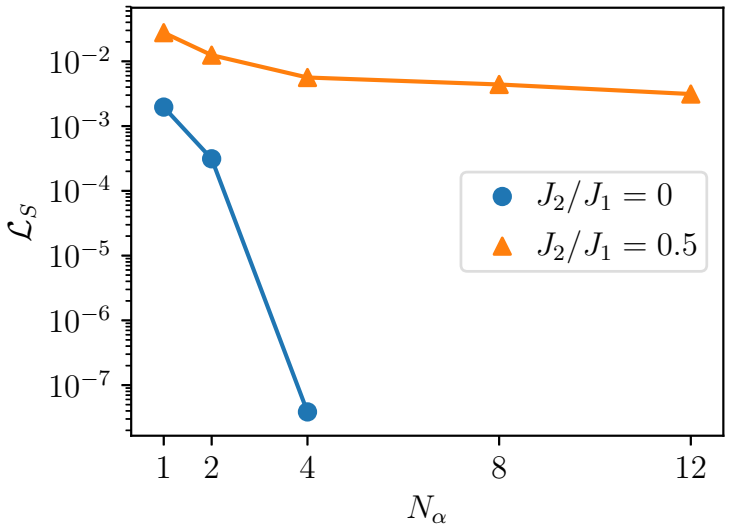

Figure G.3: Optimal values of the loss function of Eq. (G.5) as a function of the number of hidden units N_α, for the cases $J_2 = 0$ (blue circles) and $J_2/J_1 = 0.5$ (orange triangles).

Regression of the sign structure

The second regression analysis regards the sign structure of the wave function, $\text{sign}\left(\langle\sigma|\Upsilon_0\rangle\right)$, which we fit by the following function:

$$\mathcal{C}_{\text{sign}}(\sigma) = \exp\left[i\sum_R\sum_\alpha \log\cosh\left(b^\alpha + \sum_j W_j^\alpha \sigma^z_{j+_R}\right)\right]. \tag{G.4}$$

$\mathcal{C}_{\text{sign}}(\sigma)$ is essentially a translationally invariant RBM [cf. Eq. (5.4)] with an extra imaginary unit at the exponent. We employ real biases and weights such that the resulting fitting function is a pure phase. This function is used to approximate the sign structure of $|\Upsilon_0\rangle$, by minimizing the following loss function:

$$\mathcal{L}_S = 1 - \left|\sum_\sigma |\langle\sigma|\Upsilon_0\rangle|^2 \times \text{sign}\left(\langle\sigma|\Upsilon_0\rangle\right) \times \mathcal{C}_{\text{sign}}(\sigma)\right|. \tag{G.5}$$

The results of the regression of the sign structure are reported in Fig. G.3. In the case $J_2 = 0$, where the ground state wave function follows the Marshall-Peierls rule for the signs [172], the loss function essentially drops to zero when a few hidden units are considered ($N_\alpha = 4$), suggesting the fact that our imaginary-valued fitting function, closely related to the RBM state, can exactly reproduce $\text{sign}(\langle\sigma|\Upsilon_0\rangle)$. On the other hand, in the frustrated regime, where the sign structure is more complicated, the fitting procedure provides far less accurate results. This questions the possibility of accurately approximating the (real) sign structure of frustrated models by employing a complex-valued neural network.

Bibliography

[1] L. D. Landau, Phys. Z. Sowjet. **11**, 26 (1937).

[2] P. Pfeuty, Annals of Physics **57**, 79 (1970).

[3] D. C. Tsui, H. L. Stormer, and A. C. Gossard, Phys. Rev. Lett. **48**, 1559 (1982).

[4] H. L. Stormer, D. C. Tsui, and A. C. Gossard, Rev. Mod. Phys. **71**, S298 (1999).

[5] R. B. Laughlin, Phys. Rev. Lett. **50**, 1395 (1983).

[6] X. G. Wen and Q. Niu, Phys. Rev. B **41**, 9377 (1990).

[7] B. Zeng, X. Chen, D.-L. Zhou, and X.-G. Wen, ArXiv e-prints, arXiv:1508.02595 (2015).

[8] X.-G. Wen, Science **363** (2019).

[9] R. de-Picciotto, M. Reznikov, M. Heiblum, V. Umansky, G. Bunin, and D. Mahalu, Nature **389**, 162 EP (1997).

[10] H. Bethe, Zeitschrift für Physik **71**, 205 (1931).

[11] L. Pitaevskii and S. Stringari, Journal of Low Temperature Physics **85**, 377 (1991).

[12] L. Faddeev and L. Takhtajan, Physics Letters A **85**, 375 (1981).

[13] C. Lacroix, P. Mendels, and F. Mila, eds., *Introduction to frustrated magnetism* (Springer Berlin Heidelberg, 2011).

[14] L. Balents, Nature **464**, 199 (2010).

[15] L. Savary and L. Balents, Rep. Prog. Phys. **80**, 016502 (2016).

[16] Y. Zhou, K. Kanoda, and T.-K. Ng, Rev. Mod. Phys. **89**, 025003 (2017).

[17] J. Knolle and R. Moessner, Annual Review of Condensed Matter Physics **10**, 451 (2019).

[18] P. Anderson, Mat. Res. Bull. **8**, 153 (1973).

[19] P. Fazekas and P. W. Anderson, The Philosophical Magazine: A Journal of Theoretical Experimental and Applied Physics **30**, 423 (1974).

[20] G. Rumer, Göttingen Nachr. Tech., 337 (1932).

[21] L. Pauling, The Journal of Chemical Physics **1**, 280 (1933).

[22] L. C. Pauling, Proceedings of the Royal Society of London. Series A. Mathematical and Physical Sciences **196**, 343 (1949).

[23] C. Lhuillier and G. Misguich, "Introduction to quantum spin liquids", in *Introduction to frustrated magnetism: materials, experiments, theory*, edited by C. Lacroix, P. Mendels, and F. Mila (Springer Berlin Heidelberg, Berlin, Heidelberg, 2011), pp. 23–41.

[24] B. Bernu, P. Lecheminant, C. Lhuillier, and L. Pierre, Phys. Rev. B **50**, 10048 (1994).

[25] L. Capriotti, A. Trumper, and S. Sorella, Phys. Rev. Lett. **82**, 3899 (1999).

[26] S. White and A. Chernyshev, Phys. Rev. Lett. **99**, 127004 (2007).

[27] M. R. Norman, Rev. Mod. Phys. **88**, 041002 (2016).

[28] X. G. Wen, F. Wilczek, and A. Zee, Phys. Rev. B **39**, 11413 (1989).

[29] B. Bauer, L. Cincio, B. P. Keller, M. Dolfi, G. Vidal, S. Trebst, and A. W. W. Ludwig, Nature Communications **5**, 5137 (2014).

[30] G. Misguich, B. Bernu, C. Lhuillier, and C. Waldtmann, Phys. Rev. Lett. **81**, 1098 (1998).

[31] G. Misguich, C. Lhuillier, B. Bernu, and C. Waldtmann, Phys. Rev. B **60**, 1064 (1999).

[32] A. Kitaev, Annals of Physics **321**, January Special Issue, 2 (2006).

[33] Z. Nussinov and J. van den Brink, Rev. Mod. Phys. **87**, 1 (2015).

[34] S. M. Winter, A. A. Tsirlin, M. Daghofer, J. van den Brink, Y. Singh, P. Gegenwart, and R. Valentí, Journal of Physics: Condensed Matter **29**, 493002 (2017).

[35] S. Trebst, ArXiv e-prints, arXiv:1701.07056 (2017).

[36] G. Jackeli and G. Khaliullin, Phys. Rev. Lett. **102**, 017205 (2009).

[37] P. Henelius and A. W. Sandvik, Phys. Rev. B **62**, 1102 (2000).

[38] F. Becca, L. Capriotti, A. Parola, and S. Sorella, "Variational wave functions for frustrated magnetic models", in *Introduction to frustrated magnetism: materials, experiments, theory*, edited by C. Lacroix, P. Mendels, and F. Mila, Springer Series in Solid-State Sciences (Springer (Berlin), 2011), p. 379.

[39] U. Schollwöck, Annals of Physics **326**, January 2011 Special Issue, 96 (2011).

[40] R. Orús, Annals of Physics **349**, 117 (2014).

[41] J. Wen, S.-L. Yu, S. Li, W. Yu, and J.-X. Li, npj Quantum Materials **4**, 12 (2019).

[42] K. Beach and A. W. Sandvik, Nuclear Physics B **750**, 142 (2006).

[43] C. K. Majumdar and D. K. Ghosh, Journal of Mathematical Physics **10**, 1388 (1969).

[44] B. S. Shastry and B. Sutherland, Phys. Rev. Lett. **47**, 964 (1981).

[45] G. Misguich, "Quantum spin liquids and fractionalization", in *Introduction to frustrated magnetism: materials, experiments, theory*, edited by C. Lacroix, P. Mendels, and F. Mila (Springer Berlin Heidelberg, Berlin, Heidelberg, 2011), pp. 407–435.

[46] S. T. Bramwell, "Neutron scattering and highly frustrated magnetism", in *Introduction to frustrated magnetism: materials, experiments, theory*, edited by C. Lacroix, P. Mendels, and F. Mila (Springer Berlin Heidelberg, Berlin, Heidelberg, 2011), pp. 45–78.

[47] B. Dalla Piazza, M. Mourigal, N. Christensen, G. Nilsen, P. Tregenna-Piggott, T. Perring, M. Enderle, D. McMorrow, D. Ivanov, and H. M. Ronnow, Nat. Phys. **11**, 62 (2015).

[48] A. Auerbach, *Interacting electrons and quantum magnetism* (Springer-Verlag, 1994).

[49] A. L. Chernyshev and M. E. Zhitomirsky, Phys. Rev. B **79**, 144416 (2009).

[50] H. M. Rønnow, D. F. McMorrow, R. Coldea, A. Harrison, I. D. Youngson, T. G. Perring, G. Aeppli, O. Syljuåsen, K. Lefmann, and C. Rischel, Phys. Rev. Lett. **87**, 037202 (2001).

[51] N. B. Christensen, H. M. Rønnow, D. F. McMorrow, A. Harrison, T. G. Perring, M. Enderle, R. Coldea, L. P. Regnault, and G. Aeppli, Proceedings of the National Academy of Sciences **104**, 15264 (2007).

[52] R. R. P. Singh and M. P. Gelfand, Phys. Rev. B **52**, R15695 (1995).

[53] O. F. Syljuåsen and P. A. Lee, Phys. Rev. Lett. **88**, 207207 (2002).

[54] W. Zheng, J. Oitmaa, and C. J. Hamer, Phys. Rev. B **71**, 184440 (2005).

[55] O. F. Syljuåsen and H. M. Rønnow, Journal of Physics: Condensed Matter **12**, L405 (2000).

[56] A. W. Sandvik and R. R. P. Singh, Phys. Rev. Lett. **86**, 528 (2001).

[57] A. V. Syromyatnikov, Journal of Physics: Condensed Matter **22**, 216003 (2010).

[58] C.-M. Ho, V. N. Muthukumar, M. Ogata, and P. W. Anderson, Phys. Rev. Lett. **86**, 1626 (2001).

[59] E. A. Ghioldi, M. G. Gonzalez, L. O. Manuel, and A. E. Trumper, **113**, 57001 (2016).

[60] H. Shao, Y. Q. Qin, S. Capponi, S. Chesi, Z. Y. Meng, and A. W. Sandvik, Phys. Rev. X **7**, 041072 (2017).

[61] F. Ferrari and F. Becca, Phys. Rev. B **98**, 100405 (2018).

[62] M. Powalski, K. P. Schmidt, and G. S. Uhrig, SciPost Phys. **4**, 001 (2018).

[63] R. Verresen, F. Pollmann, and R. Moessner, Phys. Rev. B **98**, 155102 (2018).

[64] A. L. Chernyshev and M. E. Zhitomirsky, Phys. Rev. Lett. **97**, 207202 (2006).

[65] M. E. Zhitomirsky and A. L. Chernyshev, Rev. Mod. Phys. **85**, 219 (2013).

[66] M. Mourigal, W. T. Fuhrman, A. L. Chernyshev, and M. E. Zhitomirsky, Phys. Rev. B **88**, 094407 (2013).

[67] S. Ito, N. Kurita, H. Tanaka, S. Ohira-Kawamura, K. Nakajima, S. Itoh, K. Kuwahara, and K. Kakurai, Nature Communications **8**, 235 (2017).

[68] Y. Shirata, H. Tanaka, A. Matsuo, and K. Kindo, Phys. Rev. Lett. **108**, 057205 (2012).

[69] R. Verresen, R. Moessner, and F. Pollmann, Nature Physics **15**, 750 (2019).

[70] F. Ferrari and F. Becca, Phys. Rev. X **9**, 031026 (2019).

[71] M. Mourigal, M. Enderle, A. Klöpperpieper, J.-S. Caux, A. Stunault, and H. M. Rønnow, Nature Physics **9**, Article, 435 EP (2013).

[72] M. Karbach, G. Müller, A. H. Bougourzi, A. Fledderjohann, and K.-H. Mütter, Phys. Rev. B **55**, 12510 (1997).

[73] J.-S. Caux and J. M. Maillet, Phys. Rev. Lett. **95**, 077201 (2005).

[74] J.-S. Caux and R. Hagemans, Journal of Statistical Mechanics: Theory and Experiment **2006**, P12013 (2006).

[75] R. Coldea, D. A. Tennant, A. M. Tsvelik, and Z. Tylczynski, Phys. Rev. Lett. **86**, 1335 (2001).

[76] R. Coldea, D. A. Tennant, and Z. Tylczynski, Phys. Rev. B **68**, 134424 (2003).

[77] M. Kohno, O. A. Starykh, and L. Balents, Nature Physics **3**, Article, 790 EP (2007).

[78] T.-H. Han, J. S. Helton, S. Chu, D. G. Nocera, J. A. Rodriguez-Rivera, C. Broholm, and Y. S. Lee, Nature **492**, 406 EP (2012).

[79] M. Punk, D. Chowdhury, and S. Sachdev, Nature Physics **10**, 289 EP (2014).

[80] G. Baskaran, S. Mandal, and R. Shankar, Phys. Rev. Lett. **98**, 247201 (2007).

[81] R. Feynman, R. Leighton, and M. Sands, *The feynman lectures on physics, vol. iii: the new millennium edition: quantum mechanics*, The Feynman Lectures on Physics (Basic Books, 2011).

[82] J. Knolle, D. L. Kovrizhin, J. T. Chalker, and R. Moessner, Phys. Rev. Lett. **112**, 207203 (2014).

[83] C. Kittel, *Introduction to solid state physics* (Wiley, 1986).

[84] X. Wen, *Quantum field theory of many-body systems: from the origin of sound to an origin of light and electrons*, Oxford Graduate Texts (Oxford University Press, 2004).

[85] X.-G. Wen, Phys. Rev. B **65**, 165113 (2002).

[86] F. Becca and S. Sorella, *Quantum monte carlo approaches for correlated systems* (Cambridge University Press, 2017).

[87] T. Li, EPL (Europhysics Letters) **103**, 57002 (2013).

[88] G. Carleo, I. Cirac, K. Cranmer, L. Daudet, M. Schuld, N. Tishby, L. Vogt-Maranto, and L. Zdeborová, ArXiv e-prints, arXiv:1903.10563 (2019).

[89] S. Bieri, C. Lhuillier, and L. Messio, Phys. Rev. B **93**, 094437 (2016).

[90] B. Huang, Y. B. Kim, and Y.-M. Lu, Phys. Rev. B **95**, 054404 (2017).

[91] N. Read and B. Chakraborty, Phys. Rev. B **40**, 7133 (1989).

[92] J. Reuther, S.-P. Lee, and J. Alicea, Phys. Rev. B **90**, 174417 (2014).

[93] Y.-D. Li, Y.-M. Lu, and G. Chen, Phys. Rev. B **96**, 054445 (2017).

[94] B. Huang, W. Choi, Y. B. Kim, and Y.-M. Lu, Phys. Rev. B **97**, 195141 (2018).

[95] G. Chen, A. Essin, and M. Hermele, Phys. Rev. B **85**, 094418 (2012).

[96] Y.-M. Lu and Y. Ran, Phys. Rev. B **84**, 024420 (2011).

[97] W.-J. Hu, F. Becca, A. Parola, and S. Sorella, Phys. Rev. B **88**, 060402 (2013).

[98] I. Affleck and J. Marston, Phys. Rev. B **37**, 3774 (1988).

[99] J. Gubernatis, N. Kawashima, and P. Werner, *Quantum monte carlo methods: algorithms for lattice models* (Cambridge University Press, 2016).

[100] N. Metropolis, A. W. Rosenbluth, M. N. Rosenbluth, A. H. Teller, and E. Teller, The Journal of Chemical Physics **21**, 1087 (1953).

[101] S. Sorella, Phys. Rev. B **64**, 024512 (2001).

[102] S. Sorella, Phys. Rev. B **71**, 241103 (2005).

[103] W. H. Press, S. A. Teukolsky, W. T. Vetterling, and B. P. Flannery, *Numerical recipes 3rd edition: the art of scientific computing*, 3rd ed. (Cambridge University Press, New York, NY, USA, 2007).

[104] T. Li and F. Yang, Phys. Rev. B **81**, 214509 (2010).

[105] F. Ferrari, S. Bieri, and F. Becca, Phys. Rev. B **96**, 104401 (2017).

[106] B. Dalla Piazza, (2014) `10.5075/epfl-thesis-6090`.

[107] F. Ferrari, A. Parola, S. Sorella, and F. Becca, Phys. Rev. B **97**, 235103 (2018).

[108] S. R. White and I. Affleck, Phys. Rev. B **54**, 9862 (1996).

[109] S. Eggert, Phys. Rev. B **54**, R9612 (1996).

[110] H. Yokoyama and Y. Saiga, Journal of the Physical Society of Japan **66**, 3617 (1997).

[111] A. Lavarélo and G. Roux, The European Physical Journal B **87**, 229 (2014).

[112] L. Vanderstraeten, J. Haegeman, F. Verstraete, and D. Poilblanc, Phys. Rev. B **93**, 235108 (2016).

[113] D. Hendry and A. E. Feiguin, ArXiv e-prints, arXiv:1907.01384 (2019).

[114] T. Barthel, U. Schollwöck, and S. R. White, Phys. Rev. B **79**, 245101 (2009).

[115] S. Yunoki and S. Sorella, Phys. Rev. B **74**, 014408 (2006).

[116] R. Kaneko, L. F. Tocchio, R. Valentí, F. Becca, and C. Gros, Phys. Rev. B **93**, 125127 (2016).

[117] J. des Cloizeaux and J. J. Pearson, Phys. Rev. **128**, 2131 (1962).

[118] B. Lake, D. A. Tennant, J.-S. Caux, T. Barthel, U. Schollwöck, S. E. Nagler, and C. D. Frost, Phys. Rev. Lett. **111**, 137205 (2013).

[119] A. Sandvik, Phys. Rev. B **56**, 11678 (1997).

[120] M. Calandra Buonaura and S. Sorella, Phys. Rev. B **57**, 11446 (1998).

[121] C. L. Henley, Phys. Rev. Lett. **62**, 2056 (1989).

[122] H.-C. Jiang, H. Yao, and L. Balents, Phys. Rev. B **86**, 024424 (2012).

[123] S.-S. Gong, W. Zhu, D. Sheng, O. Motrunich, and M. Fisher, Phys. Rev. Lett. **113**, 027201 (2014).

[124] L. Wang, Z.-C. Gu, F. Verstraete, and X.-G. Wen, Phys. Rev. B **94**, 075143 (2016).

[125] D. Poilblanc and M. Mambrini, Phys. Rev. B **96**, 014414 (2017).

[126] L. Wang and A. Sandvik, Phys. Rev. Lett. **121**, 107202 (2018).

[127] R. Haghshenas and D. Sheng, Phys. Rev. B **97**, 174408 (2018).

[128] D. Poilblanc, M. Mambrini, and S. Capponi, ArXiv e-prints, arXiv:1907.03678 (2019).

[129] A. W. Sandvik, Phys. Rev. Lett. **98**, 227202 (2007).

[130] R. G. Melko and R. K. Kaul, Phys. Rev. Lett. **100**, 017203 (2008).

[131] I. Affeck, M. P. Gelfand, and R. R. P. Singh, **27**, 7313 (1994).

[132] I. Affleck and B. I. Halperin, Journal of Physics A: Mathematical and General **29**, 2627 (1996).

[133] L. Vanderstraeten, J. Haegeman, and F. Verstraete, Phys. Rev. B **99**, 165121 (2019).

[134] L. Balents, M. P. A. Fisher, and C. Nayak, Phys. Rev. B **60**, 1654 (1999).

[135] N. Ma, G.-Y. Sun, Y.-Z. You, C. Xu, A. Vishwanath, A. W. Sandvik, and Z. Y. Meng, Phys. Rev. B **98**, 174421 (2018).

[136] J. G. Rau, P. A. McClarty, and R. Moessner, Phys. Rev. Lett. **121**, 237201 (2018).

[137] E. Shender, Sov. Phys. JETP **56**, 178 (1982).

[138] B. Schmidt and P. Thalmeier, Physics Reports **703**, Frustrated two dimensional quantum magnets, 1 (2017).

[139] R. R. P. Singh, W. Zheng, J. Oitmaa, O. P. Sushkov, and C. J. Hamer, Phys. Rev. Lett. **91**, 017201 (2003).

[140] Z. Zhu, P. A. Maksimov, S. R. White, and A. L. Chernyshev, Phys. Rev. Lett. **120**, 207203 (2018).

[141] J. Iaconis, C. Liu, G. B. Halász, and L. Balents, SciPost Phys. **4**, 003 (2018).

[142] Z. Zhu and S. R. White, Phys. Rev. B **92**, 041105 (2015).

[143] W.-J. Hu, S.-S. Gong, W. Zhu, and D. Sheng, Phys. Rev. B **92**, 140403 (2015).

[144] Y. Iqbal, W.-J. Hu, R. Thomale, D. Poilblanc, and F. Becca, Phys. Rev. B **93**, 144411 (2016).

[145] O. A. Starykh, A. V. Chubukov, and A. G. Abanov, Phys. Rev. B **74**, 180403 (2006).

[146] W. Zheng, J. O. Fjærestad, R. R. P. Singh, R. H. McKenzie, and R. Coldea, Phys. Rev. B **74**, 224420 (2006).

[147] J. Ma, Y. Kamiya, T. Hong, H. B. Cao, G. Ehlers, W. Tian, C. D. Batista, Z. L. Dun, H. D. Zhou, and M. Matsuda, Phys. Rev. Lett. **116**, 087201 (2016).

[148] E. A. Ghioldi, A. Mezio, L. O. Manuel, R. R. P. Singh, J. Oitmaa, and A. E. Trumper, Phys. Rev. B **91**, 134423 (2015).

[149] E. A. Ghioldi, M. G. Gonzalez, S.-S. Zhang, Y. Kamiya, L. O. Manuel, A. E. Trumper, and C. D. Batista, Phys. Rev. B **98**, 184403 (2018).

[150] L. Chen, D.-W. Qu, H. Li, B.-B. Chen, S.-S. Gong, J. von Delft, A. Weichselbaum, and W. Li, Phys. Rev. B **99**, 140404 (2019).

[151] Y. Li, G. Chen, W. Tong, L. Pi, J. Liu, Z. Yang, X. Wang, and Q. Zhang, Phys. Rev. Lett. **115**, 167203 (2015).

[152] Y. Li, H. Liao, Z. Zhang, S. Li, F. Jin, L. Ling, L. Zhang, Y. Zou, L. Pi, Z. Yang, J. Wang, Z. Wu, and Q. Zhang, Scientific Reports **5**, Article, 16419 EP (2015).

[153] L. Ding, P. Manuel, S. Bachus, F. Grußler, P. Gegenwart, J. Singleton, R. D. Johnson, H. C. Walker, D. T. Adroja, A. D. Hillier, and A. A. Tsirlin, ArXiv e-prints, arXiv:1901.07810 (2019).

[154] M. M. Bordelon, E. Kenney, C. Liu, T. Hogan, L. Posthuma, M. Kavand, Y. Lyu, M. Sherwin, N. P. Butch, C. Brown, M. J. Graf, L. Balents, and S. D. Wilson, Nature Physics (2019) 10.1038/s41567-019-0594-5.

[155] D. A. Huse and V. Elser, Phys. Rev. Lett. **60**, 2531 (1988).

[156] Y.-M. Lu, Phys. Rev. B **93**, 165113 (2016).

[157] X.-Y. Song, C. Wang, A. Vishwanath, and Y.-C. He, ArXiv e-prints, arXiv:1811.11186 (2018).

[158] T. Tay and O. Motrunich, Phys. Rev. B **83**, 235122 (2011).

[159] G. Carleo and M. Troyer, Science **355**, 602 (2017).

[160] J. Chen, S. Cheng, H. Xie, L. Wang, and T. Xiang, Phys. Rev. B **97**, 085104 (2018).

[161] G. Torlai, G. Mazzola, J. Carrasquilla, M. Troyer, R. Melko, and G. Carleo, Nat. Phys. **14**, 447 (2018).

[162] G. Torlai and R. Melko, ArXiv e-prints, arXiv:1801.09684 (2018).

[163] D.-L. Deng, X. Li, and S. Das Sarma, Phys. Rev. X **7**, 021021 (2017).

[164] X. Gao and L.-M. Duan, Nat. Comm. **8**, 662 (2017).

[165] D.-L. Deng, X. Li, and S. Das Sarma, Phys. Rev. B **96**, 195145 (2017).

[166] Y. Nomura, A. Darmawan, Y. Yamaji, and M. Imada, Phys. Rev. B **96**, 205152 (2017).

[167] S. Clark, J. Phys. A: Math. and Theor. **51**, 135301 (2018).

[168] I. Glasser, N. Pancotti, M. August, I. Rodriguez, and J. Cirac, Phys. Rev. X **8**, 011006 (2018).

[169] K. Choo, G. Carleo, N. Regnault, and T. Neupert, Phys. Rev. Lett. **121**, 167204 (2018).

[170] N. Le Roux and Y. Bengio, Neural Comput. **20**, 1631 (2008).

[171] M. Capello, F. Becca, M. Fabrizio, S. Sorella, and E. Tosatti, Phys. Rev. Lett. **94**, 026406 (2005).

[172] W. Marshall and R. Peierls, Proc. Royal Soc. Lon. Series A. Math. and Phys. Sciences **232**, 48 (1955).

[173] N. Read and S. Sachdev, Phys. Rev. Lett. **62**, 1694 (1989).

[174] H. Schulz, T. Ziman, and D. Poilblanc, J. Phys. I France **6**, 675 (1996).

[175] K. Choo, T. Neupert, and G. Carleo, Phys. Rev. B **100**, 125124 (2019).

[176] M. Baity-Jesi, L. Sagun, M. Geiger, S. Spigler, G. B. Arous, C. Cammarota, Y. LeCun, M. Wyart, and G. Biroli, in Proceedings of the 35th international conference on machine learning, Vol. 80, edited by J. Dy and A. Krause, Proceedings of Machine Learning Research (Oct. 2018), pp. 314–323.

[177] T. Vieijra, C. Casert, J. Nys, W. De Neve, J. Haegeman, J. Ryckebusch, and F. Verstraete, ArXiv e-prints, arXiv:1905.06034 (2019).

[178] J. Carrasquilla, A. di Ciolo, F. Becca, V. Galitski, and M. Rigol, Phys. Rev. B **88**, 241109 (2013).

[179] J. J. Sakurai, *Modern quantum mechanics; rev. ed.* (Addison-Wesley, Reading, MA, 1994).

[180] Martín Abadi, Ashish Agarwal, Paul Barham, Eugene Brevdo, Zhifeng Chen, Craig Citro, Greg S. Corrado, Andy Davis, Jeffrey Dean, Matthieu Devin, Sanjay Ghemawat, Ian Goodfellow, Andrew Harp, Geoffrey Irving, Michael Isard, Y. Jia, Rafal Jozefowicz, Lukasz Kaiser, Manjunath Kudlur, Josh Levenberg, Dan Mané, Rajat Monga, Sherry Moore, Derek Murray, Chris Olah, Mike Schuster, Jonathon Shlens, Benoit Steiner, Ilya Sutskever, Kunal Talwar, Paul Tucker, Vincent Vanhoucke, Vijay Vasudevan, Fernanda Viégas, Oriol Vinyals, Pete Warden, Martin Wattenberg, Martin Wicke, Yuan Yu, and Xiaoqiang Zheng, *TensorFlow: large-scale machine learning on heterogeneous systems*, Software available from tensorflow.org, 2015.

[181] D. P. Kingma and J. Ba, ArXiv e-prints, arXiv:1412.6980 (2014).